The Detection and Removal of Pollutants in Aquatic Environments: Developing Sensitive Electrochemical Sensors and Using Magnetic Adsorbents

A thesis submitted to Maynooth University in fulfilment of the requirements for the degree of

Doctor of Philosophy

By

Tian Yu, B.Sc.

Department of Chemistry,

Maynooth University,

Maynooth, Co. Kildare,

February 2024

Research Supervisor: Prof. Carmel Breslin

Head of Department: Prof. Denise Rooney

Table of Contents

Declaration

I hereby certify that this thesis has not been submitted before, in whole or part, to this or any other university for any degree, and is, except where stated otherwise, the original work of the author.

This thesis has been prepared in accordance with the PhD regulations of Maynooth University and is subject to copyright. For more information see PhD Regulations (December 2022)

Signed: Tian Yu Data 09/02/2024

Tian Yu B.Sc (Hon.)

Acknowledgement

How time flies! The study at Maynooth University for four years is drawing to an end in the twinkling of an eye. On the occasion of completing my PhD thesis, I would like to express my sincerest gratitude and best wishes to my alma mater and everyone who has helped me.

Firstly, I would like to thank my supervisor, Professor Carmel Breslin for her immeasurable help, significant support and patient guidance over the past few years during my PhD study as well as her concern in life, which makes me feel at home here. I was so lucky to meet a kind-hearted and patient supervisor, who gave me confidence and strength to overcome one difficulty after another. I will forever be indebted to her.

I would like to thank my supervisor for bringing me into this excellent research team four years ago. The topic selection of the thesis, the resolution of specific problems in the experiment, and the final completion of the thesis all gathered a lot of her efforts. Moreover, her profound knowledge, rigorous academic attitude and tireless exploration spirit towards science will benefit me throughout my life. She will be my role model on the path of scientific research. Here, I would like to express my heartfelt gratitude and sincerest respect to her! Wishing her good health, peace, happiness and all the best. I wish she will achieve greater success in her future career.

Thanks to all the Professors and Doctors in my Progression Meeting, Denise Rooney, John McCaffrey, John Stephens, Eithne Dempsey, Tobias Krämer, Elisa Fadda, Diego Montagner, for your kind help, support and constructive suggestions, which were very helpful for my further research work.

Thanks to all the Professors in my PhD Viva, John P. Lowry, John Cassidy and Thomas Naughton, for your warm help, support, constructive suggestions for the revison of my thesis, patience guidence and encourage, which would be very helpful for my further development. I will never forget you for a lifetime. Wishing you good health, peace, happiness and all the best. I wish you will achieve greater success in your future career.

Thanks to all the technical staffs for all your kind help! To Ollie and Karen, thanks for your kind help with the SEM measurements. To Donna and Carol, thanks for your kind help when encountering some problems. To Noel and Walter, thanks for your warm help while meeting some problems in life. To Orla and Anne, thanks for your kind help during my time demonstrating.

Thanks to all the staffs of the chemistry department for making me feel welcome.

Thanks to all my colleagues for all your warm help! To Caytlin and Colm, thanks for your generous help while meeting with difficulties in life and work. To Rupa, thanks for your friendly help and hard work during writing the research paper. To Pedro, thanks for your kind help and fruitful discussion in the lab. To the other members in our research group, past and present, Bronach, Daniele, Gillian, Joe, Luke, Marilia, Tara, Yiran, thanks for your warm help and companionship. Your cheers and laughter have made my graduate career rich and colorful! I wish everyone all the best in the future!

I wish to express my appreciation to the Irish Research Council for funding my work and life for the past three years, to Department of Chemistry and Maynooth University for supporting my work for the past several years.

I would like to thank my parents for their care, understanding, support and selfless help. I hope my family has good health, peace and happiness.

After graduating with a PhD, I will return to China. I will remember every one of you, my friends. I will always cherish this friendship. I hope our friendship lasts forever! Finally, I wish you all good health, successful careers and much joy and happiness in your lives.

Abbreviations

Abbreviation	Full name
˚C	Degree celsius
λ_{max}	Wavelength at Maximum Absorbance
A	Absorbance
AA	Ascorbic Acid
AC	Ammonium Chloride
AFM	Atomic Force Microscope
A-GCE	Activated Glassy Carbon Electrode
A cm^{-2}	Current density-amps per centimetre squared
AuNPs	Gold Nanoparticles
BiFE	Bismuth Film Electrode
CA	Citric Acid
4-Cl-2MP	4-Chloro-2-methylphenol
CD	Circular Dichroism
CE	Counter Electrode
CLC	Capillary Liquid Chromatography
CV	Cyclic Voltammetry
CPA	Constant Potential Amperometry
CPE	Carbon Paste Electrode
2,4-DB	4-(2,4-Dichlorophenoxy) butyric Acid
dm^3	Cubic decimetre
DME	Dropping Mercury Electrode
DMF	Dimethylformamide
DPASV	Differential Pulse Anodic Stripping Voltammetry
DPV	Differential Pulse Voltammetry
E_{app}	Applied Potential
EDX	Energy Dispersive X-Ray

EIS	Electrochemical Impedance Spectroscopy
FT-IR	Fourier Transform Infrared Spectroscopy
FQ	Fluoroquinolone Antibiotics
GC	Gas Chromatography
GCE	Glassy Carbon Electrode
g-C_3N_4	Graphitic Carbon Nitride
Glu	Glucose
GO	Graphene Oxide
Gr	Graphene nanoplatelets (10 μm)
h	Hour
HAc	Acetic Acid
HC	Hydrocortisone
HPLC	High-Performance Liquid Chromatography
I	Current
IR	Infrared
LEVO	Levofloxacin
LOD	Limit of Detection
LSV	Linear Sweep Voltammetry
MCPA	4-Chloro-2-methylphenoxyacetic acid
MOF	Metal Organic Framework
mL	Millilitre
mol	Mole
min	Minute
MTZ	2-Methyl-5-nitroimidazole-1-ethanol
mV	Millivolt
MWCNT	Multiwalled Carbon Nanotubes
nm	Nanometre
NPs	Nanoparticles
NPV	Normal Pulse Voltammetry
o-NP	*o*-Nitrophenol

p-ABSA	p-Aminobenzene Bulfonic Acid
PANI	Polyaniline
PBS	Phosphate Buffer Solution
PDDA	Poly(diallyldimethylammonium chloride)
PDPP	Pyridine Diketopyrrolopyrrole
pH	Logarithmic scale of concentration of hydronium ions
p-NP	*p*-Nitrophenol
QN	Quinolone Antibiotic
RE	Reference Electrode
rGO	Reduced Graphene Oxide
s	Second
SCE	Saturated Calomel Electrode
SEM	Scanning Electron Microscopy
SECM	Scanning Electrochemical Microscopy
SERS	Surface Enhanced Raman Spectroscopy
SPE	Screen Printed Electrode
SWCNT	Single-Walled Carbon Nanotube
SWV	Square Wave Voltammetry
SY	Sunset Yellow
TBACl	Tetrabutylammonium Chloride
UV-Vis	Ultraviolet-visible
ν	Scan rate
V	Volt
WE	Working Electrode

Abstract

With the rapid development of industry and economies across the world, the problem of environmental pollution in aquatic environments has become one of the key issues facing the World. Consequently, the development of efficient and sensitive analytical techniques to determine the levels of organic pollutants in water environments and cost-effective strategies to remove these pollutants, are now more important than ever before.

In this thesis, sensitive and selective electrochemical sensors with very good long-term stability were developed for the detection of 4-chloro-2-methylphenoxyacetic acid (MCPA), *p*-nitrophenol (*p*-NP), metronidazole (MTZ), and levofloxacin (LEVO). Two strategies were employed in the development of these sensors. Firstly, glassy carbon electrode (GCE) was activated to generate active sites to enhance the electron-transfer process. Secondly, binder-free nanocomposites were employed to facilitate the detection of MCPA, *p*-NP, MTZ and LEVO. The nanocomposites included graphene, bismuth and copper nanostructures. These were all formed using electrodeposition, avoiding the need to use binders that are typically employed with drop casting. Using these approaches, impressive limits of detection of 8.0 nM, 0.18 nM, 0.9 nM and 11.86 nM were achieved in the electrochemical detection of (1) MCPA at activated GCE, (2) *p*-NP with bismuth dendrites deposited onto activated GCE, (3) MTZ with the sequential electrodeposition of graphene nanoplatelets (Gr) and bismuth and (4) LEVO with the sequential electrodeposition of Gr and copper at GCE, respectively. Further, graphene supported magnetic nanocomposites (Gr/Fe) were fabricated and used as adsorbents for the potential removal of MCPA, *p*-NP, MTZ and LEVO from aquatic environments. Iron nanostructures were employed as the magnetic component. These nanocomposites not only prevent the aggregation of the graphene sheets, but also can endow graphene with magnetic properties. This makes the magnetic graphene adsorbents easy to separate by external magnetic fields, greatly simplifying the recycling process. The adsorption kinetics and adsorption isotherms were studied, and the reproducibility, selectivity and reusability of the magnetic Gr/Fe composites were evaluated.

Chapter 1

Introduction and Literature Review

1.1 Introduction

The work reported in this thesis has five objectives:

1. To develop a novel electrochemical sensor for the determination of 4-chloro-2-methylphenoxyacetic acid (MCPA) through simple activation of a glassy carbon electrode (GCE). MCPA is one of the more commonly employed herbicides. MCPA is harmful to aquatic species, animals and can impact on human health even at relatively low concentrations. Therefore, its sensitive detection using simple and cost-effective methods is important.

2. To form a bismuth based electrochemical sensor for the detection of *para*-nitrophenol (*p*-NP) through a simple activated GCE modified with bismuth. *p*-NP is an important intermediate of chemical raw materials, thereby easily entering the environment. *p*-NP not only can generate carcinogen nitrosamine, increasing the risk of cancer in humans, but also can cause protein denaturation in the human body, leading to a series of symptoms including dizziness, anemia, liver, and nervous system damage. Accordingly, the accurate detection of *p*-NP in drinking water is of great significance as it is closely related to human life and health.

3. To fabricate a bismuth-graphene based electrochemical sensor for the determination of metronidazole (MTZ) via successive electrodeposition of graphene and bismuth. MTZ has been commonly employed in the treatment of infections caused by bacteria in both humans and animals. Nevertheless, MTZ has genotoxic and mutagenic side effects. Its accumulation in the aquatic environment can be hazardous to both humans and aquatic life. Consequently, it is necessary to establish a simple and fast high-performance analysis method for MTZ.

4. To develop a copper-graphene based electrochemical sensor for the detection of levofloxacin (LEVO) via successive electrodeposition of graphene and copper. LEVO is widely used in the clinical treatment of bacterial infections in humans and other animals. A large amount of LEVO can enter the environment through metabolites in human and animal bodies, and the wastewater generated by pharmaceutical factories, leading to increasing the concentration of LEVO in the environment. High concentrations of LEVO can cause interference or even interruption in the circle of

ecosystems. Moreover, the long-term presence of LEVO in the environment can lead to antibiotic resistance in pathogenic bacteria, which can enter the human and animal food chain, thereby increasing the threat to their health. Hence, developing a simple and effective detection method for LEVO is of great significance in relation to human health.

5. To find a removal method for MCPA, *p*-NP, MTZ and LEVO, from aqueous solutions. Nowadays, many removal methods have been utilised in water treatment, including adsorption, membrane separation, degradation and biological treatment. Among them, the adsorption method is considered as a superior and widely employed technique because it is relatively low-cost, easy to operate, and has fewer harmful secondary products. For this technology, the use of effective adsorbents is crucial for ensuring water treatment efficiency. Therefore, using adsorbents to remove the four pollutants from aqueous solution and evaluating the adsorption capacity under the different experimental conditions can provide a theoretical basis and technical guidance for the remediation of pollutants from water environments.

In this Introduction chapter, an introduction to the pollutants to be determined, electrochemical sensors, the modification of working electrodes and the removal of the pollutants is described. The materials used in the electrode modification processes and their contribution to electrochemical sensors are also introduced and discussed.

In Chapter 2, the relevant experimental materials, preparation of the solutions, techniques and apparatus used, along with an overview of the theories and related equations employed in this thesis are detailed.

In Chapter 3, the experiment results, and main findings for the activated GCE (A-GCE) used as a sensor are presented and discussed. Within this chapter the preparation and characterisation of the activated GCE sensor is described. The GCE is simply activated through an electrochemical technique and the optimum parameters for the sensing performance are obtained. The activated GCE is then utilised as a sensor for the detection of MCPA, displaying good detection performance.

In Chapter 4, the research results and findings are presented and discussed for the bismuth modified A-GCE used as a sensor (A-GCE/Bi). This chapter includes the

preparation and characterisation of A-GCE/Bi in which the successful electrodeposition of bismuth onto the surface of the A-GCE is achieved. The developed A-GCE/Bi sensor was then used for the determination of *p*-NP. Compared to the A-GCE sensor, the A-GCE/Bi sensor displayed enhanced sensing performance for the determination of *p*-NP under the same experiment conditions.

In Chapter 5, the experimental results and findings are provided and discussed for the bismuth and graphene (Gr) modified sensor. This chapter presents the preparation and characterisation of Bi and Gr modified GCE sensor (GCE/Gr/Bi), which was successfully fabricated by the successive electrodeposition of both the Gr and Bi on the surface of the GCE. The developed sensor was then employed for the detection of MTZ, giving an electrochemical sensor with a renewable electrode surface.

In Chapter 6, the research results and findings are shown and discussed for the copper and graphene (Gr) modified sensor. This chapter includes the fabrication and characterisation of a Cu and Gr modified GCE sensor (GCE/Gr/Cu), which was successfully prepared by the successive electrodeposition of both the Gr and Cu on the surface of the GCE. The prepared sensor was then used for the detection of LEVO, achieving sensitive detection of LEVO.

In Chapter 7, the experimental results and findings are presented and discussed for the removal of the four pollutants from aqueous solutions using magnetic graphene as an adsorbent. The removal efficiency was evaluated, and adsorption models were analysed. The magnetic adsorbent was successfully synthesised by modifying Gr with Fe (Fe/Gr) and its recyclability was investigated.

In Chapter 8, the final conclusions for the results and findings in this thesis are summarised, relating to both the developed sensors and the removal of the four pollutants from aqueous solutions.

1.2 Research Background of the Thesis

The water environment is one of the basic elements that constitute the human living environment, and it is an important place for the survival and development of human society. Due to the rapid development of industry and economy as well as the rapid

increase in population, a large amount of domestic sewage, industrial and agricultural wastewater, and waste residues are discharged into the water environment, leading to a sharp deterioration of the global ecological environment. Serious environment pollution incidents occur frequently, thus posing a serious threat to human health. Therefore, providing clean and safe water resources, especially drinking water, is a huge challenge in modern society. The pollutants in water environments are generally divided into inorganic pollutants, organic pollutants, and microorganism. Typical organic pollutants include organic pesticides, nitrophenols, and antibiotics [1]. The enriched organic pollutants pose a threat to the water environment, seriously affecting human health and ecological structure. Currently, researchers are attempting to remove organic pollutants using a series of methods, such as physical degradation, chemical degradation and biodegradation [2]. However, it is difficult to remove organic pollutants completely. More seriously, the organic pollutants still have toxicity at low concentrations. In addition, once accumulated in the human body, the organic pollutants can cause various acute and chronic diseases, including reproductive, neurological, immune system disorders, and even cancer [3]. Thus, the long-term accumulation of low concentrations of organic pollutants in water environments poses a threat to ecological security and human health.

Therefore, the sensitive detection of low concentrations of organic pollutants in water environments has become an important aspect in the monitoring and governance of water environments. The removal of pollutants from water environments is more challenging, especially the development of reusable adsorbents. Therefore, the development of accurate, fast, and sensitive electrochemical sensors and efficient and reusable adsorbents for the removal of organic pollutants from water are the focus in this thesis. MCPA was selected as a representative of pesticides, *p*-NP as a representative of nitrophenols, and MTZ and LEVO serve as representatives of antibiotics. In total, four electrochemical sensors were developed and used for their detection and the magnetic adsorbents were utilised to remove them from aqueous solutions.

1.3 Roles of the Four Selected Compounds

1.3.1 Role of 4-chloro-2-methylphenoxyacetic acid (MCPA)

Pesticides have increasingly become a fundamental part of modern agriculture, forestry, and sustainable food supplies throughout the whole world [4]. However, pesticides are chemical substances, which not only can kill a variety of pests, but also are contaminating natural ecosystems and threatening biodiversity [5]. The accumulation of pesticide residues may cause great harm to the environment and human health [6]. Pesticides are broadly divided into fungicides, insecticides, rodenticides, and herbicides [7]. Among herbicides, 4-Chloro-2-methylphenoxyacetic acid (MCPA, as shown in Figure 1-1) is one of the more commonly employed herbicides. It is widely utilised in agriculture in marginal and upland agricultural areas due to its effectiveness in weed control [8]. Normally, MCPA is used through spraying and thereby it is frequently found in plants, soil, and water [9], causing serious pollution in the environment. Moreover, owing to its relatively good solubility in water and rather poor adsorption by the soil substrate, MCPA can easily enter surface and ground water bodies [10]. Indeed, MCPA has been observed in several water systems, including rivers and streams, during various water quality monitoring programmes [11].

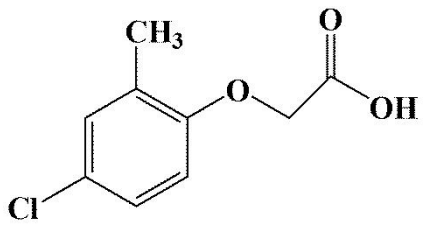

Figure 1-1. The molecular structure of MCPA.

MCPA is harmful to aquatic species [12] and animals [13] and can impact on human health even at relatively low concentrations [14]. The World Health Organisation (WHO) provides a guideline value of 2 μg/L of MCPA in drinking water (WHO, 2003) [15]. The European Commission Drinking Water Directive 98/83/EC, which concerns

the quality of water intended for human consumption, stipulates that the maximum concentration of any individual pesticides in drinking water is 0.1 μg/L and the maximum concentration of the total sum of all pesticides present is 0.5 μg/L [16,17].

1.3.2 Role of *p*-nitrophenol (*p*-NP)

Phenols involve endogenous and exogenous phenols. The phenols contained in plants are called endogenous phenols, which are beneficial to human and plant health, whereas the exogenous phenols not only are harmful to human and plant, but also can cause serious environmental pollution. The exogenous phenols mainly include phenol and its derivatives, such as nitrophenol, naphthol, and cresol [18]. Nitrophenols, including *o*-nitrophenol, *m*-nitrophenol and *p*-nitrophenol, are important intermediates of chemical raw materials. They are widely employed in manufacturing medications, insecticides, and dyes [19]. The toxicity and stability of nitrophenol are the reasons for their adverse effects on plants, animals, and humans. Due to high chemical stability and resistance to microbial decomposition, nitrophenol pollutants can exist in water for a long time, and they can be continuously accumulated in the food chain, thereby entering the human body. The ingestion or inhalation of nitrophenol can lead to drowsiness, nausea, cyanosis, and headache [20,21]. Nitrophenols have been recognised as a serious pollutant by the US Environmental Protection Agency. Due to the high solubility in water, *p*-NP is widespread in industrial effluents from fine chemical and production industries, thereby entering the environment. The European Commission has set the maximum limit for drinking water at 0.1 ppb, and the United States Environmental Protection Agency has stipulated a maximum concentration of *p*-NP in daily drinking water at 60 ppb (0.43 μM) [22]. The chemical structure of *p*-NP, also called 4-nitrophenol, is shown in Figure 1-2.

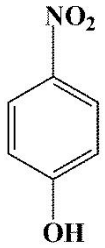

Figure 1-2. The molecular structure of *p*-NP.

1.3.3 Role of metronidazole (MTZ)

Antibiotics, as a class of antibacterial drugs used to kill or inhibit bacterial growth, have been widely employed in the treatment of human diseases, animal husbandry, and aquaculture because of their ability to prevent bacterial infections and promote growth. Antibiotics enter the aquatic environment through the discharge of wastewater treatment plants, industrial wastewater as well as wastewater from livestock and aquaculture, as shown in Figure 1-3 [23]. With the excessive use of antibiotics, the consumption of antibiotics is increasing year by year across the world. It is estimated that the global consumption of antibiotics for edible animals will be increased by 52% from 2013 to 2030 [24], indicating that antibiotic pollution will become increasingly a more serious problem. Due to the misuse and overuse of antibiotics, multidrug-resistant bacteria have spread all over the world, giving rise to an increasing number of life-threatening infections, which are difficult to treat with currently available medicines [25].

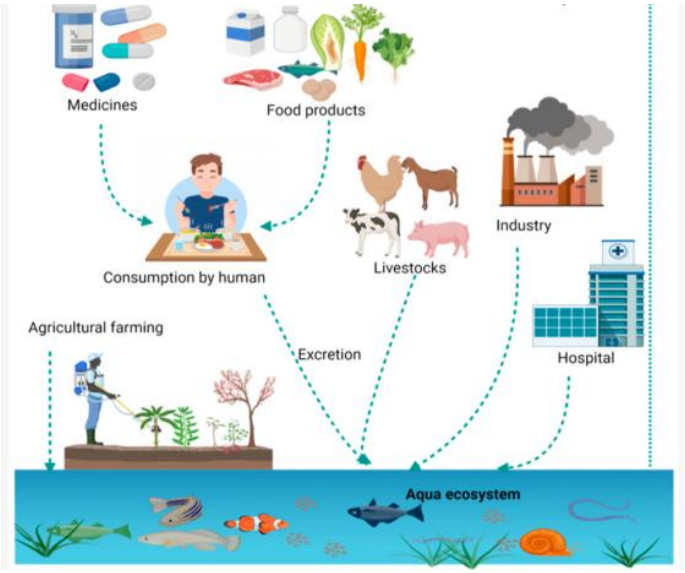

Figure 1-3. Pathways for antibiotics entering the environment [23].

MTZ (see Figure 1-4) belongs to the nitroimidazole family and has been widely employed as an anti-inflammatory and antimicrobial drug to treat the infections caused by bacteria such as helicobacter pylori [26], giardia lamblia and trichomonas vaginalis [27]. In addition, MTZ can also effectively treat oral and dental infections, respiratory tract infections and Crohn´s disease [28]. Thus, MTZ has been extensively used to treat

infections in both humans and animals. However, MTZ has genotoxic and mutagenic side effects and long-term or excessive use of MTZ may cause leucopenia, multiple neuritis, and even cancer [29]. Due to high solubility and good stability in water, MTZ can persist for considerable time in water environments. Indeed, MTZ with high concentration has been found in water supply system in urban areas [30], which can be hazardous to human, animal, and aquatic life.

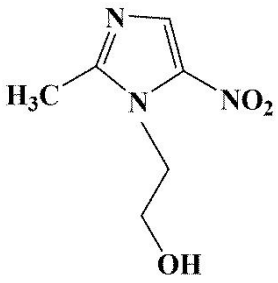

Figure 1-4. The molecular structure of MTZ.

1.3.4 Role of levofloxacin (LEVO)

Among various antibiotics, quinolone antibiotics (QNs) have attracted special attention. Since the first generation of QNs was introduced in 1962, as naphthoic acid, thousands of QNs have been synthesised, and the fourth generation of QNs are now widely available [31]. The fluoroquinolone antibiotics (FQs), belonging to the third generation of artificially synthesised QNs, greatly improved the broad-spectrum antibacterial activity due to the introduction of fluorine atoms, showing good antibacterial effect on both gram-positive and gram-negative bacteria and mycoplasma [32]. Levofloxacin (LEVO, as shown in Figure 1-5) as a typical representative of FQs has been extensively used to treat respiratory, urinary, chronic bronchitis, sinusitis, and skin infections [33]. Thus, at present, LEVO is widely employed in the clinical treatment of bacterial infections in humans and animals because of strong tissue penetration, high drug tolerance, long half-life, and high bioavailability [34]. Nevertheless, it is indicated that the misuse and overuse of LEVO may give rise to serious adverse reactions, such as gastrointestinal reactions, toxic side reactions of the central nervous system, and mental

disorders [35]. With the discharge of metabolites from human and animal bodies and the wastewater generated by pharmaceutical factories and disinfecting human residential areas, the concentration of LEVO is increasing in aquatic environments. In addition, the high solubility of LEVO in the water environment and its tendency to accumulate may pose a potential risk to the water environment and human health.

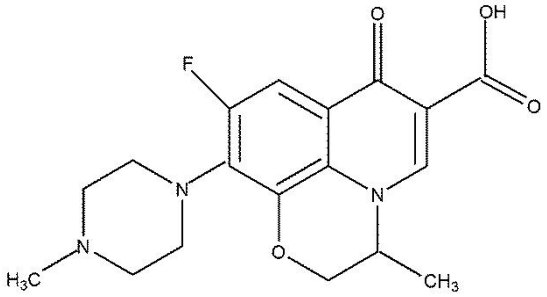

Figure 1-5. The molecular structure of LEVO.

1.4 The Detection of MCPA, *p*-NP, MTZ and LEVO

Many analytical methods have been developed for the determination of MCPA, *p*-NP, MTZ and LEVO, including gas chromatography (GC) [36-38], capillary liquid chromatography (CLC) [39], high performance liquid chromatography (HPLC) [40-43], capillary electrophoresis [44,45], solid phase extraction coupled with ion mobility spectrometry [46], electrochemiluminescence [47] and chemiluminescence [48,49], spectrophotometry analysis [50-53], Surface Enhanced Raman Spectroscopy (SERS) [54-56], fluorescence analysis [57-59], fluorescence polarization immunoassay [60], and circular dichroism (CD) [61]. However, these methods are restricted by the need for expensive instrumentation and a high degree of user expertise, cumbersome sample treatment procedures and time-consuming analysis processes and high detection costs. These methods are not suitable for the rapid and on-site analysis of water samples. Therefore, there is a need for the development of an effective, sensitive, and simple method to detect analytes such as the four compounds, MCPA, *p*-NP, MTZ and LEVO, in aquatic environments. Electrochemical sensors have real potential in addressing these needs.

1.5 Electrochemical Sensors

The word ″sensor″ originates from the Latin word *sentire*, meaning to ″sense″. In the past, people mainly relied on their eyes, ears, nose, skin to sense changes in color, sound, odor, and temperature from external stimulus to obtain information. Sensors are an extension of these five sense organs of humans. Sensors mostly rely on imitating human sensory organs to obtain information, for example, light sensors correspond to the human body's visual organs, gas sensors correspond to the human body's olfactory organs, sound sensors correspond to the human body's auditory organs, chemical sensors correspond to the human body's taste organs, while temperature and pressure sensors correspond to the human body's tactile organs. Thus, it can be said that different sensors have different sensory functions.

Electrochemical sensors are a very important branch among the chemical sensors and are a widely used type of chemical sensors. The electrochemical sensor is based on electroanalytical techniques to measure the electrochemical charge transfer reaction at the electrode interface of the sensor. The principle of an electrochemical sensor is to convert the signals generated by detecting molecules or substances into electrical signals, thereby analysing the targets qualitatively and quantitatively. Electrochemical sensors generally consist of three parts: recognition element, signal converter and signal output device, as shown in Figure 1-6. The output signals have variability, such as the voltage, current, or electrochemical impedance, thereby the electrochemical sensors can be classified into several main categories including amperometric sensor, potentiometric sensor or impedimetric sensor [62].

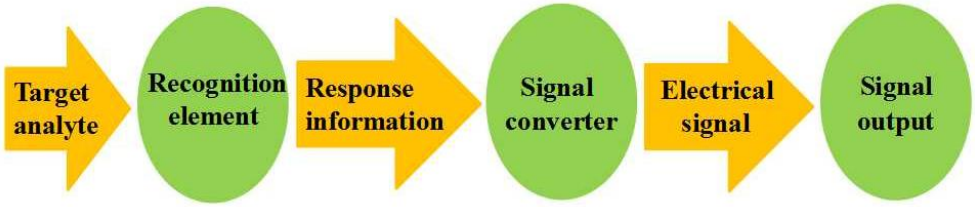

Figure 1-6. A schematic diagram illustrating the major components of an electrochemical sensor.

Compared with other detection techniques, electrochemical sensors overcome the disadvantages of high cost and complex operation, and have several advantages, including low cost, small working space, simple structure, high selectivity, high sensitivity, fast and accurate detection, easy integration and miniaturisation and good stability, easily transported to various water bodies to give onsite and real-time detection. Thus, electrochemical sensors have attracted more and more attention. So far, the world of electrochemical sensors is diverse and is rapidly developing due to its high demand and continuous technological improvements. At present, electrochemical sensors have shown very broad application prospects in fields, such as industry [63], agriculture [64], biomedicine [65], environmental monitoring [66], food safety [67], in situ water-based research [68], life science research [69] and other fields [70]. With the applied range becoming more and more widespread and the emergence of nanotechnology and nanomaterials, the development of novel electrochemical sensors has been accelerated.

1.6 Functionalisation of Working Electrodes

Among the components of electrochemical sensors, the sensitive components, namely the electrode materials, are a key part that affects the performance of the electrochemical sensors. In terms of electrode materials, such as carbon, platinum, or gold, the glassy carbon electrode (GCE) is one of the most widely used working electrodes. Glassy carbon is prepared by direct pyrolysis of a phenolic resin. Carbonisation studies indicate that the unique structure of the final glassy carbon is a direct consequence of the production of very stable aromatic ribbon molecules by the coalescence of phenolic polymer chains at an early stage of pyrolysis [71,72]. For this reason, the GCE displays a series of advantages including good conductivity, high chemical stability, small coefficient of thermal expansion, high hardness, high smoothness, it is easily polishing into a mirror surface and has a wide potential window. Moreover, the GCE is chemically inert and has a high hydrogen overpotential, so GCE is widely used in electrochemistry and analytical chemistry.

The performance of the GCE as a working electrode greatly depends on its surface property. As the reaction kinetics of untreated GCE surfaces are slow, it does not satisfy the need of trace level analysis. To improve the performance of GCE and expand its application scope, all kinds of ways have been attempted to functionalise the surface of the GCE. Among the functionalisation methods, chemical and electrochemical methods are the most commonly used strategies.

1.6.1 Activation of GCE

Unmodified or bare GCE, is not effective in the detection of trace substances as it has very few active sites for electron transfer. Consequently, the activation of the electrode surface before its use is very important. It has been shown that the activation process not only cleans the electrode surface but also changes the microstructure and chemical property of the electrode surface [73]. This can affect the sensitivity of the electrode for the detection of the target analytes. Several techniques have been utilised to activate the electrode and highly sensing performance has been obtained after the activation of the electrode. The activation methods include mechanical polishing [74], solvent cleaning [75], vacuum heat treatment [76], laser-based thermal treatment [77]， microwave plasma treatment [78]， radio-frequency plasma treatment [79] and electrochemical polarisation [80].

Among the activation methods listed above, the electrochemical technique has several advantages: (i) compared to other tedious and complex modification materials, the electrochemical activation process has simplicity, efficiency and is low cost; (ii) the electrochemical activation is recognised as environmentally friendly owing to the less involvement of hazardous chemicals. To date, carbon nanotubes [81], activated carbon [82] and glassy carbon electrodes [83] have been activated by the electrochemical oxidation when polarised to high potentials which are typically beyond the oxygen evolution reaction. At these high potentials, $OH^{\bullet}$ radicals are generated which can attack the C–C bonds, resulting in the formation of abundant oxygen-containing functional groups, such as phenol, carbonyl, and carboxylic groups [84]. These oxygenated groups increase the rate of the electron transfer process and enhance the electrochemical detection performance. For example, Tenent et al. observed a large increase in the

electron transfer rate for the $Fe^{II/III}$ ion on the locally oxidised carbon surface in comparison to the unoxidised region using scanning electrochemical microscopy (SECM) [85]. Indeed, a series of electrochemical sensors based on activated GCE have been successfully employed in the electrochemical detection of imidacloprid [86], uric acid [87], acetaminophen [88] and sunset yellow [89].

The commonly used electrochemical oxidation methods for the activation of GCE include constant potential anodic oxidation, constant current oxidation and cyclic voltammetry scanning to high anodic potentials. In addition, to achieve the best performance and improve reproducibility, after electrochemical oxidation, the activated GCE are followed by cathodic reduction processes or continuous cycling until the cyclic voltammograms reach a steady state. For instance, Huang et al. used electrochemical oxidation at 1.75 V for 300 s firstly, and then electrochemical reduction at −1.75 V for 300 s in 0.1 M PBS to activate GCE. This was followed by scanning between 0 and 0.8 V for 20 cycles in PBS until a stable voltammogram was attained [87]. The activated GCE was further utilised to detect uric acid, showing the higher anodic peak current compared to untreated GCE, which was attributed to the formation of rich oxygen-containing groups during the anodically pretreating process. The pretreated GCE was successfully applied to measure uric acid in different concentrations from 0.1 – 15 μM, delivering a LOD of 0.02 μM, in which LOD is defined as limit of detection and calculated based on $3S_b$/sensitivity, where S_b is the standared deviation. In addition, the activated GCE showed good selectivity and was employed to determine uric acid in human urine and serum samples, providing good recoveries.

Figure 1-7. Activation steps of GCE and the redox mechanism of the sunset yellow (SY) at the A-GCE [89].

Lu et al. used the cyclic voltammetry scanning method to activate GCE in 0.1 M PBS at the scan rate of 100 mV s^{-1} by cycling in the potential range between −2.0 V and 2.0 V vs. SCE for 10 cycles. The authors employed the activated GCE to determine sunset yellow in the concentration range of 0.005−1.0 µM, giving the LOD of 0.00167 µM, as shown in Figure 1-7 [89].

Mao et al. used anodic oxidation at a potential of 2.0 V vs. Ag/AgCl for 220 s, cathodic reduction at −1.0 V for 60 s and CV scanning in the potential range of −0.5 to 0.8 V for 3 cycles to prepare an activated GCE in PBS. The sensor was subsequently employed for the simultaneous detection of Cd^{2+} and Pb^{2+} in the concentration ranges of 0.05 to 5 µM with LODs of 17 nM for Cd^{2+} and 0.3 nM for Pb^{2+} [90]. These studies indicate that the activated electrode can detect not only a single component, but also multiple components simultaneously and reveals good selectivity.

In another work, GCE was activated by electrochemical anodisation in 0.5 M H_2SO_4. The authors utilised the activated GCE to achieve the simultaneous determination of ranitidine and metronidazole [91], as shown in Figure 1-8. It has also been shown using Atomic Force Microscope (AFM) images that electrochemical activation in 0.1 M H_2SO_4 gives rise to an increase in the roughness of the GCE and this also appears to be beneficial in its use as a sensor [92].

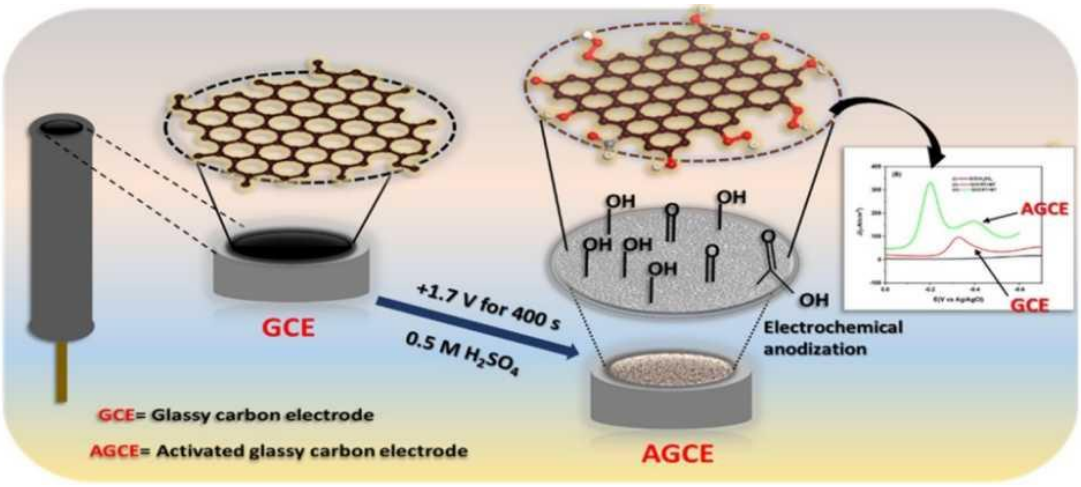

Figure 1-8. Simple electrochemical activation of GCE in H_2SO_4 for the detection of ranitidine and metronidazole [91].

Usually, the electrochemical activation of GCE is carried out in acidic medium or neutral medium at a wide potential range. The work of Temoçin confirmed that alkaline media can also be employed to activate GCE. The GCE was activated by electrochemically cycling between 0.0 and 0.9 V vs. Ag/AgCl at 30 mV s^{-1} for 40 cycles in 0.5 M NaOH. Different voltammograms were observed depending on the number of activation cycles used and this was attributed to the formation of a new electrode surface with carbonyl, carboxyl, and hydroxyl radical species [93].

Apart from the direct use of electrochemically activated GCE sensors, the activation of GCE is also attracting attention in the fabrication of GCE with electrocatalytic materials. For example, Li et al. firstly activated GCE by successive sweeps in the potential range of 0 to 1.8 V vs. SCE at 50 mV s^{-1} for 25 cycles in 0.1 M PBS (pH 7.0), and then fabricated NiOOH on the activated GCE surface by physical adsorption. The prepared electrode displayed a highly sensitive response to the oxidation of glucose and methanol. It was concluded that the increase in the surface area of the activated GCE and the generation of C−O functional groups promoted the adsorption of the NiOOH component [94].

In summary, these investigations suggest that the electrochemical activation of GCE can be performed in a wide pH range including strong acids, weak acids, neutral, and basic media, using constant or scanning potentials. Furthermore, the electrochemical activation of GCE can be utilised as an initial tool to provide a better surface for further functionalisation with other components. Therefore, the electrochemical activation of GCE is receiving increasing attention in the fabrication of sensors.

1.6.2 Modification of GCE

In 1975, the introduction of chemically modified electrodes broke through traditional electrochemistry [95,96]. At that time, most studies were limited to the interfaces between bare electrodes and electrolytes. By tailoring the molecules on the surface of the electrodes, the electrodes can be designed with predetermined functions as intended, so that the desired reactions occur selectively on the surface of the electrodes, achieving

the design of electrode function at the molecular level. Now, chemically modified electrodes are a very active research field in electrochemistry and electroanalytical chemistry. Many functional materials, such as graphene and metal nanoparticles, are used as the modifiers to prepare chemically modified electrodes, delivering a series of electrochemical sensors with good detection performance. Some of these modifiers, which are used in this thesis, are now introduced, and discussed.

1.6.2.1 Graphene modified GCE

Graphene was discovered in 2004 by Novoselov and Geim et al. [97], hereby they won the Nobel Prize for Physics in 2010. The emergence of graphene has opened an exciting new field for the scientific and technological advancement of two-dimensional nanomaterials. Due to the excellent physical and electronic properties, compared to other carbon-based nanomaterials, graphene has become a fast-growing star in materials research.

1.6.2.1.1 Structure, property and application of graphene

Graphene possesses a two-dimensional, single layered sp^2-hybridised carbon atomic sheet that is close-packed in a honeycomb lattice structure [98]. Due to its unique structure, graphene not only has excellent electronic, optical, magnetic, thermal and mechanical properties, but also possesses superior characteristics including high chemical stability, high conductivity (mobility of charge carriers reaches 200000 cm^2 V^{-1} s^{-1}) [99], thermal conductivity (~5000 W m^{-1} K^{-1}) [100], impressive mechanical strength (fracture strength reaching 125 GPa) [101], inherent flexibility (values of its Young's modulus reach ~1100 GPa) [101] and a huge specific surface area (2630 m^2 g^{-1}) [102]. These surprising features have led to the rapid development of graphene in physics, chemistry, biology, materials, and related interdisciplinary subjects [103]. So far, graphene has exhibited broad application prospects in functional devices varying from graphene bulbs, graphene superconductors to graphene chips [104] across applications in biotechnology [105], biomedicine [106], materials [107], catalysis [108], electronics and optoelectronics [109], energy conversion and storage devices [110].

1.6.2.1.2 Source of graphene

Since graphene was isolated in 2004, different preparation methods have been employed in its synthesis. The preparation methods can be divided into two key categories: the top-down and bottom-up methods [111]. The top-down approach involves exfoliation from graphite, using chemical, electrochemical, and mechanical methods to overcome the van der Waals forces between the layers to form graphene. In the bottom-up approach, graphene is formed atom by atom, which includes biomass pyrolysis, thermal annealing, epitaxial growth, and chemical vapor deposition. In this method, high energy is required to decompose and graphitise the carbon-containing materials to produce graphene.

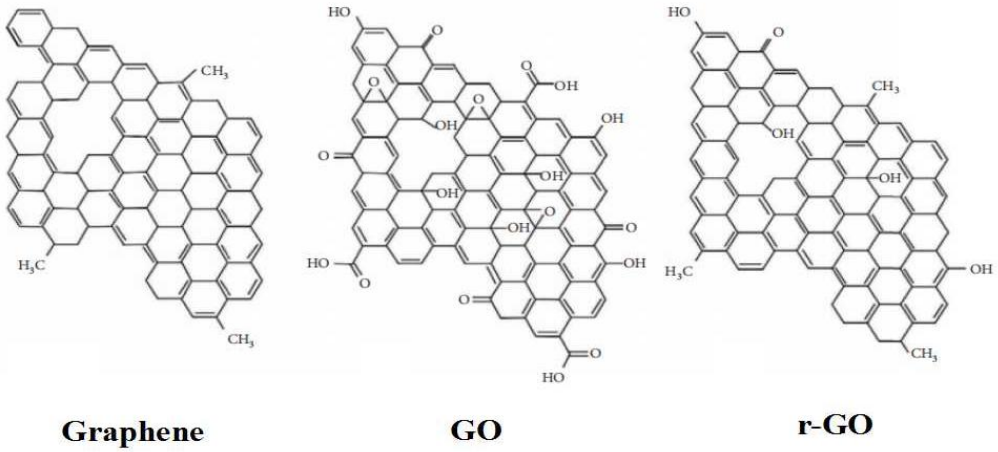

Figure 1-9. Structure of graphene, graphene oxide (GO), and reduced graphene oxide (rGO) [111].

It is noteworthy that each of the preparation methods of graphene has its advantages and drawbacks, and the functional characteristics and surface functional groups of graphene are different. Figure 1-9 shows the structures of graphene, graphene oxide (GO) and reduced graphene oxide (rGO), which are synthesised using different preparation methods [111]. Compared to graphene, the GO surface contains abundant oxygen-containing functional groups, hydroxyl, carboxyl, and epoxy bonds, which provides it with good hydrophilicity [112] and biocompatibility [113], and makes it easy

to be modified through covalent or noncovalent interactions with other molecules [114]. Thus, GO is easier dispersed in water or organic solvents to produce a more stable suspension than graphene. It is evident that the number of oxygen-containing groups on rGO is reduced while the conjugated network structure in the rGO is restored, compared to the GO, thereby the rGO possesses a high specific surface area, good electronic conductivity, and mechanical strength. Accordingly, rGO has been applied as a promising material in the fabrication of electrochemical sensors [115].

1.6.2.1.3 Graphene-based electrochemical sensors

Graphene, as a star in materials science in the 21st century, has been widely applied in the development of electrochemical sensors. Since graphene displays high chemical stability, high electron transfer mobility, large specific surface area and wide potential window, it has become an ideal candidate in constructing electrochemical sensors [116,117]. Moreover, the low cost and non-toxic characteristics of graphene facilitate the construction of environmentally friendly and cost-effective electrochemical sensors with high sensing performance [118]. Accordingly, a large variety of electrochemical sensors based on graphene and its derivatives have been developed and their sensing performance to various analytes was investigated with satisfactory results. These include biomolecules [119], additives in food and drink [120], antibiotics [121], pesticides [122], and pollutants in the environment [123].

GO has been used in the development of several sensors. A GO-modified GCE was formed by using dispersed GO in dimethylformamide (DMF) to coat the GCE surface which was used directly for the detection of *p*-NP, giving the concentration of *p*-NP ranging from 0.1 to 120 μM with the LOD of 0.02 μM [124]. Moreover, the GO was modified by pyridine diketopyrrolopyrrole (PDPP) polymer through strong hydrogen bonding and π–π interactions to form a PDPP-GO composite material, which was drop cast on the GCE to obtain the modified electrode, GCE/PDPP-GO [125], shown in Figure 1-10. It showed a sensitive sensor response to the electrochemical reduction of *p*-NP, delivering a LOD of 0.10 μM.

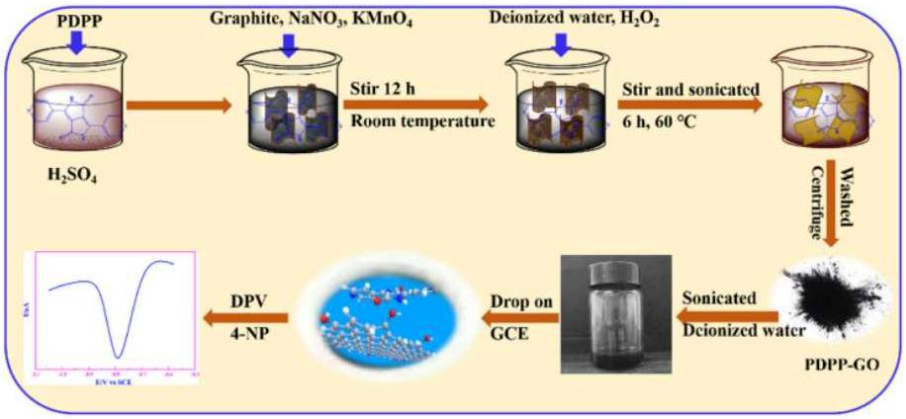

Figure 1-10. The synthetic processes of PDPP-GO/GCE [125].

Fe_2O_3 modified GO was obtained by a hydrothermal synthesis strategy. The obtained Fe_2O_3@GO nanocomposite was utilised for the modification of GCE, and the prepared modified electrode (Fe_2O_3@GO/GCE) gave rise to the sensitive determination of MTZ in the linear range of 1 to 1680 µM with the LOD of 55 nM [126].

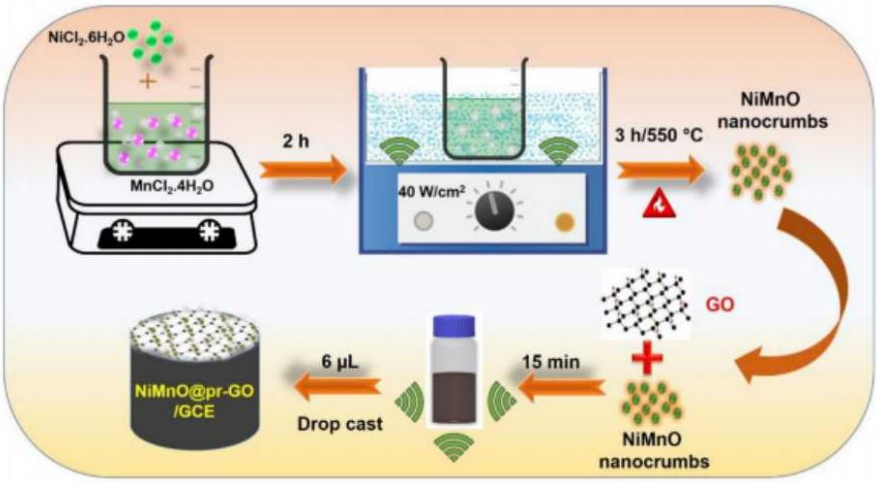

Figure 1-11. Sonochemical synthesis process of NiMnO@pr-GO nanocomposite [127].

Another nanocomposite formed by combining nickel-manganese oxide nanoparticles with rGO, was prepared by ultrasonication, and then used to decorate the GCE, NiMnO@pr-GO, as shown in Figure 1-11, which exhibited higher electrocatalytic

activity for the reduction of MTZ, giving a LOD of 90 nM [127]. The superior sensing performance of the modified electrode was attributed to the combination of electrocatalytic activity of the rGO and NiMnO nanocrumbs. Recently, flower-like cobalt modified rGO (f-Co@rGO) was successfully synthesised by a simple one-pot hydrothermal reduction method using GO and Co^{III} acetylacetonate as the starting materials. This nanocomposite modified GCE realised ultrasensitive electrochemical detection of MTZ with a LOD of 0.015 nM [128].

In addition, poly(p-aminobenzene sulfonic acid) and rGO (poly(p-ABSA)-rGO) film modified GCE was fabricated by electrochemically scanning the potential from −1.5 to 2.5 V for 5 cycles in PBS containing 2.0 mM of p-ABSA and 0.1 mg/mL GO. The sensor was used in the determination of LEVO in the concentration range of 2.0 to 30.0 μM and gave a LOD of 0.12 μM [129]. The rGO was also decorated with poly(diallyldimethylammonium chloride) solution (PDDA) and gold nanoparticles (AuNPs) to form the hybrid composite Au/PDDA/rGO, which was coated on the GCE to construct an electrochemical sensor for LEVO [130]. These studies indicate that graphene and its derivatives are interesting in the development of electrochemical sensors and exhibit enhanced sensing performance for the detection of analytes.

1.6.2.2 Bismuth film modified electrodes

Bismuth is inexpensive and has comparatively little toxicity. It has been employed in the preparation of different nanomaterials with unique structure, remarkable physical and chemical properties, which have made it suitable for various applications, including electronics, storage and conversion energy, photocatalysis and sensors as well as other biomedical applications [131]. Bismuth modified electrodes are often termed bismuth film electrodes (BiFEs), which have gained a lot of attention due to their good environmental qualities, wide negative potential window, partial insensitivity to dissolved oxygen and high hydrogen overpotential. Since Wang et al. first utilised BiFE as a sensor for the stripping voltammetric analysis of Pb, Cd, Zn in 2000 [132], BiFEs have developed rapidly and the application scope of BiFEs is also constantly expanding.

1.6.2.2.1 Preparation of BiFEs

The substrates that support BiFEs are mainly based on carbon materials, such as glassy carbon electrodes (GCEs) [133], graphite electrodes [134], carbon fiber microelectrodes [135], carbon paste electrodes [136], boron doped diamond electrodes [137], screen printed electrodes [138], and pencil electrodes [139]. Among them, GCE is widely used due to its low background current and good stability. Moreover, some metal materials, such as Cu, Pt, Au etc. were also used as the substrates of BiFEs [140]. Regardless of which electrode is utilised as the substrate, before the deposition of bismuth film, the substrates need to be pre-treated with mechanical polishing or chemical activation. The mechanical polishing can provide a fresh and smooth electrode surface, improving the reproducibility of electrode, while the chemical activation can increase the active sites on the electrode surface, which is conducive to the deposition of bismuth films.

The methods for preparing BiFEs normally include electroplating and sputtering, among them the electroplating is mostly used in current research. The electroplating processes can be carried out in three different ways: (i) **ex−situ**: the electroplating of Bi film is completed prior to transferring the BiFE to the solution in which the analytes are present [141]. The electroplating process is mostly carried out in acidic environments as Bi^{III} are easily hydrolysed at high pH. Parameters such as the concentration of Bi^{III} ions, deposition potential, deposition time, using stirring or static solution, can affect the thickness and morphology of bismuth films on the electrodes; (ii) **in−situ**: Bi^{III} are added directly into the solution containing analytes and the analytes are incorporated as the Bi film is formed. For this in situ approach, the selection of deposition potential and deposition time is closely related to the analytes. This approach is widely used in anodic stripping voltammetry due to its simplicity and less consumption of time. The in situ electroplating process can be conducted in acidic and alkaline solutions. Li et al. concluded that in highly alkaline solutions, Bi^{III} ions form soluble hydroxides, which can be dissolved in water and electrochemically reduced on the electrode surface, Equation 1−1 [142].

$$Bi^{3+} + OH^{-} = Bi\,(OH)^{2+} \qquad (1-1)$$

Bismuth oxides, such as Bi_2O_3, have also been used by first modifying the surface with the oxides, followed by electrochemical reduction to generate metallic bismuth on the electrode at a certain deposition potential through Equation 1–2 [143].

$$Bi_2O_3\,(s) + 3H_2O + 6e^- \rightarrow 2Bi\,(s) + 6OH^- \qquad (1–2)$$

This approach is usually used with carbon paste electrodes (CPE) as the substrate due to easy mixing of carbon paste with Bi_2O_3. Although this approach is simple and low cost, it has its limitations. Therefore, among these three approaches, ex situ and in situ are the most widely utilized for the construction of BiFEs.

The sputtering method has been utilised to grow bismuth films on silicon substrates [144]. The prepared bismuth film showed a rough structure composed of many uniformly sized nanoparticles, to give rise to an increase of the active sites, compared with BiFEs formed by other methods. Moreover, the bismuth films were combined with other functional composites to form the modified electrodes which have extended the application field of BiFEs.

1.6.2.2.2 Application of BiFEs

BiFEs have been used as effective sensors not only for the determination of over 20 elements in the periodic table or their compounds [145], but also for the determination of organic compounds such as pollutants, drugs, insecticides, and some bioactive substances [146,147]. For example, Muna et al. fabricated a sensor to selectively determine heavy metals Pb and Cd with bismuth and antimony over a GCE (Sb/Bi-GCE) [148]. The fabricated nanocomposite exhibited a remarkable performance towards sensing Pb^{II} and Cd^{II} and therefore, the current response was enhanced compared to the bare GCE, Sb/GCE and Bi/GCE. The differential pulse anodic stripping voltammetry (DPASV) produced better analytical outcomes, showing that the LOD was 0.01 ppb for Pb^{II} and 0.5 ppb for Cd^{II} using Sb/Bi-GCE. Another example is that of Al-Harbi who fabricated a sensitive sensor to detect cetirizine dihydrochloride at pH 8.0 with bismuth

deposited on the GCE (Bi/GCE), which displayed good sensing performance for the determination of cetirizine dihydrochloride with a LOD of 1.5 nM and a linear concentration range of 5 to 1200 nM [149]. Moreover, BiFEs have also been utilised in the electroanalytical studies of pollutants that enter water environments and consequently drinking water and the food chain. For example, Gerent et al. used the in situ approach to deposit a bismuth film on GCE to fabricate a BiFE and detected the pesticide parathion in skimmed milk, achieving a LOD of 55.7 nM [150].

Food safety issues have always been a focus of attention as the excessive use of food additives pose a threat to human health. Asadpour-Zeynali et al. fabricated a nanocomposite on the GCE based on bismuth and chitosan and successfully determined the food additive tartrazine in chocolates with a bismuth-chitosan nanocomposite modified GCE [151]. These studies clearly demonstrate the widespread versatility and scientific importance of bismuth-based electrodes and indicate that the interest in their research and development is still growing.

1.6.2.3 Copper-based modified electrodes

Copper is an abundant metal on earth with low toxicity. It is inexpensive and has excellent conductivity, ductility, and stability, hence the copper is widely used in industries. Compared to the noble metals (e.g., Au and Ag), the conductivity of metallic Cu is like Au and Ag, and the precursor for the synthesis of the Cu is relatively abundant, cheaper, and readily available from commercial sources. Furthermore, Cu nanocomposites retain their original property while endowing them with new physical and chemical features, such as catalytic, thermal, electrical, optical, and magnetic properties. Therefore, Cu nanocomposites have been widely investigated and are more favorable than the noble metals for various applications.

1.6.2.3.1 Preparation of copper-based modified electrodes

Among the various methods for modifying electrodes with Cu nanocomposites, requiring sometimes a series of complex physical/chemical procedures, the electrodeposition approach has simplicity, good repeatability, and high stability. Thus, it has already gathered significant interest [152]. In general, a suitable reductive potential, which can electrochemically reduce the metal ions in solution to the metal alone, is

applied to the working electrode, giving rise to the deposition of the metals on the electrode surface. As the electrodeposited metal materials retain good electrical contact with the electrode, the electrodeposition method makes them easily integrated into electrical devices. In addition, different electrodeposition parameters, such as copper precursor type, copper solution concentration, electrolyte, acidity, applied potential, deposition time, current or integrated charge and temperature can affect the morphologies of the electrodeposited metals. Accordingly, electrodeposition is an effective and scalable method to grow desired structures on electrode surfaces [153].

1.6.2.3.2 Application of copper-based modified electrodes

Inspired by the existing and potential applications of Cu nanocomposites, the studies on Cu nanocomposites are growing rapidly in recent years. The Cu nanocomposites have exhibited potential applications in physics, chemistry, biology, food, materials, energy, and the environment. The analytical applications of the Cu nanocomposites used as sensors have also been explored [154], including fluorescence sensors in the determination of various analytes, such as metal ions, anions, biomolecules, small molecules, and biological labeling and bioimaging, chemiluminescence sensors for the detection of H_2O_2, and colorimetric sensors to detect H_2O_2, glucose and Fe^{3+}. However, the development of electrochemical sensors based on the Cu nanocomposites is relatively limited. Most studies fabricate Cu nanocomposites on electrodes to develop electrochemical sensors for the detection of glucose. Kang et al. used electrodeposited Cu nanocomposites on multiwall carbon nanotube (MWCNTs)-modified GCE to fabricate a nonenzymatic glucose biosensor, which showed the synergistic electrocatalytic activity for the oxidation of glucose in alkaline media and achieved sensitive detection of glucose in a concentration range from 0.7 to 3500 μM with a LOD of 0.21 μM [155]. In addition, a novel electrochemical biosensor based on Cu nanocomposites for the detection of miRNA was developed by Dai et al., who used DNA-miRNA heteroduplexes as the template to synthesise Cu nanocomposites, which can electrocatalyse H_2O_2 reduction, producing electrochemical signals proportional to the concentration of miRNA, thereby realising the determination of miRNA in the linear

concentration range from 25 to 300 fM with a LOD of 8.2 fM, as shown in Figure 1-12 [156]. Furthermore, Cu nanocomposites were fabricated on single-walled carbon nanotube (SWCNT) modified screen-printed Ag working electrodes to develop a nitrate sensor, giving a LOD of 0.281 nM [157].

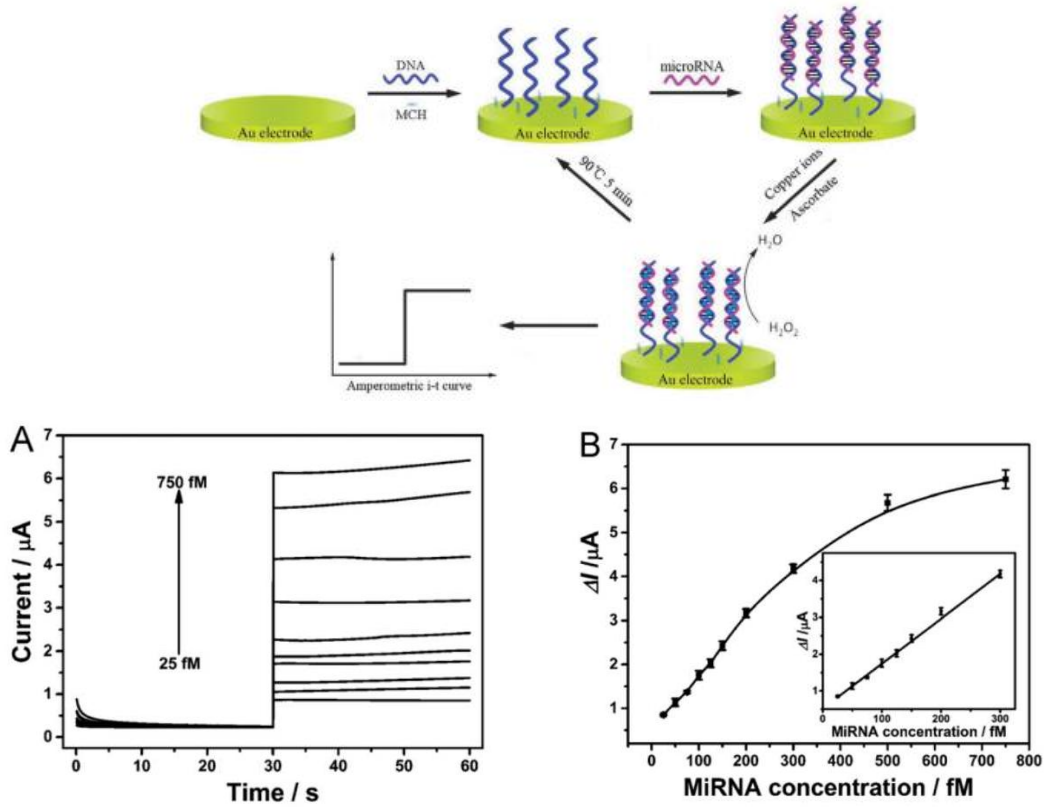

Figure 1-12. Principle of a reusable miRNA biosensor based on the electrocatalytic property of DNA–miRNA heteroduplexes-templated CuNCs. (A) i-t curves for the range of CmiRNA from 25 to 750 fM; (B) Calibration curve for DI versus CmiRNA. Inset: a linear range of CmiRNA from 25 to 300 fM [156].

These studies demonstrate that Cu-based nanocomposites are promising sensors to determine different analytes due to their advantages including non-toxicity, low cost, and ease of preparation.

1.7 Removal of Pollutants

The continuous discharge of pollutants from different activities, such as industries, agriculture, mining, aquaculture, and domestic households, to water resources causes pollution of the water environment and deterioration of water quality [158,159].

Electrochemical sensors can be employed to quantitatively monitor the concentration of pollutants in water environments. The next crucial issue is to remove pollutants from water environments to improve water quality, reducing environmental-related health consequences, and producing a suitable environment for aquatic organisms.

Various techniques have been utilised to treat these pollutants, such as sedimentation/flocculation/coagulation [160], chemical precipitation [161], chemical separation [162], adsorption [163,164], electrocatalytic degradation [165], photocatalytic degradation [166], and biological treatment [167]. However, many of these techniques have limitations in industrial applications, owing to time-consuming processes, high capital and operating costs, large amounts of sludge generated, subsequent treatment issues, technical requirement for the compounds with different structural characteristics, and so on.

Among these treatment methods, adsorption is recognised as a preferred technology because it has a series of advantages, including flexibility, simple operation procedures, comparatively low operating costs, insensitivity to toxic contaminants, high removal efficiency and fewer secondary treatments [168]. Different types of materials, including biological, organic, mineral materials, zeolites, polymer materials, and carbonaceous materials, have been used as adsorbents for the removal of pollutants [169]. Among these different adsorbents, the carbon-based materials, such as activated carbon, fullerenes, carbon nanotubes, graphene, etc., have been extensively investigated and employed as adsorbents due to their outstanding features, including high chemical stability, rich pore structures, large specific surface areas, convenience of physical and chemical modifications, and excellent performance for removing various pollutants [170]. Especially, graphene and its composite materials, due to their unique features, are considered as the most advanced and promising adsorbents among all the carbon-based materials.

1.7.1 Graphene-based composite materials as adsorbents

The structure and property of graphene and its derivatives have been described in Section 1.6.2.1. Graphene and its derivatives not only possess oxygenated functional groups on its surface, but also have large delocalised π-electron systems, which increase

the active sites. Accordingly, graphene and its derivatives can efficiently adsorb pollutants through cation and anion attraction, hydrogen bonding, π–π interactions, hydrophobic interaction, and ion exchange to achieve the removal of pollutants, as shown in Figure 1-13 [171]. These multiple bonding modes between graphene-based materials and pollutants indicate that they are suitable for adsorption applications and have been used to remove various pollutants in aqueous solutions. For example, graphene was used as the adsorbent to remove Bisphenol A [172] and methylene blue [173] from aqueous solutions through hydrogen bonding and π–π interactions, showing good removal efficiency. Fan et al. utilised graphene as the adsorbent for the removal of chlorophenols, such as 2-chlorophenol, 4-chlorophenol, 2,4-dichlorophenol and 2,4,6-trichlorophenol [174].

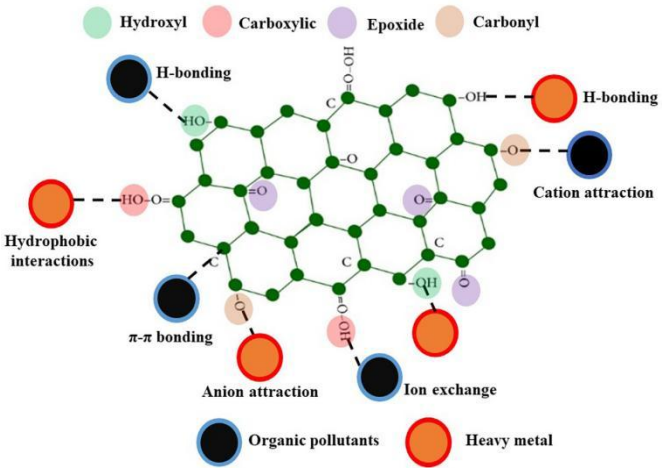

Figure 1-13. The adsorption process of the pollutants onto the graphene [171].

Besides graphene, GO and rGO, these materials have been further functionalised using covalent or non-covalent modification to construct hybrid composite materials. The purpose is to achieve enhanced adsorption capacity by combining the graphene with the components that also have adsorption properties. On the one hand, the adsorption property of each component can be fully utilised, on the other hand, the synergistic effect between the composites could be realised. Using this approach, Wang et al. synthesised 3D graphene aerogel mesoporous silica composite adsorbents to remove four phenolic compounds including hydroquinone, resorcinol, catechol, and phenol [175]. Sun et al. fabricated β-cyclodextrin with rGO to produce 3D composites

for the efficient removal of Bisphenol A in aqueous solution [176]. Ahsan et al. assembled metal-organic compounds with GO for the removal of Bisphenol A from aqueous solution [177]. Moreover, the hybrid microspheres consisting of GO and crospolyvinylpyrrolidone were also prepared for the removal of 2,4,6-trichlorophenol [178]. Apart from the above-mentioned phenolic compounds, the graphene-based composite materials can be employed to adsorb pharmaceuticals, antibiotics, pesticides, herbicides, dyes, and other aromatic compounds [179]. These findings indicate that graphene-based composite materials not only achieve better adsorption efficiency than the single component, but also enlarge the adsorption range for the pollutants.

1.7.2 Graphene-based magnetic adsorbents

Although graphene and its derivatives display good adsorption performance for the removal of pollutants, they have some shortcomings. For instance, GO has strong hydrophilicity, leading to difficulties in separation and recycling; on the other hand, the π - π interaction between graphene layers results in the restacking and agglomeration of the graphene sheets to give a reduction of adsorption capacity. These issues hinder the practical application of graphene-based adsorption materials. The addition of magnetic metal or metal oxide nanoparticles with graphene, GO and rGO is an effective solution to some of these issues. These nanoparticles not only can be intercalated within the graphene layers to overcome the aggregation problem of the graphene sheets, but also can endow graphene with magnetic properties. Magnetic adsorbents are of great interest as they can be easily collected by external magnetic fields, greatly simplifying the recycling process.

Magnetic materials mainly involve Fe, Co, Ni and Fe_3O_4 [180]. Among them, Fe and Fe_3O_4 have been widely used owing to their strong magnetism and convenience in their synthesis. A simple method is to directly utilise the intrinsic magnetic composite as magnetic adsorbent for the removal of the pollutants [181]. Nevertheless, the intrinsic magnetic materials may not have satisfactory adsorption properties. Accordingly, to achieve better adsorption performance, it is necessary to combine the intrinsic magnetic composite with other materials with good adsorption performance, such as graphene and its derivatives. To date, composite materials containing graphene and Fe or Fe_3O_4

have been synthesised and employed as effective adsorbents for the removal of some pollutants from water environments.

For example, Li et al. employed magnetite/diazonium modified rGO to form magnetic graphene composite for the adsorption of 4-chlorophenol and 2,4-dichlorophenol and isolated the spent adsorbent from aqueous solution by an external magnetic field [182]. Deliyanni et al. synthesised a magnetic graphene composite, GO-PANI/Fe_3O_4 (PANI: polyaniline), and used it for the removal of Bisphenol A [183]. Adel et al. modified rGO with $MgFe_2O_4$ via electrostatic interactions to prepare a magnetic adsorbent which was applied for the removal of methylene blue dye from aqueous solutions [184]. Again, the adsorbent was recovered by using an external magnet. Hota et al. used Fe_3O_4 nanoparticles to functionalise GO/g–C_3N_4 nanosheets to form GO/g–C_3N_4–Fe_3O_4 composites and employed it to remove tetracycline antibiotic and methylene blue [185]. Clearly, the introduction of Fe_3O_4 nanoparticles onto GO/g–C_3N_4 nanosheets not only enhances the adsorption capacity but also make the adsorbent easily separable from aqueous solution.

Furthermore, graphene and its derivatives have been employed to support nanoscale zero-valent iron (nZVI) and used as efficient adsorbents for the removal of pollutants. Zhang et al. prepared GO coupled nZVI and used it in removing oxytetracycline from wastewater [186]. Masud et al. synthesised rGO-nZVI nanocomposite, which was utilised as the adsorbent, for the removal of a complex mixture of 12 diverse pharmaceutical and personal care products, including antibiotic, anti-inflammatory, anti-seizure, and antidepressant pharmaceuticals, in wastewater [187]. Wang et al. fabricated the GO-load nZVI and applied it in removing tetrabromobisphenol A [188].

These studies indicated that magnetic graphene decorated with nanocomposites Fe_3O_4 and nZVI display a positive effect on the removal of various pollutants. As a result, magnetic field assisted adsorbents have promising potential for the removal of various pollutants from the aqueous system.

Based on the discussion above, it is obvious that the application of graphene-based composite materials as adsorbents for the removal of different pollutants is rapidly growing year by year as observed from the publication of research and review articles.

Consequently, to treat water systems or wastewater, graphene-based composite materials as adsorbents exhibit promising applications.

1.8 References

[1] Alharbi, O. M. L.; Basheer, A. A.; Khattab, R. A.; Ali, I. Health and environmental effects of persistent organic pollutants. *J. Mol. Liq*. **2018**, *263*, 442–453, doi:10.1016/j.molliq.2018. 05.029.

[2] Wang, S. H.; Yan, W. F.; Zhao, F. Recovery of solid waste as functional heterogeneous catalysts for organic pollutant removal and biodiesel production. *Chem. Eng. J.* **2020**, *401*, 126104, doi:10.1016/j.cej.2020.126104.

[3] Hartmann, J.; van Driezum, I.; Ohana, D.; Lunch, G.; Berendsen, B.; Wuijts, S.; van der Hoek, J. P.; Husman, A. M. D. The effective design of sampling campaigns for emerging chemical and microbial contaminants in drinking water and its resources based on literature mining. *Sci. Total Environ.* **2020**, *742*, 140546, doi: 10.1016/j.scitotenv.2020.140546.

[4] Pretty, J. Intensification for redesigned and sustainable agricultural systems. *Science*, **2018**, *362*, eaav0294, doi: 10.1126/science.aav0294.

[5] Wolfram, J.; Stehle, S.; Bub, S.; Petschick, L. L.; Schulz, R. Water quality and ecological risks in European surface waters-monitoring improves while water quality decreases. *Environ. Int.* **2021**, *152*, 106479, doi: 10.1016/j.envint.2021.106479.

[6] Huang, Y. B.; Zhai, J.; Liu, L. H.; Shang, Z. Y.; Zhang, X.; Huang, H.; Shen, B. X.; Chen, G. X. Recent developments on nanomaterial probes for detection of pesticide residues: A review, *Anal. Chim. Acta*, **2022**, *1215*, 339974, doi: 10.1016/j.aca. 2022.339974.

[7] Pundir, C. S.; Malik, A.; Preety. Bio-sensing of organophosphorus pesticides: review. *Biosens. Bioelectron*. **2019**, *140*, 111348, doi: 10.1016/j.bios.2019.111348.

[8] Morton, P. A.; Cassidy, R.; Floyd, S.; Doody, D. G.; McRoberts, W. C.; Jordan, P. Approaches to herbicide (MCPA) pollution mitigation in drinking water source catchments using enhanced space and time monitoring. *Sci. Total Environ*. **2021**, *755*, 142827, doi: 10.1016/j.scitotenv.2020.142827.

[9] Paszko, T.; Muszyński, P.; Materska, M.; Bojanowska, M.; Kostecka, M.; Jackowska, I. Adsorption and degradation of phenoxyalkanoic acid herbicides in soils: A review. *Environ. Toxicol. Chem*. **2016**, *35*, 271–286, doi: 10.1002/etc.3212.

[10] Pozo, O.; Pitarch, E.; Sancho, J. V.; Hernández, F. Determination of the herbicide 4-chloro-2-methylphenoxyacetic acid and its main metabolite, 4-chloro-2-methyl phenol in water and soil by liquid chromatography-electrospray tandem mass spectrometry. *J. Chromatogr. A*, **2001**, *923*, 75–85, doi:10.1016/S0021-9673(01) 01006-8.

[11] Glozier, N. E.; Struger, J.; Cessna, A. J.; Gledhill, M.; Rondeau, M.; Ernst, W. R.; Sekla, M. A.; Cagampan, S. J.; Sverko, E.; Murphy, C. Occurrence of glyphosate and acidic herbicides in select urban rivers and streams in Canada. *Environ. Sci. Pollut. Res*. **2012**, *19*, 821–834, doi: 10.1007/s11356-011-0600-7.

[12] Piotrowska, A.; Syguda, A.; Chrzanowski, Ł.; Heipieper, H. J. Toxicity of synthetic herbicides containing 2,4-D and MCPA moieties towards Pseudomonas putida mt-2 and its response at the level of membrane fatty acid composition. *Chemosphere*, **2016**, *144*, 107–112, doi: 10.1016/j.chemosphere.2015.08.067.

[13] Wunnapuk, K.; Liu, X.; Gobe, G. C.; Endre, Z. H.; Peake, P. W.; Grice, J. E.; Roberts, M. S.; Buckley, N. A. Kidney biomarkers in MCPA-induced acute kidney injury in rats: Reduced clearance enhances early biomarker performance. *Toxicol. Lett*. **2014**, *225*, 467–478, doi: 10.1016/j.toxlet.2014.01.018.

[14] Pahwa, M.; Harris,S. A.; Hohenadel, K.; McLaughlin, J. R.; Spinelli, J. J. Pahwa, P.; Dosman, J. A.; Blair, A. Pesticide use, immunologic conditions, and risk of non Hodgkin lymphoma in Canadian men in six provinces. *Int. J. Cancer*. **2012**, *131*, 2650–2659, doi: 10.1002/ijc.27522.

[15] World Health Organisation. (**2003**). MCPA in drinking water (p. 10). Retrieved from http://www.who.int/water_sanitation_health/dwq/chemicals/mcpa.pdf

[16] Bailey, S.; Reade, J. P.; Burn, A.; Zappala, S. Pesticides. In Hester, R. E.; Harrison, R. M. Issues in environmental science and technology. Agricultural chemicals and the environment: Issues and potential solutions, **2017**, 43 (2nd. ed, Vol. 43, pp. 45–93). Cambridge, England: The Royal Society of Chemistry.

[17] Council of the European Commission. (1998). Council Directive 98/83/EC of 3 November 1998 on the quality of water intended for human consumption. Pub. L. No. Directive 98/83/EC, 98/83/EC OJ L330 p32.

[18] Dabrowski A.; Podkoscielny P.; Hubicki Z.; Barczak, M. Adsorption of phenolic compounds by activated carbon-a critical review. *Chemosphere*, **2005**, *58*, 1049–1070, doi: 10.1016/j.chemosphere.2004.09.067.

[19] Karim, F.; Fakhruddin, A. N. M.; Recent advances in the development of biosensor for phenol: a review. *Rev. Environ. Sci. Bio.* **2012**, *11*, 261–274, doi: 10.1007/s11157-012-9268-9.

[20] Qiu, N.; Liu, Y.; Xiang, M.; Lu, X. M.; Yang, Q.; Guo, R. A facile and stable colorimetric sensor based on three-dimensional graphene/mesoporous Fe_3O_4 nanohybrid for highly sensitive and selective detection of p-nitrophenol, *Sensor. Actuat. B-Chem*. **2018**, *266*, 86–94, doi: 10.1016/j.snb.2018.03.059.

[21] Zhang, J. J.; Cui, S. Q.; Ding, Y. P.; Yang, X. X.; Guo, K.; Zhang, J. T. Two-dimensional mesoporous $ZnCo_2O_4$ nanosheets as a novel electrocatalyst for detection of o-nitrophenol and p-nitrophenol, *Biosens. Bioelectron.* **2018**, *112*, 177–185, doi: 10.1016/j.bios.2018.03.021.

[22] Wei, Y.; Kong, L. T.; Yang, R.; Wang, L.; Liu, J. H.; Huang, S. J. Single-walled carbon nanotube/pyrenecyclodextrin nanohybrids for ultrahighly sensitive and selective detection of p-nitrophenol, *Langmuir*, **2011**, *27*, 10295–10301, doi: 10.1021/la201691c.

[23]Dawadi, S.; Thapa, R.; Modi, B.; Bhandari, S.; Timilsina, A. P.; Yadav, R. P.; Aryal, B.; Gautam, S.; Sharma, P.; Thapa, B. B. Technological advancements for the detection of antibiotics in food products, *Processes* **2021**, *9*, 1500, doi: 10.3390/pr9091500.

[24] Li, H. P.; Wu, J. Y.; Meng, F. P.; Li, A. F. Immunochromatographic assay for the detection of antibiotics in animal-derived foods: A review, *Food Control*, **2021**, *130*, 108356, doi: 10.1016/j.foodcont.2021.108356.

[25] Ensafi, A. A.; Amini. M.; Rezaei, B. Multianalyte antibiotic detection on an electrochemical microfluidic Platform. *Anal. Chem*. **2016**, *88*, 10036–10043, doi: 10.1021/acs.analchem.6b02294.

[26] Malfertheiner, P.; Megraud, F.; O'Morain, C.; Bazzoli, F.; El-Omar, E.; Graham,

D.; Hunt, R.; Rokkas, T.; Vakil, N.; Kuipers, E. J. Current concepts in the management of helicobacter pylori infection: The maastricht III consensus report, *Gut*, **2007**, *56*, 772–781, doi: 10.1136/gut.2006.101634.

[27] Freeman, C. D.; Klutman, N. E.; Lamp, K. C. Metronidazole. A therapeutic review and update, *Drugs,* **1997**, *54*, 679–708, doi: 10.2165/00003495- 199754050-00003.

[28] Ceruelos, A. H.; Romero-Quezada, L. C.; Ledezma, J. C. R.; Contreras, L. L. Therapeutic uses of metronidazole and its side effects: An update, *Eur. Rev. Med. Pharmacol. Sci.* **2019**, *23*, 397–401, doi: 10.26355/eurrev_201901_16788.

[29] Vilian, A. T. E.; Ranjith, K. S.; Lee, S. J.; Umapathi, R.; Hwang, S. K.; Oh, C.W.; Huh,Y. S.; Han, Y. K. Hierarchical dense Ni-Co layered double hydroxide supported carbon nanofibers for the electrochemical determination of metronidazole in biological samples, *Electrochim. Acta*, **2020**, *354*, 136723, doi: 10.1016/j.electacta.2020.136723.

[30] Quincey, D. J.; Kay, P.; Wilkinson, J.; Carter, L. J.; Brown, L. E. High concentrations of pharmaceuticals emerging as a threat to Himalayan water sustainability, *Environ. Sci. Pollut. Res.* **2022**, *29*, 16749–16757, doi: 10.1007/s11356-021-18302-8.

[31] King, D. E.; Malone, R.; Lilley, S. H. New classification and update on the quinolone antibiotics. *Am. Fam. Physician*, **2000**, *61*, 2741–2748, doi: 10.1016/S0095-4543(05)70210-4.

[32] Abdel-Haleem, F. M.; Mahmoud, S.; Abdel-Ghani, N. E. T.; El Nashar, R. M.; Bechelany, M.; Barhoum, A. Polyvinyl chloride modified carbon paste electrodes for sensitive determination of levofloxacin drug in serum, urine, and pharmaceutical formulations, *Sensor*, **2021**, *21*, 3150, doi: 10.3390/s21093150.

[33] Koçak, C. C.; Aslişen, B.; Karabiberoğlu, S.; Özdokur, K. V.; Aslan, A.; Koçak, S. Electrochemical determination of levofloxacin using poly(pyrogallol red) modified glassy carbon electrode, *ChemistrySelect*, **2022**, *7*, e202201864, doi: 10.1002/slct.202201864.

[34] Locatelli, M.; Ciavarella, M.T.; Paolino, D.; Celia, C.; Fiscarelli, E.; Ricciotti, G.; Pompilio, A.; Di Bonaventura, G.; Grande, R.; Zengin, G.; Di Marzio, L. Determination of ciprofloxacin and levofloxacin in human sputum collected from cystic fibrosis patients using microextraction by packed sorbent-high performance liquid

chromatography photodiode array detector, *J. Chromatogr. A*, **2015**, *1419*, 58–66, doi: 10.1016/j.chroma.2015.09.075.

[35] Liang, X.; Liu, H. M.; Du, Y.; Li, W. Z.; Wang, M.; Ge, B.; Zhao, L. M. Terbium functionalized covalent organic framework for selective and sensitive detection of LVX based on fluorescence enhancement, *Colloids and Surfaces A*, **2020**, *606*, 125429, doi: 10.1016/j.colsurfa.2020.125429.

[36] Catalina, M. I.; Dallüge, J., Vreuls, R. J. J.; Brinkman, U. A. T. Determination of chlorophenoxy acid herbicides in water by in situ esterification followed by in-vial liquid–liquid extraction combined with large-volume on-column injection and gas chromatography-mass spectrometry. *J. Chromatogr. A* **2000**, *877*, 153–166, doi: 10.1016/S0021-9673(00)00242-9.

[37] Sobhi, H. R.; Esrafili, A.; Farahani, H.; Gholami, M.; Baneshi, M. M. Simultaneous derivatization and extraction of nitrophenols in soil and rain samples using modified hollow-fiber liquid phase microextraction followed by gas chromatography-mass spectrometry, *Environ. Monit. Assess.* **2013**, *185*, 9055–9065, doi:10.1007/s10661-013-3235-y.

[38] Ho, C.; Sin, D. W. M.; Wong, K. M.; Tang, H. P. O. Determination of dimetridazole and metronidazole in poultry and porcine tissues by gas chromatography-electron capture negative ionization mass spectrometry *Anal. Chim. Acta*, **2005**, *530*, 23–31, doi: 10.1016/j.aca.2004.09.004.

[39] Rosales-Conrado, N.; León-González, M. E.; Pérez-Arribas, L.V.; Polo-Díez, L. M. Capillary liquid chromatography of chlorophenoxy acid herbicides and their esters in apple juice samples after preconcentration on a cation exchanger based on polydivinylbenzene-N-vinylpyrrolidone, *J. Chromatogr. A* **2005**, *1076*, 202–206, doi: 10.1016/j.chroma.2005.04.026.

[40] Seebunrueng, K.; Phosiri, P.; Apitanagotinon, R.; Srijaranai, S. A new environment-friendly supramolecular solvent-based liquid phase microextraction coupled to high performance liquid chromatography for simultaneous determination of six phenoxy acid herbicides in water and rice samples. *Microchem. J.* **2020**, *152*, 104418, doi: 10.1016/j.microc.2019.104418.

[41] Yamauchi, Y.; Ido, M.; Ohta, M.; Maeda, H. High performance liquid chromatography with an electrochemical detector in the cathodic mode as a tool for the determination of p-nitrophenol and assay of acid phosphatase in urine samples, *Chem. Pharm. Bull*. **2004**, *52*, 552–555, doi: 10.1248/cpb.52.552.

[42] dos Anjos, M. V.; Bergoza, L.; Fonseca, G.; Possa, E.; dos Santos, P.; Silva, S. M. E.; Tasso, L. Fast determination of free metronidazole in rat plasma and peritoneal fluid using HPLC-UV method, *Biomed. Chromatogr*. **2023**, *37*, e5543, doi: 10.1002/bmc.5543.

[43] Toker, S. E.; Kizilcay, G. E.; Sagirli, O. Determination of levofloxacin by HPLC with fluorescence detection in human breast milk, *Bioanalysis,* **2021**, *13*, 1063–1070, doi:10.4155/bio-2021-0058.

[44] Tabani, H.; Fakhari, A. R.; Shahsavani, A.; Behbahani, M.; Salarian, M.; Bagheri, A.; Nojavan, S. Combination of graphene oxide-based solid phase extraction and electro membrane extraction for the preconcentration of chlorophenoxy acid herbicides in environmental samples. *J. Chromatogr. A*, **2013**, *1300*, 227–235, doi: 10.1016/j.chroma.2013.04.026.

[45] Zhang, H. Y.; Wang, M.; Zhao, J. Y.; Shi, Z. H. Sandwich-type spontaneous injection of nitrophenols for capillary electrophoresis analysis, *Anal. Method,* **2012**, *4*, 2177–2182, doi: 10.1039/c2ay25207d.

[46] Mohammadnejad, M.; Gudarzi, Z.; Geranmayeh, S.; Mahdavi, V. HKUST-1 metal-organic framework for dispersive solid phase extraction of 2-methyl-4-chloro phenoxyacetic acid (MCPA) prior to its determination by ion mobility spectrometry. *Microchim. Acta*, **2018**, *185*, 495, doi: 10.1007/s00604-018-3014-0.

[47] Yang, Y.; Fang, G.; Wang, X.; Zhang, F.; Liu, J.; Zheng, W.; Wang, S. Electrochemiluminescent graphene quantum dots enhanced by MoS_2 as sensing platform: a novel molecularly imprinted electrochemiluminescence sensor for 2-methyl-4-chlorophenoxyacetic acid assay. *Electrochim. Acta,* **2017**, *228*, 107–113, doi: 10.1016/j.electacta.2017.01.043.

[48] Torres-Cartas, S.; Gómez-Benito, C.;Meseguer-Lloret, S. FI on-line chemilu minescence reaction for determination of MCPA in water samples. *Anal. Bioanal. Chem.* **2012**, *402*, 1289–1296, doi:10.1007/s00216-011-5567-1.

[49] Chen, D. H.; Peng, R. L.; Zhou, H.; Liu, H. Sensitive determination of 4-nitrophenol based on its enhancement of a peroxyoxalate chemiluminescence system containing graphene oxide quantum dots and fluorescein, *Microchim. Acta*, **2016**, *183*, 1699–1704, doi: 10.1007/s00604-016-1799-2.

[50] Qu, F.; Chen, P.; Zhu, S. Y.; You, J. M. High selectivity of colorimetric detection of p-nitrophenol based on Ag nanoclusters, *Spectrochim. Acta A*, **2017**, *171*, 449–453, doi: 10.1016/j.saa.2016.08.043.

[51] Nugrahani, I; Aliah, A. I. The -NO_2 vibrational spectra of metronidazole for analytical method development using Fourier Transform Infrared compared to the UV-VIS spectrophotometry, *Biointerface Res. Appl. Chem*. **2019**, *9*, 4446–4451, doi: 10.33263/BRIAC96.446451.

[52] Abedalwafa, M. A.; Li, Y.; Ni, C. F.; Yang, G.; Wang, L. Non-enzymatic colorimetric sensor strip based on melamine-functionalized gold nanoparticles assembled on polyamide nanofiber membranes for the detection of metronidazole, *Anal. Method*, **2019**, *11*, 3706–3713, doi: 10.1039/c9ay01114e.

[53] Gholse, Y. N.; Chaple, D. R.; Kasliwal, R. H. Development and validation of novel analytical simultaneous estimation based UV spectrophotometric method for doxycycline and levofloxacin determination, *Biointerace Res. Appl. Chem.* **2022**, *12*, 5458–5478, doi: 10.33263/BRIAC124.54585478.

[54] Wang, J. C.; Qiu, C. C.; Mu, X. J.; Pang, H.; Che, X. C.; Liu, D. M. Ultrasensitive SERS detection of rhodamine 6G and p-nitrophenol based on electrochemically roughened nano-Au film, *Talanta*, **2020**, *210*, 120631, doi: 10.1016/j.talanta.2019.120631.

[55] Huyen, L. M.; Phuc, N. T.; Khanh, H. T. D.; Hung, L.V.T. Increasing charge transfer of SERS by the combination of amorphous Al_2O_3-Al thin film and ZnO nanorods decorated with Ag nanoparticles for trace detection of metronidazole, *RSC Advances*, **2023**, *13*, 9732–9748, doi: 10.1039/d3ra01134h.

[56] Yang, Z. C.; Chen, G. Q.; Ma, C. Q.; Gu, J.; Zhu, C.; Li, L.; Gao, H. Magnetic Fe_3O_4@COF@Ag SERS substrate combined with machine learning algorithms for detection of three quinolone antibiotics: Ciprofloxacin, norfloxacin and levofloxacin. *Talanta,* **2023**, *263*, 124725, doi: 10.1016/j.talanta.2023.124725.

[57] Ding, Y. F.; Tan, W. Z.; Zheng, X. D.; Ji, X. L.; Song, P. F.; Bao, L. M.; Zhang, C. T.; Shang, J. J.; Qin, K. H.; Wei, Y. L. Serratia marcescens-derived fluorescent carbon dots as a platform toward multi-mode bioimaging and detection of p-nitrophenol, *Analyst*, **2021**, *146*, 683–690, doi: 10.1039/d0an01624a.

[58] Xu, N.; Li, H. W.; Wu, Y. Q. Hydrothermal synthesis of polyethylenimine-protected high luminescent Pt-nanoclusters and their application to the detection of nitroimidazoles, *Anal. Chim. Acta*, **2017**, *958*, 51–58, doi: 10.1016/j.aca.2016.12.033.

[59] Wang, C. X.; Qin, F. F.; Tang, S. Y.; Li, X. M.; Li, T. T.; Guo, G. Q.; Gu, C. J.; Wang, X.; Chen, D. Construction of graphene quantum dots ratiometric fluorescent probe by intermolecular electron transfer effect for intelligent and real-time visual detection of ofloxacin and its L-isomer in daily drink, *Food Chem*. **2023**, *411*, 135514, doi: 10.1016/j.foodchem.2023.135514.

[60] Shanin, I. A.; Shaimardanov, A. R.; Thai, N. T. D.; Eremin, S. A. Determination of fluoroquinolone antibiotic levofloxacin in urine by fluorescence polarization immunoassay, *J. Anal. Chem*. **2015**, *70*, 712-717, doi: 10.1134/S1061934815060167.

[61] Khalil, A.; Kashif, M. Interaction studies of levofloxacin with human lysozyme in a ternary complex using multispectroscopic and computational analysis: A circular dichroism method for the quantitation of levofloxacin, *J. Mol. Liq*. **2023**, *370*, 121023, doi: 10.1016/j.molliq.2022.121023.

[62] Baranwal, J.; Barse, B.; Gatto, G.; Broncova, G.; Kumar, A. Electrochemical sensors and their applications: a review. Chemosensors, **2022**, 10, 363, doi:10.3390/chemosensors10090363.

[63] Fan, S. Y.; Khuntia, S.; Ahn, C. H.; Zhang, B.; Tai, L. Electrochemical Devices to Monitor Ionic Analytes for Healthcare and Industrial Applications, *Chemosensors,* **2022**, *10*, 22, doi: 10.3390/chemosensors10010022.

[64] Kim, M. Y.; Lee, K. H. Electrochemical sensors for sustainable precision agriculture-A review, *Front. Chem*. **2022**, *10*, 848320, doi:10.3389/fchem.2022.848320.

[65] Li, W.; Luo, W. X.; Li, M. Y.; Chen, L. Y.; Chen, L. Y.; Guan, H.; Yu, M. J. The Impact of recent developments in electrochemical POC sensor for blood sugar care. *Front. Chem.*, **2021**, *9*, 723186, doi: 10.3389/fchem.2021.723186.

[66] He, Q. G.; Wang, B.; Liang, J.; Liu, J.; Liang, B.; Li, G. L.; Long, Y. H.; Zhang, G. Y.; Liu, H. M. Research on the construction of portable electrochemical sensors for environmental, *Mater. Today Adv*. **2023**, *17*, 100340, doi:0.1016/j.mtadv. 2022.100340.

[67] Lu, Z. Y.; Wang,Y. Y.; Li, G. K. Covalent organic frameworks-based electrochemical sensors for food safety analysis, *Biosensors-Basel*, **2023**, *13*, 291, DOI: 10.3390/bios13020291.

[68] Cuartero M., Crespo G.A. All-solid-state potentiometric sensors: a new wave for in situ aquatic research, *Curr. Opin. Electrochem*. **2018**, *10*, 98–106, doi: 10.1016/ j.coelec.2018.04.004.

[69] Wasiewska, L. A.; Juska, V. B.; Seymour, I.; Burgess, M.; Duffy, C. G.; O'Riordan, A. electrochemical nucleic acid-based sensors for detection of escherichia coli and shiga toxin-producing E. coli-Review of the recent developments, *Compr. Rev. Food Sci. Saf.* **2023**, *22*, 1839–1863, doi: 10.1111/1541-4337.13132.

[70] Tong, X.; Ga, L.; Bi, L. G.; Ai, J. Wearable electrochemical sensors based on nanomaterials for healthcare applications, *Electroanalysis*, **2023**, *35*, 2200228, doi: 10.1002/elan.202200228.

[71] Jenkins, G. W.; Kawamura, K.; Ban, L. L. Formation and structure of polymeric carbons, *Proc R Soc Lond A Math Phys Sci*. **1972**, *327*, 501–517, doi: 10.1098/rspa.1972.0060.

[72] Jenkins, G. M.; Kawamura, K. Structure of glassy Carbon, *Nature*, **1971**, *231*,175–176, doi:10.1038/231175a0.

[73] McCreery, R. L. Advanced carbon electrode materials for molecular electrochemistry, *Chem. Rev*. **2008**, *108*, 2646–2687, doi:10.1021/cr068076m.

[74] Dekanski, A.; Stevanović, J.; Stevanović, R.; Nikolić, B. Ž.; Jovanović, V. M. Glassy carbon electrodes: I. Characterization and electrochemical activation, *Carbon*, **2001**, *39*, 1195–1205, doi: 10.1016/S0008-6223(00)00228-1.

[75] Ranganathan, S.; Kuo, T. C.; McCreery, R. L. Facile preparation of active glassy carbon electrodes with activated carbon and organic solvents, *Anal. Chem*. **1999**, *71*, 3574–3580, doi:10.1021/ac981386n.

[76] Fagan, D.T.; Hu, I. F.; Kuwana,T. Vacuum heat-treatment for activation of glassy carbon electrodes, *Anal. Chem*. **1985**, *57*, 2759–2763, doi: 10.1021/ac00291a006.

[77] Poon, M.; McCreery, R. L. In situ laser activation of glassy carbon electrodes, *Anal. Chem*. **1986**, *58*, 2745 – 2750, doi: 10.1021/ac00126a036.

[78] Declements, R.; Swain, G. M.; Dallas, T.; Holtz, M. W.; Herrick, R. D.; Stickney, J. L. Electrochemical and surface structural characterization of hydrogen plasma treated glassy carbon electrodes, *Langmuir*, **1996**, *12*, 6578–6586, doi: 10.1021/la960380v.

[79] Schreurs, J.; van den Berg, J.; Wonders, A.; Barendrecht, E. Characterization of a glassy-carbon-electrode surface pretreated with rf-plasma, *Recl. Trav. Chim. Pays-Bas*. **2010**, *103*, 251−259, doi: 10.1002/recl.19841030902.

[80] Bowling, R.; Packard, R.T.; McCreery, R. L. Mechanism of electrochemical activation of carbon electrodes: role of graphite lattice defects, *Langmuir*, **1989**, *5*, 683−688, doi: 10.1021/la00087a022.

[81] Holloway, A. F.; Wildgoose, G. G.; Compton, R. G.; Shao, L. D.; Green, M. L. H. The influence of edge-plane defects and oxygen-containing surface groups on the voltammetry of acid-treated, annealed and 'super-annealed' multiwalled carbon nanotubes. *J. Solid State Electrochem*. **2008**, *12*, 1337−1348, doi: 10.1007/s10008-008-0542-2.

[82] Liu, X. X.; Wang,Y. L.; Zhan, L.; Qiao, W. M.; Liang, X. Y.; Ling, L. C. Effect of oxygen containing functional groups on the impedance behavior of activated carbon-based electric double-layer capacitors. *J. Solid State Electrochem*. **2011**, *15*, 413−419, doi: 10.1007/s10008-010-1100-2.

[83] Healy, B.; Rizzuto, F.; de Rose, M.; Yu, T.; Breslin, C. B. Electrochemical determination of acetaminophen at a carbon electrode modified in the presence of β-cyclodextrin: role of the activated glassy carbon and the electropolymerised β-cyclodextrin. *J. Solid State Electrochem*. **2021**, *25*, 2599−2609, doi:10.1007/s10008-021-05044-3.

[84] Rana, A.; Baig, N.; Saleh, T. A. Electrochemically pretreated carbon electrodes and their electroanalytical applications – A review， *J. Electroanal. Chem*. **2019**, *833*, 313–332, doi: 10.1016/j.jelechem.2018.12.019.

[85] Tenent R. C.; Wipf, D. O. Local electron transfer rate measurements on modified and unmodified glassy carbon electrodes. *J. Solid State Electrochem*. **2009**, 13, 583−590, doi: 10.1007/s10008-008-0689-x.

[86] Lv, Y.; Sun, J.; Qiao, S.; Zhang, M.; Li, J. A facile, inexpensive and green electrochemical sensor for sensitive detection of imidacloprid residue in rice using activated electrodes. *Anal. Method*, **2021**, *13*, 3649 − 3658, doi: 10.1039/d1ay00984b.

[87] Huang, D. Q.; Cheng, Y.; Xu, H. Y.; Zhang, H.; Sheng, L. Q.; Xu, H. J.; Liu, Z. D.; Wu, H.; Fan, S. H. The determination of uric acid in human body fluid samples using glassy carbon electrode activated by a simple electrochemical method. *J. Solid State Electrochem.* **2015**, *19*, 435−443, doi: 10.1007/s10008-014-2614-9.

[88] Chiavazza, E.; Berto, S.; Giacomino, A.; Malandrino, M.; Barolo, C.; Prenesti, E.; Vione, D.; Abollino, O. Electrocatalysis in the oxidation of acetaminophen with an electrochemically activated glassy carbon electrode. *Electrochim. Acta*, **2016**, *192*, 139−147, doi: 10.1016/j.electacta.2016.01.187.

[89] Yan, Y.; Bao, C. Q.; Zou, J.; Xiao, J. L.; Zhong, W.; Gao, Y. S. Highly sensitive electrochemical sensor for sunset yellow based on electrochemically activated glassy carbon electrode, *Molecules*, **2022**, *27*, 5221, doi: 10.3390/molecules27165221.

[90] Mao, D. P.; Duan, P. H.; Piao, Y. X. Acid phosphate-activated glassy carbon electrode for simultaneous detection of cadmium and lead, *J. Electroanal. Chem*. **2022**, *925*, 116898, doi: 10.1016/j.jelechem.2022.116898.

[91] Karim, R.; Saha, P.; Akter, R.; Falguni, R.; Shital, R. A.; Awal, A.; Al Mamun, M.; Ahammad, A. J. S. Simultaneous determination of ranitidine and metronidazole at low potential using an acid-activated glassy carbon electrode, *ChemistrySelect*, **2023**, *8*, e202204174, doi: 10.1002/slct.202204174.

[92] Thiagarajan, S.; Tsai, T. H.; Chen, S. M. Easy modification of glassy carbon electrode for simultaneous determination of ascorbic acid, dopamine and uric acid, *Biosens. Bioelectron*. **2009**, *24*, 2712–2715, doi: 10.1016/j.bios.2008.12.010.

[93] Temoçin, Z. Modification of glassy carbon electrode in basic medium by electrochemical treatment for simultaneous determination of dopamine, ascorbic acid and uric acid, *Sensors Actuators B Chem.* **2013**, *176*, 796–802, doi: 10.1016/j.snb.2012.09.078.

[94] Li, S. J.; Guo, W.; Yuan, B. Q.; Zhang, D. J.; Feng, Z. Q.; Du, J. M. Assembly of ultrathin NiOOH nanosheets on electrochemically pretreated glassy carbon electrode for

electrocatalytic oxidation of glucose and methanol, *Sensors Actuators B Chem*. **2017**, *240*, 398–407, doi: 10.1016/j.snb.2016.09.002.

[95] Watkins, B. F.; Behling, J. R.; Kariv, E.; Miller, L. L. Chiral electrode, *J . Am. Chem. Soc*. **1975**, *97*, 3549−3550, doi: 10.1021/ja00845a061.

[96] Moses, P. R.; Wier, L.; Murray. R. W. Chemically modified tin oxide electrode, *Anal. Chem*. **1975** , *47*, 1882−1886, doi: 10.1021/ac60362a043.

[97] Novoselov, K. S.; Geim, A. K.; Morozov, S. V.; Jiang, D.; Zhang, Y.; Dubonos, S. V.; Grigorieva, I. V.; Firsov, A. A. Electric Field Effect in Atomically Thin Carbon Films, *Science*, **2004**, *306*, 666–669, doi: 10.1126/science.1102896.

[98] Guo, S. J.; Dong, S. J. Graphene nanosheet: synthesis, molecular engineering, thin film, hybrids, and energy and analytical applications, *Chem. Soc. Rev*. **2011**, *40*, 2644–2672, doi: 10.1039/c0cs00079e.

[99] Park, S.; Ruoff, R. S. Chemical methods for the production of graphenes, *Nat. Nanotechnol*. **2009**, *4*, 217–224, doi:10.1038/NNANO.2009.58.

[100] Balandin, A. A.; Ghosh, S.; Bao, W.; Calizo, I.;Teweldebrhan, D.; Miao, F.; Lau, C. N. Superior thermal conductivity of single-layer graphene, *Nano Lett*. **2008**, *8*, 902–907, doi: 10.1021/nl0731872.

[101] Lee, C.; Wei, X.; Kysar, J. W.; Hone, J. Measurement of the elastic properties and intrinsic strength of monolayer graphene, *Science*, **2008**, *321*, 385–388. doi:10.1126/science.1157996.

[102] Rao, C. N. R.; Sood, A. K.; Subrahmanyam, K. S.; Govindaraj, A. Graphene: The new two-dimensional nanomaterial, *Angew. Chem. Int. Ed*. **2009**, *48*, 7752–7777, doi: 10.1002/anie.200901678.

[103] Zhu, C. Z.; Dong, S. J. Recent progress in graphene-based nanomaterials as advanced electrocatalysts towards oxygen reduction reaction, *Nanoscale*, **2013**, *5*, 1753–1767, doi: 10.1039/c2nr33839d.

[104] Ren, S.; Rong, P.; Yu, Q. Preparations, properties and applications of graphene in functional devices: A concise review, *Ceram. Int*. **2018**, *44*, 11940–11955, doi: 10.1016/j.ceramint.2018.04.089.

[105] Mudusu, K. R. Nandanapalli, S. Lee, Y. B. Hahn, Recent advances in graphene monolayers growth and their biological applications: A review, *Adv. Colloid Interface Sci*. **2020**, *283*, 102225, doi: 10.1016/j.cis.2020.102225.

[106] Bhardwaj, K.; Mujawar, M.; Mishra,Y. K.; Hickman, N.; Chavali, M.; Kaushik, A. Bio-inspired graphene-based nano-systems for biomedical applications, *Nanothchnology*, **2021**, *32*, 502001, doi:10.1088/1361-6528/ac1bdb.

[107] Al Faruque, M. A.; Syduzzaman, M.; Sarkar, J.; Bilisik, K.; Naebe, M. A Review on the production methods and applications of graphene-based materials, *Nanomaterials*, **2021**, *11*, 2414, doi: 10.3390/nano11092414.

[108] Yam, K. M.; Guo, N.; Jiang, Z. L.; Li, S. L.; Zhang, C. Graphene-based heterogeneous catalysis: role of graphene, *Catalysis*, **2020**, *10*, 53, doi: 10.3390/catal10010053.

[109] Wang, Z. X.; Hemmetter, A.; Uzlu, B.; Saeed, M.; Hamed, A.; Kataria, S.; Negra, R.; Neumaier, D.; Lemme, M. C. Graphene in 2D/3D heterostructure diodes for high performance electronics and optoelectronics, *Adv. Electron. Mater*. **2021**, *7*, 2001210, doi: 10.1002/aelm.202001210.

[110] Tale, B.; Nemade, K. R.; Tekade, P. V. Graphene based nano-composites for efficient energy conversion and storage in Solar cells and Supercapacitors : A Review, *Polym-Plast. Tech. Mater*. **2021**, *60*, 784–797, doi:10.1080/25740881.2020.1851378.

[111] Edward, K.; Mamun, K.; Narayan, S.; Assaf, M.; Rohindra, D.; Rathnayake, U. State-of-the-art graphene synthesis methods and environmental concerns, *Appl. Environ. Soil Sci*. **2023**, 8475504, doi: 10.1155/2023/8475504.

[112] Dreyer, D. R.; Park, S.; Bielawski, C. W.; Ruoff, R. S. The chemistry of graphene oxide. *Chem. Soc. Rev*. **2010**, *39*, 228–240, doi:10.1039/b917103g.

[113] Liu, Y.; Yu, D.; Zeng, C.; Miao, Z.; Dai, L. Biocompatible graphene oxide-based glucose biosensors. *Langmuir*, **2010**, *26*, 6158–6160, doi:10.1021/la100886x.

[114] Wang, Y.; Li, Z.; Wang, J.; Li, J.; Lin, Y. Graphene and graphene oxide: Biofunctionalization and applications in biotechnology. *Trends Biotechnol*. **2011**, *29*, 205–212, doi:10.1016/j.tibtech.2011.01.008.

[115] Zhou, M.; Zhai, Y.; Dong, S. Electrochemical sensing and biosensing platform based on chemically reduced graphene oxide. *Anal. Chem*. **2009**, *81*, 5603–5613. doi:10.1021/ac900136z.

[116] Novoselov, K. S.; Fal′ko, V. I.; Colombo, L.; Gellert, P. R.; Schwab, M. G.; Kim, K. A Roadmap for graphene. *Nature*, **2012**, *490*, 192–200, doi:10.1038/nature11458.

[117] Murthy, H. C. A.; Kelele, K. G.; Ravikumar, C.R.; Nagaswarupa, H.P.; Tadesse, A.; Desalegn, T. Graphene-supported nanomaterials as electrochemical sensors: A mini review. *Results Chem.* **2021**, *3*, 100131, doi: 10.1016/j.rechem.2021.100131.

[118] Hsine, Z.; Mlika, R.; Jaffrezic-Renault, N.; Korri-Youssoufi, H. Review-Recent progress in graphene based modifified electrodes for electrochemical detection of dopamine, *Chemosensors*, **2022**, *10*, 249, doi: 10.3390/chemosensors10070249.

[119] Suhito, I. R.; Koo, K. M.; Kim,T. H. Recent advances in electrochemical sensors for the detection of biomolecules and whole cells, *Biodedicines*, **2021**, *9*, 15, doi:10.3390/biomedicines9010015.

[120] Pei, J. J.; Ren, T.; Huang,Y. G.; Chen, R.; Jin, W. G.; Shang, S. F.; Wang, J. Z.; Liu, Z.; Liang, Y. K.; Abd El-Aty, A. M. Application of graphene and its derivatives in detecting hazardous substances in food: A comprehensive review, *Front. Chem.* **2022**, *10*, 894759, doi: 10.3389/fchem.2022.894759.

[121] Fu, L.; Mao, S. D.; Chen, F.; Zhao, S. C.; Su, W. T.; Lai, G. S.; Yu, A. M.; Lin, C. T. Graphene-based electrochemical sensors for antibiotic detection in water, food and soil: A scientometric analysis in CiteSpace (2011–2021), *Chemosphere*, **2022**, *297*, 134127, doi: 10.1016/j.chemosphere.2022.134127.

[122] Zheng, Y. H.; Mao, S. D.; Zhu, J. W.; Fu, L.; Moghadam, M. A scientometric study on application of electrochemical sensors for detection of pesticide using graphene-based electrode modifiers, *Chemosphere*, **2022**, *307*, 136069, doi: 10.1016/j.chemosphere.2022.136069.

[123] Benjamin, R.; Eli José, M. R. Graphene-based electrochemical sensors for detection of environmental pollutants, *Curr. Opin. Environ. Sci. Health*, **2022**, *29*, 100381, doi: 10.1016/j.coesh.2022.100381.

[124] Li, J. H.; Kuang, D. Z.; Feng, Y. L.; Zhang, F. X.; Xu, Z. F.; Liu, M. Q. A graphene oxide-based electrochemical sensor for sensitive determination of

4-nitrophenol, *J. Hazard. Mater*. **2012**, *201–202*, 250–259, doi:10.1016/j.jhazmat.2011.11.076.

[125] Jia, L.; Hao, J.; Wang, S.; Yang, L.; Liu, K. Sensitive detection of 4-nitrophenol based on pyridine diketopyrrolopyrrole-functionalized graphene oxide direct electrochemical sensor, *RSC Adv*. **2023**, *13*, 2392–2401, doi: 10.1039/d2ra07239d.

[126] Liu, Z. P.; Wang, Z. J.; Xu, Y. A powerful electrochemical sensor based on Fe_2O_3 nanoparticle-graphene oxide nanocomposites for determination of metronidazole as an antibacterial drug, *Int. J. Electrochem. Sci*. **2022**, *17*, 220731, doi: 10.20964/2022.07.11.

[127] Vivekanandan, K.; Subash, V.; Chen, S. M.; Chen, S. H. Sonochemical synthesis of nickel-manganous oxide nanocrumbs decorated partially reduced graphene oxide for efficient electrochemical reduction of metronidazole, *Ultrason. Sonochem*. **2020**, *68*, 105176, doi: 10.1016/j.ultsonch.2020.105176.

[128] Huang, J. Z.; Qiu, Z. X.; Lin, J. H.; Lin, J. L.; Zhu, F. Q.; Lai,G. H.; Li,Y. L. Ultrasensitive determination of metronidazole using flower-like cobalt anchored on reduced graphene oxide nanocomposite electrochemical sensor, *Microchem. J*. **2023**, *188*, 108444, doi: 10.1016/j.microc.2023.108444.

[129] Han, L.; Zhao, Y. F.; Chang, C.; Li, F. A novel electrochemical sensor based on poly(p-aminobenzene sulfonic acid)-reduced graphene oxide composite film for the sensitive and selective detection of levofloxacin in human urine, *J. Electroanal. Chem*. **2018**, *817*, 141–148, doi: 10.1016/j.jelechem.2018.04.008.

[130] Borowiec, J.; Yan, K.; Tin, C. C.; Zhang, J. D. Synthesis of PDDA functionalized reduced graphene oxide decorated with gold nanoparticles and its electrochemical response toward levofloxacin, *J. Electrochem. Soc*. **2015**, *162*, H164-H169, doi: 10.1149/2.0811503jes.

[131] Li, G. R.; Xu, H.; Lu, X. F.; Feng, J. X.; Tong, Y. X.; Su, C.Y. Electrochemical synthesis of nanostructured materials for electrochemical energy conversion and storage. *Nanoscale*, **2013**, *5*, 4056–4069, doi: 10.1039/C3NR00607G.

[132] Wang, J.; Lu, J.; Hocevar, S.B.; Farias, P. A. M.; Ogorevc, B. Bismuth-coated carbon electrodes for anodic stripping voltammetry, *Anal. Chem*. **2000**, *72*, 3218–3222, doi: 10.1021/ac000108x.

[133] Hwang, G. H.; Han, W. K.; Hong, S. J.; Park, J. S.; Kang, S. G. Determination of trace amounts of lead and cadmium using a bismuth/glassy carbon composite electrode, *Talanta*, **2008**, *77*, 1432–1436, doi: 10.1016/j.talanta.2008.09.028.

[134] Palisoc, S.; Vitto, R. I. M.; Natividad, M. Determination of heavy metals in herbal foods supplements using bismuth/multi-walled carbon nanotubes/nafion modified graphite electrodes sourced from waste batteries. *Sci. Report*, **2019**, *9*, 18491, doi: 10.1038/s41598-019-54589-x.

[135] Brinic, S.; Vladislavic, N.; Buzuk, M.; Bralic, M.; Solic, M. Bismuth film random array carbon fiber microelectrodes for determination of cysteine and N-acetyl cysteine, *J. Electroanal. Chem*. **2013**, *705*, 86–90, doi: 10.1016/j.jelechem.2013.07.031.

[136] Baldrianova, L.; Svancara, I.; Vlcek, M.; Economou, A.; Sotiropoulos, S. Effect of Bi(III) concentration on the stripping voltammetric response of in situ bismuth-coated carbon paste and gold electrodes. *Electrochim. Acta*, **2006**, 52, 481–490, doi: 10.1016/j.electacta.2006.05.029.

[137] Kruusma, J.; Banks, C. E.; Compton, R. G. Mercury-free sono-electroanalytical detection of lead in human blood by use of bismuth-film-modified boron-doped diamond electrodes, *Anal. Bioanal. Chem*. **2004**, *379*, 700–706, doi: 10.1007/s00216-004-2639-5.

[138] Colozza, N.; Cacciotti, I.; Moscone, D.; Arduini, F. Effects of humidity, temperature and bismuth electrodeposition on electroanalytical performances of nafion-coated printed electrodes for Cd^{2+} and Pb^{2+} detection, *Electroanalysis*, **2019**, *32*, 345–357, doi: 10.1002/elan.201900432.

[139] Dehghanzade, M.; Alipour, E. Voltammetric determination of diazepam using a bismuth modified pencil graphite electrode, *Anal. Method*, **2016**, *8*, 1995–2004, doi: 10.1039/c6ay00098c.

[140] Li, D. Y.; Jia, J. B.; Wang, J. G. Preparation and application of chemically modified bismuth film electrode, *Chinese J. Anal. Chem*. **2012**, *40*, 321–327, doi: 10.3724/SP.J.1096.2012.10704.

[141] Arduini, F.; Calvo, J. Q.; Amine, A.; Palleschi, G.; Moscone, D. Bismuth-modified electrodes for lead detection, *Trends Anal. Chem*. **2010**, *29*, 1295–1304, doi:10.1016/j.trac.2010.08.003.

[142] Li, D. Y.; Jia, J. B.; Wang, J. G. A study on the electroanalytical performance of a bismuth film-coated and Nafion-coated glassy carbon electrode in alkaline solutions, *Microchim. Acta*, **2010**,*169*, 221–225, doi: 10.1007/s00604-010-0337-x.

[143] Krolicka, A.; Pauliukaite, R.; Svancara, I.; Metelka, R.; Bobrowski, A.; Norkus, E.; Kalcher, K.; Vytras, K. Bismuth-film-plated carbon paste electrodes, *Electrochem. Commun*. **2002**, *4*, 193-196, doi: 10.1016/S1388-2481(01)00301-0.

[144] Kokkinos, C.; Economou, A.; Raptis, I.; Efstathiou, C. E. Lithographically fabricated disposable bismuth-film electrodes for the trace determination of Pb(II) and Cd(II) by anodic stripping voltammetry, *Electrochim. Acta*, **2008**, *53*, 5294–5299, doi: 10.1016/j.electacta.2008.02.079.

[145] Svancara, I.; Prior, C.; Hocevar, S. B.; Wang, J. A Decade with bismuth-based Electrodes in Electroanalysis, *Electroanalysis*, **2010**, *22*, 1405-1420, doi: 10.1002/elan.200970017.

[146] Sivasubramanian, P. D.; Chang, J. H.; Nagendran, S.; Dong, C. D.; Shkir, M.; Kumar, M. A review on bismuth-based nanocomposites for energy and environmental applications, *Chemosphere*, **2022**, *307*, 135652, doi: 10.1016/j.chemosphere.2022.135652.

[147] Jovanovski, V.; Hočevar, S. B.; Ogorevc, B. Bismuth electrodes in contemporary electroanalysis, *Curr. Opin. Electrochem*. **2017**, *3*, 114–122, doi: 10.1016/j.coelec.2017.07.008.

[148] Muna, W.; Barrera, E.; Robinson, L.; Majeed, H.; Jones, K.; Damschroder, A.; Vila, A. Electroanalytical performance of a bismuth/antimony composite glassy carbon electrode in detecting lead and cadmium, *Electroanalysis*, **2023**, *35*, e202300019, doi: 10.1002/elan.202300019.

[149] Al-Harbi, E. A. Fabrication and Application of bismuth-film modified glassy carbon electrode as sensor for highly sensitive determination of cetirizine dihydrochloride in pharmaceutical products and water samples, *Int. J. Electrochem. Sci*. **2021**, *16*, 211036, doi: 10.20964/2021.10.37.

[150] Gerent, G. G.; Spinelli, A. Environmentally-friendly in situ plated bismuth-film electrode for the quantification of the endocrine disruptor parathion in skimmed milk. *J. Hazard. Mater*. **2016**, *308*, 157–163, doi: 10.1016/j.jhazmat.2016.01.038.

[151] Asadpour-Zeynali, K.; Aleshi, M. Electrochemical modification of glassy carbon electrode by bismuth-chitosan nanosheets for electrocatalytic reduction and determination of tartrazine, *Port. Electrochim. Acta*, **2015**, *32*, 369–379, doi: 10.4152/pea.201406369.

[152] Milan Paunovic, M. S. *Fundamentals of Electrochemical Deposition*. Wiley: **2006**.

[153] Akbari, R.; Mohammadizadeh, M. R.; Antonini, C.; Guittard, F.; Darmanin, T. Controlling morphology and wettability of intrinsically superhydrophobic copper-based surfaces by electrodeposition, *Coatings*, **2022**, *12*, 1260, doi: 10.3390/ coatings12091260

[154] Hu, X.; Liu,T. T.; Zhuang, Y. X.; Wang, W.; Li,Y.Y.; Fan,W. H.; Huang,Y. M. Recent advances in the analytical applications of copper nanoclusters, *Trends Anal. Chem*. **2016**, *77*, 66–75, doi: 10.1016/j.trac.2015.12.013.

[155] Kang, X.; Mai, Z.; Zou, X.; Cai, P.; Mo, J. A sensitive nonenzymatic glucose sensor in alkaline media with a copper nanocluster/multiwall carbon nanotube modified glassy carbon electrode, *Anal. Biochem*. **2007**, *363*, 143–150, doi: 10.1016/j.ab.2007.01.003.

[156] Wang, Z.; Si, L.; Bao, J.; Dai, Z. A reusable microRNA sensor based on the electrocatalytic property of heteroduplex-templated copper nanoclusters, *Chem. Commun*. **2015**, *51*, 6305–6307, doi: 10.1039/c5cc01081k.

[157] SInam, A. K. M.; Angeli, M. A. C.; Shkodra, B.; Douaki, A.; Avancini, E.; Magagnin, L.; Petti, L.; Lugli, P. Flexible screen-printed nitrate sensors with Cu nanoclusters: a comparative analysis on the effect of carbon nanotubes, International Conference on Flexible and Printable Sensors and Systems (FLEPS), Proceedings of the 2021 IEEE, **2021**, doi: 10.1109/FLEPS51544.2021.9469810.

[158] Chowdhury, S.; Mazumder, M. A. J.; Al-Attas, O.; Husain, T. Heavy metals in drinking water: occurrences, implications, and future needs in developing countries. *Sci. Total Environ*. **2016**, *569–570*, 476–488, doi: 10.1016/j.scitotenv. 2016.06.166.

[159] Liu, Y.; Huo, Y.; Wang, X. X.; Yu, S.; Ai, Y.; Chen, Z.; Zhang, P.; Chen, L.; Song, G.; Alharbi, N. S.; Rabah, S. O.; Wang, X. K. Impact of metal ions and organic

ligands on uranium removal properties by zeolitic imidazolate framework materials. *J. Clean. Prod*. **2021**, *278*, 123216, doi:10.1016/j.jclepro.2020.123216.

[160] Cheng, S. Y.; Show, P. L.; Juan, J. C.; Chang, J. S.; Lau, B. F.; Lai, S. H.; Ng, E. P.; Yian, H. C.; Ling, T. C. Landfill leachate wastewater treatment to facilitate resource recovery by a coagulation-flocculation process via hydrogen bond. *Chemosphere*, **2021**, *262*, 127829, doi: 10.1016/j.chemosphere.2020.127829.

[161] Pohl, A. Removal of heavy metal ions from water and wastewaters by sulfur-containing precipitation agents. *Water Air Soil Pollut*. **2020**, *231*, 503, doi.org/10.1007/s11270-020-04863-w.

[162] Thamaraiselvan, C.; Thakur, A. K.; Gupta, A.; Arnusch, C. J. Electrochemical removal of organic and inorganic pollutants using robust laser-induced graphene membranes. *ACS Appl. Mater. Interfaces*, **2021**, *13*, 1452–1462, doi: 10.1021/acsami.0c18358.

[163] Zhang, W. T.; Huang, W. G.; Tan, J.; Huang, D. W.; Ma, J.; Wu, B. D. Modeling, optimization and understanding of adsorption process for pollutant removal via machine learning: Recent progress and future perspectives. *Chemosphere*, **2023**, *311*, 137044, doi: 10.1016/j.chemosphere.2022.137044.

[164] Rout, D. R.; Jena, H. M. Removal of malachite green dye from aqueous solution using reduced graphene oxide as an adsorbent. *Mater. Today Proc*. **2021**, 47, 1173–1182, doi: 10.1016/j.matpr.2021.03.406.

[165] Wu, J. C.; Chuang, Y. H.; Liou, S. Y. H.; Li, Q. L.; Hou, C. H. In situ engineering of highly conductive TiO_2/carbon heterostructure fibers for enhanced electrocatalytic degradation of water pollutants. **2022**, *429*, 128328, doi: 10.1016/j.jhazmat.2022.128328.

[166] Rout, D. R.; Chaurasia, S.; Jena, H. M. Enhanced photocatalytic degradation of malachite green using manganese oxide doped graphene oxide/zinc oxide (GO-ZnO/Mn_2O_3) ternary composite under sunlight irradiation. *J. Environ. Manag*. **2022**, *318*, 115449, doi: 10.1016/j.jenvman.2022.115449.

[167] Cherniak, S. L.; Almuhtaram, H.; McKie, M. J.; Hermabessiere, L.; Yuan, C.; Rochman, C. M.; Andrews, R. C. Conventional and biological treatment for the removal

of microplastics from drinking water. *Chemosphere*, **2022**, *288*, 132587, doi: 10.1016/j.chemosphere.2021.132587.

[168] Zhu, Q.; Wang, J. C.; Zhang, L.; Yan, D. H.; Yang, H. J.; Zhang, L. Z.; Miao, X. Y. Research progress of graphene for the adsorption, enrichment and analysis of environmental pollutants. *Bull. Mater. Sci*. **2023**, *46*, 17, doi: 10.1007/s12034-022-02856-5.

[169] Ibrahim, Q.; Creedon, L.; Gharbia, S. A literature review of modelling and experimental studies of water treatment by adsorption processes on nanomaterials. *Materials*, **2022**,*12*, 360, doi: 10.3390/membranes12040360.

[170] Kesamseetty, V. R.; Singampalli, R.; BabuTadiboyina, A.; Narasipuram, V. K. P.; Prasad, K. V.; Hanumanthrayappa, M.; Ratnakaram, V. N.; Sannapaneni, J.; Kadiyala, C. B. N. Role of carbon materials in the removal of organic pollutants: an abridged review, *Biointerface Res. Appl. Chem.* **2022***,* 12, 1974–1997, doi:10.33263/ BRIAC122.19741997.

[171] Rout, D. R.; Jena, H. M.; Baigenzhenov, O.; Hosseini-Bandegharaei, A. Graphene-based materials for effective adsorption of organic and inorganic pollutants: A critical and comprehensive review, *Sci. Total Environ*. **2023**, *863*, 160871, doi: 10.1016/j.scitotenv.2022.160871.

[172] Xu, J.; Wang, L.; Zhu, Y. F. Decontamination of Bisphenol A from aqueous solution by graphene adsorption, *Langmuir* **2012**, *28*, 8418−8425, doi: 10.1021/la301476p.

[173] Liu, T. H.; Li, Y. H.; Du, Q. J.; Sun, J. K.; Jiao, Y. Q.; Yang, G. M.; Wang, Z. H. Xia, Y. Z.; Zhang, W.; Wang, K. L.; Zhu, H. W.; Wu, D. H, Adsorption of methylene blue from aqueous solution by graphene, *Colloid Surface B*. **2012**, *90*, 197–203, doi:10.1016/j.colsurfb.2011.10.019.

[174] Fan, H. T.; Zhao, C. Y.; Liu, S.; Shen, H. Adsorption characteristics of chlorophenols from aqueous solution onto graphene. *J. Chem. Eng. Data*, **2017**, *62*, 1099–1105, doi: 10.1021/acs.jced.6b00918.

[175] Wang, X.; Lu, M.; Wang, H.; Pei, Y.; Rao, H.; Du, X. Three-dimensional graphene aerogels–mesoporous silica frameworks for superior adsorption capability of phenols. *Sep. Purif. Technol*. **2015**, *153*, 7–13, doi:10.1016/j.seppur.2015.08.030.

[176] Sun, Z.; Zhao, L.; Liu, C.; Zhen, Y.; Zhang, W.; Ma, J. A novel 3D adsorbent of reduced graphene oxide-β-cyclodextrin aerogel coupled hardness with softness for efficient removal of Bisphenol A. *Chem. Eng. J.* **2019**, *372*, 896–904, doi: 10.1016/j.cej.2019.04.217.

[177] Ahsan, M. A.; Jabbari, V.; Islam, M. T.; Turley, R. S.; Dominguez, N.; Kim, H.; Castro, E.; Hernandez-Viezcas, J. A.; Curry, M. L.; Lopez, J.; Gardea-Torresdey, J. L.; Noveron, J. C. Sustainable synthesis and remarkable adsorption capacity of MOF/ graphene oxide and MOF/CNT based hybrid nanocomposites for the removal of Bisphenol A from water. *Sci. Total Environ*. **2019**, *673*, 306–317, doi: 10.1016/j.scitotenv.2019.03.219.

[178] Lv, X.; Li, S. Graphene oxide-crospolyvinylpyrrolidone hybrid microspheres for the efficient adsorption of 2,4,6-trichlorophenol. *ACS Omega*, **2020**, *5*, 18862–18871, doi: 10.1021/acsomega.0c02028.

[179] Kong, Q. P.; Zhang, H. Z.; Lan, Y. L.; Shi, X. Q.; Fang, Z. L.; Chang, Q.; Liu, J.; Wei, C. H. Functional graphene oxide for organic pollutants removal from wastewater: a mini review, *Environ. Technol*. **2022**, *44*, 3183-3195, doi: 10.1080/09593330.2022.2053754.

[180] Wang, Q. Q.; Gao, T.; Hao, L.; Guo, Y. X.;Liu, W. H.; Guo, L. Y.; Wang, C.; Wang, Z.; Wu, Q. H. Advances in magnetic porous organic frameworks for analysis and adsorption applications, *Trends Anal. Chem*. **2020**, *132*, 116048, doi: 10.1016/j.trac.2020.116048.

[181] Phouthavong, V.; Yan, R. X.; Nijpanich, S.; Hagio, T.; Ichino, R.; Kong, L.; Li, L. Magnetic adsorbents for wastewater treatment: advancements in their synthesis methods, *Materials*, **2022**, *15*, 1053, doi: 10.3390/ma15031053.

[182] Shen, X.; Chen, X.; Sun, D.; Wu, T.; Li, Y. Fabrication of a magnetite/ diazonium functionalized-reduced graphene oxide hybrid as an easily regenerated adsorbent for efficient removal of chlorophenols from aqueous solution. *RSC Adv*. **2018**, *8*, 7351–7360, doi: 10.1039/C8RA00503F.

[183] Rekos, K.; Kampouraki, Z. C.; Sarafifidis, C.; Samanidou, V.; Deliyanni, E. Graphene oxide based magnetic nanocomposites with polymers as effective Bisphenol A nanoadsorbents. Materials (Basel), **2019**, *12*, 1987. doi:10.3390/ma12121987.

[184] Adel, M.; Ahmed, M. A.; Mohamed, A. A. Synthesis and characterization of magnetically separable and recyclable crumbled $MgFe_2O_4$/reduced graphene oxide nanoparticles for removal of methylene blue dye from aqueous solutions. *J. Phys. Chem. Solids*, **2021**, *149*, 109760, doi: 10.1016/j.jpcs.2020.109760.

[185] Sahoo, S. K.; Padhiari, S.; Biswal, S. K.; Panda, B. B.; Hota, G. Fe_3O_4 nanoparticles functionalized GO/g-C_3N_4 nanocomposite: an efficient magnetic nanoadsorbent for adsorptive removal of organic pollutants. *Mater. Chem. Phys*. **2020**, *244*, 122710, doi: 10.1016/j.matchemphys.2020.122710.

[186] Zhang, L.; Miao, Y.; Zhang, D.; Gao, B.; Zhuo, J. X. Removal of oxytetracycline from imulated wastewater by graphene loaded zero-valent iron, *Fresen. Environ. Bull*. **2021**, *30*, 5887–5895.

[187] Masud, A.; Soria, N. G. C.; Aga, D. S.; Aich, N. Adsorption and advanced oxidation of diverse pharmaceuticals and personal care products (PPCPs) from water using highly efficient rGO-nZVI nanohybrids, *Environ. Sci. Water Re*s. *Technol*. **2020**, *6*, 2223–2238, doi: 10.1039/d0ew00140f.

[188] Wang, W. B.; Dong, Q. L.; Mao, Y. T.; Zhang, Y. F.; Gong, T. T.; Li, H. GO accelerate iron oxides formation and tetrabromobisphenol A removal enhancement in the GO loaded NZVI system, *Environ. Pollut*. **2023**, *316*, 120512, doi: 10.1016/j.envpol.2022.120512.

Chapter 2

Experimental Materials and Research Methods

2.1 Introduction

The main research in this thesis is focused on the fabrication and characterisation of functional composite materials on the surface of GCE as well as their applications as sensors for the detection of pollutants in aquatic environments. The functional composite materials include graphene and metal nanoparticles (Bi and Cu nanoparticles or nanostructures). These composite materials were assembled by simple electrodeposition and the fabricated composite films were characterised by SEM, EDX and elemental mapping, FTIR and UV-visible spectroscopy, and electrochemical measurements. These composite materials modified electrodes were used as electrochemical sensors for the detection of four pollutants in aquatic environments, namely MCPA, *p*-NP, MTZ and LEVO. All fabrication processes, characterisation and application of the composite materials modified electrodes are described in the following sections. At the same time, the experimental techniques and apparatus used in this study are described briefly.

2.2 Experimental section

2.2.1 Chemical Reagents

All the chemical reagents used in this thesis were of analytical grade. They were purchased from Merck/Sigma Aldrich directly and used as received, without any further purification steps. All the chemical reagents used are listed in Table 2-1.

Table 2-1. Chemical reagents used for experiments in this thesis.

Reagent name	Chemical formula
Acetic acid	CH_3COOH (HAc)
Ammonium chloride	NH_4Cl

Ascorbic acid	$C_6H_8O_6$
Bismuth nitrate	$Bi(NO_3)_3$
4-Chloro-2-methylphenoxyacetic acid	$C_9H_9ClO_3$
4-Chloro-2-methylphenol	C_7H_7OCl
Calcium chloride	$CaCl_2$
Citric acid	$C_6H_8O_7$
Copper acetate	$Cu(CH_3COO)_2$, $(Cu(Ac)_2)$
Copper sulphate	$CuSO_4$
4-(2,4-dichlorophenoxy) butyric acid)	$C_{10}H_{10}Cl_2O_3$
Dipotassium hydrogen phosphate	K_2HPO_4
Ethanol	CH_3CH_2OH
Ferrous sulfate	$FeSO_4$
Glucose	$C_6H_{12}O_6$
Graphene nanoplatelets	Gr
Hydrochloric acid	HCl
Hydrocortisone	$C_{21}H_{30}O_5$
Levofloxacin	$C_{18}H_{20}FN_3O_4$
Magnesium chloride	$MgCl_2$
Methanol	CH_3OH
2-Methyl-5-nitroimidazole-1-ethanol	$C_6H_9N_3O_3$
p-Nitrophenol	$NO_2C_6H_4OH$
o-nitrophenol	$NO_2C_6H_4OH$
Nitric acid	HNO_3
Phosphoric acid	H_3PO_4
Potassium chloride	KCl
Potassium dihydrogen phosphate	KH_2PO_4
Potassium ferricyanide	$K_3[Fe(CN)_6]$
Potassium ferrocyanide	$K_4[Fe(CN)_6]$
Potassium phosphate	K_3PO_4
Sodium acetate	CH_3COONa (NaAc)
Sodium carbonate	Na_2CO_3

Sodium borohydride	$NaBH_4$
Sodium chloride	NaCl
Sodium hydroxide	NaOH
Sodium nitrate	$NaNO_3$
Sodium nitrite	$NaNO_2$
Sodium sulphate	Na_2SO_4
Sulphuric acid	H_2SO_4
Tetrabutyl ammonium chloride	$C_{16}H_{36}ClN$
Zinc chloride	$ZnCl_2$

2.2.2 Instruments

All the instruments used in this thesis are listed in Table 2-2.

Table 2-2. Instruments used in completing various experiments

Equipment Name	Model
EDX instrument	Oxford Instrument INCAz-act ESX
Electronic balance	Sartorius Models TE612 and TE214s
Electrochemical workstation	CHI760C
High speed tabletop centrifuge	Thermoscientific SORVALL ST 8
Magnetic stirrer apparatus	Fisherbrand
pH meter	METTLER TOLEDO
Potentiostat	Solartron 1287 coupled with a 1255 FRA (Solartron)
SEM	Hitachi S-3200-N
Thermo Fisher IR spectrometer	Nicolet iS50 FT-IR microscope
Ultrasonic cleaner	BRANSON 1510
UV-Vis Spectrometer	CARY 50 Conc

2.2.3 The Preparation of Solutions

2.2.3.1 Buffer PBS

Phosphate solutions (PBS) were prepared at different concentrations of 0.1 M and 0.05 M with different pH values adjusted by diluted H_3PO_4, HNO_3, HCl or NaOH solutions.

2.2.3.2 Buffer acetate solution

Buffer acetate solution was prepared with a concentration of 0.1 M NaAc with pH values of 4.5 adjusted by diluted CH_3COOH (HAc).

2.2.3.3 MCPA solution

A stock solution of MCPA at a concentration of 4.0 mM was prepared in PBS buffer. More dilute solutions were prepared by serial dilutions of the stock solution.

2.2.3.4 MTZ solution

The MTZ solution was prepared at a concentration of 4.0 mM dissolved in PBS buffer. Other concentrations of MTZ were prepared through serial dilution.

2.2.3.5 LEVO solution

The stock LEVO solution was prepared at the concentration of 1.0 mM dissolved in PBS buffer. This stock solution was used to prepare lower concentrations by serial dilution of the 1.0 mM LEVO.

2.2.3.6 *p*-NP solution

A stock solution of 1.0 mM *p*-NP was prepared in PBS buffer. Other solutions at lower concentrations were obtained by diluting the 1.0 mM solution of *p*-NP.

2.2.3.7 $Bi(NO_3)_3$ solution

$Bi(NO_3)_3$ solutions were prepared in two different manners. Firstly, 10 mM $Bi(NO_3)_3$ $5H_2O$ solution was prepared in 0.1 M HNO_3 to give complete dissolution without any insoluble hydroxides. This solution was then diluted with 0.1 M acetate buffer at a pH of 4.5 to give the 1.0 mM $Bi(NO_3)_35H_2O$ in 0.01 M HNO_3 and 0.09 M acetate with a final pH of 1.2~1.5. Secondly, a 5.0 mM $Bi(NO_3)_35H_2O$ solution was made in 1.0 M HNO_3.

2.2.3.8 Potassium ferricyanide and Potassium ferrocyanide solution

The solution (1.0 mM) was prepared using the mixture of $K_3[Fe(CN)_6]$ and $K_4[Fe(CN)_6]$ dissolved in 0.1 M KCl solution. This solution was employed as an electrochemical probe and used to estimate the electroactive surface area of the sensors.

2.2.3.9 Graphene (Gr) suspension

The suspension of Gr (1.0 mg/mL) was prepared by dispersing Gr nanoplatelets in a 0.1 M phosphate buffer (PBS) solution at a pH of 7.0 using ultrasonication for 30 min.

2.2.3.10 $Cu(Ac)_2$ solution

10 mM $Cu(Ac)_2$ was prepared in NaAc + HAc (0.1 M) at pH 4.5.

2.2.3.11 NaOH solution

0.1 M NaOH was prepared in distilled water.

2.2.4 Fabrication of the modified electrodes

A GCE (3 mm in diameter) was employed throughout this thesis. Before its use, the GCE was polished on a micro-cloth (Aka-Napel cloth), using progressively smaller sized diamond suspensions (Akasol) with a final 1 μm particle size, until a mirror finish was obtained. Then, the polished GCE was sonicated for a certain period of 10 min and rinsed thoroughly with deionised water.

2.2.4.1 The activated GCE (A-GCE)

The GCE was activated in a 0.05 M PBS by cycling the polished and cleaned GCE at different potential ranges between –2.0 V and 2.5 V vs. SCE at 100 mV s^{-1} for the different cycles to form the activated glassy carbon, A-GCE. The resulting A-GCE was thoroughly rinsed with deionised water, and then the cleaned A-GCE was utilised in the electrochemical detection of analytes in 0.1 M PBS at different pH.

2.2.4.2 Bismuth modified GCE (GCE/Bi)

The GCE/Bi was fabricated by immersing the polished and cleaned GCE in a 5.0 mM or 1.0 mM $Bi(NO_3)_3$ solution and applying different potentials from –0.75 to –1.0 V vs. SCE for a certain period of time to reduce Bi^{3+} to Bi^0 on the surface of the GCE.

2.2.4.3 Graphene modified GCE (GCE/Gr)

Gr was electrochemically deposited on the surface of GCE to form GCE/Gr by scanning for 5, 10 and 15 cycles at a scan rate of 50 mV s^{-1} in the potential range from –1.5 V to

0.8 V vs. SCE with magnetic stirring of the Gr dispersion, to keep it well dispersed in the solution phase.

2.2.4.4 Copper modified GCE (GCE/Cu)

The GCE/Cu was prepared by immersing the polished and cleaned GCE in 10 mM $Cu(Ac)_2$ dissolved in NaAc and HAc with a pH of 4.5. The copper nanostructures were formed by applying a potential of 0.7 V for 5 s, a potential of −0.45 V for 2.5 s, and finally, a potential of −0.25 V for 30 s, 50 s, 80 s and 100 s to deposit Cu on the surface of the GCE.

2.2.4.5 Bismuth modified A-GCE (A-GCE/Bi)

Firstly, the A-GCE was prepared according to the procedure described in Section 2.2.4.1; then the A-GCE/Bi was formed according to the procedure described in Section 2.2.4.2.

2.2.4.6 Graphene and bismuth modified GCE (GCE/Gr/Bi)

Firstly, the GCE/Gr was constructed according to the procedure described in Section 2.2.4.3; then the GCE/Gr//Bi was fabricated according to the procedure described in Section 2.2.4.2.

2.2.4.7 Graphene and copper modified GCE (GCE/Gr/Cu)

Firstly, the GCE/Gr was formed according to the procedure described in Section 2.2.4.3; then the GCE/Gr/Cu was prepared according to the procedure described in Section 2.2.4.4.

2.2.5 Preparation of Magnetic Adsorbent and Study on Adsorbability

2.2.5.1 Preparation of graphene nanoplatelets (Gr) modified with zero-valent iron nanostructures (Fe), Gr/Fe

The Gr/Fe was prepared using the liquid-phase reduction method based on the following chemical reaction Equation 2–1 [1]:

$$3Fe^{2+} + BH_4^- + 3H_2O \rightarrow 3Fe^0 + H_2BO_3^- + 6H^+ + H_2\uparrow \quad (2–1)$$

Graphene nanoplatelets (1 g) and $FeSO_47H_2O$ (1 g) were mixed in 100 mL distilled water with stirring vigorously for 20 min in a nitrogen atmosphere, then $NaBH_4$ solution (0.22 M, 50 mL) was added into the mixed solution dropwise at the speed of 1–2 drops per second and vigorously stirred continuously under nitrogen atmosphere.

After all of the $NaBH_4$ solution had been added, the obtained mixed solution was stirred at room temperature in a sealed 200 mL glass beaker continuously for 10 h to completely deplete $NaBH_4$ and $FeSO_47H_2O$. After that, the vacuum filtration was used to collect the Gr/Fe composite, which was quickly rinsed by distilled water and absolute ethanol thoroughly, followed by vacuum drying at room temperature. Finally, the Gr/Fe composite was kept in a sealed bottle for future use and the amount of zero-valent iron component on the surface of Gr was estimated to be ca. 170 mg/g.

2.2.5.2 Adsorption experiments

All adsorption experiments were carried out in sealed 200 mL glass beakers that contained a certain amount of adsorbent and 100 mL of a solution in the appropriate concentration of adsorbate. The beakers were placed on the magnetic stirrer at a stirring speed of 200 rpm at room temperature. After a certain period, the adsorbent was separated from the solution by the magnet and the UV-vis spectra of unadsorbed

adsorbates were measured and recorded. Their concentrations in the solution were analysed with the Beer-Lambert law at their maximum absorption wavelengths.

2.2.5.2.1 The preparation of the adsorbate solutions

A certain mass of MCPA, *p*-NP, MTZ and LEVO were dissolved in distilled water as a stock solutions (1.0 mM) and was further diluted with a certain amount of distilled water to the required concentrations before use.

2.2.5.2.2 Adsorbent dosage experiments

The effect of adsorbent dosage on the adsorption of the four compounds was investigated by adding different dosages of the adsorbent (10 – 80 mg) to 100 mL solutions of 0.1 mM adsorbate.

2.2.5.2.3 Adsorption kinetics experiments

All adsorption kinetic experiments were performed with an initial solution concentration of 0.1 mM adsorbate at room temperature to determine the minimum time required for adsorbent adsorption to reach the equilibrium. The concentration of each solution was recorded at different time intervals from 20 to 720 min.

2.2.5.2.4 Adsorption experiments at different pH

The effect of the initial solution pH on the adsorption of the adsorbate by the adsorbent was tested in a pH range of 3.0 to 9.0 with a concentration of 0.1 mM adsorbate at room temperature. The solution pH was adjusted by adding a solution of 0.05 M HCl or 0.05 M NaOH.

2.2.5.2.5 Recovery experiments

The adsorbent was separated by the magnet after it adsorbed the adsorbate, then the separated adsorbent was immersed in 0.1 M NaOH for 10 min and rinsed in sequence first with distilled water for five times with stirring, followed, with absolute ethanol for five times to remove the adsorbed adsorbate. Finally, the cleaned adsorbent was dried in an oven at 60℃overnight.

2.3 Electrochemical experiments

2.3.1 Electrochemistry

In electrochemistry, there are two important physical quantities or fundamental observables, the current (*I*) and potential (*E*). The current represents the flow of charge driven by the force called the potential. In a typical electrochemical experiment, one of the two observables is normally controlled whilst the evolution of the other one is recorded. The response of electrochemical systems to external stimuli depends on many variables, including the property and concentration of analytes.

2.3.2 The Electrochemical cell set-up

In this thesis, most of the developed composite materials were prepared and characterised by electrochemical methods. All the electrochemical experiments were conducted at room temperature, using a Solartron 1287 potentiostat or CHI 760C electrochemical workstation. Each system was controlled by a computer including various software packages (CorrWare for Windows^{TM}, Version 3.0 and CHI 760C softaware, Version 14.08, respectively). The schematic of the electrochemical system is represented in Figure 2-1.

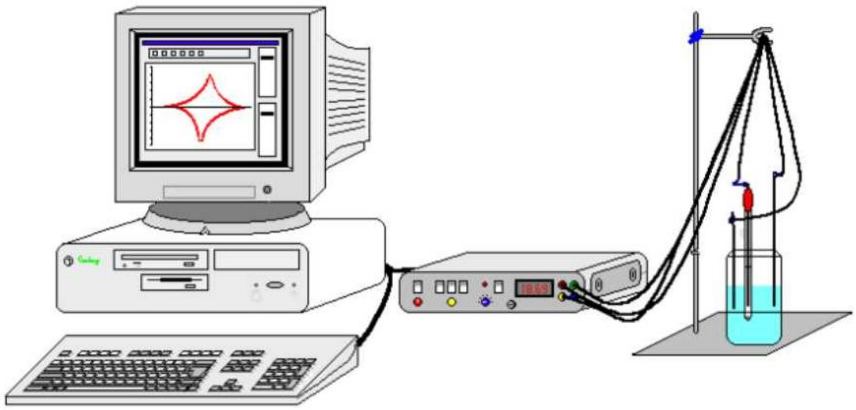

Figure 2-1. Schematic of the electrochemical system used for all electrochemical measurements [2].

In the electrochemical system, a standard three-electrode cell was used, comprising a GCE or modified GCE as the working electrode (WE), a high surface area platinum wire as the counter electrode (CE), and a saturated calomel electrode (SCE) served as the reference electrode (RE). For clarity, a representative of the electrochemical cell used is displayed in Figure 2-2(a). The electrochemical cell includes a glass cylinder covered by a Teflon lid with three holes and three electrodes. Before the use of GCE, it was polished and cleaned according to the procedure described in the section 2.2.4. For the SCE reference electrode, it was stored in a saturated KCl solution to protect the porous frit from drying out when it was not in use. During the electrochemical measurements, to prevent KCl solution from polluting the supporting electrolyte solution, the SCE reference electrode was washed using distilled water. When the electrochemical experiments were carried out, the three electrodes were immersed in the supporting electrolyte solution, followed by connecting to the potentiostat or electrochemical workstation. As shown in Figure 2-2(b), current flows between WE and CE, while potential is measured between the WE and RE.

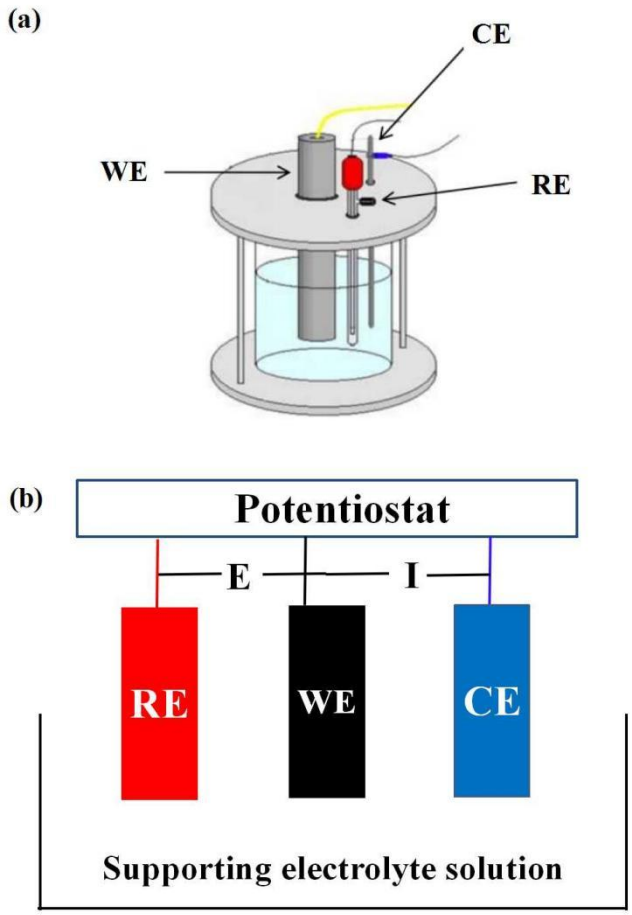

Figure 2-2. Schematic of the electrochemical cell used in the electrochemical system.

2.3.3 Electrochemical techniques

In this thesis, different electrochemical techniques were applied. For the preparation of the modified electrodes, both potentiostatic and cyclic voltammetry were used. For the characterisation of the modified electrodes and detection of the analytes, cyclic voltammetry (CV) and differential pulse voltammetry (DPV) were employed. These techniques are now described.

2.3.3.1 Potentiostatic technique

Constant Potential Amperometry (CPA) means that a constant potential, which is sufficient to either oxidise or reduce the analyte, is applied to the working electrode, while the resultant current output (I) with respect to time (t) is monitored and recorded

as the *I-t* curve. In this thesis, the potentiostatic technique was used to electrodeposit Bi and Cu nanoparticles on the surface of the GCE or modified GCE to prepare the modified electrodes applied in Chapters 4-6. In addition, this technique was applied to the removal of the Bi film from the modified electrode for obtaining a new clean electrode surface in Chapters 4-5.

2.3.3.2 Cyclic Voltammetry (CV)

CV is a common electrochemical research method, and it has been recognised as one of the widely used and most useful electrochemical techniques. During the operation of CV, the electrode potentials are scanned repeatedly for one or more times at different scan rates with a triangular waveform, as shown in Figure 2-3, meaning CV is a dynamic electrochemical technique. In Figure 2-3, the initial applied potential (E_i) is scanned to a vertex potential (E_v), then scanning is reversed, and the vertex potential is swept back to the final potential (E_f), generating a triangular waveform over time. Usually, the final applied potential is equal to the initial applied potential, $E_f = E_i$. The potential range is chosen according to different reduction and oxidation reactions occurring alternately on the electrode surface, and then the current-potential curves are recorded when the applied potentials are varied between two selected potential limits at the scan rate. The current-potential curves are called Cyclic Voltammograms or Cyclic Voltammetry curves, as described in Figure 2-4.

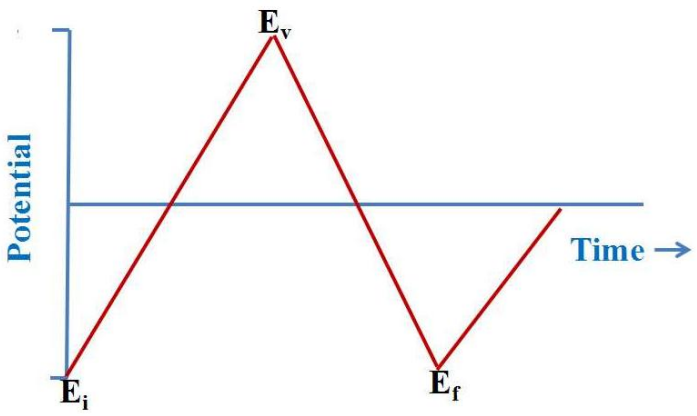

Figure 2-3. Triangular waveform formed as potential is changed over time.

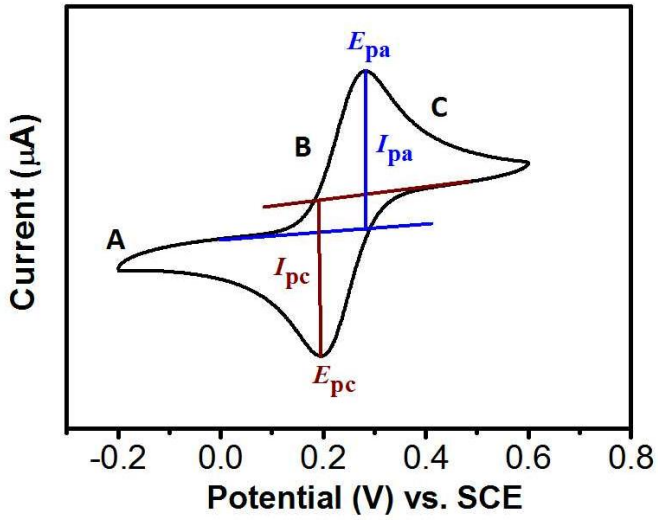

Figure 2-4. Cyclic Voltammogram

For clarity, the redox reaction of the species A in the solution is taken as an example, Equation 2–2. When the positive potential is applied to the WE and the $\boldsymbol{E_i}$ is swept to the $\boldsymbol{E_v}$, the species A in the solution gives one electron to the electrode surface, thereby generating species A^+, meaning the evolution of the electrochemical reaction from the species A to the species A^+ takes place at the electrode surface, described in Figure 2-5(a). From Figure 2-4, with increasing the applied potential, a peak current is reached to give a maximum value and then decreases again. This peak current ($\boldsymbol{I_{pa}}$) is termed the oxidation or anodic peak while the potential corresponding to the maximum current is called the oxidation or anodic peak potential ($\boldsymbol{E_{pa}}$). In turn, when the $\boldsymbol{E_v}$ is swept back to $\boldsymbol{E_f}$, the species A^+ in the solution obtains one electron from the electrode surface, to give A, Figure 2-5(b). Again, a peak is observed, Figure 2-4. This peak containing the maximum current ($\boldsymbol{I_{pc}}$) is called the reduction or cathodic peak while the potential corresponding to the maximum current is called the reduction or cathodic peak potential ($\boldsymbol{E_{pc}}$).

$$\mathbf{A - e^- \rightleftarrows A^+} \qquad (2\text{–}2)$$

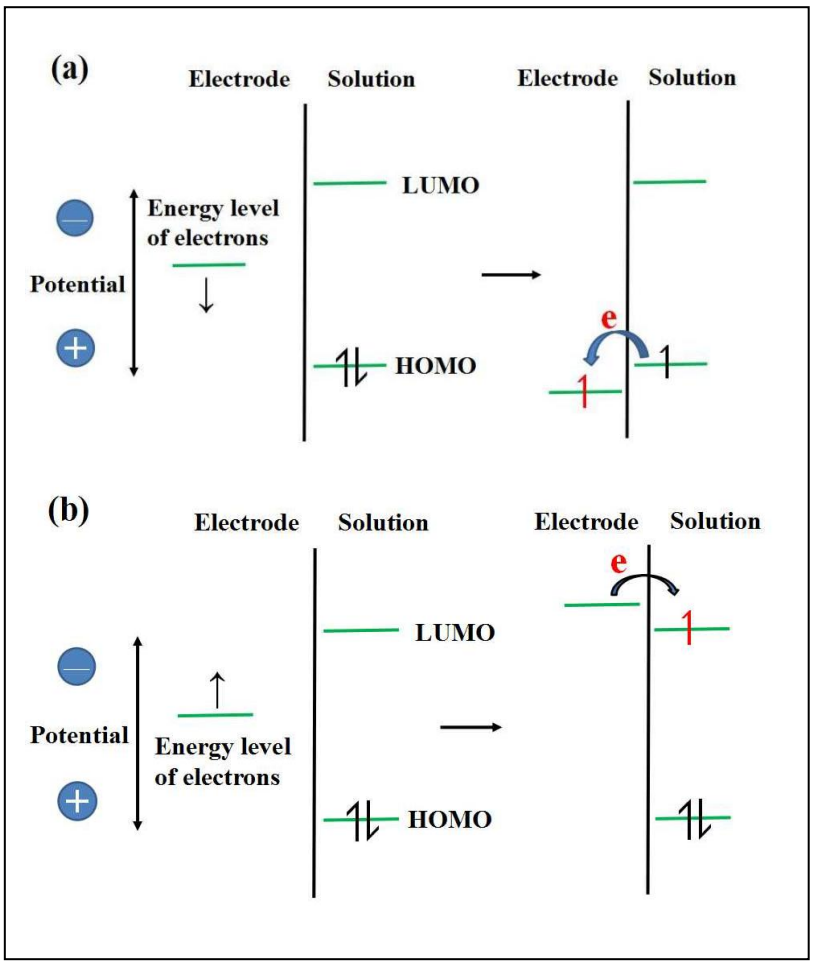

Figure 2-5. Representation of **(a)** oxidation and **(b)** reduction process of a species, A, in solution. HOMO represents the highest occupied molecular orbitals and LUMO expresses the lowest unoccupied molecular orbitals [3].

The maximum current, I_{pa} or I_{pc}, observed in Figure 2-4, is due to diffusion processes and the formation of a diffusion layer. The position (A) in Figure 2-4 corresponds to the uniform bulk concentration at time, t = 0. As the potential is scanned in the forward direction (B) the oxidation of A occurs and the rate of oxidation increases with increasing potential, hence the concentration of species A is depleted at the electrode surface. This lower concentration at the electrode surface gives a higher concentration gradient (initially), giving rise to the increasing current. According to Fick's law of diffusion, more flux to the electrode surface occurs, hence a higher current is obtained. As the potential is further driven in the anodic direction, the concentration of the species A at the electrode surface will eventually go to zero (C). Simultaneously, the volume in the solution that is depleted of species A will increase and the

concentration gradient will begin to decrease. As the concentration gradient decreases, less flux to the surface occurs, hence the current will begin to decrease again.

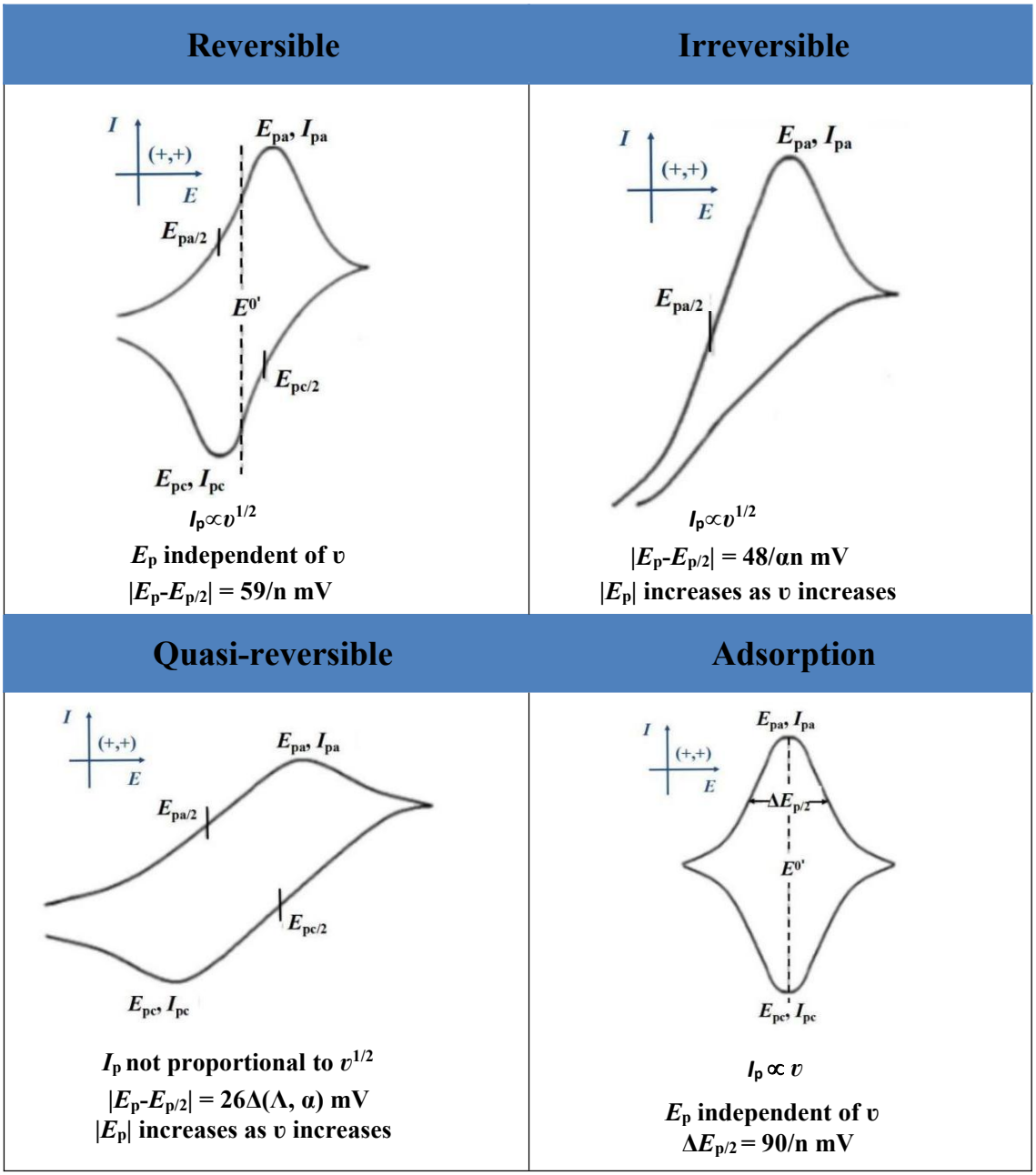

Figure 2-6. Representative cyclic voltammograms of reversible, irreversible, quasi-reversible or adsorption processes. $E_{0'}$ is the formal potential for a reversible system, $E_{0'} = (E_{pa} + E_{pc}) / 2$, n is the number of electrons transferred in the redox process and α is the electron transfer coefficient. The factor $\Delta(\Lambda, \alpha)$ is a function of α and $\Lambda = k^0/(\upsilon DF/RT)^{1/2}$, where D is the diffusion coefficient of the electroactive species and k^0 is the standard heterogeneous rate constant [2].

The four main Cyclic Voltammograms are shown in Figure 2-6, indicating whether the reaction process of the redox species on the electrode surface is reversible, irreversible, quasi-reversible or adsorption controlled [4]. Generally, several main parameters are used to describe the reaction process, such as peak current ($\boldsymbol{I_p}$), peak potential ($\boldsymbol{E_p}$), potential width at half peak $|\boldsymbol{E}_p - \boldsymbol{E}_{p/2}|$, potential scan rate ($\boldsymbol{v}$) as indicated in Figure 2-6. For reversible and adsorption systems, the peak potentials ($\boldsymbol{E_p}$) do not change with the scan rates ($\boldsymbol{v}$), whereas the peak potentials ($|\boldsymbol{E_p}|$) increase with an increase of the scan rates for irreversible and quasi-reversible systems. In addition, for reversible and irreversible processes, the peak currents ($\boldsymbol{I_p}$) change linearly with the square root of scan rates ($\boldsymbol{v^{1/2}}$) indicative of diffusion-controlled processes, whereas the peak current ($\boldsymbol{I_p}$) changes linearly with the scan rate ($\boldsymbol{v}$) for reversible adsorbed species. The exact diagnostic equations employed to confirm these redox characteristics are described in detail in various electrochemistry textbooks [3,4].

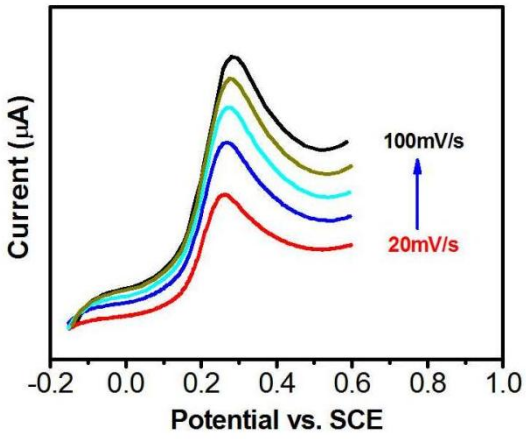

Figure 2-7. Representative voltammograms at different scan rates.

Representative voltammograms at different scan rates are shown in Figure 2-7. It is evident that the peak current increases with an increase of the scan rate. This observation is ascribed to the fact that at slow scan rates the diffusion layer will grow much further from the electrode surface and the flux to the electrode surface will be smaller, giving rise to a smaller concentration gradient, thereby the current will be lower at slow scan rates and higher at high scan rates.

The cyclic voltammograms at different scan rates can provide kinetic information concerning the electrochemical process such as diffusion-controlled or adsorption-controlled process. A linear response of the peak current to the square root of scan rate indicates a diffusion-controlled reaction, as described by the Randles-Sevcik equation. The Randles-Sevcik equation for reversible or quasi-reversible systems is given in Equation 2–3 and for an irreversible system with Equation 2–4 [5].

$$i_p = (2.69 \times 10^5)\, n^{3/2} D^{1/2} v^{1/2} AC \qquad (2\text{–}3)$$

$$i_p = -(2.99 \times 10^5)\, n\, (\alpha n')^{1/2} D^{1/2} v^{1/2} AC \qquad (2\text{–}4)$$

Here i_p is the peak current (A), n is the number of electrons transferred, D is the diffusion coefficient ($cm^2\ s^{-1}$), v is the scan rate ($V\ s^{-1}$) and C is the concentration (mol/mL), α is the charge transfer coefficient and n' is the number of electrons transferred up to and including the rate determining step, A is the area of the electrode (cm^2).

When both the oxidation and reduction species are stable, reversible electrochemical behaviour can be observed, where the kinetics of the electron transfer process is fast [6]. In $Fe(CN)_6^{3-}/Fe(CN)_6^{4-}$, quasi-reversible electrochemical behaviour can be observed due to good stability of $Fe(CN)_6^{3-}$ and $Fe(CN)_6^{4-}$, hence this mixed solution is often used as the electrochemical probe to determine the electroactive area of the electrode. In Chapters 3 and 6, the electroactive area of the activated GCE was determined in the mixed solution of $Fe(CN)_6^{3-}$ and $Fe(CN)_6^{4-}$.

2.3.3.3 Differential Pulse Voltammetry (DPV)

Pulse voltammetry was explored to improve the sensitivity of voltammetric measurements through significantly increasing the ratio of Faraday current to non-Faraday current. This is achieved by diminishing the double layer capacitance so that the current recorded is totally faradaic in nature. There are several types of pulsed techniques, such as normal pulse voltammetry (NPV), differential pulse voltammetry

(DPV) and square wave voltammetry (SWV). In this thesis, the DPV technique was utilised to determine the concentrations of the analytes and to investigate the influence of the solution pH on the oxidation or reduction potential of the analytes in Chapters 3-4.

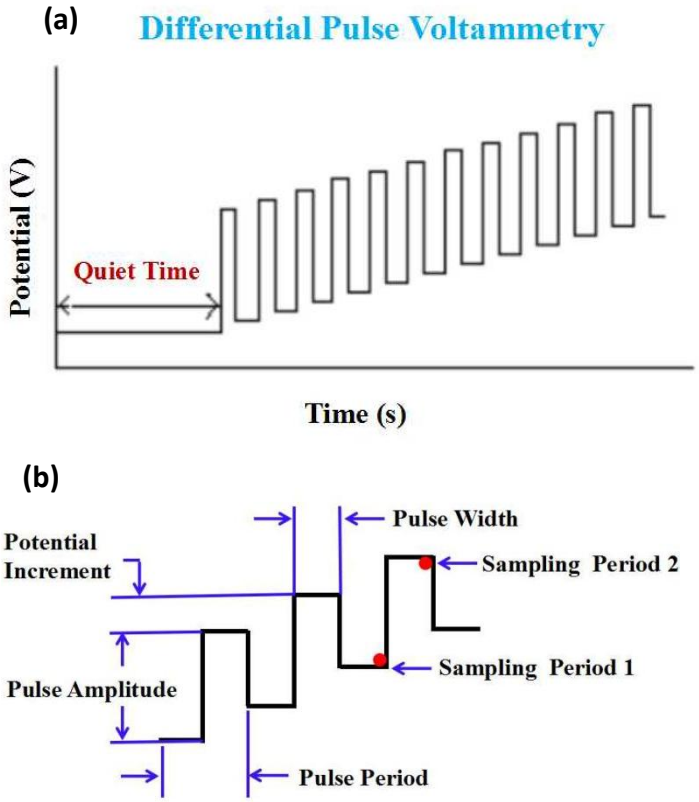

Figure 2-8. Schematic of DPV technique, showing the step method used **(a)** and the parameter settings required **(b)**. The red dots represent the points at which the currents are measured [7].

In the DPV technique, the potential is incremented and increased at a fixed rate, and the pulses applied are of the same magnitude each time, as displayed in Figure 2-8(a). Moreover, the current values are measured shortly before the pulse is applied and at the end of the pulse, as shown in the red dots in Figure 2-8(b), then the difference between the measured two values is recorded and plotted as a function of the applied potential. The specific parameters are provided in Chapters 3-4.

2.3.3.4 Electrochemical impedance spectroscopy (EIS)

EIS was used to examine the properties and stability of the modified electrodes with different analytes. The EIS measurements were carried out using a Solartron 1287 potentiostat coupled with a 1255 FRA (Solartron). The experimental data were recorded at the potential at which the analytes were reduced or oxidised based on their CV curves, with a small sinusoidal excitation voltage of 10 mV. Moreover, the frequency of the alternating potential was varied enabling the impedance of the electrochemical system measured to be attained as a function of frequency. The ratio of AC potential to the AC current signal is called the impedance, while the phase angle of the impedance ϕ is also measured. In this thesis, the frequency range of 10^{-3} to 10^{5} Hz was applied. All experiments were conducted over extended periods of time, usually over a 24-h period, to ensure that the system measured was under steady-state conditions. The electrochemical system is considered as an equivalent circuit composed of elements mainly including resistance (R), capacitance (C) and diffusional terms, which are connected in series and parallel. The information on the composition of equivalent circuit and the size of each element can be obtained from the EIS measurement data. These circuit elements can be employed to obtain details on the capacitance and charge transfer resistance of the materials. In addition, as the EIS technique is a frequency domain measurement method, which can be measured in a wide frequency range, more kinetics and electrode interface structure information can be attained compared to the conventional electrochemical methods.

2.4 Surface Analysis

2.4.1 Scanning Electron Microscopy (SEM)

During the SEM measurement, a narrow focused high-energy electron beam is used to scan the sample. Various physical information from the sample through the interaction between the high-energy electrons, visible electromagnetic waves and the sample being

measured, is collected, amplified and re-imaged to characterise the sample. As the electrons cannot travel freely through air, the electron source, lenses, and sample must be under vacuum condition. SEM allows the imaging of objects on a micrometre (μm) to a nanometre (nm) scale.

For the SEM, there are two main components, which are the electron column and the control console. Among them, the electron column is composed of an electron gun and a series of lenses that direct the electrons downwards to the sample. Many SEMs contain a tungsten wire heated by passing a current through it, then this tungsten wire emits light forming an electron cloud around it. A voltage (kV) in the range from 1 to 30 kV is applied to an electron gun, causing electrons to eject from a tungsten filament and accelerate down the optic column to form the electron beam in a spray pattern, which is focused on the sample through the series of electromagnetic lenses. According to Equation 2–5, a higher applied voltage produces electrons with higher energy and shorter wavelength. For instance, an electron beam accelerated at 80 kV can give a wavelength of 0.004 nm. Moreover, the observable resolution got by a microscope, *d*, between two small adjacent particles, is proportional to the wavelength of the incident beam, λ. Accordingly, higher resolutions can be obtained using higher accelerating voltages.

$$\lambda = \left(\frac{1.5}{V}\right)^{1/2} \qquad (2–5)$$

The electron-optical column is mounted on a vacuum chamber [8]. The electron gun is placed on top of the column. The sample is contained in a specimen chamber. As shown in Figure 2-9 [9], when the electron beam interacts (elastic interaction) with the sample to a depth of ca. 1 μm, the backscattered electrons originating from the sample surface are emitted, generating a signal to create an image [10].

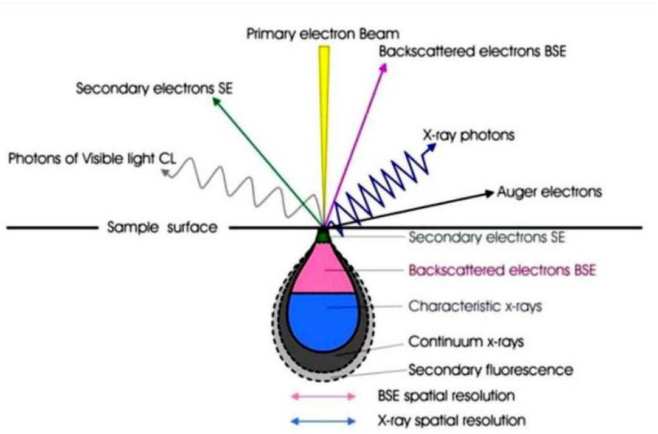

Figure 2-9. Schematic representation of electron-sample interactions in the SEM. The volume of interaction of the electron beam with the sample surface and corresponding areas from which different signals originate [9].

In addition, with the interaction of the incident electrons with the nuclei and electrons of the sample, inelastic scattering occurs, generating other signals, such as secondary electrons, X-ray emissions and auger electrons. These signals provide additional information about the sample including texture, chemical composition, and crystalline structure.

2.5 Spectroscopy

Spectroscopy is an important interdisciplinary subject mainly related to physics and chemistry. It studies the interaction between electromagnetic radiation and matter through spectra. Light is electromagnetic radiation formed by the superposition of electromagnetic waves of various wavelengths (or frequencies), such as X-ray, Ultraviolet-Visible and Infrared light, etc.

2.5.1 Energy Dispersive X-Ray Spectroscopy (EDX)

In combination with SEM measurement, EDX spectroscopy refers to the method used to analyse the chemical composition of a sample and the obtained spectrum as X-rays can be produced when the electron beam is bombarded at the sample.

EDX allows for local trace element analysis of the sample within approximately 0.5–2 μm in depth [11]. The incident electron beam interacts with the electrons in the

inner shell of the sample, resulting in the ejection of an electron in the inner shell to generate holes, which are filled by the electrons in the outer shell as the electrons in the outer shell possess higher energy compared with that in the inner shell. This transition of the electrons from higher to lower energy level emits the energy in the form of X-rays. Accordingly, each element in the sample gives the characteristic X-ray signal. According to this information, EDX can be used to identify the elemental composition of a sample. Apart from the qualitative analysis, EDX can also be employed to conduct quantitative analysis for the elements in a sample [12]. This can be performed by calculating the peak area of each identified element in a sample and converting the calculated peak area into weight or atomic percentage. Nevertheless, the quality of the quantitative analysis relates to the surface roughness of the sample [13]. Therefore, the EDX was only used for the qualitative analysis of the modified electrodes.

2.5.2 Ultraviolet-Visible Spectroscopy (UV-Vis spectroscopy)

Ultraviolet-Visible (UV-Vis) spectroscopy is employed extensively for research and analysis in Chemistry. It is a very useful analytical technique used to determine the analytes with very low concentrations in the solution. In this method the analytes are exposed to radiation, and then the amount of radiation absorbed by the analytes are measured and recorded. The amount and type of radiation absorbed by the analytes depend on the concentration, atomic or molecular structures of the analytes. Using ultraviolet-visible spectroscopy, the quantitative analysis is based on the Beer-Lambert law, as shown in Equation 2–6:

$$A = \varepsilon bc \tag{2–6}$$

where, A is the absorbance, ε is the molar extinction coefficient, which is related to the property of the absorbing species and the wavelength (λ) of the incident light, b is the path length in cm and c is the concentration of the absorbing species in mol/L. Usually, a Varian Cary series spectrophotometer and a 1 cm wide quartz crystal cuvette were employed for all the qualitative and quantitative analyses. In this thesis, UV-Vis spectroscopy was used to investigate the adsorption and removal of four pollutants by the fabricated adsorbents.

2.5.3 Infrared Spectroscopy (IR spectroscopy)

Infrared (IR) spectra were measured using a Thermo Fisher IR spectrometer (Nicolet iS50 FT-IR microscope), as shown in Figure 2-10. The measured samples were finely ground with a pestle in a mortar or deposited on the surface of flat substrates. When a beam of infrared light with continuous wavelengths passes through a molecule and the vibrational or rotational frequency of a certain group in the molecule is the same as the frequency of infrared light, the infrared light at this wavelength is absorbed by the molecule. This leads to the transition of the vibrational (rotational) energy level from the original ground state to the higher energy level, causing changes of vibrational energy within the molecule in the form of bending and stretching motions. If the compound has a dipole moment, then it will be IR-active. The absorption of IR energy leads to the oscillation in the dipole moment which is related to specific vibrational modes. Therefore, infrared spectroscopy is essentially an analytical method that is frequently used to help determine the molecular structure of substances. The normal range of IR frequency used is between 4000 and 400 cm^{-1}. Typically, Infrared spectra are presented by the wavelength (nm) or wavenumber (reciprocal of the wavelength, cm^{-1}) as the horizontal axis representing the position of the absorption peak, and transmittance (T%) or absorbance (A) as the vertical axis representing the absorption intensity. In this thesis, IR spectra were used in the analysis of the bismuth-modified sensors and in the analysis of the adsorbents.

Figure 2-10. The photograph of IR instrument.

2.6 Reference

[1] Chen, Z. X.; Jin, X. Y.; Chen, Z. L.; Megharaj, M.; Naidu, R. Removal of methyl orange from aqueous solution using bentonite-supported nanoscale zero-valent iron. *J. Colloid Interface Sci*. **2011**, *363*, 601–607, doi: 10.1016/j.jcis.2011.07.057.

[2] Fox, C. M. Electrochemical Synthesis of Silver Nanoparticles for Applications in Nitrate Detection, Catalysis and Antibacterial Activity, PhD, NUIM, **2014**.

[3] Bard, A. J.; Faulkner, L. R. *Electrochemical methods: Fundamentals and Applications*; 2nd ed.; Wiley, **2000**.

[4] Brett, C. M. A. Brett, A. M. O. *Electrochemistry: Principles, Methods, and Applications*; Oxford University Press, Incorporated, **1993**.

[5] Brett, C. M. A.; Brett, A. M. O. *Electroanalysis*; Oxford University Press, **1998**; Vol. 64.

[6] Greef, R.; Peter, L. M.; Pletcher, D.; Robinson, J. *Instumental Methods in Electrochemistry*; Horwood Publishing Limited, **1985**.

[7] Harley, C. The Formation of an Electrochemical Sensor for the Selective Detection of Dopamine, PhD, NUIM, **2009**.

[8] Szynkowska, M. I. In *Encyclopedia of Analytical Science*; Elsevier: **2005**.

[9] http//www. Jeol.co.jp.

[10] Zhou, W.; Wang, Z. L. *Scanning Microscopy for Nanotechnology: Techniques and Applications*; 1st ed.; Springer, **2006**.

[11] Goldstein, P. E. J. I.; Joy, C.; Romig, A. D.; Lyman, C. E.; Fiori, C.; Lifshin, E. *Scanning Electron Microscopy and X-Ray Microanalysis*, Plenum Press, **1992**.

[12] Goldstein, J.; Newbury, D. E.; Joy, D. C.; Lyman, C. E.; Echlin, P.; Lifshin, E.; Sawyer, L.; Michael, J. R. *Scanning Electron Microscopy and X-ray Microanalysis*; 3rd ed.; Springer, **2003**.

[13] Kanani, N. *Electroplating: Basic Principles, Processes and Practice*; Elsevier Science, **2005**.

Chapter 3

Developing a Sensitive Electrochemical Sensor for the Detection of 4-Chloro-2-methylphenoxyacetic Acid (MCPA) through a Simple Activation of GCE

3.1 Introduction

It is well known that pesticides and herbicides possess the capacity to kill a wide variety of pests, so they are widely utilised in modern agriculture and sustainable food supply in the world [1]. At the same time, due to their overuse, the negative impact of these pesticides and herbicides, composed of chemical substances, is causing environmental pollution, and threatening biodiversity [2]. There are currently many types of pesticides including fungicides, insecticides, rodenticides and herbicides etc [3]. Among them, MCPA is considered as one of the more commonly used herbicides in agriculture because of its effectiveness in weed control [4]. Normally, MCPA is employed in marginal and upland agricultural areas through spraying, thereby it is often detected in plants, soil and water [5,6], causing serious environmental pollution problems [7]. In addition, MCPA is soluble in water while poorly adsorbed on the soil substrate, and therefore it easily gets into the surface and ground water bodies [8]. Indeed, MCPA has often been detected in water systems, such as rivers and streams [8,9]. However, MCPA is harmful to aquatic species [10] and animals [11], and even under relatively low concentrations, it can pose a threat to human health [12]. Therefore, developing fast, sensitive, and simple detection methods for the analysis of MCPA is important from both a human health and environmental aspect. Efficient and simple detection methods are also important in providing useful information about removing MCPA from aquatic environments.

To date, a series of detection methods of MCPA have been explored, such as high performance liquid chromatography (HPLC) [13], capillary electrophoresis [14], solid phase extraction coupled with ion mobility spectrometry [15], electrochemiluminescence [16] and chemiluminescence [17] etc. Nevertheless, most methods suffer from expensive instruments, the requirement of highly trained technicians, complicated preparation sample processes and time-consuming analyses. Electrochemical sensors have gained more attention due to their unique advantages, which include rapid and reliable detection and they are also cost-effective and easily transported to various water bodies to provide onsite and real-time detection. However,

the electrochemical-based sensors for the detection of MCPA are reported rarely. On searching the literature, it is found that only three papers are reported by Brett and co-workers [18,19] and Bialek et al. [20]. Brett and co-workers used β-CD, multi-walled carbon nanotubes (MWCNTs) and polyaniline modified GCE to detect MCPA, giving a linear concentration range of 10 to 100 μM and a LOD of 0.99 μM [18]. In the study by Bialek et al., a carbon paste electrode was constructed by the modification of powdered activated carbon or mesoporous silica, providing a linear concentration range from 10 to 500 μM [20].

In this work, an activated GCE (A-GCE) was manufactured by simply cycling GCE in a weak acidic PBS solution. The A-GCE was used for the electrochemical detection of MCPA.

3.2 Experimental Section

The electrochemical experiments, including CV and DPV, were conducted using a Solartron 1287 or CHI 760C potentiostat. EIS was measured with a Solartron 1287 potentiostat connected with a 1255 FRA (Solartron). The surface morphology was characterised by SEM with a Hitachi S-3200-N microscope containing a tungsten filament electron source.

A standard three-electrode system was used for the electrochemical measurements. GCE was polished and cleaned according to the procedure described in the Section 2.2.4. The A-GCE was prepared according to the procedure described in Section 2.2.4.1. In this section, two procedures were applied to the MCPA electrochemical studies: (i) the measurements were recorded using a freshly prepared A-GCE; (ii) the results were collected in the steady state of the A-GCE, which was obtained by cycling the freshly prepared A-GCE for 30 cycles in PBS or MCPA solution until steady state voltammograms were obtained. For the CV experiments, unless otherwise stated, a scan rate of 100 mV s^{-1} was used. For the DPV measurements, the parameters were set up as a pulse amplitude of 50 mV, pulse width of 0.05 s, sampling width of 0.0167 s, a pulse period of 0.50 s, and an increment of 4 mV. The EIS measurements were performed at a

fixed potential from 1.1 to 1.5 V vs. SCE in 0.1 M PBS containing MCPA using a perturbation potential of 10 mV. In order to achieve the steady state conditions, a 3-h polarisation period was used for all data recorded. Then, the collected data were fitted to an equivalent circuit. In addition, the study on the long-term stability of the A-GCE was carried out by initially cycling the A-GCE to achieve the steady-state voltammograms, then the A-GCE in the steady-state was stored in 0.1 M PBS. After different intervals this electrode was taken out and the voltammograms were recorded again, subsequently, the recorded voltammograms were compared with the initial data.

3.3 Results and Discussion

3.3.1 Preparation of A-GCE

The polished GCE was immersed in a weak acidified PBS for its activation by cycling in the potential range of –2.0 to 2.4 V vs. SCE for 30 cycles. Typical voltammograms from 1 to 30 cycles in PBS are depicted in Figure 3-1.

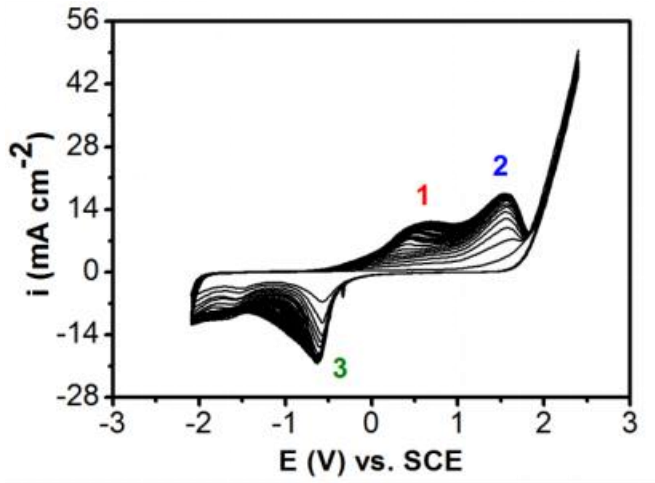

Figure 3-1. CV curves recorded in the potential range of –2.0 and 2.4 V vs. SCE at 100 mV s^{-1} in weak acidified PBS (pH 5.3) during the activation of GCE with 30 cycles.

It can be seen clearly that there are two oxidation waves at about 0.70 V (peak 1) and 1.5 V vs. SCE (peak 2), while a sharp reduction wave is observed at about –0.60 V vs. SCE (peak 3) and a smaller less defined reduction wave appears at about –1.9 V vs.

SCE. For all peaks (peaks 1-3), the peak currents increase with the increase of cycling, which is related to the oxidation and reduction of the electrode. The peaks 1 and 2 correspond to the formation of oxygen-containing groups at the higher potential while the sharp peak 3 relates to the reduction of the oxygen-containing groups formed. Additionally, it is evident that for peak 3, as the number of cycles increases, the peak potentials remain basically unchanged, however for peak 1, a considerable shift in the potential is observed, increasing from about 0.45 V for the first cycle to about 0.70 V vs SCE for 30th cycle.

3.3.2 Influence of anions on preparation of A-GCE

The influence of the anions in the supporting electrolytes on the activation of GCE was investigated. The anions involving SO_4^{2-}, PO_4^{3-} and Cl^- were selected for the study. Under the same experimental conditions, including the potential range, scan rate, scanning cycle, solution pH and concentration of anions, the CV curves of the polished GCE in the supporting electrolytes containing different anions were recorded. For comparison, CV curves of the 10th cycle for SO_4^{2-}, PO_4^{3-} and Cl^- anions are shown in Figure 3-2.

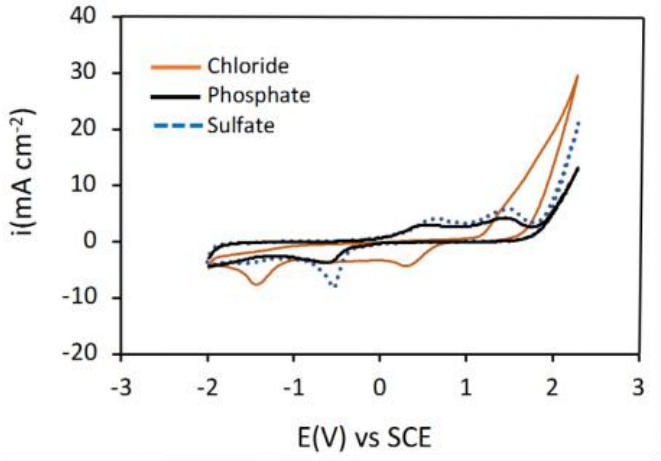

Figure 3-2. CV curves recorded at 100 mV s^{-1} between the potential limits of –2.0 and 2.4 V vs. SCE in slightly acidified pH 5.3 solutions during the activation of GCE in 0.05 M phosphate, 0.05 M sulfate and 0.05 M chloride, showing 10th cycle.

It is obvious that the anions in the supporting electrolytes have a significant influence on the activation of GCE. The systems containing SO_4^{2-} and PO_4^{3-} anions show similar CV curves, however the CV curve in the presence of the Cl^- anion is clearly different. The specific difference is that the onset of the oxygen evolution reaction appears at a much lower overpotential than seen with the SO_4^{2-} and PO_4^{3-} system. In addition, the characteristic oxidation waves observed in the vicinity of 0.7 and 1.5 V vs SCE seen with the SO_4^{2-} and PO_4^{3-} systems are no longer evident for the Cl^- system. The reason may be due to the combination of the Cl^- ions with the $OH^{\bullet}$ species generated during the evolution reaction of oxygen to produce different reactive chloride intermediates [21], for example, $ClOH^{\bullet -}$, which have the potential to change the activation process of GCE.

To determine the efficiency of these activated electrodes as sensors, they were assessed in the electrochemical oxidation of MCPA. The A-GCEs, activated in the presence of anions SO_4^{2-}, PO_4^{3-}, Cl^- and CH_3COO^- (Ac^-), were used to detect 4.0 mM MCPA and these voltammograms are shown in Figure 3-3(a). The recorded CV curve of GCE in the Ac^- system shows a very low peak current, while much higher peak currents are evident with the PO_4^{3-} and SO_4^{2-}. The comparisons of the four anions versus the oxidation peak currents of MCPA at the activated GCEs are illustrated in Figure 3-3(b).

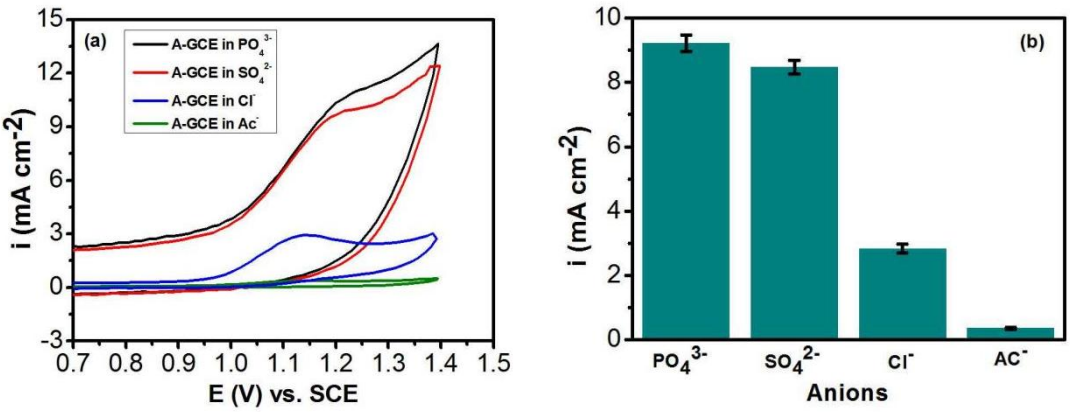

Figure 3-3. Voltammograms of 4.0 mM MCPA at the A-GCE activated in different anion containing electrolytes **(a)** and peak currents recorded in 4.0 mM MCPA for activated GCEs formed in different anion containing electrolytes **(b)**.

It is evident that the type of the anions in the activation solutions exhibits a considerable influence on the activation of the electrode, on the one hand, the good detection of MCPA is seen in the presence of SO_4^{2-} and PO_4^{3-} anions, whereas the poor detection of MCPA is found in the presence of Cl^- and Ac^- anions. The means of their currents were obtained as 9.22±0.26 for PO_4^{3-}, 8.47±0.21 for SO_4^{2-}, 2.84±0.14 for Cl^- and 0.36±0.030 for AC^- in the unit of mA cm^{-2} based on the triplicate measuremnets (n = 3). Such observation suggests that the anions $SO_4^{2-}$and $PO_4^{3-}$are beneficial for the activation of the electrode, thereby promoting the electrochemical oxidation of MCPA.

3.3.3 Morphology characterisation of A-GCE surface

To support the deduction above, the SEM technique was employed to characterise the morphology of the GCE surface after activation in the anions SO_4^{2-}, PO_4^{3-} and Cl^-. Their typical SEM micrographs are illustrated in Figure 3-4.

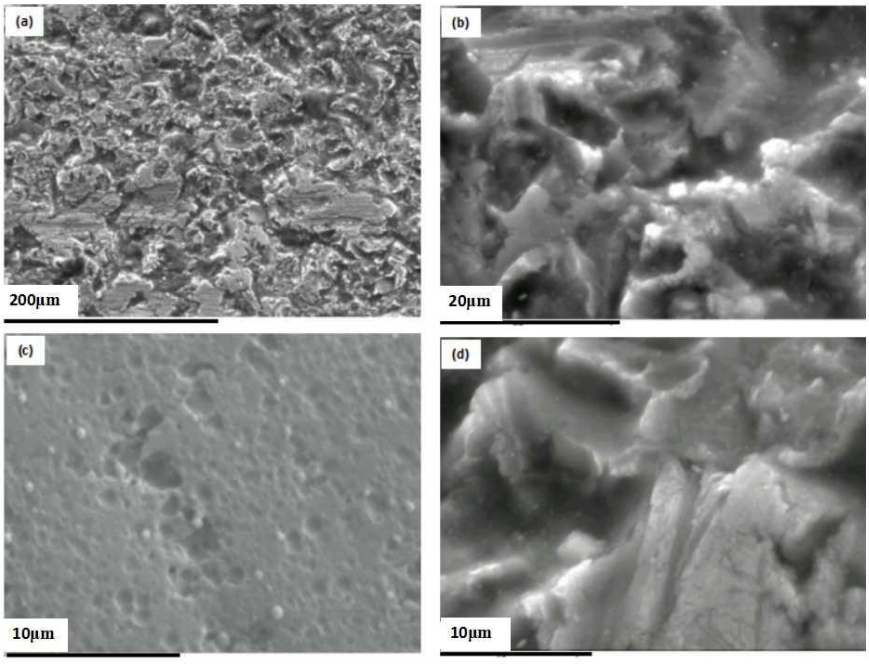

Figure 3-4. SEM micrographs recorded after cycling of the GCE electrode in the potential range from –2.0 to 2.4 V vs. SCE for 30 cycles at 100 mV s^{-1} in (a) PO_4^{3-} (b) PO_4^{3-} at a higher magnification (c) Cl^- and (d) SO_4^{2-} systems.

It is noticed that an etched-like surface is observed with the PO_4^{3-} system (see Figure 3-4 (a) and (b)), which is consistent with the observation in the report by Yi et al. [22]. The authors ascribed the degradation of GCE to opening ring in the graphitic structure with the formation of oxides. Meanwhile, a similar morphology is observed with the activated GCE in the SO_4^{2-} system (see Figure 3-4 (d)). Comparatively, the morphology of the activated GCE in Cl^- system is very different from the SO_4^{2-} and PO_4^{3-} systems, showing the formation of a porous lace-like film. This observation is consistent with the discussion in Section 3.3.2, where it is purposed that reactive chloride intermediates are generated on cycling the GCE into the oxygen evolution reaction region. These reactive species may etch the GCE to give the porous lace-like films.

3.3.4 Optimisation of experimental parameters for the activated electrode A-GCE

In order to get the best performance of the activated GCE for the electrochemical detection of MCPA, three experimental parameters, such as activation solution pH, the applied potential ranges and the number of scanning cycles, were investigated for the preparation of the activated GCE. First, the study on the pH of the activation solution indicated that the optimum detection of MCPA was seen when the GCE was activated in the PO_4^{3-}solution adjusted to a pH of 5.3, whereas slightly lower peak currents were found after the activation of GCE in neutral solutions, and in more acidic solutions. Second, the effects of the activation potential window from –2.0 to 2.0, 2.1, 2.2, 2.3, 2.4 and 2.5 V vs. SCE were investigated and the oxidation peak currents of MCPA versus the potential ranges are depicted in Figure 3-5. It is evident that the optimum potential window for the activation of GCE is from –2.0 to 2.4 V vs. SCE, whereas after extending the potential window to 2.5 V, more oxygen was generated and the generated oxygen would destroyed the electrode surface, resulting in the decrease of the peak currents. Finally, the influences of the number of scanning cycles on the activation performance of GCE were examined from 5 to 45 cycle and the oxidation peak currents of MCPA versus the number of scanning cycles are displayed in Figure 3-6. It can be noticed that higher peak currents are given with the 30 scanning cycles, thus the 30

cycles were selected for the activation of GCE. Based on these studies, the optimum activation conditions of GCE for the electrochemical oxidation of MCPA were confirmed as cycling from –2.0 to 2.4 V vs SCE, with 30 cycles in a PBS (0.05 M) adjusted to a pH of 5.3.

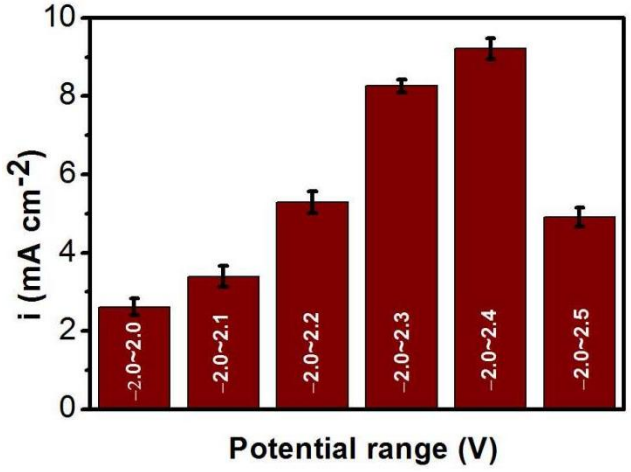

Figure 3-5. MCPA oxidation peak currents as a function of activation potential window obtained from CV curves performed in triplicate (n = 3) at 100 mV s^{-1} in 4.0 mM MCPA in PBS, second cycle data used.

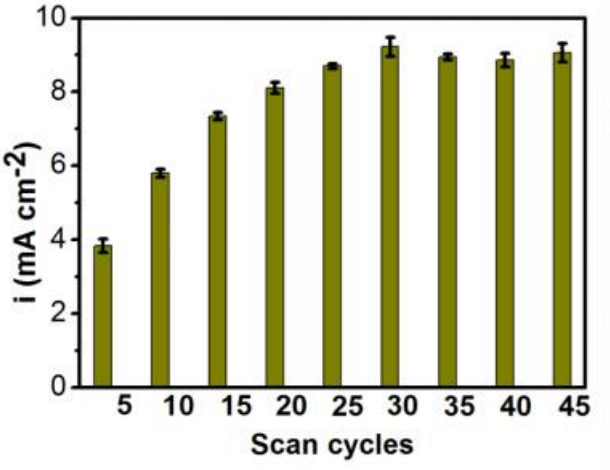

Figure 3-6. MCPA peak currents as a function of activation cycles obtained from CV curves performed in triplicate (n = 3) at 100 mV s^{-1} in 4.0 mM MCPA in PBS, second cycle data used.

Under the optimum activation conditions, the freshly prepared A-GCE was initially utilised to determine MCPA at a relatively high concentration (4.0 mM) using CV. For

comparison, the CV curves recorded for the activated GCE in PO_4^{3-} system and the unmodified GCE are represented in Figure 3-7. It is easy to see that the A-GCE facilitates the electrochemical oxidation of MCPA as the oxidation peak current of MCPA at the A-GCE is considerably higher at 11.23 mA cm^{-2} compared to the unmodified GCE with a much lower peak current of 1.32 mA cm^{-2}. It is also evident from these CV curves that the activation of GCE gives rise to a much higher capacitance current, which is probably connected with the etched surface, as shown in Figure 3-4 (a) and (b).

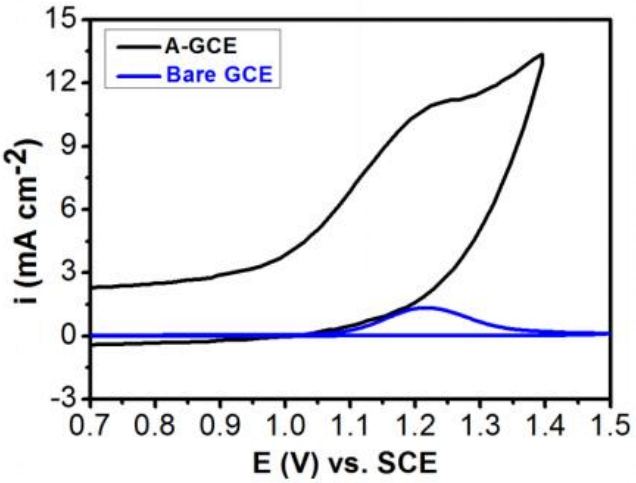

Figure 3-7. CV curves recorded using unmodified GCE (blue) and activated GCE (black) in 4.0 mM MCPA in PBS performed at 100 mV s^{-1}, second cycle data used.

3.3.5 EIS characterisation of the A-GCE

The GCE activated under the optimum activation conditions was further investigated by using electrochemical impedance spectroscopy (EIS). The representative EIS and their fitted data for unmodified GCE and activated GCE recorded in PBS containing MCPA at 1.2 V vs. SCE are shown in Figure 3-8(a), and the corresponding equivalent circuit is given in the inset in Figure 3-8(a), where R1 means the solution resistance, R2 represents the charge transfer resistance, and CPE1 is a constant phase element. Equation 3–1 gives the generalised expression of the complex impedance of the CPE, which corresponds to an inductor with $L = 1/A$ for $n = -1$, to a resistor with $R = 1/A$ for

n = 0 and to a capacitor with $C = A$ for n = 1. In this case it was utilised to represent a non-ideal capacitor, giving $0.8 \leq n < 1$.

$$Z_{CPE} = \frac{1}{\omega^n A} e^{-i\frac{\pi}{2}n} \qquad (3\text{–}1)$$

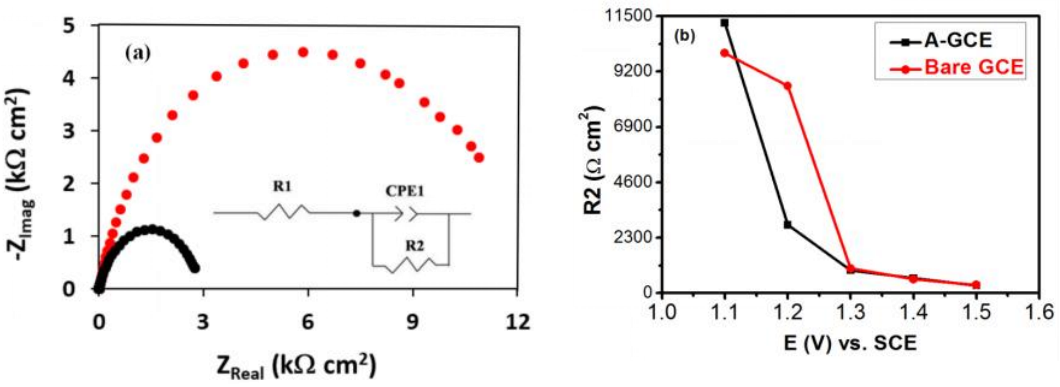

Figure 3-8. (a) The electrochemical impedance spectra for bare GCE (red) and activated GCE (black) recorded in PBS at 1.2 V vs. SCE and **(b)** charge transfer resistance (R2) plotted as a function of the applied potential for bare (red) and activated GCE (black).

In order to coincide with the potentials that are required to oxidise MCPA, a 3-h polarisation period at 1.2 V vs. SCE was carried out, and then the EIS data were recorded at this potential. The complex plane plots of the unmodified GCE and activated GCE electrodes are compared, as shown in Figure 3-8(a), which show similar data for both electrodes. Additionally, semicircles are clearly exhibited and no evidence of any additional resistance or diffusion paths is observed for the A-GCE. Such observation points out that the modified and unmodified electrodes are similar, and even at these relatively high potentials the systems are stable, with the A-GCE showing a somewhat more conducting surface. Further, at 1.2 V vs. SCE, where oxidation of MCPA is observed in the CV curve, the charge transfer resistance was estimated at 2.9 kΩ cm^2 for A-GCE and 120.6 kΩ cm^2 for the unmodified GCE electrode, clearly demonstrating the good conducting property of the A-GCE. The constant phase elements with n values of 0.83 represent non-ideal capacitances. Interestingly, this value was somewhat higher for the A-GCE (8.43 x 10^{-4} Ω^{-1} s$^{0.83}$ for A-GCE and 3.37 x 10^{-4}

Ω^{-1} $s^{0.83}$ for unmodified GCE). This higher capacitance is consistent with the etched surface, Figure 3-4(a) and (b) and the high capacitive currents observed in Figure 3-7.

Moreover, the EIS data were recorded at different applied potentials. Then the charge-transfer resistance (R2) was computed as a function of the applied potential and is plotted in Figure 3-8(b), which again indicates that the A-GCE remains conducting at these high potentials. However, both electrodes give nearly identical values in the vicinity of 1.3 V to 1.5 V vs. SCE. The lower charge-transfer resistance values observed, are probably related to the oxygen evolution reaction. Furthermore, the stability of the A-GCE was monitored by measuring the impedance over a 24-h period. The results indicated that nearly identical data were obtained from 3-h to 24-h, suggesting very good stability at these relatively high potentials.

3.3.6 Steady-state and reproducibility of the A-GCE

Under the optimum experimental conditions, the freshly prepared A-GCE was used to detect MCPA. Although, the freshly prepared A-GCE gives higher peak currents compared to the unmodified GCE (see Figure 3-7), the currents of the oxidation waves for MCPA decrease with increasing cycling. Therefore, to establish if freshly activated GCE or previously cycled A-GCE reaching steady-state could give the best sensor performance for the detection of MCPA, the reproducibility of both approaches was investigated. In this case, the freshly prepared A-GCE was firstly cycled between –0.1 V and 1.5 V vs. SCE in the MCPA or PBS for 30 cycles to achieve steady−state conditions. For comparison, five A-GCE were freshly prepared and five A-GCE in the steady−states were also made, and then they were employed to detect MCPA. The recorded data are illustrated in Table 3-1. It is obvious that lower peak currents are given in the steady−state condition with average percentage drop of 89.2%, but improved reproducibility is realised, giving the RSD at 0.19% for steady state conditions compared with 5.0% for the freshly prepared A-GCE. Therefore, the steady−state conditions were employed in all following electrochemical studies.

Table 3-1. Reproducibility of the A-GCE in the detection of 4.0 mM MCPA.

	Peak Current (mA cm^{-2})					Mean	RSD (%)
	1	2	3	4	5	(n = 5)	(n = 5)
Freshly prepared A-GCE	11.207	11.946	11.146	10.697	12.021	11.40±0.57	5.0
	Peak Current (mA cm^{-2})					Mean	RSD (%)
	1	2	3	4	5	(n = 5)	(n = 5)
A-GCE in the steady-state	1.219	1.217	1.218	1.220	1.222	1.22±0.0023	0.19

3.3.7 Influence of the solution pH

As shown in Scheme 3-1, the electrochemical oxidation reaction of MCPA occurs irreversibly accompanied by the transfer of one electron and one proton to generate 4-chloro-2-methylphenol. Thus, the solution pH is anticipated to affect the electrochemical oxidation process of MCPA. For this purpose, the influence of the solution pH on the oxidation reaction of MCPA was studied from a pH of 2.5 to 8.3 using the DPV technique. Representative DPV curves are displayed in Figure 3-9, where it is apparent that both the oxidation peak current and oxidation peak potential depend on the solution pH. It is clear from Figure 3-9(a) that the highest oxidation peak current is seen in the slightly acidic solution at a pH of 5.3. On the other hand, as the pH further increases the peak current decreases. This observation is consistent with the participation of H^+ ions in the electrochemical oxidation reaction process (see Scheme 3-1). The p*K*a of MCPA is about 3.07 (it is reported typically between 3.05 and 3.13) [23], meaning that the MCPA becomes more neutral when the solution becomes more acidic, with the neutral MCPA existing at a pH of 3.0. In addition, this neutral form is less soluble in aqueous solution, and this is probably the reason for the particularly low peak current observed at a pH of 2.5.

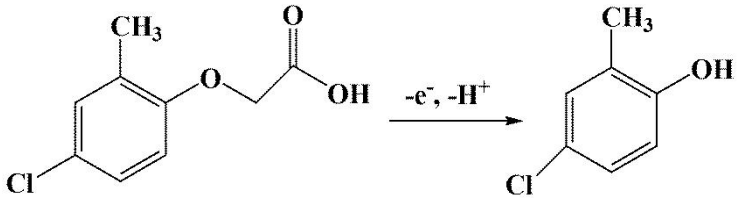

Scheme 3-1. The structure of MCPA and its electrochemical oxidation to 4-chloro-2-methylphenol [18].

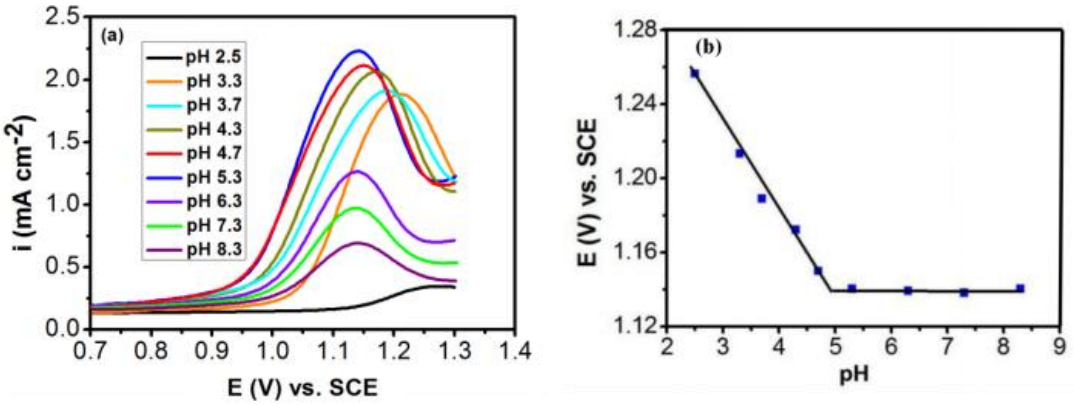

Figure 3-9. (a) DPV curves of the A-GCE in the steady−state recorded in 4.0 mM MCPA in a PBS at different pH values and **(b)** peak potential, E_p, plotted as a function of pH.

Furthermore, the peak potential as a function of the solution pH is plotted, as shown in Figure 3-9(b), where a linear trend is seen between a pH of 2.5 and about 5.0, giving the regression equation: $E_p = -0.048$ pH + 1.37 ($R^2 = 0.987$). By comparing this obtained slope of 0.048 with the theoretical slope of 0.059m/n, in which m corresponds to the number of protons transferred and n represents the number of electrons transferred, the m/n value was estimated as 0.82, and this case is consistent with the transfer of equal numbers of protons and electrons, as revealed in Scheme 3-1. In addition, for the solution pH changing from 5 to 9, there is no change observed in the peak potential, which is similar to the case reported by Brett and co-workers [18].

3.3.8 Influence of scan rates

The oxidation reaction process of MCPA at the surface of A-GCE was investigated by changing the scan rates using CV technique to determine if this process proceeded

under diffusion or adsorption control. For this purpose, using A-GCE in the steady−state, the oxidation peak currents of MCPA at different scan rates were recorded, and the oxidation peak currents as a function of the scan rates were plotted. As illustrated in Figure 3-10(a), the relationship between the oxidation peak currents and the scan rates gives a linear plot (R^2 = 0.998), demonstrating that the oxidation reaction of MCPA at the A-GCE is an absorption-controlled process. Subsequently, the logarithm of the current as a function of the logarithm of the scan rate was plotted in Figure 3-10(b), from which the slope of the plot was obtained as 1.0, confirming an adsorption-controlled process for the MCPA oxidation.

Furthermore, based on the relationship in Equation 3–2, where E_p expresses the peak potential, $E_{p/2}$ represents the half-wave potential, n is the number of electrons transferred, and α is the charge-transfer coefficient, then the value of $E_p - E_{p/2}$ was calculated being 98.4 mV for the unmodified GCE and 78 mV for the A-GCE. Taking n = 1, the α value was calculated as 0.6 for the A-GCE. It is noticed that the value of 0.6 is close to the value of 0.55, which is normally used as a representative α value.

$$E_p - E_{p/2}\,(\text{mV}) = (47.7/\alpha n) \qquad (3\text{–}2)$$

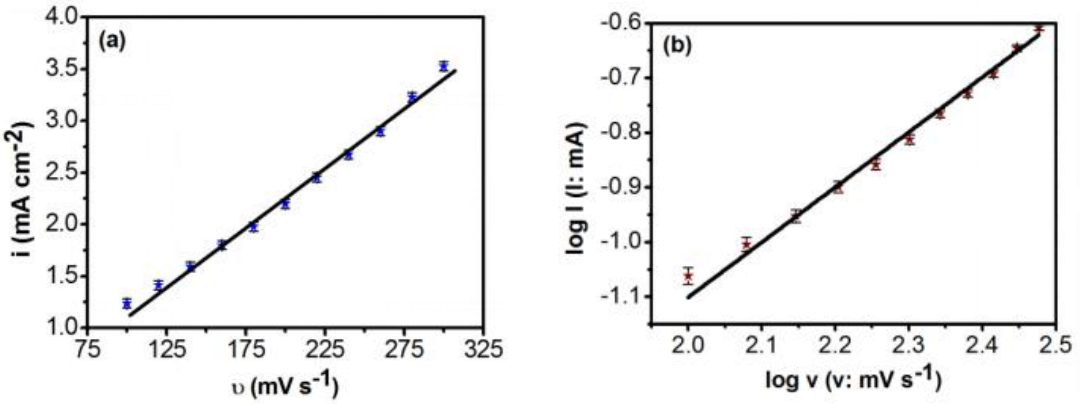

Figure 3-10. (a) The oxidation peak currents versus the scan rates and **(b)** logarithm of oxidation peak currents versus logarithm of scan rates for A-GCE in the steady−state.

In addition, by comparing Figure 3-11(a) and (b), it is evident that there is a clear shift in the peak potential (E_p) of about 110 mV, from 1.25 V vs. SCE for unmodified GCE to 1.14 V vs. SCE for the A-GCE, suggesting a more thermodynamically feasible

oxidation reaction on the surface of A-GCE. In both cases, the linear relationships of the peak potentials versus the logarithm of the scan rate were determined. The linear regression equations were obtained as $E_p = 0.025 \ln\nu + 1.24$ ($R^2 = 0.980$) for the A-GCE in the steady state, $E_p = 0.046 \ln\nu + 1.40$ ($R^2 = 0.969$) for the unmodified GCE, and $E_p = 0.0411 \ln\nu + 1.30$ ($R^2 = 0.965$) (not shown) for the freshly prepared A-GCE. According to the Laviron equation [24], the slope of the linear plot could be represented by Equation 3–3, where R and F are the universal constants, and T expresses the thermodynamic temperature. In accordance with this relationship, the value of αn was calculated as 0.55 for the unmodified GCE, 0.62 for the freshly prepared A-GCE and 1.0 for the A-GCE in the steady−state. For irreversible electrochemical reactions, the α value of 0.55 was applied, then the number of electrons involved in the electrochemical oxidation reaction of MCPA was computed as 1.0, 1.1 and 1.8 for the unmodified GCE, freshly prepared A-GCE and A-GCE in the steady state, respectively. The values obtained for the unmodified GCE and freshly prepared A-GCE are in very good agreement with Scheme 3-1, however the slope of 0.025 V deviates considerably from the ideal value of 0.047 V for the A-GCE in the steady−state.

$$E_{pa}/\log\nu = 2.3\ RT/\alpha nF \qquad (3–3)$$

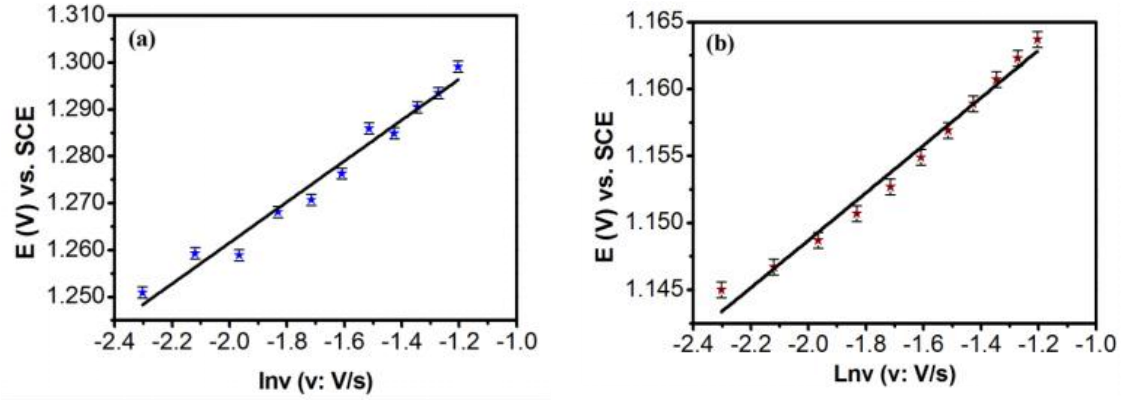

Figure 3-11. The oxidation peak potentials as a function of the logarithm of scan rate for **(a)** unmodified GCE and **(b)** A-GCE in the steady−state.

3.3.9 Electrochemical detection of MCPA using the A-GCE

After a series of characteristic experiments for the A-GCE, the performance of the A-GCE in the electrochemical detection of MCPA was investigated using two techniques involving CV and DPV. The freshly prepared A-GCE was firstly cycled for 30 cycles in PBS, and then aliquots of the MCPA were added and the corresponding voltammograms were recorded. The obtained voltammograms are shown in Figure 3-12(a), where the oxidation peak currents increase with an increase of the MCPA concentration. Subsequently, these peak currents were plotted as a function of the MCPA concentration, and the obtained plot is presented in Figure 3-12(b).

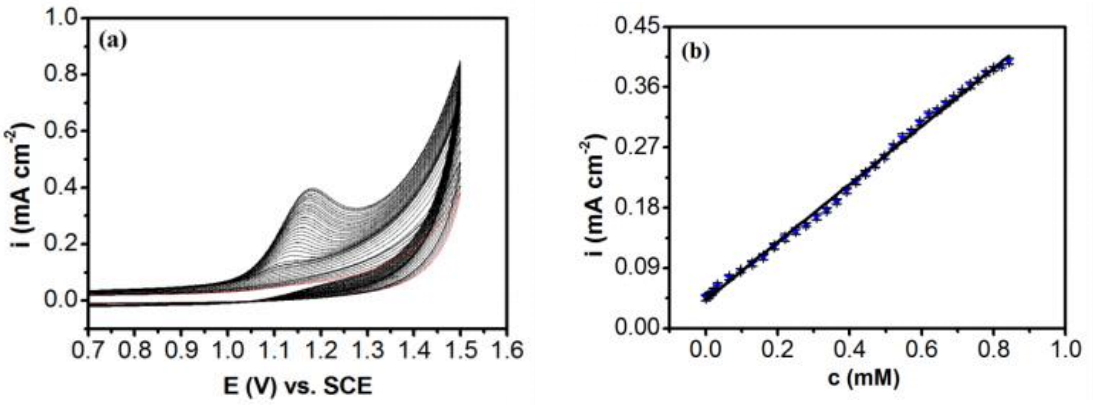

Figure 3-12. (a) Steady-state CV curves recorded at 100 mV s^{-1} for MCPA at concentrations from 1 to 850 μM and **(b)** peak currents as a function of the MCPA concentration. All data were recorded with A-GCE in triplicate (n = 3), red curve recorded in blank PBS.

It can be seen that excellent linearity was achieved with an R^2 value of 0.998, and the linear regression equation was given as, i = 0.4322[MCPA] + 0.0427, where the concentration of MCPA was expressed in mM and i in mA cm^{-2}. In addition, very good reproducibility was observed, as demonstrated by the small error bars (mean of slope is 0.4366 mA cm^{-2} mM^{-1}±0.0016). Considering Figure 3-12(b), the linear region extends over a considerable concentration range from 1 to 850 μM. The LOD was computed to be 0.02 μM (mean of LOD is 0.0198 μM±7.1×10^{-4}) based on Equation 3–4, where S_b represents the standard deviation of the baseline which was recorded in blank PBS for eleven times, m is the sensitivity, or slope of the linear calibration plot.

$$LOD = \frac{3S_b}{m} \tag{3-4}$$

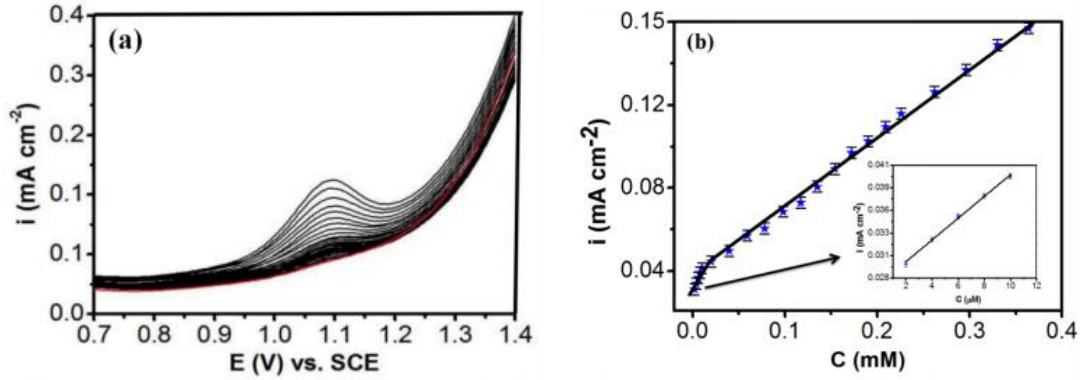

Figure 3-13. (a) steady-state DPV curves of MCPA at concentrations from 2 to 168 μM and **(b)** peak currents as a function of MPCA concentration, the inset shows the concentration range from 2 to 10 μM. All data recorded with activated GCE in triplicate (n = 3), red curve recorded in blank PBS.

Similarly, using the DPV technique, the recorded voltammograms are depicted in Figure 3-13(a), then the relationship of the peak currents versus the concentration of MCPA was plotted, as exhibited in Figure 3-13(b), showing two linear regions due to the DPV technique having higher sensitivity than the CV. Again, excellent linearity was found at the low concentration range, from 2 to 10 μM, the linear regression equation was deduced as i = 0.978[MCPA] + 0.064 (R^2 = 0.993), where the concentration of MCPA is given as mM, and i is in units of mA cm^{-2}. The LOD was computed as 0.008 μM with the mean 0.0082 μM± 3.6×10^{-4} .

Furthermore, the detecting performance of the A-GCE is compared to the previously developed sensors for MCPA and 4-(2,4 dichlorophenoxy)butyric acid, as listed in Table 3-2. From this analysis, it is clearly observed that the simply activated GCE sensor compares very well with the previous reported studies, providing a wider linear range and lower LOD values.

Table 3-2. Performance comparison of MCPA electrochemical sensors.

Electrode materials	LOD /μM	Linear region /μM	Reference
PANi/CNT/β-CD	0.99	10 –100	[18]
PANi/CNT/β-CD	1.1	10 – 50	[19]
Powdered activated carbon (Norit SX-2) paste	0.7	10 – 500	[20]
Mesoporous silica SBA-15 carbon paste	1.3	10 – 500	[20]
[1]Co-porphyrin/molecularly imprinted polymer	40	200 – 2000	[25]
Activated GCE	0.02 (CV) 0.008 (DPV)	1 – 850 2 – 10	This work

[1]Employed in the detection of 4-(2,4 dichlorophenoxy)butyric acid.

3.3.10 Evaluation of selectivity and stability

For the development of a new sensor, the selectivity is an important and significant element, thus the selectivity of A-GCE for the detection of MCPA was studied. A number of water contaminants, involving the Cu(II) ion, nitrate, nitrite, sulfate and tetrabutylammonium chloride (TBACl), a widely employed industrial chemical, that has also been utilised as a low-residue bactericide, were chosen as the interferents for the selectivity study. These salts were added to the PBS containing MCPA, where the concentrations of interferents were set at $CuSO_4$ of 5.0 mM, $NaNO_3$ of 9.4 mM, $NaNO_2$ of 11.6 mM and TBACl of 3.0 mM, giving the equal mass ratio of 1:1 for MCPA and the interferent. Then the CV curves were recorded in the interferent-containing solutions, and the obtained data were compared with that obtained in the absence of the interferent. The data are summarised in Figure 3-14 and Table 3-3, where the level of interference was marked using the relative current intensity as, I/I_0, where I_0 corresponds to the

oxidation peak current of MCPA measured in the absence of the interferent, and *I* refers to the oxidation peak current of MCPA recorded in the presence of the interferent. From Figure 3-14 and Table 3-3, it can be found that there is no significant interference observed for these contaminants, indicating that the developed sensor has good selectivity. Additionally, the reproducibility is also good, as evidenced from the error bars, and the difference between the pure MCPA solution and the interferent-containing MCPA solutions is well below 5%.

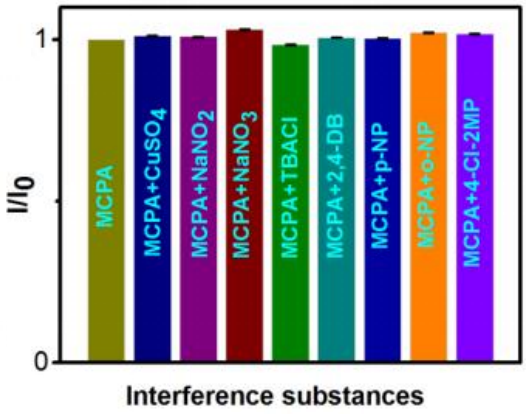

Figure 3-14. Normalised peak currents of MCPA versus the eight interferents with a mass ratio of 1:1. All data recorded with A-GCE in triplicate (n = 3).

Table 3-3. The effect of the interference on the detection of MCPA.

Sample	Mean of I/I_0	RSD (%) (n = 3)
MCPA	1	—
MCPA + $CuSO_4$	1.012 ± 0.011	1.09
MCPA + $NaNO_2$	1.009 ± 0.0095	0.95
MCPA + $NaNO_3$	1.032 ± 0.012	1.16
MCPA + TBACl	0.985 ± 0.0097	0.97
MCPA + 2,4-DB	1.007 ± 0.0098	0.97
MCPA + *p*-NP	1.004 ± 0.011	1.10
MCPA + *o*-NP	1.021 ± 0.012	1.12
MCPA + 4-Cl-2MP	1.018 ± 0.011	1.08

Table 3-4. The redox potentials of the interference at A-GCE.

Compounds	Oxidation potential (V) vs. SCE	Reduction potetial (V) vs. SCE
MCPA	1.14	—
2,4-DB	—	−1.4
p-NP	0.18	−0.68, 0.15
o-NP	−0.24, 0.26	−0.60, −0.26, 0.23
4-Cl-2MP	0.10, 0.25, 0.40, 0.70	−0.02, 0.20, 0.36

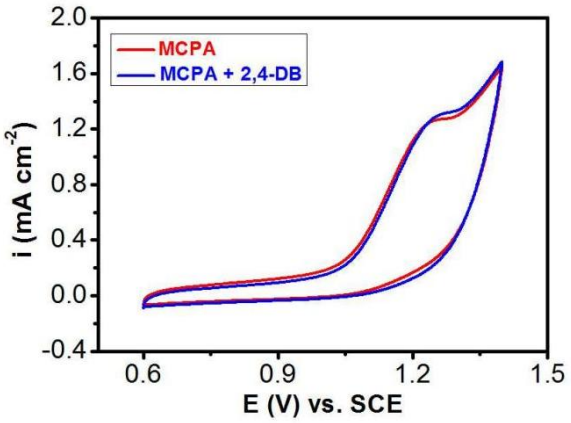

Figure 3-15. CV curves of MCPA in the absence and presence of 2,4-DB.

Apart from these contaminants that are not structurally related to MCPA, additional structurally related contaminants were selected. They include 3.2 mM 4-(2,4-dichlorophenoxy) butyric acid (2,4-DB), 5.8 mM *o*-nitrophenol (*o*-NP), 5.8 mM *p*-nitrophenol (*p*-NP) and 5.6 mM 4-chloro-2-methylphenol (4-Cl-2MP). These compounds all have phenol rings that are similar to MCPA and they are also electroactive. The oxidation/reduction peaks of these contaminants were indeed found at the A-GCE, as listed in Table 3-4, however, their redox peaks were observed at very different applied potentials compared with that of MCPA, thereby giving no significant interference with the detection of MCPA using the A-GCE. Taking the 2,4-DB as an example, the CV curves of MCPA and the mixture of MCPA and 2,4-DB are shown in Figure 3-15. It is clearly seen that the presence of 2,4-DB does not affect the

determination of MCPA. This good selectivity observed may be due to the hydrogen bonding interaction between the carboxylic group in the MCPA molecule and the oxygenated groups (such as OH), which are generated during the activation process of the GCE.

Furthermore, the stability is an equally important factor for the performance of a developed sensor. The freshly prepared A-GCE was cycled in the MCPA solution for 30 cycles to achieve the steady−state, and then the A-GCE in the steady−state was employed to determine MCPA. The stability of the A-GCE was monitored in the PBS over 30 days. At different time intervals, the A-GCE was removed from the PBS and transferred to the freshly prepared MCPA solution, and the CV curves were measured. Then the A-GCE was rinsed with distilled water thoroughly and immersed in the storage solution. This operation was repeated several times, the obtained data are illustrated in Figure 3-16. Although there is some variation over the 30-day period, there is no evidence of any significant loss in the sensing ability of the A-GCE, with the standard deviations in the peak currents < 5%. Such observation demonstrates obviously that the simply activated GCE has very good stability under steady-state conditions.

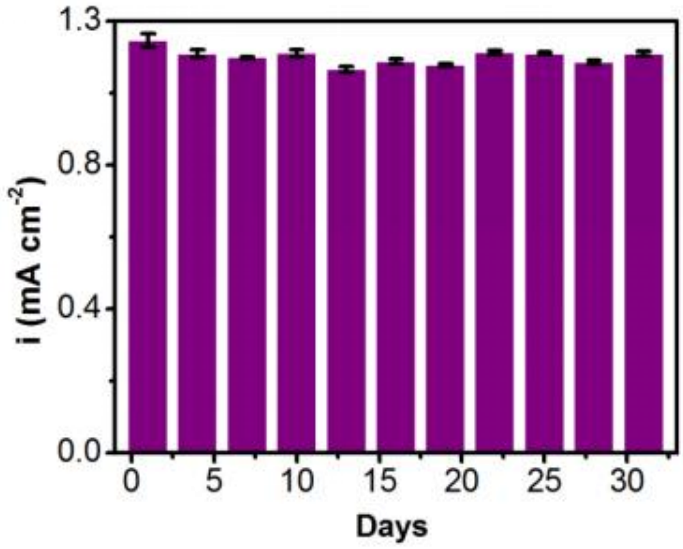

Figure 3-16. The stability study of the A-GCE in the steady state over 30 days in 4.0 mM MCPA solution. All data recorded with A-GCE in triplicate (n = 3).

3.3.11 Electrochemical detection of MCPA metabolite

Considering the CV curves shown in Figure 3-7, it can be seen that the oxidation of MCPA in the potential range between 0.7 and 1.5 V vs. SCE gives an irreversible electrochemical reaction process with a broad oxidation peak. This irreversible oxidation reaction process leads to the production of 4-chloro-2-methylphenol (4-Cl-2-MP) called the MCPA metabolite, as illustrated in Scheme 3-1. After extending the electrochemical window (between 0.7 and 1.5 V vs. SCE) to lower applied potentials (between –0.1 and 1.5 V vs. SCE) the electrochemical behaviour of the MCPA metabolite was observed, and this is evident in Figure 3-17(a), where in the vicinity of –0.10 V to 0.15 V vs. SCE, the emergence of redox waves becomes evident. In addition, in Figure 3-17(a), the broad reduction wave, which is labeled as peak 1, depends on the concentration of MCPA. It is clear that the currents of peak 1 increase with the increase of the MCPA concentration (see Figure 3-17(b)). The reduction of 4-Cl-2-MP has previously been described in Scheme 3-2 [19]. Interestingly, this reduction peak cannot be observed at the unmodified GCE, whereas it is clearly evident at the A-GCE at relatively low concentrations of 0.14 mM for MCPA. Comparatively, Białek et al. [20] used a modified carbon paste electrode to measure the CV curve of MCPA and found only a single irreversible oxidation peak, which corresponds to the oxidation of MCPA, during cycling in the potential range from 0.0 to 1.5 V vs. SCE, suggesting that the emergence of this reduction wave is connected with the oxygenated species formed during the activation of the GCE.

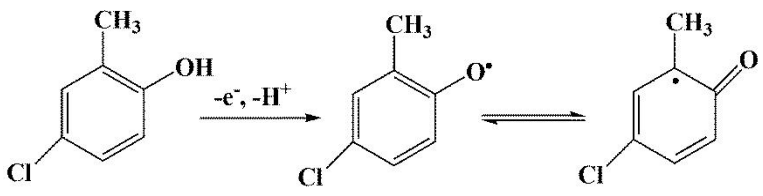

Scheme 3-2. Reduction of 4-chloro-2-methylphenol as proposed by Rahemi et al. [19].

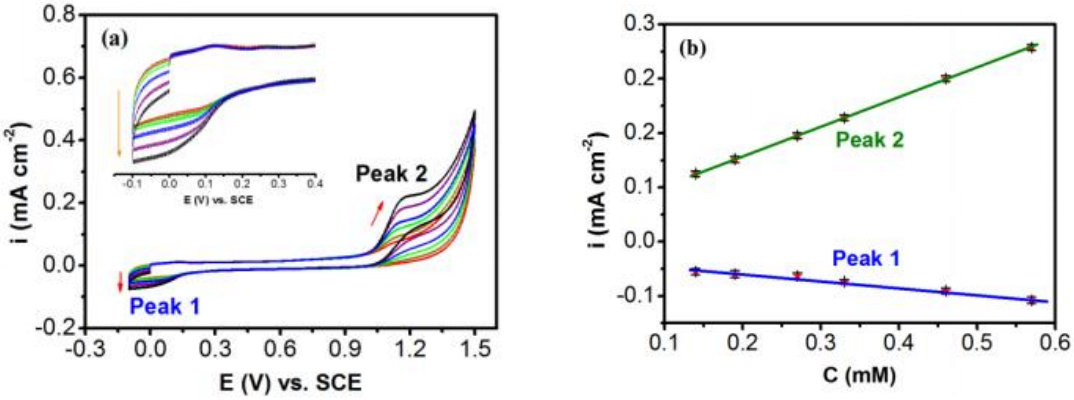

Figure 3-17. (a) CV curves recorded for the A-GCE at 100 mV s^{-1} in MCPA at concentrations from 0.14 to 0.57 mM and **(b)** peak currents plotted as a function of MCPA concentration.

To confirm this assignment for the MCPA metabolite, 4-Cl-2-MP was used as the analyte. First, the freshly prepared A-GCE was cycled in the 4-Cl-2MP-containing solution for 30 cycles to achieve the steady state, and then the A-GCE in the steady state was employed to detect 4-Cl-2MP at different concentrations, the corresponding voltammograms were recorded, as illustrated in Figure 3-18(a). Obviously, peak 1 in Figure 3-17(a) corresponds to the broad reduction wave between 0.0 and –0.1 V vs. SCE, shown in Figure 3-18(a), and this peak is consistent with the reduction reaction outlined in Scheme 3-2.

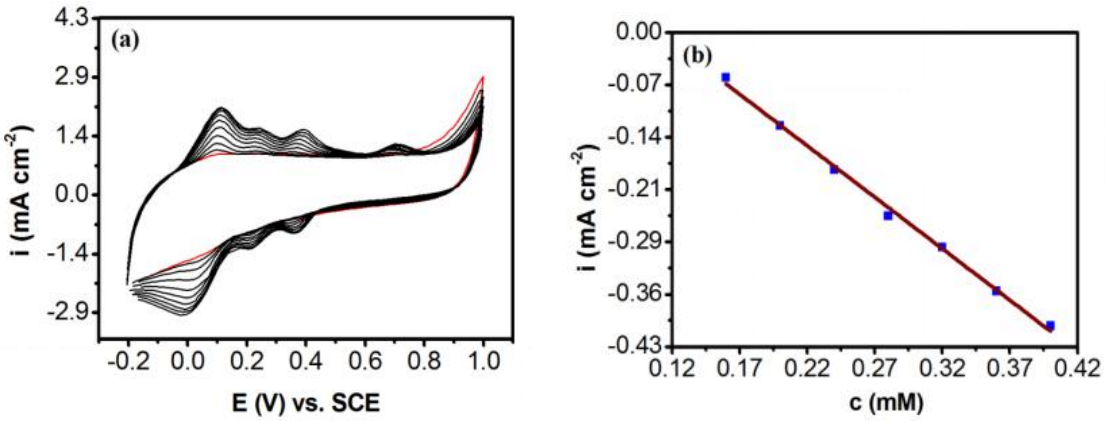

Figure 3-18. (a) CV curves recorded for the freshly prepared A-GCE at 100 mV s^{-1} in 4-Cl-2-MP at 0.12, 0.16, 0.20, 0.24, 0.32, 0.36 and 0.40 mM, where the red trace was recorded in PBS (blank) and **(b)** calibration curve recorded with activated GCE at steady state condition in the detection of 4-Cl-2-MP.

Further, using steady-state condition, the linear calibration curve was obtained in the 4-Cl-2MP solution, as described in Figure 3-18(b), where the peak current of the reduction wave centred between 0.0 and –0.1 V vs. SCE was taken. From Figure 3.18(b), it can be seen that a good linearity is achieved, demonstrating that the A-GCE is an effective sensor for the detection of the MCPA metabolite.

In addition, on further inspecting the CV curves in Figure 3-18(a), it is apparent that these curves resemble the electrochemistry of phenols [26]. In Figure 3-18(a), a clear oxidation wave is observed at about 0.10 V vs. SCE followed by a quasi-reversible couple in the vicinity of 0.20 V to 0.40 V vs. SCE, while an additional oxidation wave is clear at about 0.70 V vs. SCE. The quasi-reversible two electron, two proton transfer reaction, associated with the conversion between the quinone and the hydroquinone compounds, Scheme 3-3, can be assigned to the redox couple at about 0.39 V vs. SCE, with a peak separation of 26 mV. The oxidation wave seen at about 0.10 V vs. SCE is more difficult to explain, but it appears to be connected with the initial reduction of the MCPA metabolite, Scheme 3-2. Based on the discussion, it is concluded that the A-GCE can also be used in the electrochemical detection of the MCPA metabolite.

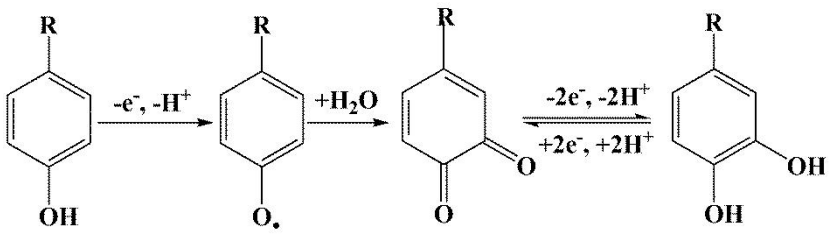

Scheme 3-3. Electrochemistry of *p*-phenol compounds.

3.4 Conclusion

In this work, a novel and simple electrochemical sensor for the detection of MCPA was developed through the simple activation of GCE. Impressive electrochemical detection was obtained, which showed a wide dynamic linear region, from 1 to 850 μM, and a low LOD of 0.02 μM obtained using the CV technique, while the LOD value was further reduced to 0.008 μM using DPV technique. Moreover, the developed sensor exhibited good reproducibility and stability. Further, it was found

that 4-chloro-2-methylphenol produced from the electrochemical oxidation of MCPA can be reduced at the A-GCE. This observation demonstrates that the A-GCE can not only be used in the electrochemical detection of MCPA, but may also be employed to follow the degradation efficiency of MCPA by monitoring the 4-chloro-2-methylphenol concentration.

3.5 References

[1] Pretty, J. Intensification for redesigned and sustainable agricultural systems. *Science*, **2018**, *362*, eaav0294, doi: 10.1126/science.aav0294.

[2] Wolfram, J.; Stehle, S.; Bub, S.; Petschick, L. L.; Schulz, R. Water quality and ecological risks in European surface waters-monitoring improves while water quality decreases. *Environ. Int.* **2021**, *152*, 106479, doi: 10.1016/j.envint.2021.106479.

[3] Pundir, C. S.; Malik, A.; Preety, Bio-sensing of organophosphorus pesticides: a review. *Biosens. Bioelectron*. **2019**, *140*, 111348, doi: 10.1016/j.bios.2019.111348.

[4] Morton, P. A.; Cassidy, R.; Floyd, S.; Doody, D. G.; McRoberts, W. C.; Jordan, P. Approaches to herbicide (MCPA) pollution mitigation in drinking water source catchments using enhanced space and time monitoring. *Sci. Total Environ*. **2021**, *755*, 142827, doi: 10.1016/j.scitotenv.2020.142827.

[5] Tran, A. T. K.; Hyne, R. V.; Doble, P. Determination of commonly used polar herbicides in agricultural drainage waters in Australia by HPLC. *Chemosphere*. **2007**, *67*, 944–953, doi: 10.1016/j.chemosphere.2006.11.002.

[6] Paszko, T.; Muszyński, P.; Materska, M.; Bojanowska, M.; Kostecka, M.; Jackowska, I. Adsorption and degradation of phenoxyalkanoic acid herbicides in soils: A review. *Environ. Toxicol. Chem*. **2016**, *35*, 271–286, doi: 10.1002/etc.3212.

[7] Pozo, O.; Pitarch, E.; Sancho, J. V.; Hernández, F. Determination of the herbicide 4-chloro-2-methylphenoxyacetic acid and its main metabolite, 4-chloro-2-methylphenol in water and soil by liquid chromatography-electrospray tandem mass spectrometry. *J. Chromatogr. A*, **2001**, *923*, 75–85, doi: 10.1016/S0021-9673(01)01006-8.

[8] Glozier, N E.; Struger, J.; Cessna, A. J.; Gledhill, M.; Rondeau, M.; Ernst, W. R.; Sekela, M. A.; Cagampan, S. J.; Sverko, E.; Murphy, C.; Murray, J. L.; Donald, D. B.

Occurrence of glyphosate and acidic herbicides in select urban rivers and streams in Canada. *Environ. Sci. Pollut. Res*. **2012**, *19*, 821–834, doi: 10.1007/s11356-011-0600-7.

[9] Rippy, M. A.; Deletic, A.; Black, J.; Aryal, R.; Lampard, J. L.; Tang, J. Y. M.; McCarthy, D.; Kolotelo, P.; Sidhu, J.; Gernjak, W. Pesticide occurrence and spatio-temporal variability in urban run-off across Australia. *Water Res.* **2017**, *115*, 245–255, doi: 10.1016/j.watres.2017.03.010.

[10] Piotrowska, A.; Syguda, A.; Chrzanowski, L.; Heipieper, H. J. Toxicity of synthetic herbicides containing 2,4-D and MCPA moieties towards Pseudomonas putida mt-2 and its response at the level of membrane fatty acid composition. *Chemosphere*, **2016**, *144*, 107–112, doi:10.1016/j.chemosphere.2015.08.067

[11] Wunnapuk, K.; Liu, X.; Gobe, G. C.; Endre, Z. H.; Peake, P. W.; Grice, J. E.; Roberts, M. S.; Buckley, N. A. Kidney biomarkers in MCPA-induced acute kidney injury in rats: Reduced clearance enhances early biomarker performance. *Toxicol. Lett*. **2014**, *225*, 467–478, doi: 10.1016/j.toxlet.2014.01.018.

[12] Pahwa, M.; Harris, S. A.; Hohenadel, K.; McLaughlin, J. R.; Spinelli, J. J.; Pahwa, P.; Dosman, J. A.; Blair, A. Pesticide use, immunologic conditions, and risk of non Hodgkin lymphoma in Canadian men in six provinces. *Int. J. Cancer*. **2012**, *131*, 2650–2659, doi:10.1002/ijc.27522.

[13] Seebunrueng, K.; Phosiri, P.; Apitanagotinon, R.; Srijaranai, S. A new environment-friendly supramolecular solvent-based liquid phase microextraction coupled to high performance liquid chromatography for simultaneous determination of six phenoxy acid herbicides in water and rice samples. *Microchem. J*. **2020**, *152*, 104418, doi: 10.1016/j.microc.2019.104418.

[14] Tabani, H.; Fakhari, A. R.; Shahsavani, A.; Behbahani, M.; Salarian, M.; Bagheri, A.; Nojavan, S. Combination of graphene oxide-based solid phase extraction and electro membrane extraction for the preconcentration of chlorophenoxy acid herbicides in environmental samples. *J. Chromatogr. A*, **2013**, *1300*, 227–235, doi: 10.1016/j.chroma.2013.04.026.

[15] Mohammadnejad, M.; Gudarzi, Z.; Geranmayeh, S.; Mahdavi, V. HKUST-1 metal-organic framework for dispersive solid phase extraction of

2-methyl-4-chlorophenoxyacetic acid (MCPA) prior to its determination by ion mobility spectrometry. *Microchim. Acta*, **2018**, *185*, 495, doi: 10.1007/s00604-018-3014-0.

[16] Yang, Y.; Fang, G.; Wang, X.; Zhang, F.; Liu, J.; Zheng, W.; Wang, S. Electrochemiluminescent graphene quantum dots enhanced by MoS_2 as sensing platform: a novel molecularly imprinted electrochemiluminescence sensor for 2-methyl-4-chlorophenoxyacetic acid assay. *Electrochim. Acta*, **2017**, *228*, 107–113, doi: 10.1016/j.electacta.2017.01.043.

[17] Torres-Cartas, S.; Gómez-Benito, C.; Meseguer-Lloret, S. FI on-line chemiluminescence reaction for determination of MCPA in water samples. *Anal. Bioanal. Chem*. **2012**, *402*, 1289–1296, doi: 10.1007/s00216-011-5567-1.

[18] Rahemi, V.; Vandamme, J. J.; Garrido, J. M. P. J.; Borges, F.; Brett, C. M. A.; Garrido, E. M. P. J. Enhanced host-guest electrochemical recognition of herbicide MCPA using a β-cyclodextrin carbon nanotube sensor. *Talanta,* **2012**, *99*, 288–293, doi: 10.1016/j.talanta.2012.05.053.

[19] Rahemi, V.; Garrido, J. M. P. J.; Borges, F.; Brett, C. M. A.; Garrido, E. M. P. J. Electrochemical sensor for simultaneous determination of herbicide MCPA and its metabolite 4-chloro-2-methylphenol. Application to photodegradation environmental monitoring. *Environ. Sci. Pollut. Res*. **2015**, *22*, 4491–4499, doi: 10.1007/s11356-014-3693-y.

[20] Bialek, A.; Skrzypczynska, K.; Kusmierek, K.; Swiatkowski, A. Voltammetric determination of MCPA, 4-chloro-o-cresol and o-cresol in water using a modified carbon paste electrode. *Int. J. Electrochem. Sci*. **2019**, *14*, 228–237, doi: 10.20964/2019.01.20.

[21] Farhat, A.; Keller, J.; Tait, S.; Radjenovic, J. Assessment of the impact of chloride on the formation of chlorinated by-products in the presence and absence of electrochemically activated sulfate. *Chem. Eng. J*. **2017**, *330*, 1265–1271, doi: 10.1016/j.cej.2017.08.033.

[22] Yi, Y.; Weinberg, G.; Prenzel, M.; Greiner, M.; Heumann, S.; Becker, S.; Schlögl, R. Electrochemical corrosion of a glassy carbon electrode. *Catal. Today*, **2017**, *295*, 32–40, doi: 10.1016/j.cattod.2017.07.013.

[23] Georgieva, I.; Kersten, M.; Tunega, D. Molecular modeling of MCPA herbicide adsorption by goethite (110) surface in dependence of pH. *Theor. Chem. Acc*. **2020**, *139*, 132, doi: 10.1007/s00214-020-02646-4.

[24] Laviron, E. General expression of the linear potential sweep voltammogram in the case of diffusionless electrochemical systems. *J. Electroanal. Chem*. **1979**, *101*, 19–28, doi: 10.1016/S0022-0728(79)80075-3.

[25] Mazzotta, E.; Malitesta, C. Electrochemical detection of the toxic organohalide 2,4-DB using a Co-porphyrin based electrosynthesized molecularly imprinted polymer. *Sensors Actuators, B Chem*. **2010**, *148*, 186–194, doi: 10.1016/j.snb.2010.03.089.

[26] Enache, T. A.; Oliveira-Brett, A. M. Phenol and para-substituted phenols electrochemical oxidation pathways. *J. Electroanal. Chem*. **2011**, *655*, 9–16, doi: 10.1016/j.jelechem.2011.02.022.

Chapter 4

Developing a Sensitive Electrochemical Sensor for the Detection of *p*-Nitrophenol (*p*-NP) through a Simple Activated GCE Modified with Electrodeposited Bismuth Dendrites

4.1 Introduction

Water is the source of human life and the foundation of the growth of all things. However, with the development of economy, a large number of pollutants are discharged into water, resulting in water pollution, which not only destroys the natural environment, but also endangers human health. Nitrophenols have long been recognised as a priority pollutant in aquatic environments [1]. They are utilised as precursors in the manufacture of dyes and indicators, pesticides, pharmaceuticals, and explosives and have the potential to enter the environment through the discharge of industrial wastewater [2]. Indeed, concentrations in the vicinity of 0.43 μg/L have been reported in rivers in Europe [3]. *Para*-nitrophenol (*p*-NP) or 4-nitrophenol is one isomer of nitrophenols and it has a high solubility in water and it is severely toxic, thus *p*-NP is a threat to all aquatic life and ecological environments. In particular, the nitro group is easily reduced by enzymes to a nitro radical anion, which in turn can generate a hydroxyl-amine derivative, which exerts mutagenic and carcinogenic effects [4,5]. Accordingly, the concentration levels of *p*-NP in aquatic environments are especially important. For example, the lethal (LC50) concentration, which is a good indicator of the acute toxicity of a pollutant, reflecting the concentration that kills 50% of species, has been reported for a number of aquatic species exposed to *p*-NP. The LC50 value has been reported as 540 μg/L for *D. carinata* (equivalent to 3.88 μM) over a 24 h exposure period to *p*-NP [6], while the LC50 values are 56 μg/L (0.40 μM) for Daphnia and 92 μg/L (0.66 μM) for Carp [7]. Likewise, Yan et al. [8] determined the acute and chronic concentrations of algae exposed to *p*-NP as 2180 and 218.0 μg/L, respectively. Therefore, the detection of *p*-NP at concentrations in the vicinity of low μM to nM is particularly relevant in monitoring the quality of aquatic systems.

Various analytical techniques, such as high-performance liquid chromatography (HPLC) [9.10], gas chromatography [11] and spectrophotometry [12] can be employed in the detection of *p*-NP. Nevertheless, they are not suitable for the rapid and on-site analysis of water samples. On the other hand, sensors and especially electrochemical sensors are attractive as they are simple to operate and are ideal for on-site analytical

measurements. So far, a series of electrochemical sensors based on various functional components for the detection of *p*-NP were reported [13–16]. These sensors are typically produced using MXenes [13], two dimensional layered materials [14] or metal oxide nanostructures [15] that can be time-consuming to fabricate. Moreover, they do not always provide a sufficiently low detection in the nM region for *p*-NP. For example, a CeFeP modified GCE showed a linear range to 0.1 μM [16], while detection limits of 0.61 and 2.88 μM were observed with $CuBi_2O_4$ [15] and reduced graphene oxide coupled with tungsten oxide [14], respectively.

Recently, it has been shown that when GCE electrodes are activated/oxidised by cycling to potentials beyond the oxygen evolution reaction they become very effective in facilitating electron transfer, making them attractive in the design of electrochemical-based sensors [17–20]. This has been attributed to the generation of oxygen-containing functional groups, which are formed as the C–C bonds are attacked by •OH radicals, which are generated at the high potentials [21]. Another interesting approach is the utilisation of bismuth, which is a non-toxic element. Indeed, electrodeposited bismuth films and nanostructures have been used in the electrochemical detection of metronidazole [22] and various heavy metal ions [23–25]. It has been shown that bismuth modified electrodes exhibit high overpotentials for the hydrogen evolution reaction and have low background currents. This makes bismuth interesting in the electrochemical reduction of analytes, where the adsorption and reduction of hydrogen may be a competing reaction.

In this chapter we show that a simple activated GCE modified with bismuth dendrites can be prepared within a few minutes, through the electrochemical activation of the GCE followed by the electrodeposition of bismuth. Moreover, the sensor can be easily regenerated by oxidising and removing the bismuth dendrites followed by their subsequent electrodeposition. Finally, this sensor is very well suited to monitoring *p*-NP in water and in different aquatic environments at low μM and nM concentrations.

4.2 Experimental section

The electrochemical experiments were performed using a Solartron 1287 potentiostat coupled with a 1255 FRA and a CHI 660C workstation for the preparation of the modified electrodes and CV, EIS and DPV measurements, respectively. SEM with a Hitachi S–3200–N microscope was employed for the surface morphology characterisation and an Oxford Instrument INCAz-act ESX was used for EDX studies to analyse the chemical composition of the modified electrodes. A standard three-electrode system was used for the electrochemical measurements. Four electrodes were employed. The unmodified GCE was polished and cleaned according to the procedure described in the Section 2.2.4. The GCE was then activated by cycling in a phosphate solution, Section 2.2.4.1, to give A-GCE. Bismuth was electrodeposited at the GCE to provide the GCE/Bi, as described in Section 2.2.4.2, and at the A-GCE to produce A-GCE/Bi, Section 2.2.4.5.

Unless otherwise stated, the CV experiments were recorded at 50 mV s^{-1}, and the DPV data were recorded with a pulse amplitude of 50 mV, a pulse width of 0.05 s, sampling width of 0.0167 s, a pulse period of 0.50 s, and an increment of 4 mV. The impedance data were collected at –0.8 V vs. SCE for bare GCE, –0.5 V vs. SCE for GCE/Bi, –0.7 V vs. SCE for A-GCE and –0.68 V vs. SCE for A-GCE/Bi in the buffered 100 μM *p*-NP solution, using a perturbation potential of 10 mV. The data were recorded after a 30 min polarisation period to ensure steady-state conditions. All solutions were deoxygenated with high purity nitrogen gas for a 30 min period prior to the electrochemical measurements. All experiments were performed in triplicate or quintuplicate and using the standard deviation (σ) and number of experiments performed (n) the standard error was computed as $\sigma/n^{1/2}$.

4.3 Results and Discussion

It is generally accepted that *p*-NP is reduced to *p*-hydroxylaminophenol through a $4e^-/4H^+$ transfer process, as illustrated in Scheme 4-1. This process typically occurs at

−0.79 V vs. Ag/AgCl, making this an ideal analyte for the electrodeposited bismuth dendrites. The electrochemically generated *p*-hydroxylaminophenol can be oxidised to nitrosophenol with the transfer of two electrons and two protons at about 0.15 V vs. Ag/AgCl and this redox process can often give rise to high peak currents [26]. However, the bismuth dendrites are oxidised at these potentials, and accordingly the conversion from *p*-nitrophenol to *p*-hydroxylaminophenol was the only electrochemical process followed in this work.

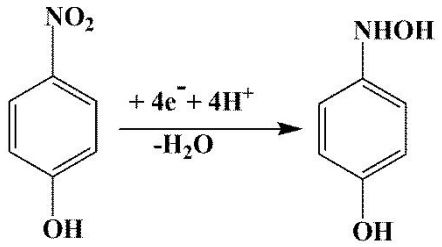

Scheme 4-1. Conversion of *p*-NP to *p*-hydroxylaminophenol.

4.3.1 Selection of modified electrodes

In order to improve the detection and sensitivity of *p*-NP, three modified electrodes were prepared as A-GCE, GCE/Bi and A-GCE/Bi and used to determine *p*-NP. A comparison of the four electrodes including bare GCE, A-GCE, GCE/Bi and A-GCE/Bi in the electrochemical reduction of *p*-NP to *p*-hydroxylaminophenol is illustrated in Figure 4-1. It is clearly evident in the voltammograms depicted in Figure 4-1(a) that the A-GCE/Bi gives the highest peak current and performs best in the detection of *p*-NP. The bare GCE exhibits a broad reduction wave centred at about –0.80 V vs. SCE, with a very low peak current of 7.82 μA. On activating the GCE (A-GCE), a sharper peak becomes evident, a much higher peak current (36.82 μA) is achieved, and the peak potential is shifted to a more thermodynamically favourable value of ca. –0.70 V vs. SCE. An even greater shift in the peak potential is seen when bismuth is electrodeposited onto the surface to form GCE/Bi, with a peak potential of ca. -0.50 V vs. SCE, but with a somewhat low peak current. However, when bismuth is electrodeposited onto the A-GCE to give A-GCE/Bi, a much higher peak current of

55.62 µA is obtained. Although the peak potential is considerably lower than the GCE/Bi, the reduction peak potential of –0.68 V vs. SCE compares very well to some recently reported materials that have been employed to detect *p*-NP with peak potentials varying from –0.73 V vs. Ag/AgCl [27] to –0.77 V vs. Ag/AgCl [28]. In addition, the ability of these four electrodes to detect *p*-NP is more clearly evident in Figure 4-1(b) where the peak current is shown at lower *p*-NP concentrations from 1.5 to 6.5 µM. Here, the A-GCE/Bi provides the highest gradient of 0.48 µA μM^{-1}, while lower values of 0.32 µA μM^{-1} for A-GCE and 0.12 µA μM^{-1} for GCE/Bi were seen, highlighting the advantage of combining the electrodeposition of bismuth with the activation of the GCE.

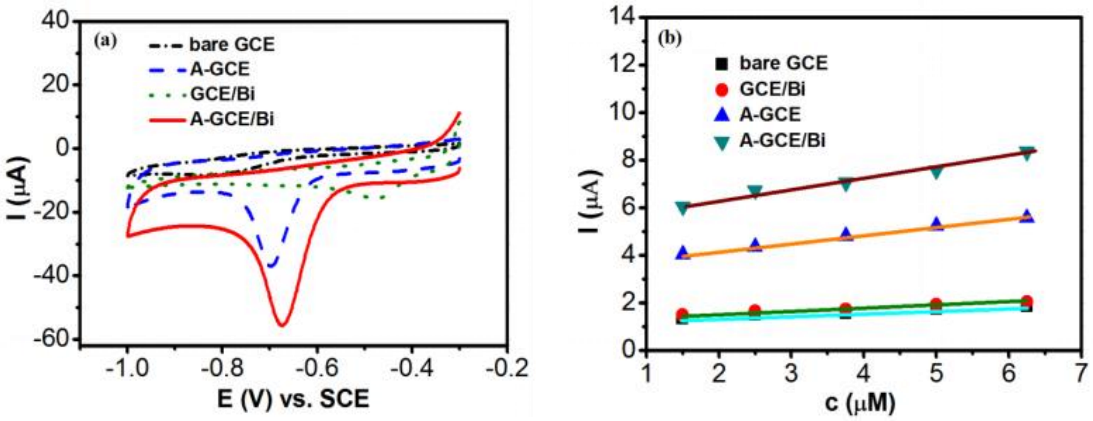

Figure 4-1. (a) CVs recorded for bare GCE, A-GCE, GCE/Bi and A-GCE/Bi in 100 µM *p*-NP and **(b)** peak currents plotted as a function of *p*-NP concentration.

4.3.2 Choice of optimum experimental conditions

In order to obtain the best detection performance for *p*-NP, the influence of the activation process of GCE on the determination of *p*-NP was investigated and the results are summarised in Figure 4-2 and the data are listed in Table 4-1 where it is evident that optimum activation occurs by cycling the GCE between the potentials of –2.0 V and 2.0 V vs. SCE at 100 mV s^{-1} for 30 cycles. With higher upper potentials of 2.2 and 2.4 V, somewhat lower peak currents were seen, and this was coupled with more capacitive background currents, suggesting an increase in the surface area of the A-GCE.

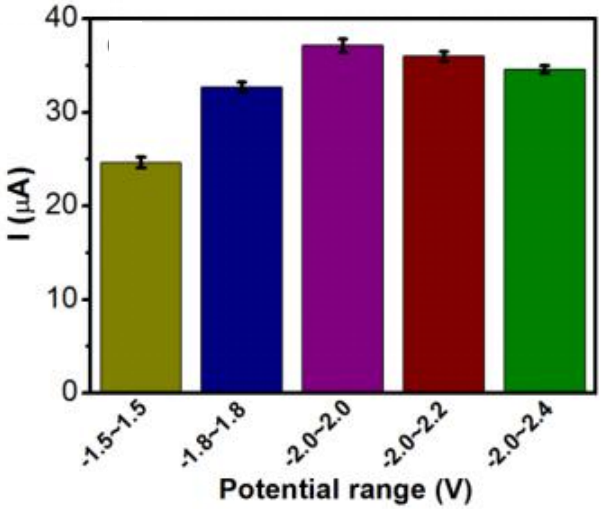

Figure 4-2. Peak current recorded in 100 μM *p*-NP as a function of the activation potential ranges used to form A-GCE. All data recorded in triplicate (n = 3).

Table 4-1. The activation potential range of A-GCE and the reduction peak currents for the determination of *p*-NP.

Potential range (V)	Mean of *p*-NP reduction current (μA)	RSD (%) n = 3
-1.5 ~ 1.5 V	24.65 ± 0.62	2.51
-1.8 ~ 1.8 V	32.71 ± 0.49	1.50
-2.0 ~ 2.0 V	37.16 ± 0.68	1.83
-2.0 ~ 2.2 V	35.98 ± 0.51	1.42
-2.0 ~ 2.4 V	34.58 ± 0.47	1.36

For the electrodeposition of bismuth, the current-time transients recorded during the electrodeposition of bismuth are shown in Figure 4-3(a) for a range of deposition potentials. It is clear from this plot that the rate of electrodeposition increases on applying more negative potentials. On application of the potential there is a sharp increase in the current, which then decays due to the charging of the double layer. This

is then followed by nucleation and growth of the bismuth deposits. Interestingly, there is no evidence for the overlapping of nuclei, as the nucleation current continues to increase with increasing deposition periods. At the higher overpotentials there is evidence of the competing hydrogen ion reduction reaction, and this is clearly seen at –1.10 V vs. SCE.

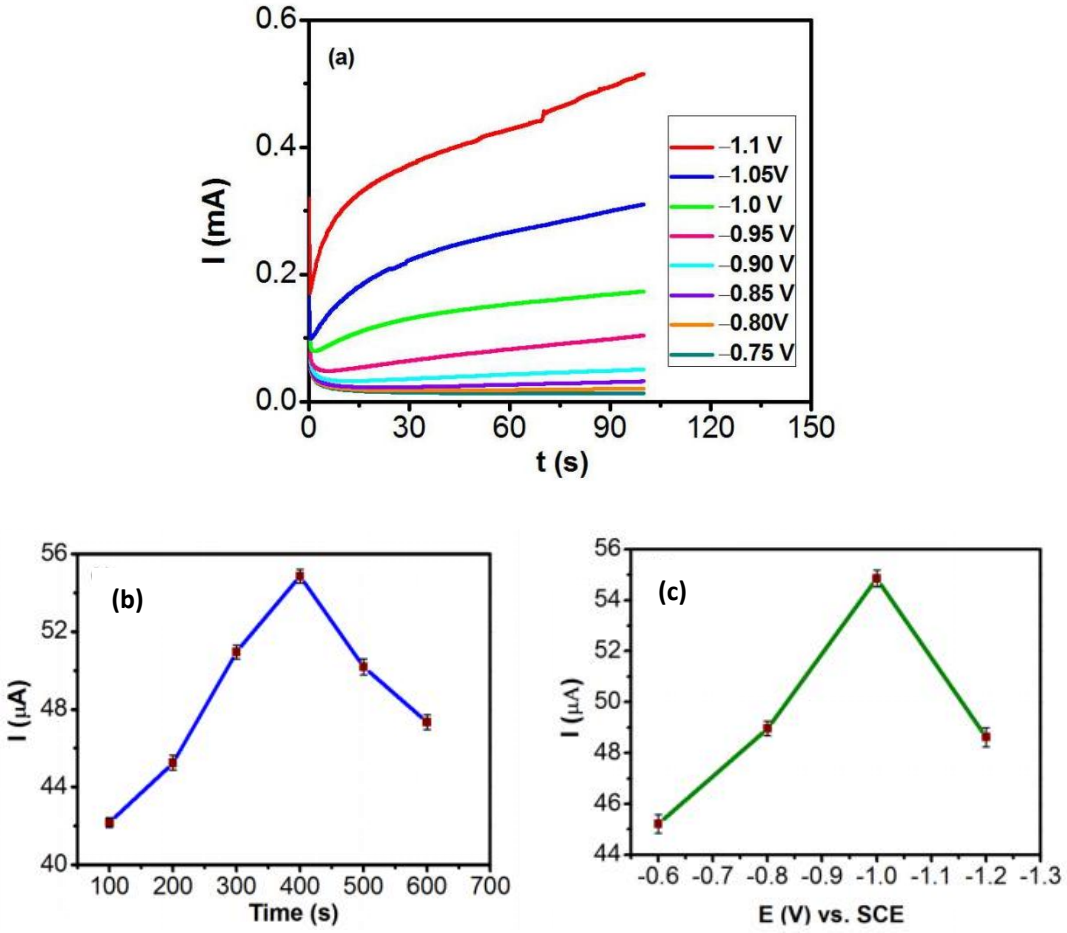

Figure 4-3. (a) Current-time transients recorded at –0.75 V, –0.80 V, –0.85 V, –0.90 V, –0.95 V, –1.0 V, –1.05 V and –1.10 V recorded in 1.0 mM $Bi(NO_3)_3$, **(b)** peak current recorded in 100 μM *p*-NP as a function of the electrodeposition time and **(c)** electrodeposition potential. All data recorded in triplicate (n = 3).

After the electrodeposition of bismuth, the formed electrodes were employed to determine *p*-NP. This is illustrated in Figure 4-3(b), where the highest peak current can be obtained with a 400 s electrodeposition period. This optimum deposition time is relatively long, but this gives rise to a 51% ± 1.35 increase in the peak current for A-GCE/Bi compared to A-GCE. In addition, the influence of the electrodeposition

potential is summarised in Figure 4-3(c), where electrodeposition at –1.0 V vs. SCE gives the highest peak current (54.86 μA ± 1.08) for the reduction of *p*-NP. The sharp decrease in the *p*-NP reduction peak current which is evident at –1.2 V vs. SCE is probably related to the competing hydrogen ion reduction reaction and evolution of H_2(g) during the electrodeposition of the bismuth dendrites in the acidic Bi(III) solution. This competing reaction will lead to lower amounts of electrodeposited bismuth and may also alter the nature of the bismuth deposits. Therefore, based on the observation above, it was found that the optimum bismuth electrodeposition parameter at the A-GCE was 400 s at –1.0 V vs. SCE.

4.3.3 Characterisation of the surface morphology

The surface morphology of the bare GCE, A-GCE and A-GCE/Bi is shown in Figure 4-4. The images in Figure 4-4(a) and (b), which represent the A-GCE/Bi electrode, indicate the formation of bismuth dendrites that are dispersed across the electrode surface. These images are very different to the A-GCE, as shown in Figure 4-4(c). The A-GCE shows evidence of surface dissolution, resembling pitting attack and these pits are uniformly dispersed across the surface. This is consistent with previous studies where it has been reported that carbon-based substrates can be oxidised when polarised at high potentials beyond the oxygen evolution reaction [17–20]. At these high potentials, OH· radicals are formed, and these can attack the C−C bonds to give oxygen-containing groups [21]. Indeed, it has been suggested that these oxygenated species facilitate and increase the rate of electron transfer, and this is consistent with the data presented in Figure 4-1(a). In Figure 4.4(d), the bare GCE is evident and is free from any surface attack. The EDX spectrum presented in the inset in Figure 4-4(d) shows the spectrum of the A-GCE/Bi, with clear indications for the presence of Bi. The oxygen occurs mainly from the oxygenated species that are present on the A-GCE. Mapping experiments are shown in Figure 4-4 for carbon (C), bismuth (Bi) and oxygen (O) and it is clear that the bismuth and oxygen are reasonably well distributed over the surface.

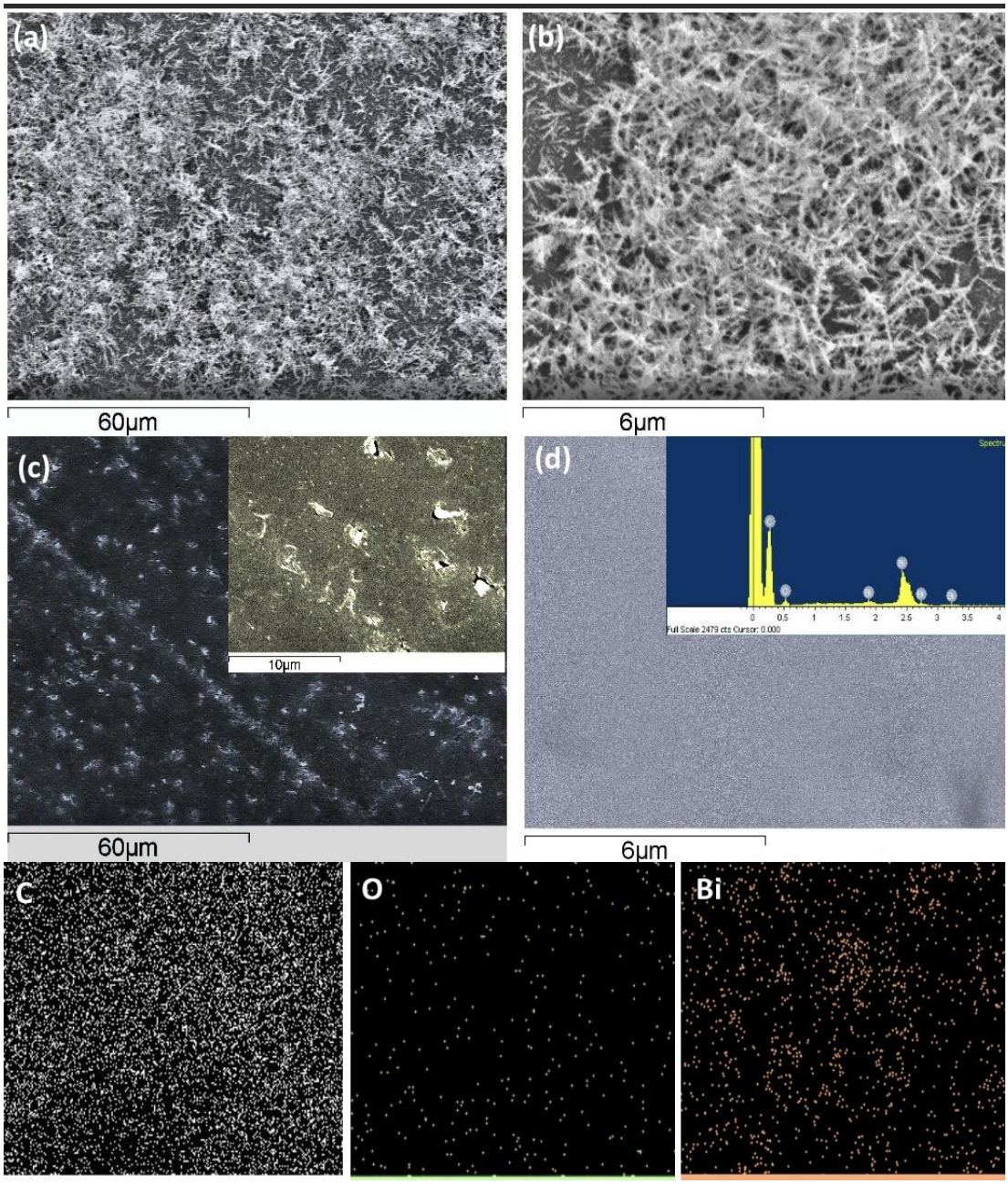

Figure 4-4. SEM micrographs recorded for A-GCE/Bi at **(a)** low and **(b)** higher magnification, **(c)** micrographs recorded for A-GCE, **(d)** micrographs for unmodified GCE with EDX spectrum recorded for A-GCE/Bi in the inset, and mapping data for C, O and Bi.

4.3.4 EIS Characterisation of the electrodes

Further, the impedance spectra of the different electrodes recorded in the presence of 100 µM *p*-NP were measured and are shown in Figure 4-5. These data were recorded at a fixed potential that coincides with the peak potentials observed in the voltammograms

for the reduction of *p*-NP. In this analysis, the experimental data are depicted as symbols, while the fitted data are shown as continuous traces.

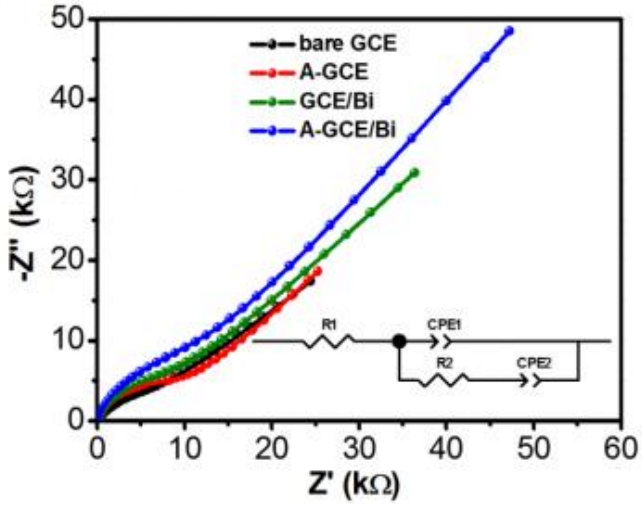

Figure 4-5. Equivalent circuit and EIS spectra recorded for bare GCE at −0.80 V, A-GCE at −0.70 V, GCE/Bi at −0.50 V and A-GCE/Bi at −0.68 V vs. SCE in 100 μM *p*-NP.

All data were fitted using the equivalent circuit provided in Figure 4-5. Here, the solution resistance is represented as R1, the charge-transfer resistance is denoted as R2, while the CPE elements represent constant phase elements, with CPE1 corresponding to the double layer capacitance and CPE2 indicating diffusional processes. As seen in Figure 4-5, the impedance profiles are similar showing a semicircle at higher frequencies and a diffusion tail at lower frequencies, with little indications that the activation of the GCE or the electrodeposition of the bismuth dendrites give rise to any reduction in the charge transfer resistance. Indeed, the lowest charge-transfer resistance of 6073 ± 342 Ω (n = 3) was obtained for the A-GCE. On the electrodeposition of the bismuth dendrites an increase in the charge transfer resistance was observed, with a 12% increase seen on the electrodeposition of bismuth at the A-GCE and a 10% increase evident on modifying the bare GCE with the bismuth dendrites. The highest capacitance (CPE1 with n > 0.86) was observed with the activated electrodes, with a value of 23.11 ± 0.45 mF (n = 3) for the A-GCE/Bi and 26.58 ± 0.72 mF (n = 3) for the A-GCE and this is consistent with the generation of oxygenated groups during the activation process.

4.3.5 Study on reaction kinetics

In order to determine if the electrochemical reduction of *p*-NP was under diffusion or adsorption control, the scan rate was varied between 20 and 200 mV s^{-1}. The resulting data were analysed using the Randles-Sevick equation, where the peak current was plotted as a function of the square root of the scan rate. In addition, the peak current was plotted as a function of scan rate and the logarithm of the peak current was plotted as a function of the logarithm of the scan rate. It was found that the reduction of *p*-NP was under typical diffusion control for the bare GCE and GCE/Bi, but on the A-GCE the rate determining-step became a mixed adsorption and diffusion process. Representative data are presented in Figure 4-6(a), (b) and (c) for the A-GCE, with the CVs shown as a function of scan rate (Figure 4-6(a)). The peak current plotted as a function of scan rate and the corresponding logarithmic plot is depicted in Figure 4-6(b) and (c), respectively. A linear relationship, with the regression equation, I_p (mA) = 0.67υ (mV s^{-1}) + 9.35 and R^2 of 0.999 was obtained. Furthermore, the slope of the logarithmic plot was computed as 0.81, indicating the emergence of a mixed diffusition-adsorption process that can be attributed to the generation of defects and oxygenated sites during the activation process that facilitate adsorption.

Interestingly, on electrodeposition of the bismuth dendrites, the mixed diffusion-adsorption process was maintained, as illustrated in Figure 4-7(a), (b) and (c). The linear regression equations were determined as, I_p (mA) = 0.99 υ (mV s^{-1}) + 11.31 with R^2 at 0.998 and log I = 0.82 log υ + 0.43, R^2 of 0.991, with I expressed as mA and υ as mV s^{-1}. Here, the slopes at 0.81± 0.025 for A-GCE and 0.82 ±0.032 for A-GCE/Bi are nearly identical, indicating a similar mixed diffusion adsorption process at the two modified electrodes.

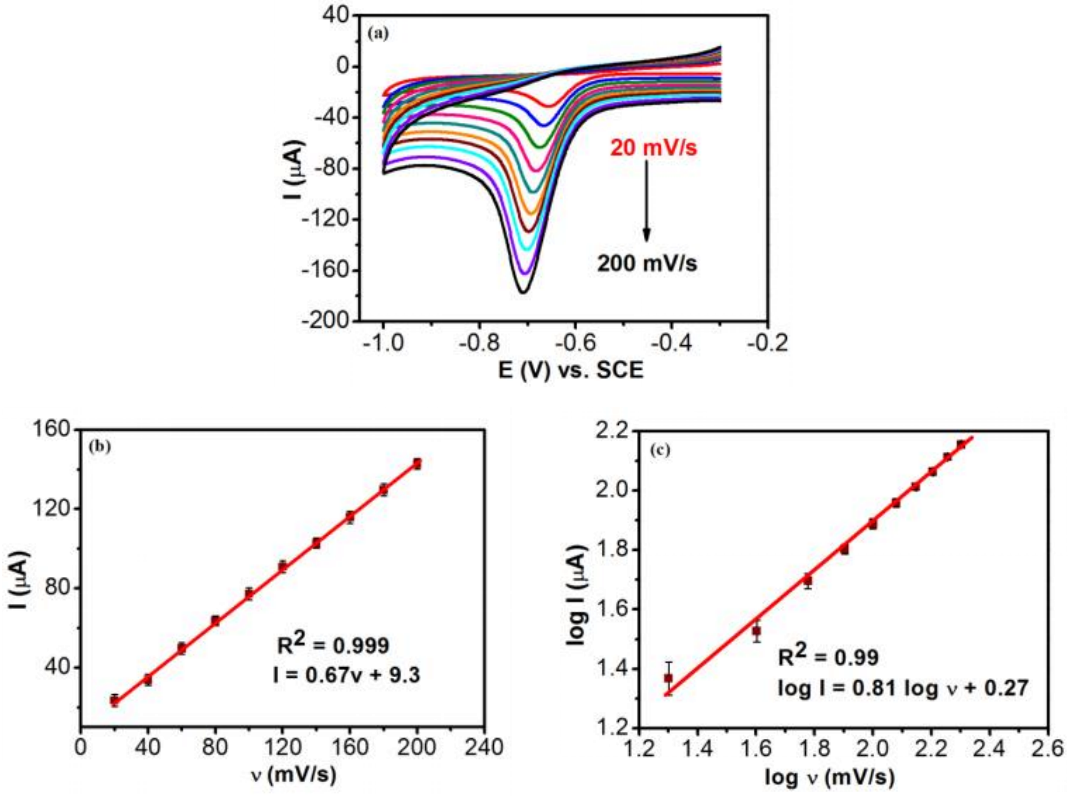

Figure 4-6. Typical CVs recorded in 100 μM *p*-NP at scan rates from 20 to 200 mV s^{-1} for the A-GCE **(a)**, peak current plotted as function of scan rate **(b)** and logarithm of peak current as a function of logarithm of scan rate **(c)**, n = 3.

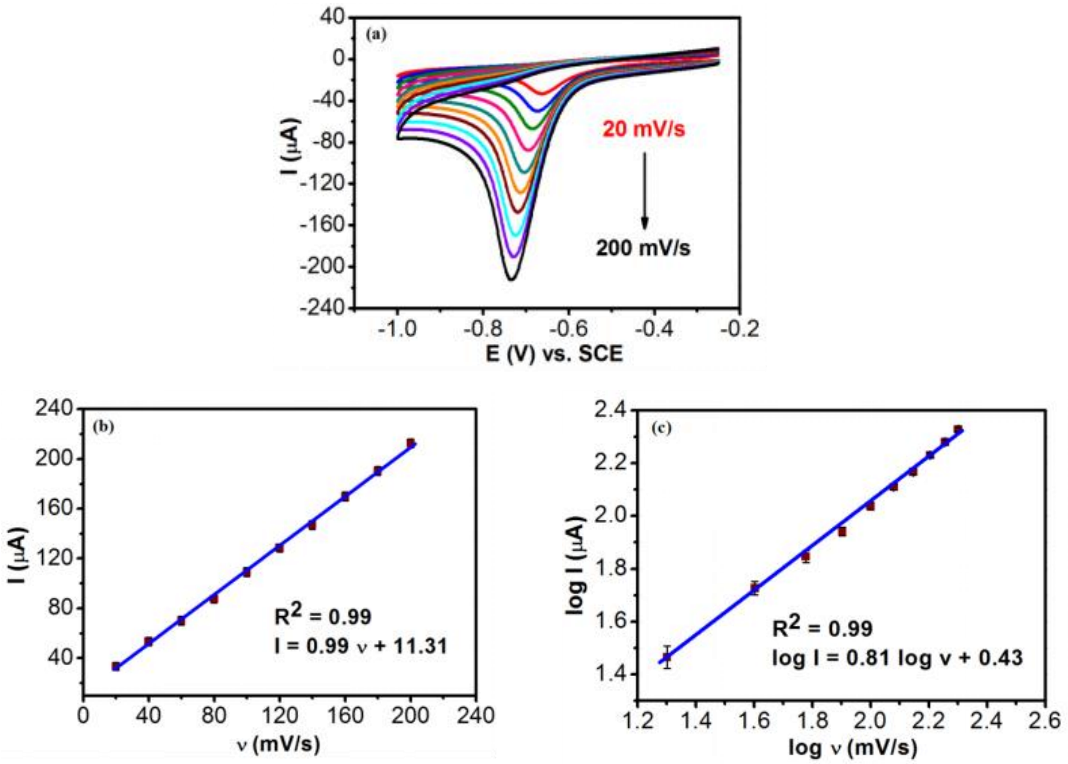

Figure 4-7. Typical CVs recorded in 100 μM *p*-NP at scan rates from 20 to 200 mV s^{-1} for the A-GCE/Bi **(a)**, peak current plotted as function of scan rate **(b)** and logarithm of peak current as a function of logarithm of scan rate **(c)**, n = 3.

On comparing the CVs shown for the A-GCE and A-GCE-Bi, Figure 4-6 (a) and 4-7 (a), it is evident that the peak potential increases at a slightly greater rate with increasing scan rate for the A-GCE/Bi. This indicates that the electron-transfer becomes somewhat slower on decorating the A-GCE with the bismuth dendrites. Accordingly, the rates of the electron transfer step were estimated using the Laviron method, which is described in Equation 4–1 and represents an irreversible redox reaction. Here, R, T and F represent the gas constant, thermodynamic temperature, and Faraday constant, respectively, while E^0 represents the standard reduction potential. The E^0 values were estimated as –596 mV vs. SCE for A-GCE and –554 mV vs. SCE for A-GCE/Bi by extrapolating the scan rate to 0 mV s^{-1}.

$$E_p = E^0 + \left(\frac{RT}{\alpha nF}\right)\ln\left(\frac{RTK_s}{\alpha nF}\right) + \frac{RT}{\alpha nF}\ln v \qquad (4–1)$$

On plotting the peak potential (E_p) as a function of the natural logarithm of the scan rate (υ), linear plots were obtained for both the A-GCE and A-GCE/Bi, as illustrated in Figure 4-8. The linear regression equations were obtained as, E_p (V) = –0.029 lnυ (mV s^{-1}) – 0.596 (R^2 = 0.995) and E_p (V) = –0.035 lnυ (mV s^{-1}) – 0.554 (R^2 = 0.998) for the A-GCE and A-GCE/Bi, respectively.

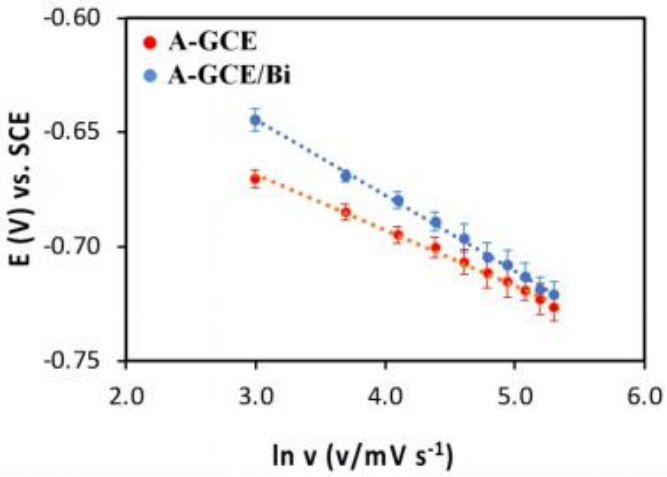

Figure 4-8. Peak potential plotted as a function of logarithm of scan rate in 100 µM *p*-NP for A-GCE and A-GCE/Bi (n = 3).

Further, on fitting these relationships to Equation 4–1, the Ks was estimated as 55.0 s^{-1} ± 1.15 for the A-GCE/Bi, but slightly higher at 62.1 s^{-1} ± 1.47 for the A-GCE, to give an approximate 1.12-fold decrease in the rate of the electron transfer step on decorating the activated GCE with the bismuth dendrites. This is in good agreement with the electrochemical impedance studies which show an increase in the charge transfer resistance on modifying the electrode with the bismuth dendrites.

Interestingly, the αn values were estimated as 1.05 for the A-GCE and 0.77 for the A-GCE-Bi, indicating a significant deviation from the theoretical value of 2.0 arising from a value of 0.5 for α when n is set at 4. However, this may be related to the nature of the *p*-NP reduction reaction, with an initial slow one-electron transfer step, Equation 4–2, followed by the transfer of three electrons, Equation 4–3 [29].

$$R–NO_2 + e^- \rightarrow R–NO_2^- \quad (\textit{slow}) \tag{4–2}$$

$$R–NO_2^- + 3e^- + 4H^+ \rightarrow R–NHOH + H_2O \ (\textit{fast}) \tag{4–3}$$

It is clear from this analysis that the improved performance of the A-GCE/Bi, Figure 4-1, is not related to an increase in the rate of electron transfer. It appears to be more connected with an increase in the surface area of the A-GCE/Bi and the transition to a mixed diffusion-adsorption process, with the bismuth dendrites providing more adsorption sites. This observation is consistent with the memory effects of the two electrodes in *p*-NP, as shown in Figure 4-9(b) for the A-GCE and Figure 4-10(b) for the A-GCE/Bi, where there is evidence of more adsorbed *p*-NP with the A-GCE/Bi based on comparing their memory effects.

4.3.6 Study on adsorption-like behaviour

The emergence of an adsorption process was further probed by determining the optimum immersion period and any related memory effects associated with the adsorption of *p*-NP. These experiments were conducted with different immersion

periods and the results are summarised in Figure 4-9 for the A-GCE and Figure 4-10 for the A-GCE/Bi.

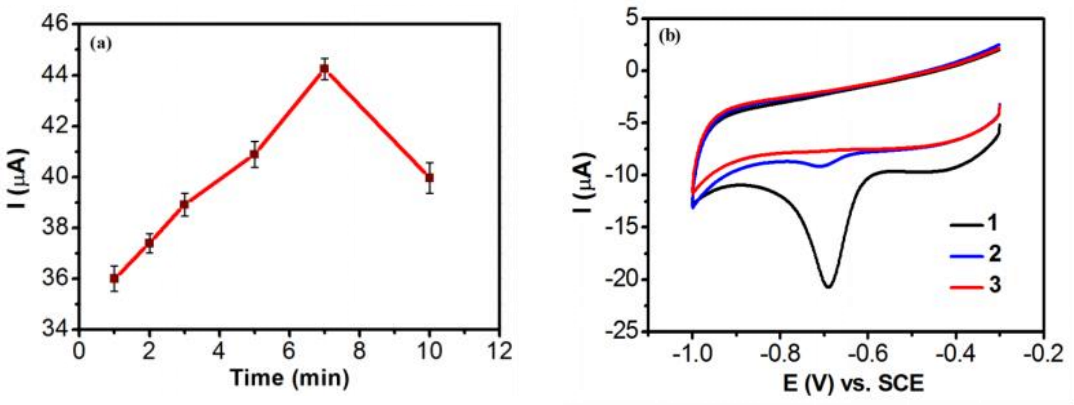

Figure 4-9. Peak currents recorded following various immersion periods in 100 μM *p*-NP for **(a)** A-GCE and memory effects recorded in PBS in the absence of *p*-NP following cycling in the presence of 100 μM *p*-NP **(b)**.

It is evident in both cases that the current becomes higher on increasing the immersion period before the voltammograms are recorded. As depicted in Figure 4-9(a), the optimum immersion period is approximately 7 min for the A-GCE, and the memory effect can be seen in Figure 4.9(b). In this case, the A-GCE was immersed in 100 μM *p*-NP for a period of time, then rinsed in deionised water and the subsequent CV curves were recorded in the absence of *p*-NP, with a fresh buffer solution being used for each CV experiment. Clear evidence for the accumulation of *p*-NP can be seen in Figure 4-9(b) with a significant reduction wave indicating the presence of *p*-NP for the first cycle, and a somewhat lower peak current for the second cycle. The corresponding experiments for the A-GCE/Bi are presented in Figure 4-10(a) and (b) and again adsorption is evident. However, the optimum accumulation time is slightly longer at 8 min, which may indicate a somewhat slower accumulation process at the bismuth dendrite modified surface. Nevertheless, there is clear evidence in Figure 4-10(b) that *p*-NP is accumulated at the surface, with a prominent peak in the phosphate solution for the first cycle and smaller peaks following the second, third and fourth cycles.

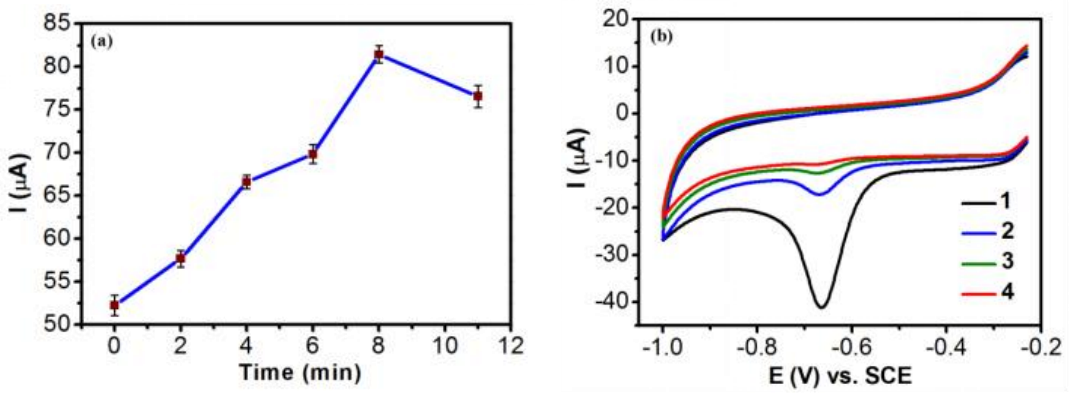

Figure 4-10. Peak currents recorded following various immersion periods in 100 μM *p*-NP for A-GCE/Bi **(a)** and memory effects recorded in PBS in the absence of *p*-NP following cycling in the presence of 100 μM *p*-NP **(b)**.

4.3.7 Influence of solution pH

As shown in Scheme 4-1, the electrochemical reduction of *p*-NP is accompanied by the transfer of protons. Therefore, the influence of the pH of the electrolyte on the reduction of *p*-NP was studied at both the A-GCE and A-GCE/Bi, Figure 4-11 and Figure 4-12.

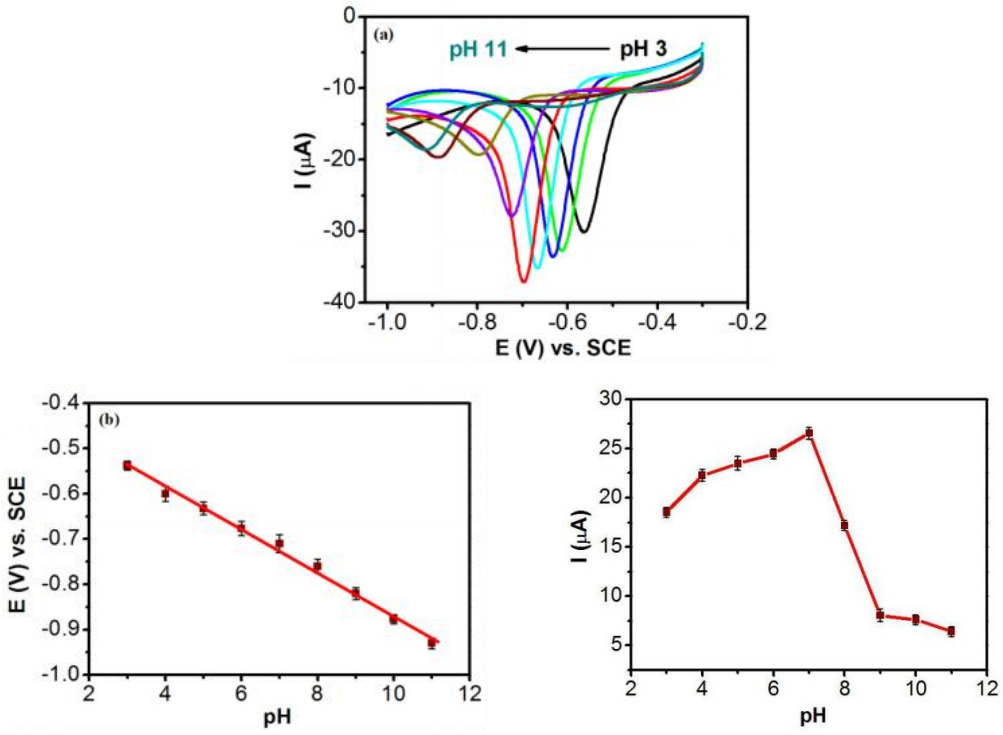

Figure 4.11. DPV recorded as a function of pH in 100 μM *p*-NP for A-GCE **(a)** and peak potential plotted as a function of pH **(b)** and peak current plotted as a function of pH **(c)**.

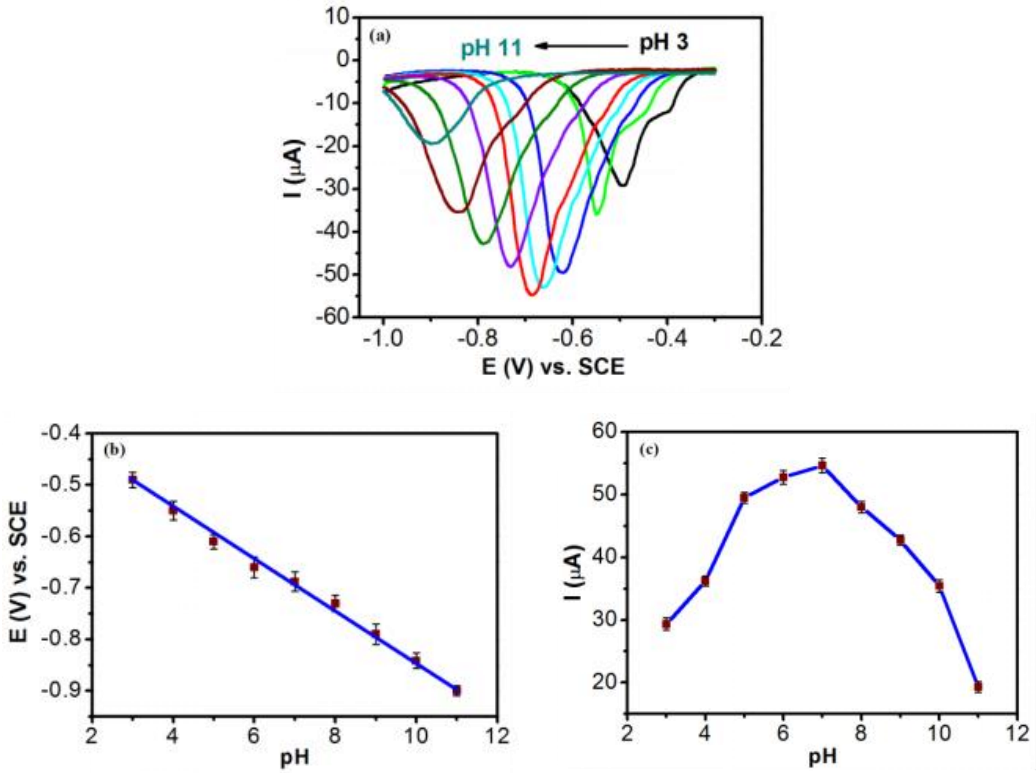

Figure 4.12. DPV recorded as a function of pH in 100 μM *p*-NP for A-GCE/Bi **(a)** and peak potential plotted as a function of pH **(b)** and peak current plotted as a function of pH **(c)**.

It was found that the pH had a significant influence on the reduction peak potential as shown in Figure 4-11 (a) for A-GCE and in Figure 4-12 (a) for A-GCE/Bi, with the peak potential shifting to lower potentials on increasing the pH of the solution. The optimum pH for both electrodes was about a pH of 7.0, Figure 4-11 (c) and 4-12 (c), while lower peak currents were evident at more acidic and alkaline pH values. On plotting the peak potential as a function of the pH (Figure 4-11 (b) and 4-12 (b)) linear plots were obtained, and the linear regression equations were deduced as E_p = –0.047 pH – 0.39 (R^2 = 0.98) for the A-GCE and E_p = –0.049 pH – 0.35 (R^2 = 0.99) for the A-GCE-Bi. These slopes are in reasonable agreement with the Nernst equation, where at 298 K, the theoretical slope is predicted as –0.0591 V/pH for the transfer of equal numbers of protons and electrons, Scheme 4-1.

4.3.8 Study on performance of sensor

The performance of A-GCE and A-GCE/Bi in the electrochemical detection of *p*-NP from 0.005 to 170 µM is illustrated in Figure 4-13 and Figure 4-14. Here, the data were recorded using DPV. The voltammograms are depicted in Figure 4-13(a,c) and 4-14(a,c) for the A-GCE and A-GCE/Bi, respectively. In both cases, the peak potentials remain essentially constant and independent of the concentration, while the peak current increases with increasing concentrations of *p*-NP.

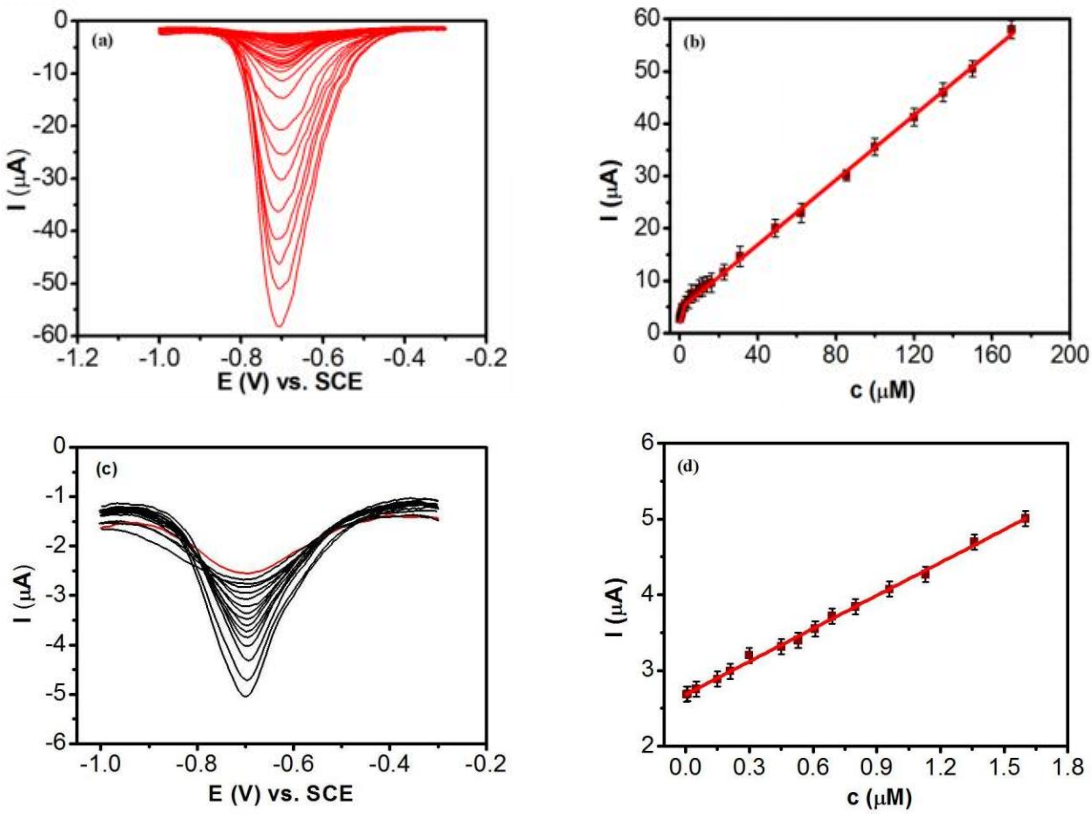

Figure 4-13. DPVs recorded as a function of concentration from 0.005 to 170 µM *p*-NP for **(a)** A-GCE, peak current plotted as a function of concentration for **(b)** A-GCE, from 0.005 to 1.6 µM *p*-NP for **(c)** A-GCE and peak current plotted as a function of lower concentrations for **(d)** A-GCE.

On plotting the peak current as a function of the concentration, linear calibration curves were obtained. The linear regression equation for the A-GCE/Bi was deduced as, I_p(µA) = 0.47 c(µM) + 5.75 (R^2 = 0.996) from 1.6 to 170 µM (Figure 4-14(b)), while with lower concentrations from 0.005 to 1.6 µM, the linear regression equation became,

I_p(μA) = 2.06 c(μM) + 1.81 (R^2 = 0.994), Figure 4-14(d) indicating a much higher gradient (2.06 μA $μM^{-1}$ or 29.4 μA $μM^{-1}$ cm^{-2}). Using the well-known expression where LOD = $3S_b$/sensitivity (S_b represents the standard deviation of the baseline), the LOD was computed as 0.18 nM. Similar results were obtained for the A-GCE, with the LOD estimated as 0.32 nM. The linear regression at higher concentrations, from 1.6 to 170 μM, was deduced as I_p(μA) = 0.323 c(μM) + 4.856, (R^2 = 0.999), Figure 4-13(b), while at lower concentrations, from 0.005 to 1.6 μM, the linear regression was obtained as, I_p (μA) = 1.4527 c(μM) + 2.68 (R^2 = 0.9976), Figure 4-13(d).

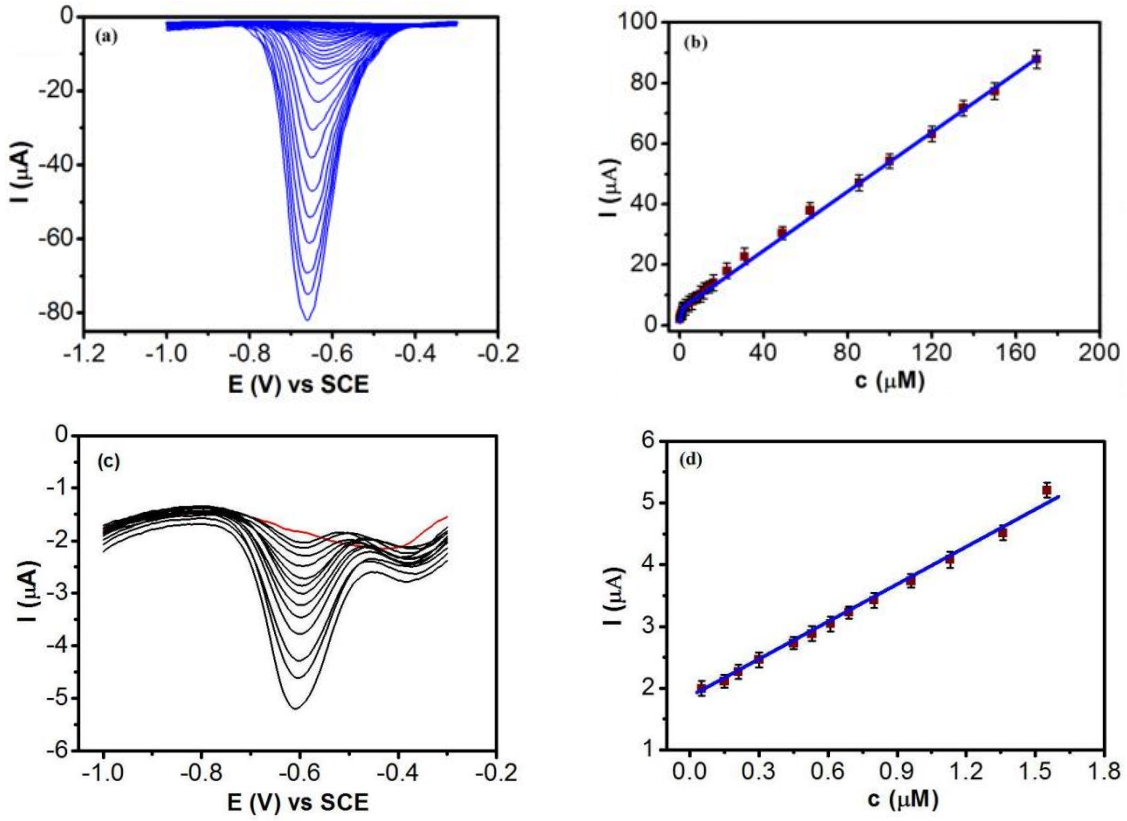

Figure 4-14. DPVs recorded as a function of concentration from 0.005 to 170 μM *p*-NP for A-GCE/Bi **(a),** peak current plotted as a function of concentration **(b),** from 0.005 to 1.6 μM *p*-NP for **(c)** A-GCE/Bi and peak current plotted as a function of lower concentrations **(c)**.

As illustrated in Table 4-2, where the linear regions and LOD values are presented for a variety of recently reported sensors for the detection of *p*-NP, this simple activated GCE and the activated GCE with bismuth dendrites compare very well. The typical concentrations of *p*-NP in aquatic environments can vary from 0.43 μg/L in rivers [3] to

concentrations ranging from 0.22 –1.65 μg/L in snow covered regions [30]. Therefore, the LOD of 0.18 nM obtained for the A-GCE/Bi, coupled with its good sensitivity of 2.06 μA μM $^{-1}$ makes it a suitable sensor for these environments and the detection of *p*-NP in the nM concentration range.

Table 4-2. Comparison with recently reported sensors for the detection of *p*-NP

Electrode materials	Technique	LOD (nM)	Linear Range (μM)	Reference
L-Cys/Nd_2O_3/rGO/GCE	SWV	20	0.05–8 10–50	[31]
Carboxymethylcellulose/ sulfated polyaniline/GCE	DPV	53	0.05–100	[32]
polyspirofluorene film/GCE	DPV	10	0.1–120	[33]
rGO-$NiCo_2O_4$/aminopropyl -triethoxysilane/GCE	DPV	5	0.005–5	[34]
AgNPs/GCE	DPV	15	0.1–350	[35]
$CeMoSe_2$/GCE	LSV	3.5	0.04–280 300–1980	[27]
Nanoparticle GC film	CV	230	0.5–3.0 3–3000	[36]
Ni_3Se_4/rGO/ITO	DPV	17.1	0.05–5 5–200	[37]
Pyridine diketopyrrolopyrrole/ GO/GCE	DPV	100	0.5–50 50–163	[38]
CeFeP/GCE	DPV	10	0.1–50	[16]
A-GCE	DPV	0.32	0.005–1.6 1.6–170	This
A-GCE/Bi	DPV	0.18	0.005–1.6 1.6–170	Work

4.3.9 Evaluation of reproducibility, selectivity and stability

The reproducibility of the A-GCE, GCE/Bi and A-GCE/Bi as sensors is summarised in Table 4-3. These data were recorded in a neutral and buffered 100 μM *p*-NP solution. Very good reproducibility is evident with all three sensors, with RSD values varying between 1.53 and 3.33%. It is also evident from this table that the A-GCE/Bi has the lowest error, with the RSD at the relatively low value of 1.53%.

Table 4-3. Reproducibility of GCE/Bi, A-GCE and A-GCE/Bi in the detection of *p*-NP (n = 5).

100 μM *p*-NP	Peak Current (μA)					Mean (n = 5)	RSD (%) (n = 5)
	1	2	3	4	5		
GCE/Bi	15.9	14.9	15.5	14.6	15.2	15.22 ± 0.51	3.33
A-GCE	37.8	35.9	36.7	37.5	36.8	36.74 ± 0.73	1.98
A-GCE/Bi	56.3	55.8	54.9	54.1	55.5	55.32 ± 0.85	1.53

The selectivity of the A-GCE/Bi sensor is represented in Figure 4-15(a) and the data are listed in Table 4-4, where the peak current recorded for 100 μM *p*-NP is designated as I_0 and the current recorded in the presence of the interferent is I with a value of unity indicating no interference. In these experiments, a 100 μM solution of *p*-NP in the presence of a 10-fold excess of the interferents was employed, except for ortho-nitrophenol (*o*-NP) and the nitro-based drug metronidazole (MTZ), where a 1:1 ratio was maintained. These two compounds were maintained at 100 μM. Very good selectivity can be seen in the presence of acetates, sulfates, nitrates, and carbonates. Likewise good selectivity is seen on the addition of hydrocortisone (HC), ascorbic acid (AA) and glucose (Glu). Nevertheless, some interference is evident with *o*-NP and MTZ, as shown in Figure 4-15 (b) and (c), respectively. This is not surprising as these two nitro-based compounds can be electrochemically reduced, and the reduction process involves the conversion of the nitro group to a hydroxylamine group.

The selectivity was further explored using a spiking and recovery approach, where a known amount of *p*-NP was added and then the sensors were employed to determine the concentration of *p*-NP in the sample. Both deionised water and tap water were employed and the results are summarised in Table 4-5. Good recovery, varying from 96.5 to 106.7%, was achieved with the A-GCE/Bi with added concentrations of 3, 6 and 10 μM *p*-NP.

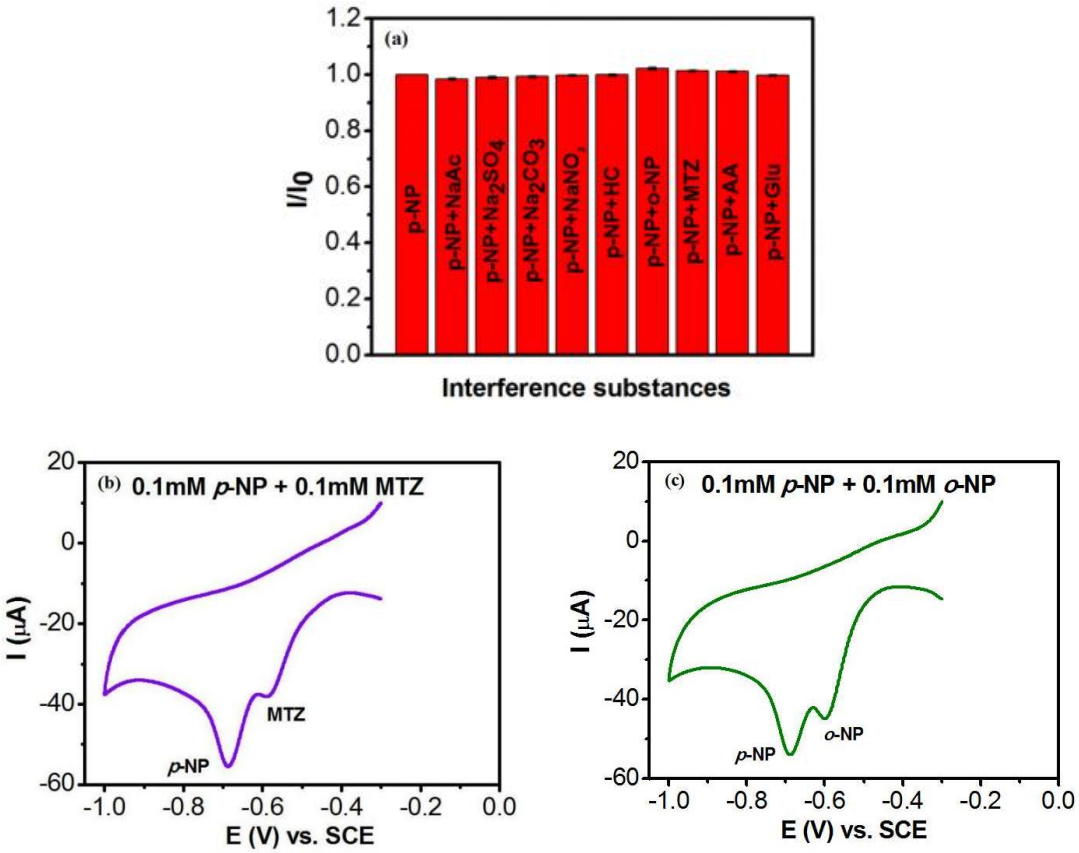

Figure 4-15. (a) Selectivity, I/I_0, for A-GCE/Bi in the presence of different interference substances, **(b)** CV recorded for A-GCE/Bi in 100 μM *p*-NP and 100 μM MTZ and **(c)** CV recorded for A-GCE/Bi in 100 μM *p*-NP and 100 μM *o*-NP.

Table 4-4. The effect of the interference on the detection of *p*-NP (n = 3).

Samples	Mean of I/I_0	RSD (%)
p-NP	1	—
p-NP + NaAc	0.9841 ± 0.0091	0.91
p-NP + Na_2SO_4	0.9904 ± 0.0092	0.93
p-NP + Na_2CO_3	0.9933 ± 0.0088	0.89
p-NP + $NaNO_3$	0.9976 ± 0.0085	0.85
p-NP + HC	0.9988 ± 0.0093	0.93
p-NP + *o*-NP	1.0323 ± 0.013	1.26
p-NP + MTZ	1.0237 ± 0.012	1.17
p-NP + AA	1.0112 ± 0.0092	0.91
p-NP + Glu	0.9977 ± 0.0095	0.96

Table 4-5. Determination of *p*-NP in deionised and tap water using A-GCE and A-GCE/Bi (n = 3).

Sensor	Sample	Added/ μM	Found/ μM	Recovery
A-GCE	Deionised water	3.0	3.18 (±0.11)	106.0%
		6.0	6.22 (±0.23)	103.7%
		10.0	9.75 (±0.18)	97.5%
A-GCE	Tap water	3.0	2.89 (±0.087)	96.3%
		6.0	6.55 (±0.18)	105.3%
		10.0	9.95 (±0.23)	99.5%
A-GCE-Bi	Deionised water	3.0	3.14 (±0.082)	104.7%
		6.0	5.87 (±0.15)	97.8%
		10.0	10.33 (±0.31)	103.3%
A-GCE-Bi	Tap water	3.0	3.20 (±0.093)	106.7%
		6.0	5.79 (±0.19)	96.5%
		10.0	9.86 (±0.22)	98.6%

The stability of the A-GCE/Bi is illustrated in Figure 4-16, where the peak current is shown as a function of the cycle number for both a stagnant solution and an agitated solution. For comparative purposes, data for the A-GCE are also shown. In both cases very good stability is observed with little change in the peak current over 50 cycles.

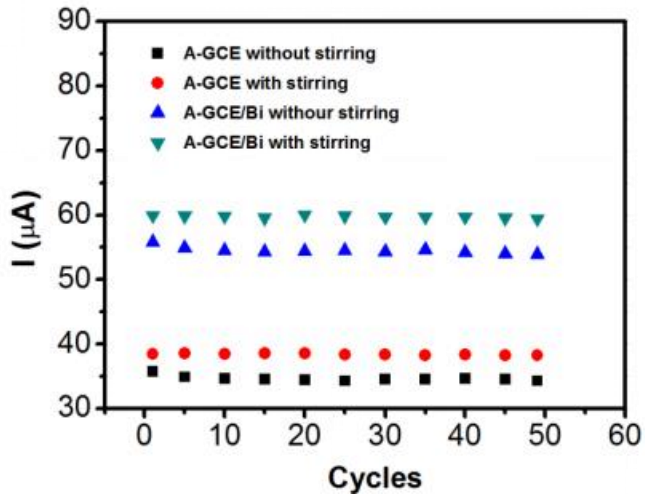

Figure 4-16. Peak current plotted as a function of cycle number for A-GCE and A-GCE/Bi with and without stirring in 100 μM *p*-NP.

4.3.10 Evaluation of regeneration

One of the advantages of decorating the A-GCE with bismuth dendrites is that the bismuth can be easily oxidised and removed from the sensor, and this can be later followed by the deposition of new and fresh dendrites of bismuth at the A-GCE. In order to explore the potential of this regeneration step, the bismuth was oxidised at a potential of 0.60 V for 10 min and then a fresh layer of bismuth was electrodeposited from the acidified 1.0 mM $Bi(NO_3)_3$ solution. The newly regenerated A-GCE/Bi was then used in the detection of 100 μM *p*-NP. These steps were repeated a total of five times and the corresponding data are shown in Figure 4-17 and Table 4-6. Here it is evident that the five voltammograms are very similar, giving nearly identical peak potentials followed by the peak currents with RSD of 3.36% lower than 5%. This clearly shows that the A-GCE/Bi sensor can be easily and readily regenerated, and this may be very relevant in complex environments where the sensor may be poisoned.

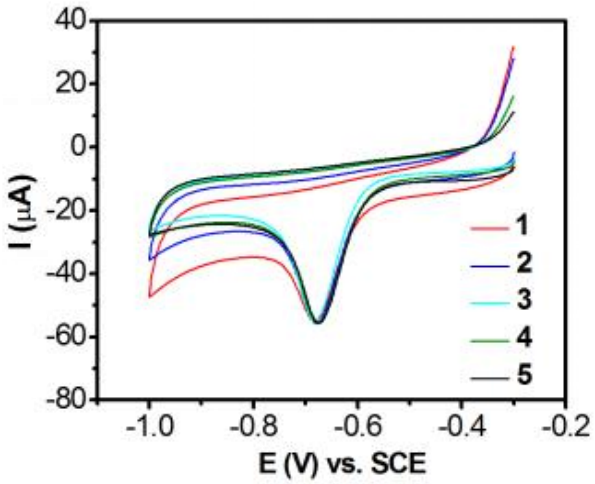

Figure 4-17. CVs recorded for A-GCE/Bi in 100 μM *p*-NP following removal and deposition of Bi dendrites.

Table 4-6. The peak currents following removal and deposition of Bi dendrites (n = 5).

Electrode	Peak currents (μA)						
	1	2	3	4	5	Mean	RSD (%)
A-GCE/Bi	40.31	43.94	43.27	41.97	41.65	42.23 ± 1.42	3.36

4.4 Conclusions

In this chapter, we show that a simple activated glassy carbon electrode combined with a 400 s period for the electrodeposition of bismuth can be used to give the effective detection of *p*-NP in aqueous systems. An impressive limit of detection of 0.18 nM and sensitivity of 29.4 μA μM $^{-1}$ cm^{-2} coupled with very good reproducibility, repeatability, recovery in water and acceptable selectivity was achieved with this simple approach. The good detection in the presence of the bismuth dendrites was attributed to enhanced adsorption of the *p*-NP. While various electrocatalytic materials have been synthesised and then drop-cast onto GCE to form a myriad of electrochemical sensors, this simple approach avoids the need for drop-casting. Moreover, the bismuth dendrites can be easily regenerated making this combination suitable for those complex media that may otherwise contaminate or poison the electrode surface.

4.5 References

[1] Li, J.; Kuang, D.; Feng, Y.; Zhang, F.; Xu, Z.; Liu, M. A graphene oxide-based electrochemical sensor for sensitive determination of 4-nitrophenol. *J Hazard Mater*. **2012**, *201–202*, 250–259, doi: 10.1016/j.jhazmat.2011.11.076.

[2] Yin, H.; Zhou, Y.; Ai, S.; Liu, X.; Zhu, L.;Lu, L. Electrochemical oxidative determination of 4-nitrophenol based on a glassy carbon electrode modified with a hydroxyapatite nanopowder. *Microchimica Acta*. **2010**, *169*, 87–92, doi:

10.1007/s00604-010-0309-1.

[3] Peñalver, R.; Jacobs, M. R.; Hegarty, S.; Regan, F. Assessment of anthropogenic pollution by monitoring occurrence and distribution of chemicals in the river Liffey in Dublin. *Environ. Sci. Pollut. Res*. **2021**, *28*, 53754–53766, doi: 10.1007/s11356-021-14508-y.

[4] Kulkarni, M.; Chaudhari, A. Microbial remediation of nitro-aromatic compounds: An overview. *J Environ Manage*. **2007**, *85*, 496–512, doi: 10.1016/j.jenvman.2007.06.009.

[5] Dai, R.; Chen, J.; Lin, J.; Xiao, S.; Chen, S.; Deng, Y. Reduction of nitro phenols using nitroreductase from E. coli in the presence of NADH. *J Hazard Mater*. **2009**, 170, 141–143, doi: 10.1016/j.jhazmat.2009.04.122.

[6] Cáceres, T.; Venkateswarlu, K.; Megharaj, M. Acute toxicity of the insecticide methyl parathion and its hydrolytic product p-nitrophenol to the native Australian cladoceran Daphnia carinata. *Ecotoxicology*. **2019**, *28*, 680–685, doi: doi.org/10.1007/s10646-019-02064-8.

[7] Yen, J. H.; Lin, K. H.; Wang, Y. S. Acute lethal toxicity of environmental pollutants to aquatic organisms. *Ecotoxicol Environ Saf*. **2002**, *52*, 113–116, doi: 10.1006/eesa.2002.2167.

[8] Yan, Z.; Wang, W.; Zhou, J.; Yi, X.; Zhang, J.; Wang, X.; Liu, Z. Screening of high phytotoxicity priority pollutants and their ecological risk assessment in China's surface waters. *Chemosphere*. **2015**, *128*, 28–35, doi: 10.1016/j.chemosphere.2015.01.015.

[9] Peñalver, A.; Pocurull, E.; Borrull, F.; Marcé, R. M. Solid-phase microextraction coupled to high-performance liquid chromatography to determine phenolic compounds in water samples. *J Chromatogr A*. **2002**, *953*, 79–87, doi: 10.1016/S0021-9673(02)00113-9.

[10] Zhang, P. P.; Shi, Z. G.; Feng, Y. Q. Determination of phenols in environmental water samples by two-step liquid-phase microextraction coupled with high performance liquid chromatography. *Talanta*. **2011**, *85*, 2581–2586, doi: 10.1016/j.talanta.2011.08.021.

[11] Sobhi, H. R.; Esrafili, A.; Farahani, H.; Gholami, M.; Baneshi, M. M. Simultaneous derivatization and extraction of nitrophenols in soil and rain samples

using modified hollow-fiber liquid phase microextraction followed by gas chromatography-mass spectrometry, *Environ. Monit. Assess*. **2013**, *185*, 9055–9065, doi:10.1007/s10661-013-3235-y.

[12] Niazi, A.; Yazdanipour, A. Spectrophotometric simultaneous determination of nitrophenol isomers by orthogonal signal correction and partial least squares, *J Hazard Mater*. **2007**, *146*, 421–427, doi: 10.1016/j.jhazmat.2007.03.063.

[13] Krishnamoorthy, R.; Muthumalai, K.; Nagaraja, T.; Rajendrakumar, R.T.; Das, S. R. Chemically eExfoliated titanium carbide MXene for highly sensitive electrochemical sensors for detection of 4-nitrophenols in drinking water, *ACS Omega*. **2022**, *7*, 42644–42654, doi: 10.1021/acsomega.2c06505.

[14] Rana, D. S.; Kalia, S.; Kumar, R.; Thakur, N.; Singh, R. K.; Singh, D. Two-dimensional layered reduced graphene oxide-tungsten disulphide nanocomposite for highly sensitive and selective determination of para nitrophenol, *Environ Nanotechnol Monit Manag*. **2022**, *18*, 100724, doi: 10.1016/j.enmm.2022.100724.

[15] Gudipati, N. S.; Vanjari, G. S.; Korutla, S.; Tammineni, R. R.; Challapalli, S. Electrochemical detection of 4-nitrophenol on nanostructured CuBi2O4 with plausible mechanism supported by DFT calculations. *J. Environ Chem Eng*. **2022**, *10*, 108758, doi: 10.1016/j.jece.2022.108758.

[16] Gopi, S.; Yun, K. Cerium-iron phosphate nano flower bifunctional electrocatalyst for efficient electrochemical detection and catalytic reduction of hazardous 4-nitrophenol. *J Environ Chem Eng*. **2022**, *10*, 108938, doi: 10.1016/j.jece.2022.108938.

[17] Healy, B.; Rizzuto, F.; de Rose, M.; Yu, T.; Breslin, C. B. Electrochemical determination of acetaminophen at a carbon electrode modified in the presence of β-cyclodextrin: role of the activated glassy carbon and the electropolymerised β-cyclodextrin, *J. Solid State Electrochem*. **2021**, *25*, 2599–2609, doi: 10.1007/s10008-021-05044-3.

[18] Yu, T.; Fenelon, O.; Herdman, K. M.; Breslin, C. B. The Electrochemical detection of 4-chloro-2-methylphenoxyacetic acid (MCPA) using a simple activated glassy carbon electrode. *J. Electrochem. Soc*. **2022**, *169*, 037514, doi: 10.1149/1945-7111/ac5c03.

[19] Faraezi, S.; Khan, M. S.; Monira, F. Z.; al Mamun, A.; Akter, T.; al Mamun, M.; Rabbani, M. M.; Uddin, J.; Ahammad, A. J. S. Sensitivity control of hydroquinone and catechol at poly(brilliant cresyl blue)-modified GCE by varying activation conditions of the GCE: An experimental and computational study, *Chem. Eng*. **2022**, *6*, 7, doi: 10.3390/chemengineering6020027.

[20] Lu, Y.; Bao, C.; Zou, J.; Xiao, J.; Zhong, W.; Gao, Y. Highly sensitive electrochemical sensor for sunset yellow based on electrochemically activated glassy carbon electrode, *Molecules*. **2022**, *27*, 5221, doi: 10.3390/molecules27165221.

[21] Rana, A.; Baig, N.; Saleh, T. A. Electrochemically pretreated carbon electrodes and their electroanalytical applications – A review. *J. Electroanal. Chem*. **2019**, *833*, 313–332, doi: 10.1016/j.jelechem.2018.12.019.

[22] Yu, T.; Glennon, L.; Fenelon, O.; Breslin, C. B. Electrodeposition of bismuth at a graphene modified carbon electrode and its application as an easily regenerated sensor for the electrochemical determination of the antimicrobial drug metronidazole. *Talanta*. **2023**, *251*, 123758, doi: 10.1016/j.talanta.2022.123758.

[23] Królicka, A.; Pauliukaite, R.; Svancara, I.; Metelka, R.; Bobrowski, A.; Norkus, E.; Kalcher, K.; Vytřas, K. Bismuth-film-plated carbon paste electrodes. *Electrochem. Commun*. **2002**, *4*, 193–196, doi: 10.1016/S1388-2481(01)00301-0.

[24] Švancara, I.; Baldrianová, L.; Tesařová, E.; Hočevar, S. B.; Elsuccary, S. A. A.; Economou, A.; Sotiropoulos, S.; Ogorevc, B.; Vytřas, K. Recent advances in anodic stripping voltammetry with bismuth-modified carbon paste electrodes. *Electroanalysis*. **2006**, *18*, 177–185, doi: 10.1002/elan.200503391.

[25] Zou, Z.; Jang, A.; MacKnight, E.; Wu, P. M.; Do, J.; Bishop, P. L.; Ahn, C. H. Environmentally friendly disposable sensors with microfabricated on-chip planar bismuth electrode for in situ heavy metal ions measurement. *Sens. Actuators B Chem*. **2008**, *134*, 18–24, doi: 10.1016/j.snb.2008.04.005.

[26] Arulraj, A. D.; Vijayan, M.; Vasantha, V. S. Highly selective and sensitive simple sensor based on electrochemically treated nano polypyrrole-sodium dodecyl sulphate film for the detection of para-nitrophenol. *Anal. Chim. Acta,* **2015**, *899*, 66–74, doi: 10.1016/j.aca.2015.09.055.

[27] Ramki, S.; Sukanya, R.; Chen, S. M.; Sakthivel, M.; Wang, J. Y. Simple

hydrothermal synthesis of defective $CeMoSe_2$ dendrites as an effective electrocatalyst for the electrochemical sensing of 4-nitrophenol in water samples. *New J. Chem*. **2019**, *43*, 17200–17210, doi: 10.1039/c9nj03891d.

[28] Sundaresan, R.; Mariyappan, V.; Chen, S. M.; Ramachandran, B.; Paulsamy, R.; Rasu, R. Construction of an electrochemical sensor towards environmental hazardous 4-nitrophenol based on $Nd(OH)_3$-embedded VSe_2 nanocomposite. *Environmental Sci. Pollut. Res*. **2023**, doi: 10.1007/s11356-023-25688-0.

[29] Čėnas, N.; Nemeikaitė-Čėnienė, A.; Kosychova, L. Single- and two-electron reduction of nitroaromatic compounds by flavoenzymes: Mechanisms and implications for cytotoxicity. *Int. J. Mol. Sci*. **2021**, *22*, 8534, doi: doi.org/10.3390/ijms22168534.

[30] Levshina, S. Petroleum products and phenols in snow cover in Khabarovsk, Southern Russian far east, *Water Air Soil Pollut*. **2012**, *223*, 3553–3563, doi: https://doi.org/10.1007/s11270-012-1136-2.

[31] Sabir, Z.; Akhtar, M.; Zulfiqar, S.; Zafar, S.; Agboola, P. O.; Haider, S.; Ragab, S. A.; Warsi, M. F.; Shakir, I. L-Cysteine functionalized Nd_2O_3/rGO modified glassy carbon electrode: A new sensing strategy for the rapid, sensitive and simultaneous detection of toxic nitrophenol isomers. *Synth Met*. **2021**, *277*, 116774, doi: 10.1016/j.synthmet.2021.116774.

[32] Alamry, K. A.; Khan, A.; Hussein, M. A.; Alfaifi, S. Y. Sensitive electrochemical detection of toxic nitro-phenol in real environmental samples using enzymeless oxidized-carboxymethyl cellulose-sulfate/sulfated polyaniline composite based electrode. *Microchem. J*. **2022**, *172*, 106902, https://doi.org/10.1016/j.microc.2021.106902.

[33] Fang, Y.; Wang, D.; Lv, X.; Xu, X.; Zhou, H.; Liu, P.; Cui, B.; Wang, L. Simultaneous electrochemical determination of nitrophenol isomers Based on spirofluorene - based microporous polymer film modified electrodes through one-step electropolymerization strategy, *Sens. Actuators B Chem*. **2021**, *333*, 129568, doi: 10.1016/j.snb.2021.129568.

[34] Khan, M. Z. H.; Zhu, J.; Liu, X. Reduced graphene oxide-conjugated urchin-like $NiCo_2O_4$ nanostructures for individual detection of o-nitro and p-amino phenol, *ACS Omega*. **2019**, *4*, 11433–11439, doi: 10.1021/acsomega.9b00804.

[35] Karuppiah, C.; Palanisamy, S.; Chen, S. M.; Emmanuel, R.; Ali, M. A.; Muthukrishnan, P.; Prakash, P.; Al-Hemaid, F. M. A. Green biosynthesis of silver nanoparticles and nanomolar detection of p-nitrophenol, J. Solid State Electrochem. **2014**, *18*, 1847–1854, doi: 10.1007/s10008-014-2425-z.

[36] Wang, P.; Xiao, J.; Liao, A.; Li, P.; Guo, M.; Xia, Y.; Li, Z.; Jiang, X.; Huang, W. Electrochemical determination of 4-nitrophenol using uniform nanoparticle film electrode of glass carbon fabricated facilely by square wave potential pulses, *Electrochim. Acta,* **2015**, *176*, 448–455, doi: 10.1016/j.electacta.2015.07.054.

[37] Wang, S.; Zhang, T.; Jia, L.; Yang, P.; He, P.; Xiao, F.; Zhou, P.; Wang, Y.; Wang, X. Electrochemical reduction of nickel selenide/reduced graphene oxide nanocomposites: Highly sensitive detection of 4-nitrophenol. *Microchem. J*. **2023**, *186*, 108252, doi: 10.1016/j.microc.2022.108252.

[38] Jia, L.; Hao, J.; Wang, S.; Yang, L.; Liu, K. Sensitive detection of 4-nitrophenol based on pyridine diketopyrrolopyrrole-functionalized graphene oxide direct electrochemical sensor. *RSC Adv*. **2023**, *13*, 2392–2401, doi: 10.1039/d2ra07239d.

Chapter 5

Developing a Sensitive Electrochemical Sensor for the Detection of Metronidazole (MTZ) through a Sequential Electrodeposition of Graphene and Bismuth on GCE

5.1 Introduction

Metronidazole (2-methyl-5-nitroimidazole-1-ethanol) (MTZ) is an antibiotic. As a class of antibacterial drugs used to kill or inhibit bacterial growth, antibiotics have been widely employed for decades. Metronidazole belongs to the nitroimidazole family of antibiotics. It has been commonly employed to treat the infections caused by bacteria including helicobacter pylori [1], giardia lamblia and trichomonas vaginalis [2]. In addition, metronidazole has been utilised in the treatment of oral and dental infections, respiratory tract infections and Crohn´s disease in recent years [3]. Moreover, it is confirmed that metronidazole is considered an effective antimicrobial agent against anaerobic bacteria, with added antiparasitic activities, thereby it is applied popularly in the treatment of infections for both humans [3] and animals [2]. However, metronidazole displays genotoxic and mutagenic side effects [3], thus its accumulation in the aquatic environment is particularly worrying as it may be harmful to both humans and aquatic life. Besides that, metronidazole is very soluble in water and shows very good stability, while its biodegradability, photodegradation, and hydrolytic decomposition ability are very poor, indicating that it can last for a long time in the aquatic environment. In fact, high levels of drugs, including MTZ, have been determined in water supply systems in urban areas [4] and these MTZ-contaminated sites face the risk of a surge in antimicrobial resistance. This issue has a direct impact on the Sustainable Development Goals of the United Nations on clean water and sanitation. Therefore, researchers are very interested in developing methods that can be used not only for the detection of metronidazole in biological media, but also for the determination of metronidazole in aquatic environment systems.

Compared with some standard analytical techniques for the determination of metronidazole, such as HPLC [5] and GC [6], the electrochemical sensors used to detect metronidazole exhibit some advantages, including simple operation and easy portability as well as little sample preparation, etc. Besides that, the electrochemical sensors are required to possess high sensitivity, selectivity, and good stability. Accordingly, the electrode surfaces are often modified by some functional composite to improve their

sensitivity, selectivity, and stability. So far, several electrode modification strategies have been employed to construct metronidazole sensors. Some carbon-based materials including carbon nanotubes [7], carbon fibres [8], diamond [9], and graphene [10], nanoparticles (NPs) including copper oxide NPs [11], silver NPs [12] and nickel manganous oxide NPs [13], etc. have been used as functional composites to modify the electrode surfaces to fabricate metronidazole sensors, which have delivered the impressive detection performance for metronidazole. Nevertheless, many of the modifiers need time-consuming synthetic procedures and the modified electrodes are prepared by drop cast methods raising stability concerns. Especially, there is little evidence to suggest that the surfaces can be easily regenerated or renewed.

According to the reports in the literature or the measurements in this work, metronidazole can be electrochemically reduced at the applied potential range of –0.4 V to –1.0 V vs. SCE. Thus, it was anticipated that the electrodeposition or electroplating of bismuth films may be suitable for the detection of metronidazole. Bismuth is a non-toxic element. The bismuth modified electrodes have been developed and suggest that metal bismuth is a good substitute for the well-known mercury electrodes, especially the dropping mercury electrode (DME) with a wide electrochemical window [14,15]. Recently, bismuth films have been applied successfully to the detection of heavy metal ions, using stripping voltammetry [16-18]. Moreover, bismuth films modified electrodes not only have achieved simultaneous determination of Cd(II) and Pb(II) ions [19,20], Cd(II), Zn(II) and Pb(II) ions [21], but also have been used in the electrochemical determination of nitrophenols [22,23]. However, bismuth film modified electrodes are rarely employed in the detection of pollutants in the environment.

In this chapter, a bismuth film was electrodeposited onto a graphene modified GCE to form a modified electrode, delivering a simple and effective electrochemical sensor for the determination of metronidazole. Furthermore, the developed sensor surface can be easily renewed by the simple oxidation and removal of the bismuth film, followed by its subsequent regeneration through electrochemical deposition.

5.2 Experimental section

The electrochemical experiments were conducted on a Solartron 1287 potentiostat coupled with a 1255 FRA and a CHI 760C electrochemical workstation for the preparation of the modified electrodes and CV, EIS and DPV measurements, respectively. SEM with a Hitachi S–3200–N microscope was employed for the surface morphology characterisation and an Oxford Instrument INCAz-act ESX was used for EDX studies to analyse the chemical composition of the modified electrodes.

A standard three-electrode system was used for the electrochemical measurements. In this experiment, four electrodes were utilized as working electrodes. First, bare GCE was polished and cleaned using the procedure described in Section 2.2.4; second, the electrode GCE/Bi was fabricated by the electrodeposition of bismuth film, Section 2.2.4.2; third, the electrode GCE/Gr was prepared by the electrodeposition of Gr, as described in Section 2.2.4.3; fourth, the combination of the electrodeposition of bismuth and Gr on GCE gives the electrode GCE/Gr/Bi, as represented in Section 2.2.4.6.

A stock solution of 4.0 mM MTZ was prepared in 0.1 M PBS at a pH of 7.0. The pH was varied between 3.0 and 13.0 by adding HNO_3 or NaOH to the 0.1 M PBS solution. Unless otherwise stated, the CV experiments were performed at a scan rate of 50 mV s^{-1}.

5.3 Results and Discussion

In this section, the formation, characterisation of the GCE/Gr, GCE/Bi and GCE/Gr/Bi electrodes, and their application in the electrochemical detection of MTZ are described and discussed.

5.3.1 Preparation of the bismuth film modified electrode

In order to prevent the formation of insoluble bismuth oxides/hydroxides, the Bi(III) solution was prepared in a pH solution of 1.5, thereby the reduction of Bi(III) at the GCE surface was carried out in acidified solution. The reduction process of Bi(III) can

be presented in Equation 5–1, where the reduction potential of Bi(III) is estimated to occur at 0.17 V vs. SCE for the concentration of 5.0 mM. Indeed, in the experiment, as displayed in Figure 5-1, it is seen that the reduction of Bi(III) begins at ca. –0.08 V vs. SCE to give rise to a unsymmetrical reduction wave corresponding to a peak potential centred at approximately –0.17 V vs. SCE. This peak potential gives an overpotential of approximately 0.34 V vs. SCE. The corresponding oxidation wave is evident with a peak potential at about –0.013 V vs. SCE, and this peak is more symmetrical as the deposited bismuth is oxidised.

$$Bi(III) + 3e^- \rightarrow Bi \qquad E = 0.215 + 0.0197 \log[Bi(III)] \qquad (5–1)$$

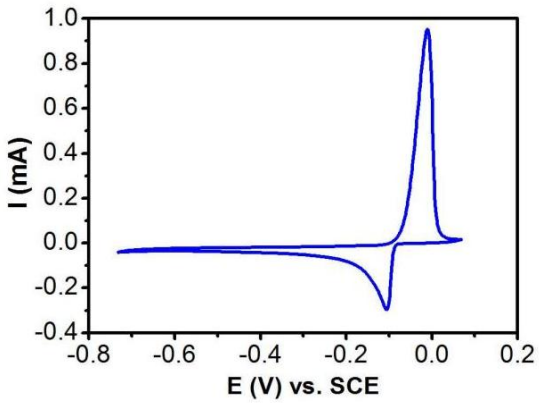

Figure 5-1. CV curve of bare GCE recorded in 5.0 mM $Bi(NO_3)_3$.

In addition, from Figure 5-1, it is also apparent that the upper potential is limited by the oxidation of the deposited bismuth which begins at a potential in the vicinity of –0.10 V vs. SCE. Accordingly, the CV curves of MTZ in PBS were recorded by cycling to an upper potential of –0.30 V vs. SCE to avoid the oxidation of bismuth film formed on the electrode surface (as the oxidation of the deposited bismuth begins at potential of –0.30 V vs. SCE when the electrode GCE/Bi is placed in MTZ at a pH 7.0).

5.3.2 Optimisation of experimental parameters for the modified electrode GCE/Bi

In order to obtain an electrode with the best performance, the influence of the deposition potential and time on the performance of the GCE/Bi electrode in the electrochemical detection of MTZ was investigated. As presented in Figure 5-2 (a), when the deposition

potential is varied from −0.8 to −1.0 V vs. SCE, the peak current of GCE/Bi for the detection of MTZ is increased, whereas at potentials lower than −1.0 V vs. SCE, the deposition of bismuth is less effective. This case is probably related to the competing hydrogen evolution reaction. Therefore, the optimum electrodeposition potential of Bi on the GCE surface is at −1.0 V vs. SCE with the short deposition time.

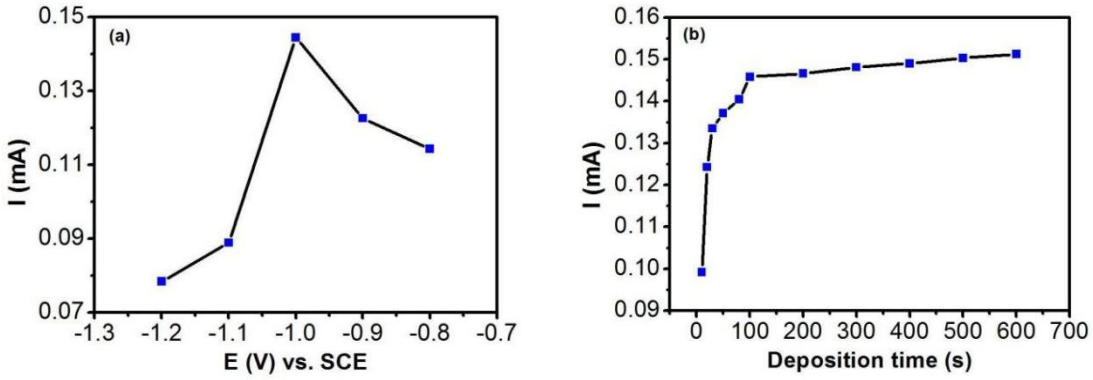

Figure 5-2. (a) Peak currents of the GCE/Bi electrode in 2.0 mM MTZ plotted as a function of the Bi deposition potentials (1.0 mM Bi(III) solution and deposition period of 100 s) and **(b)** peak currents of the GCE/Bi electrode in 2.0 mM MTZ plotted as a function of Bi deposition period at − 1.0 V vs. SCE in 1.0 mM Bi(III) solution.

The influence of the deposition time on the performance of the GCE/Bi electrode is illustrated in Figure 5-2(b). It is seen that in terms of both the detecting performance and fabrication time of the GCE/Bi electrode, the deposition time in the vicinity of 100 s gives rise to the optimum deposition period, while no further increase in the reduction current of MTZ is observed for higher deposition times. Furthermore, the electrochemical deposition of Bi at −1.0 V vs. SCE for 100 s results in a charge of $(2.670 \pm 0.003) \times 10^{-3}$ C. It is assumed that the charge is due to the reduction of Bi(III), and the competing reduction reactions are negligible, hereby approximately 1.93 μg of Bi is formed at the GCE surface based on the equation 5-2.

$$Q = nZF \qquad (5–2)$$

Where Q is the electricity quantity (C), n is the electron transfer number, Z is the

number of moles (mol) and F is the Faraday constant (96485 C mol^{-1}).

5.3.3 Influence of dissolved oxygen on the electrochemical detection of MTZ

It has been suggested that when the bismuth film modified electrodes are employed in the analysis of analytes, the removal of dissolved oxygen is not required [24]. Therefore, the influence of dissolved oxygen on the electrochemical detection of MTZ was studied by comparing deoxygenated solutions (deoxygenation for 20 min using high purity nitrogen gas), with non-deoxygenated solutions. For comparison, the unmodified GCE was also employed and representative voltammograms are presented for the two electrodes in Figure 5-3(a) and Figure 5-3(b), respectively.

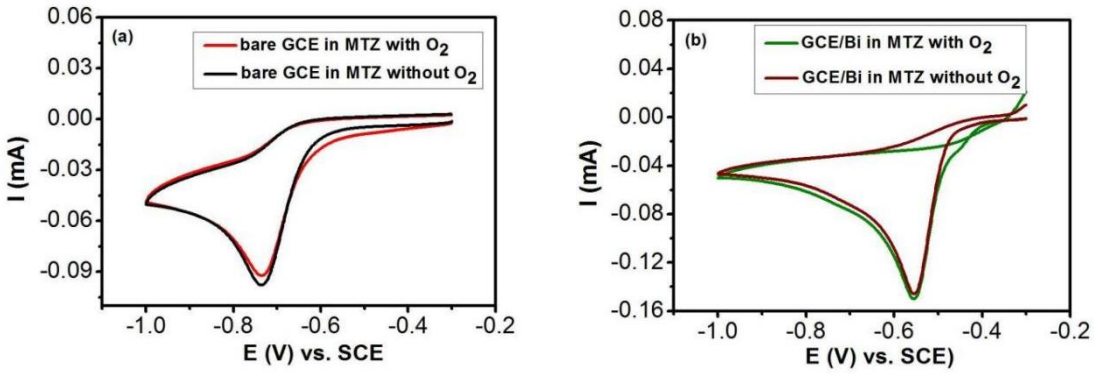

Figure 5-3. CV curves recorded at 50 mV s^{-1} of **(a)** unmodified GCE and **(b)** GCE/Bi in 2.0 mM MTZ (pH 7.0 PBS) with O_2 (non-deoxygenated) and without O_2 (deoxygenated) solutions.

The influence of the dissolved oxygen can be clearly seen with the unmodified GCE in Figure 5-3(a) with the clear onset of the reduction of oxygen at about –0.30 V vs. SCE. Furthermore, the peak current associated with the reduction of MTZ in oxygen containing solution is lower than that observed in the solution without oxygen, clearly highlighting the effect of the dissolved oxygen with the unmodifued GCE. On the other hand, the dissolved oxygen has less influence on the reduction of MTZ at the Bi modified electrode, as exhibited in Figure 5-3(b). The peak current is almost identical in the presence and absence of dissolved oxygen. However, there is some evidence that oxygen is reduced at the GCE/Bi electrode, and this appears as a pre-peak centred at

about –0.35 V vs. SCE before the onset of the MTZ reduction. This observation demonstrates that dissolved oxygen has little influence on the reduction peak current of the MTZ, hence all subsequent experiments were carried out in non-deoxygenated solutions, making them more suitable for real sample analysis at different aquatic sites.

5.3.4 Comparison of four electrodes for the electrochemical detection of MTZ

Under the optimal experimental conditions, three modified electrodes were prepared, they are GCE/Bi, GCE/Gr and GCE/Gr/Bi. Subsequently, their detection performance for MTZ were assessed and compared with that of unmodified GCE. The voltammograms of four electrodes in 0.1 mM MTZ were recorded and compared, as described in Figure 5-4, showing that the reduction of MTZ undergoes an irreversible reaction process, which is illustrated in Scheme 5.1.

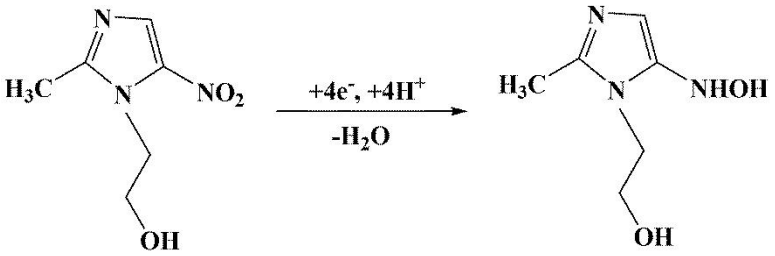

Scheme 5-1. Schematic illustrating the electrochemical reduction of MTZ, with the conversion of the –NO_2 to the –NHOH group.

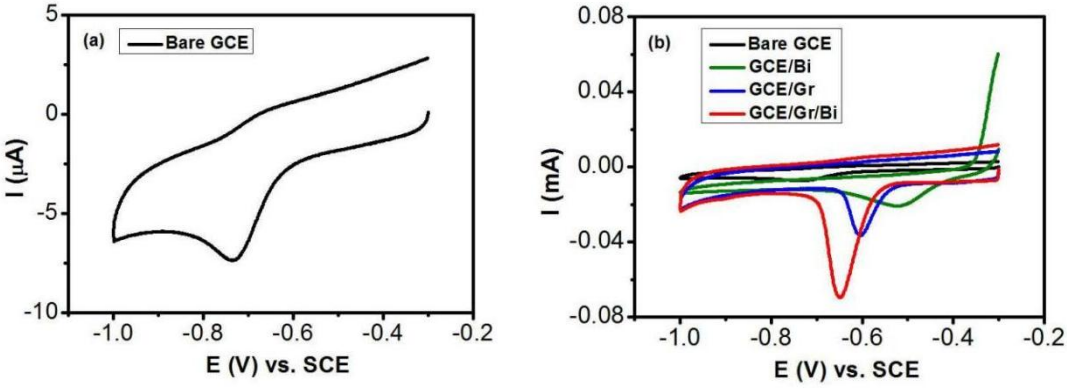

Figure 5-4. (a) CV curve of bare GCE and CV curves of bare GCE, GCE/Bi, GCE/Gr and GCE/Gr/Bi recorded in 0.1 mM MTZ in PBS (pH 7.0) at 60 mV s^{-1}.

By comparing the four electrodes in Figure 5-4, it is observed that for the unmodified GCE, the MTZ is reduced at an applied potential of –0.74 V vs. SCE accompanied by a very low peak current of 0.007 mA. After the GCE/Bi electrode was used, a considerable reduction in the overpotential is seen with a potential of –0.52 V vs. SCE while a clear increase in the peak current (0.02 mA) is observed. When the GCE/Gr electrode was employed, a further increase in the peak current of 0.037 mA at -0.61 V vs. SCE is seen. Impressively, the highest peak current is found with the GCE/Gr/Bi electrode, giving the peak potential at – 0.64 V vs. SCE and a peak current of 0.07 mA. Based on the comparison above, the highest peak current is achieved when the GCE is modified by the combination of Bi and the deposited Gr to form the GCE/Gr/Bi electrode. In addition, on comparing the GCE electrode with the GCE/Gr/Bi electrode, a 10-fold increase in the peak current is seen, clearly indicating that the GCE/Gr/Bi electrode has potential application in the electrochemical detection of MTZ.

5.3.5 Morphology characterisation of the modified electrodes

SEM, EDX and Mapping techniques were used to characterise the morphologies and composition of the GCE/Gr and GCE/Gr/Bi electrodes, as shown in Figure 5-5.

Figure 5-5(a) and (b) show SEM micrographs of the GCE/Gr electrode. The Gr sheets are clearly evident in the low magnification SEM micrograph, and the Gr sheets are well dispersed over the entire surface of the electrode, but with some evidence of aggregation at some sites. Such an observation is also evident in Figure 5-5(b) with some Gr sheets stacked. After the deposition of Bi for 100 s, as described in Figure 5-5(c) and (d) for the GCE/Gr/Bi electrode, the SEM micrographs exhibit the Bi deposited onto the Gr sheets, but also on the free GCE surface, with the Bi deposition adopting wire like deposits and also some larger nanoparticles.

Further, the EDX spectrum of the GCE/Gr/Bi electrode indicates the presence of Bi, C and O, clearly demonstrating that the Bi has been deposited at the surface of GCE, meanwhile, the presence of the oxygen is consistent with the oxygenated groups on the Gr, and possibly on the GCE. In addition, as show in Figure 5-5(f), the mapping data for Bi and C reveal that both the Bi and C are approximately evenly dispersed across the

surface of GCE.

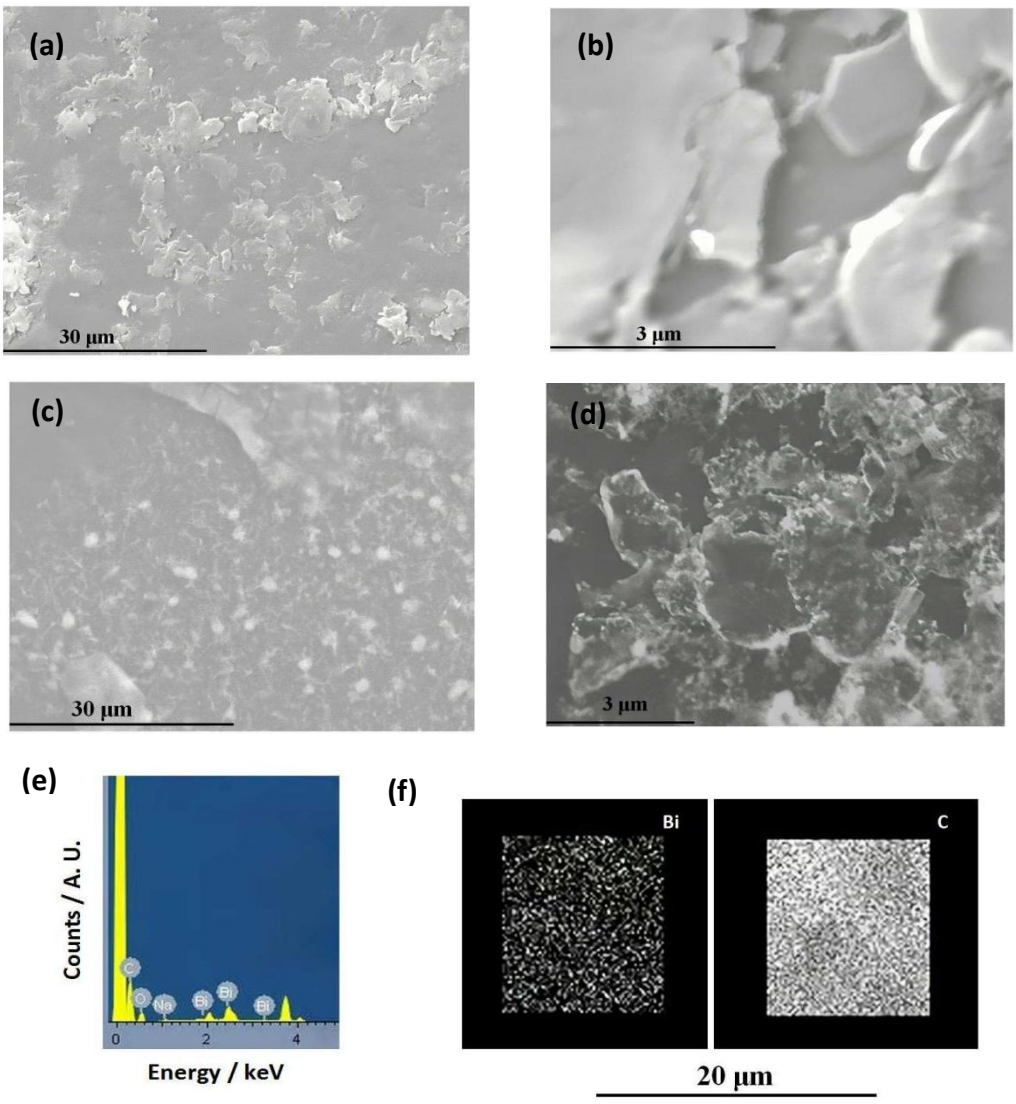

Figure 5-5. SEM micrographs of **(a)** and **(b)** GCE modified with electrodeposited Gr, **(c)** and **(d)** GCE modified with electrodeposited Gr and Bi, **(e)** EDX spectrum recorded at GCE/Gr/Bi and **(f)** mapping of Bi and C at the GCE/Gr/Bi.

5.3.6 Influence of pH and the nature of the deposited Bi

As expressed in, Scheme 5-1 the reduction of MTZ shows that the $-NO_2$ group is reduced to –NHOH, through a four-electron transfer reaction accompanied by the participation of four protons. Hence, changing the pH of the solution will cause the shift in the position of the reduction peak of MTZ. In this experiment, two electrodes, involving the bare GCE and the GCE/Bi electrode, were employed to investigate the

influence of the solution pH on the reduction peak potentials of MTZ. The obtained results are shown in Figures 5-6, where Figure 5-6(a) represents the CV curves of bare GCE in 4.0 mM MTZ with the solution pH of 3.5 to 11 and Figure 5-6(b) gives the CV curves of the GCE/Bi electrode in 4.0 mM MTZ with the solution pH of 4 to 12. It is apparent that the same variation trend in the reduction peak potentials of MTZ is observed for the two electrodes, namely, as the pH is increased, the reduction peak potentials shift to lower values, and this observation is consistent with the participation of H^+ ions in the reduction process of MTZ, as described in Scheme 5-1.

Moreover, the influence of the solution pH on the reduction peak current is summarised in Figure 5-6(c) for the bare GCE and GCE/Bi electrodes, the relationship between the pH and the current is very different with the two electrodes. Apparently, for the bare GCE electrode, the highest reduction peak current is found at a pH of 6.0, and this observation is in very good agreement with several studies [11]. However, for the GCE/Bi electrode, the highest reduction peak current is observed at a pH of 12.0, indicating a higher rate of electron transfer in the alkaline solution. Perhaps, this is related to the in-situ formation of bismuth oxide (Bi_2O_3) which becomes the thermodynamically stable phase at pH values higher than 9.0.

In Figure 5-6(b), it is clearly seen that an oxidation wave also appears with the increase of the solution pH, and this oxidation wave becomes evident as the solution pH is increased beyond a pH of 9.0. This case can be explained in terms of the formation of Bi_2O_3. According to the Pourbaix diagram of Bi, the Bi_2O_3 phase becomes thermodynamically stable at potentials in the vicinity of 0.0 to 0.8 V vs. SHE and at pH values higher than about 9.0. The conversion of Bi to Bi_2O_3 can be described by Equation 5–2, while the corresponding relationship between the electrode potential and pH is given in Equation 5–3. Using Equation 5–3, it is seen that E will become lower as the pH is increased. At a pH of 9.0, E = –0.161 V vs. SHE, which is equivalent to –0.401 V vs. SCE and this is in very good agreement with the oxidation waves observed in Figure 5-6(b). Furthermore, the peak potential shifts to lower potentials with increasing pH and this agrees well with Equation 5–3. The oxidation peak at a pH of 12 is somewhat lower and this is probably related to the solubilisation of Bi_2O_3 in this highly alkaline solution.

$$2Bi + 3H_2O \rightarrow Bi_2O_3 + 6H^+ + 6e^- \quad (5–2)$$

$$E = 0.371 – 0.0591\ pH \quad (5–3)$$

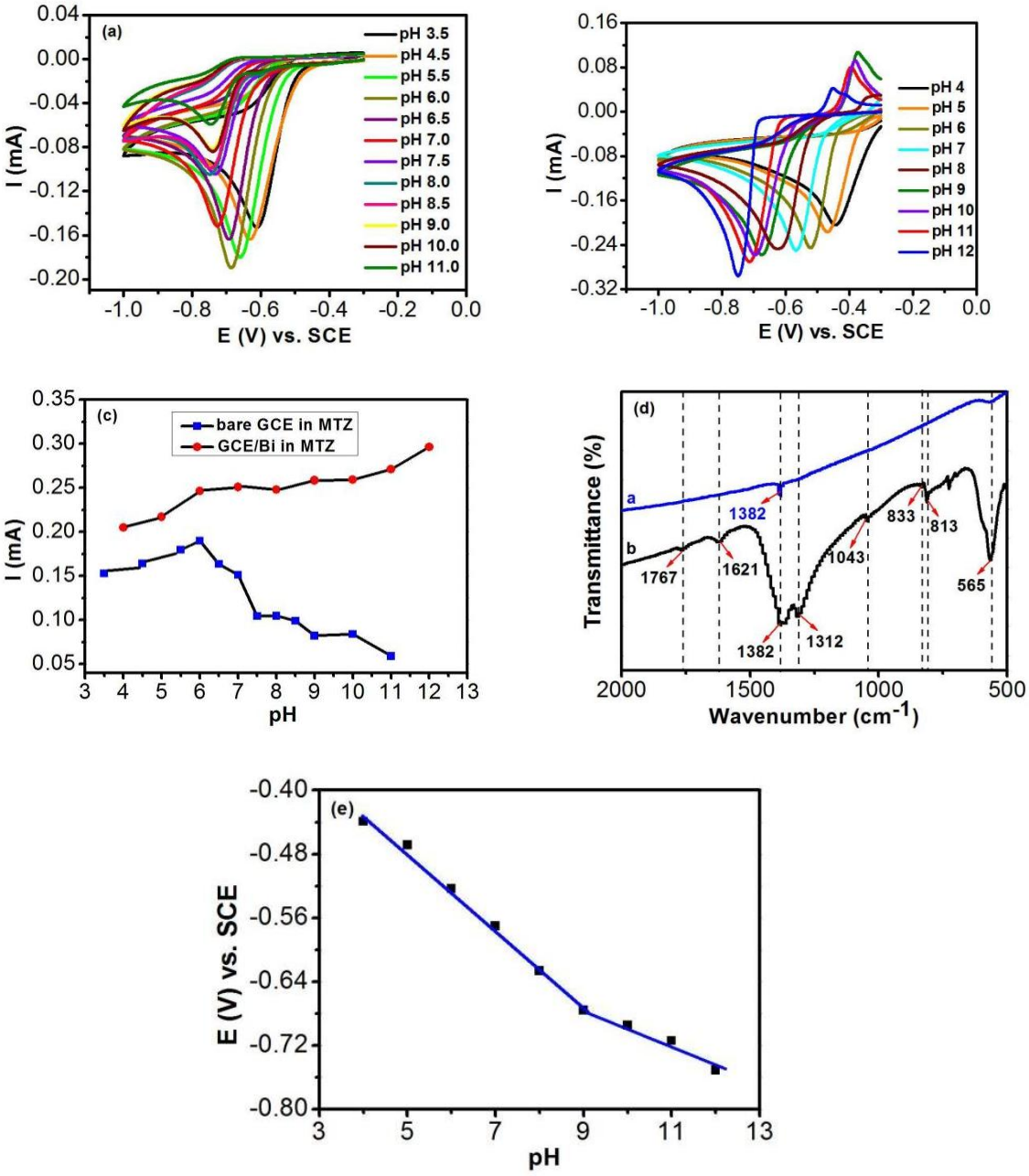

Figure 5-6. (a) CV curves of bare GCE in 4.0 mM MTZ in PBS with different pH values, **(b)** CV curves of GCE/Bi in 4.0 mM MTZ in PBS with different pH values, **(c)** reduction peak currents versus pH values for bare GCE and GCE/Bi electrodes (n = 1), **(d)** FT-IR spectra of GCE/Bi (curve a) freshly deposited and (curve b) cycled in a pH 10 PBS and **(e)** the relationship of reduction peak potentials versus pH for the GCE/Bi (n = 1).

Further, the evidence for the formation of Bi_2O_3 at pH values higher than 9.0 was obtained using FT-IR. Typical spectra are shown in Figure 5-6(d), where the spectrum recorded for the freshly prepared GCE/Bi electrode is compared with the GCE/Bi electrode cycled in a pH 10.0 PBS solution. The electrodeposited Bi has a weak peak at 1382 cm^{-1} which may be related to adsorbed nitrates, or Bi–OH, but there is no evidence of any oxide phases. However, when the electrodeposited Bi is cycled in a PBS at a pH of 10.0, additional peaks emerge, and these can be explained in terms of the formation of Bi_2O_3 and are in good agreement with data previously recorded for Bi_2O_3 [25]. In particular, the peaks observed at 813, 833 and 1043 cm^{-1} can be attributed to the stretching of Bi_2O_3 [25], while the peak at 565 cm^{-1} can be assigned to the Bi–O–Bi stretching vibration. The stronger bands at 1312 and 1382 cm^{-1} are consistent with the presence of Bi–OH [26], while the weak band at 1621 cm^{-1} is probably due to the bending vibration of adsorbed water molecules.

Finally, the relationship between the solution pH and the reduction peak potential of MTZ is exhibited in Figure 5-6 (e), where two linear regions are observed. The regression equation of the linear region between a pH of 4.0 and 9.0 was obtained as $E = -0.0487\ pH - 0.2340$ ($R^2 = 0.993$), showing good linearity. The given slope of 0.0487 V/pH is reasonably close to the theoretical value of 0.0591(m/n) V/pH obtained from the Nernst equation at 298 K, where m expresses the number of protons transferred and n represents the number of electrons involved in the electron-transfer step. There is some deviation from the theoretical slope, hereby the m/n value was computed as 0.83, which is consistent with the participation of equal numbers of protons and electrons during the electron transfer process. Nevertheless, as the pH is further increased from 9.0 to 12.0, the relationship between the solution pH and the peak potential becomes as $E = -0.0240\ pH - 0.4561$, where a lower slope is observed as the H^+ concentration is diminished. Again, this observation may be related to the formation of Bi_2O_3, which become the thermodynamically favoured phase at pH values of 9.0 and higher.

5.3.7 Influence of scan rate

In order to understand the dynamic process of the modified electrodes in the reduction reaction of MTZ, the influence of the scan rates on the electrochemical behaviours of MTZ was investigated at different electrodes including bare GCE, GCE/Bi, GCE/Gr and GCE/Gr/Bi. The influence of scan rates on the peak currents and peak potentials is shown in Figure 5-7 (a), (b) and (c) for bare GCE, Figure 5-8(a), (b) and (c) for the GCE/Bi, Figure 5-9 (a), (b) and (c) for GCE/Gr and Figure 5-10 (a), (b) and (c) for GCE/Gr/Bi at a fixed concentration of 0.1 mM MTZ.

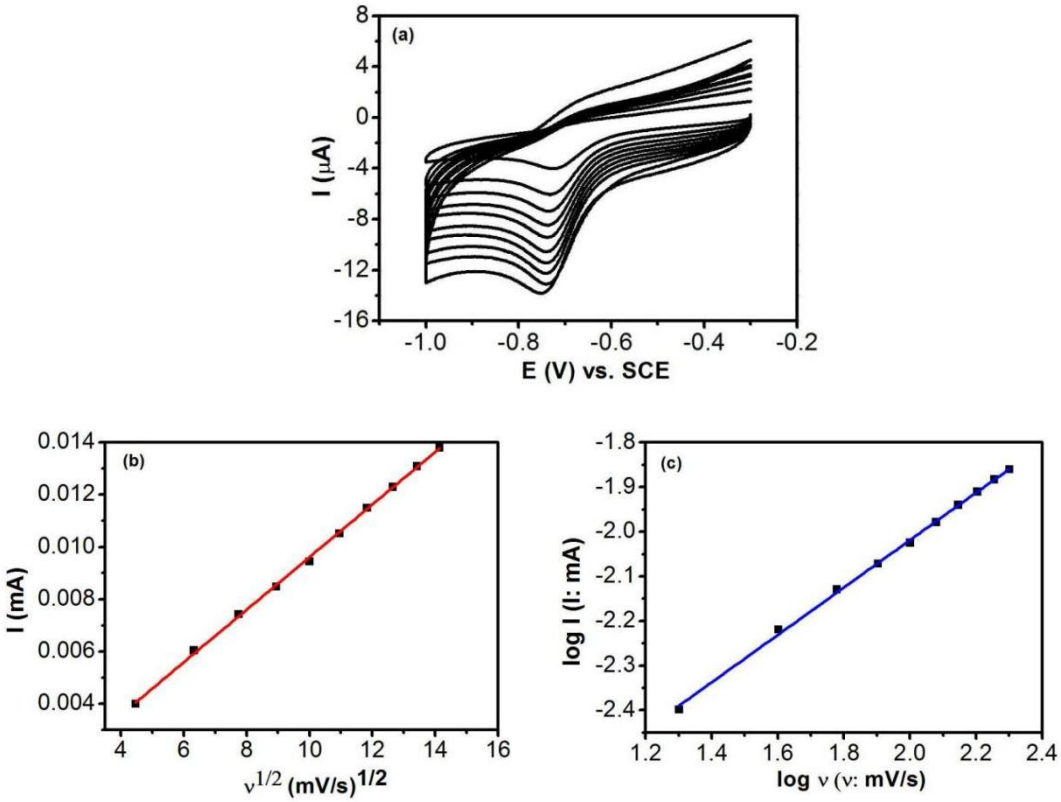

Figure 5-7. (a) CV curves of bare GCE in 0.1 mM MTZ in PBS cycled at different scan rates between 20 and 200 mV s^{-1}, **(b)** peak current plotted as a function of the square root of scan rate and **(c)** logarithm of peak current plotted as a function of the logarithm of scan rate.

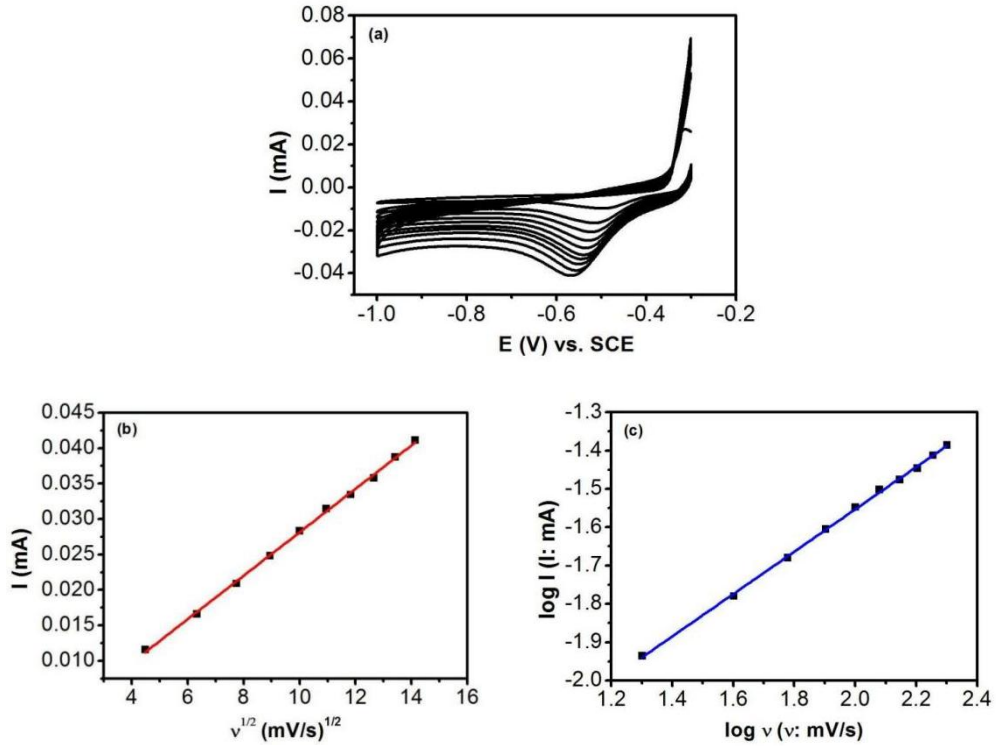

Figure 5-8. (a) CV curves of GCE/Bi in 0.1 mM MTZ in PBS at different scan rates between 20 and 200 mV s^{-1}, **(b)** MTZ peak current plotted as a function of the square root of scan rate and **(c)** logarithm of peak current plotted as a function of the logarithm of scan rate.

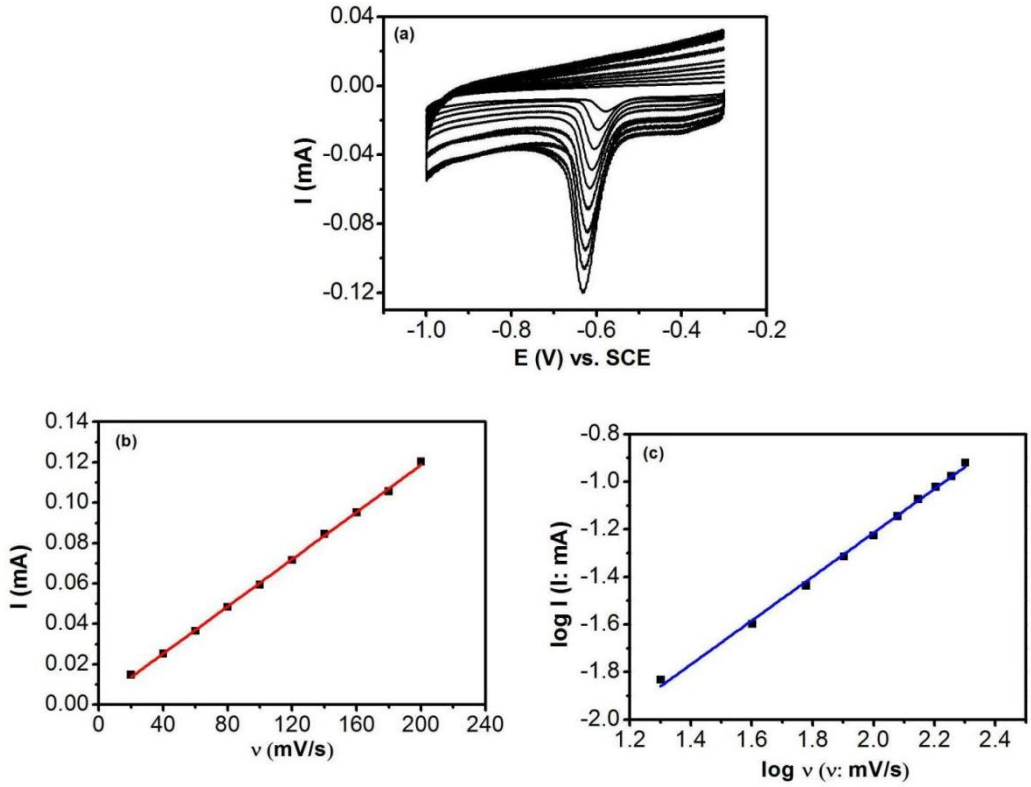

Figure 5-9. (a) CV curves of GCE/Gr in 0.1 mM MTZ in PBS at different scan rates between 20 and 200 mV s^{-1}, **(b)** MTZ peak current plotted as a function of the scan rate for GCE/Gr and **(c)** logarithm of peak current plotted as a function of the logarithm of scan rate.

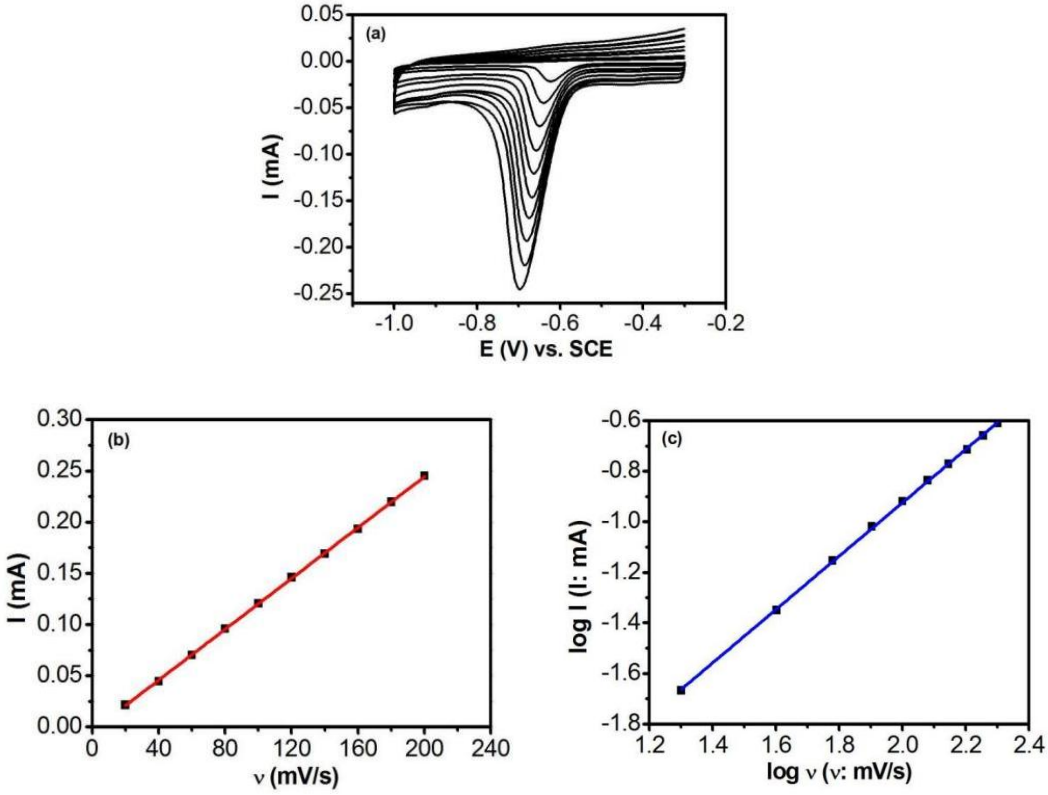

Figure 5-10. (a) CV curves of GCE/Gr/Bi in 0.1 mM MTZ in PBS at scan rates between 20 and 200 mV s^{-1}, **(b)** peak currents plotted as a function of the scan rates and **(c)** logarithm of peak currents plotted as a function of the logarithm of scan rates (n = 3).

On the bare GCE, the reduction peak current of MTZ increases with the increase of the scan rates, as shown in Figure 5-7(a). In Figure 5-7(b), on plotting the peak current as a function of the square root of the scan rate, a linear plot was obtained for the bare GCE, giving the linear regression equation as $I = 1.00 \times 10^{-3}\ v^{1/2} - 0.40 \times 10^{-3}$ (R^2 = 0.999), where I is expressed as mA and v in mV s^{-1}, indicating that the reduction of MTZ is under diffusion control at the bare GCE. Further, the logarithm of the peak current as a function of the logarithm of the scan rate was plotted in Figure 5-7(c), showing a linear relationship with a slope value of 0.5, which supports the diffusion control process of MTZ reduction at the bare GCE.

Similarly, as illustrated in Figure 5-8(a), for the GCE/Bi electrode, the reduction peak current of MTZ increases with the increase of the scan rates. Figure 5-8(b) displays the plot of the reduction peak current versus the square root of the scan rate,

delivering the linear regression equation as $I = 0.0206\ v^{1/2} + 0.0169$ ($R^2 = 0.997$), suggesting that the reduction of MTZ is also under diffusion control at the GCE/Bi electrode. In the same way, in Figure 5-8(c), the plot of the logarithm of the peak current as a function of the logarithm of the scan rate displays a linear relationship with a slope value of 0.55, which is consistent with the diffusion control process of MTZ reduction at the GCE/Bi electrode.

Further, the relationship between the reduction peak current and the scan rate was studied at the GCE/Gr and GCE/Gr/Bi electrodes. Both the CV curves of MTZ at the GCE/Gr and GCE/Gr/Bi electrodes reveal that the reduction peak current of MTZ increases with the increase of the scan rates in Figure 5-9 (a) for the GCE/Gr electrode and Figure 5-10 (a) for the GCE/Gr/Bi electrode. However, compared with the bare GCE and GCE/Bi, it is observed that the reduction peak current of MTZ at the GCE/Gr and GCE/Gr/Bi electrodes is related to the scan rate, as shown in Figure 5-9 (b) for the GCE/Gr electrode and Figure 5-10 (b) for the GCE/Gr/Bi electrode, this implies that the reduction of MTZ becomes an adsorption controlled process after the Gr nanoplatelets were deposited on the surface of the electrodes. Meanwhile, the linear regression equations were given as $I = 5.80 \times 10^{-4}\ v + 1.90 \times 10^{-3}$ ($R^2 = 0.999$) for the GCE/Gr electrode and $I = 1.24 \times 10^{-3}\ v + 4.0 \times 10^{-3}$ ($R^2 = 0.999$) for the GCE/Gr/Bi electrode, respectively. Subsequently, the corresponding analysis on the relationship between the logarithm of the peak current and the logarithm of the scan rate was carried out, in Figure 5-9(c) for the GCE/Gr electrode and Figure 5-10 (c) for the GCE/Gr/Bi electrode, two linear plots were found with slope values in the vicinity of 1.0 for the GCE/Gr (0.92) and GCE/Gr/Bi (0.99) electrodes, clearly demonstrating that the reduction of MTZ alters from a diffusion-controlled process at the bare GCE and GCE/Bi electrodes to an adsorption controlled reaction when the Gr nanoplatelets are deposited on the electrode surfaces. This means that the presence of graphene facilitates the adsorption of the MTZ on the electrodes.

For an irreversible system, the diffusion controlled reactions are governed by the Randles-Sevick equation, as expressed in Equation 5–4, where n_r expresses the total number of electrons transferred, n corresponds to the number of electrons transferred in the rate-determining step, α is the charge transfer coefficient, D is the diffusion

coefficient of MTZ, *c* represents the concentration of MTZ and *A* is the electrode surface area. In this system, the charge transfer coefficient, α, is taken to be 0.55, and n_r, which corresponds to the total number of electrons transferred during the reduction step, is 4.0, as displayed in Scheme 5-1. Generally, a single electron transfer step becomes the rate-determining step, as it is highly improbable for the simultaneous transfer of multiple electrons, thus n is set to unity.

$$I = 2.99 \times 10^5 \, n_r \, (n\alpha)^{1/2} A \, c \, D^{1/2} \nu^{1/2} \qquad (5\text{–}4)$$

Using Equation 5–4, the diffusion coefficient (D) of MTZ is computed as 4.2 x 10^{-6} cm^2 s^{-1} for the bare GCE. This computed D value is in reasonably good agreement with the value of 7.96 x 10^{-6} cm^2 s^{-1} reported by Ammar et al. [7]. According to this computed D value and comparison of two linear regression equations for the bare GCE and GCE/Bi electrodes, the surface area of the GCE/Bi electrode is estimated to be 0.180 cm^2, which shows an approximate 1.7-fold increase in the electroactive surface area after the electrodeposition of the Bi.

Further, the Equation 5–5, in which E_p and $E_{p/2}$ are the peak and half-wave potentials, is used to estimate the $n'\alpha$ value being 0.55 for the GCE/Gr/Bi electrode. This value is consistent with a one-electron transfer rate-determining step during the reduction of MTZ at the GCE/Gr/Bi electrode, as four electrons could not be transferred simultaneously.

$$E_p - E_{p/2} = \frac{47.7}{n'\alpha} \qquad (5\text{–}5)$$

Actually, a single electron transfer slow step for the reduction of MTZ at boron doped diamond has been proposed by Ammar et al. [7], as expressed in Equation 5–6. In addition, the heterogenous reaction rate constant (k^0) can be calculated according to the Equation 5-7, where F, A, C, R and T have their usual meanings [27], while the E^0 value is estimated by extrapolating ν to 0 using a plot of E_p as a function of the logarithm of ν. Then, considering a one-electron transfer rate determining step, the k^0

value was calculated to be 2.5×10^{-3} cm $s^{-1} \pm 6.3 \times 10^{-5}$ for the GCE/Gr/Bi electrode. This value suggests an efficient reduction of MTZ at the GCE/Gr/Bi electrode. The corresponding linear plot is depicted in Figure 5-11, giving a linear regression equation as $\ln I_p = -34.25 (E_p - E^0) - 14.97$ ($R^2 = 0.986$).

$$R{-}NO_2 + e^- \rightarrow R{-}NO_2^- \quad \textbf{(slow step)} \qquad (5\text{–}6)$$

$$I_p = 0.277nFACk^0 e^{-(anF(E_p - E^0)/RT} \qquad (5\text{–}7)$$

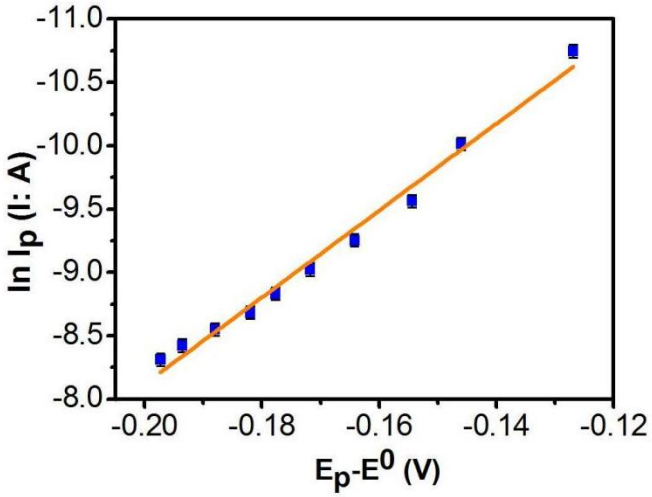

Figure 5-11. Logarithm of peak current plotted as a function of the peak potential difference, E_p-E^0 for the GCE/Gr/Bi electrode in 2.0 mM MTZ in PBS (n = 3).

5.3.8 Adsorption of MTZ at the GCE/Gr/Bi electrode

As discussed above, the reduction of MTZ at the GCE/Gr/Bi electrode becomes an adsorption-controlled reaction. Further, this observation was verified by designing a series of experiments, where the memory effect of GCE/Gr/Bi was studied together with its ability to adsorb MTZ. The experimental results obtained are summarised in Figure 5-12(a), (b) and (c). The GCE/Gr/Bi electrode was firstly immersed in 0.1 mM MTZ for a certain period of time, then this electrode was gently washed using deionised water and cycled in the blank PBS without MTZ, the measured CV curves were recorded, as displayed in Figure 5-12(a). From curves 1-4 in Figure 5-12(a), there is a clear reduction wave of MTZ, suggesting a memory effect with the electrochemical reduction of the adsorbed MTZ on the GCE/Gr/Bi electrode. Moreover, the influence of

accumulation time was investigated and the results are described in Figure 5-12(b), which indicates that the optimum accumulation period is about 300 s. This observation is consistent with adsorption of MTZ at the Gr. Further, the adsorption was explored by the UV-visible measurements. As presented in Figure 5-12(c), UV – vis spectra show the data recorded for 0.01 mM MTZ in the presence and absence of 10 mg Gr. A decrease in the absorbance is evident when Gr is added to the MTZ solution, demonstrating that the MTZ is removed from the solution phase due to adsorbing onto the Gr. Therefore, these data clearly show that the incorporated Gr within the GCE/Gr/Bi electrode facilitates the adsorption of MTZ.

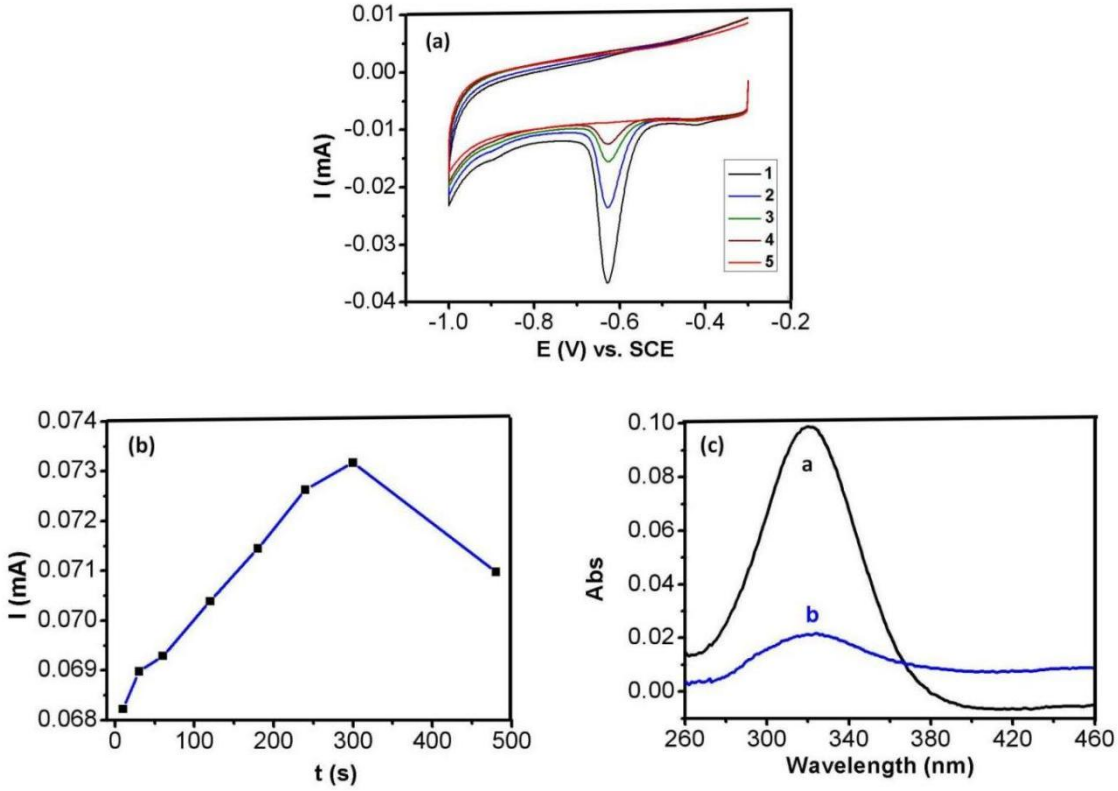

Figure 5-12. (a) Memory effects showing voltammograms 1, 2, 3, 4 and 5 recorded in PBS in the absence of MTZ for GCE/Gr/Bi, **(b)** peak current as a function of immersion period for GCE/Gr/Bi and **(c)** UV–vis spectrum of MTZ (0.01 mM) in the absence (a) and presence (b) of Gr (10 mg).

5.3.9 Sensor performance of the fabricated GCE/Gr/Bi electrode

The sensing performance of the fabricated GCE/Gr/Bi electrode in the detection of MTZ was studied by varying the concentration of MTZ and the corresponding CV

curves for a series of MTZ concentrations between 0.005 and 260 μM were recorded. The representative data are illustrated in Figure 5-13(a), while the inset shows the data recorded for concentrations from 5 to 120 nM. In Figure 5-13(a) the small reversible redox waves evident at about –0.45 V vs. SCE can be attributed to oxygenated species at the Gr nanoplatelets. From Figure 5-13(a), the reduction peak currents increase with the increase of the concentration of MTZ. When the peak current was plotted as a function of the concentration of MTZ, as represented in Figure 5-13(b), a linear plot with a regression equation as I (mA) = 0.6487c (mM) + 0.0047 (R^2 = 0.995) was obtained. This shows excellent linearity over a wide concentration region. Meanwhile, the calibration curve obtained with nM concentrations is revealed in the inset in Figure 5-13(b), again showing very good linearity. Moreover, according to the well-known equation for the limit of detection (LOD = $3S_b$/sensitivity), where S_b corresponds to the standard deviation of the baseline in the absence of the MTZ, the LOD was computed as 0.90 nM, which gives an impressive low LOD value combined with a sensitivity of 0.65 μA $\mu M^{-1} \pm 0.018$.

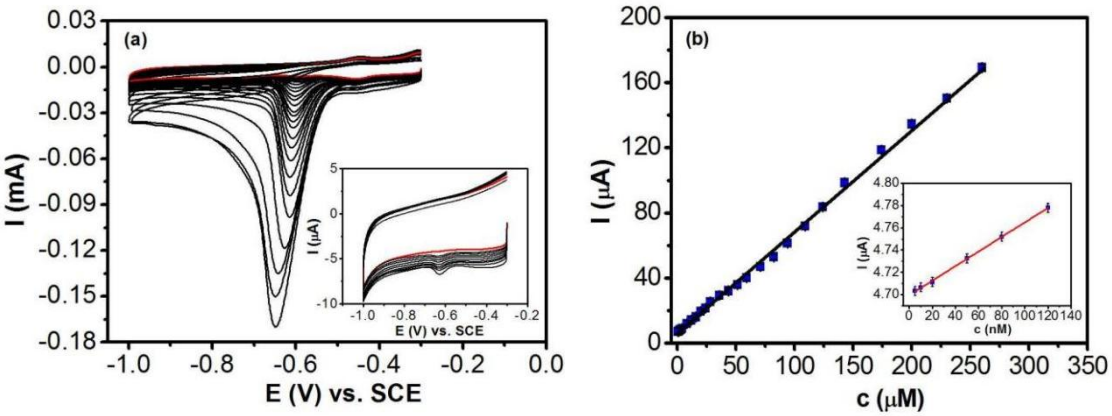

Figure 5-13. (a) CV curves of the GCE/Gr/Bi electrode recorded at 50 mV s^{-1} in MTZ at concentrations from 0.005 to 260 μM; the inset shows the CV curves of the GCE/Gr/Bi electrode in MTZ at concentrations from 5 to 120 nM; the red curve shows the CV curve of the GCE/Gr/Bi electrode recorded at 50 mV s^{-1} in blank PBS and **(b)** peak current plotted as a function of the MTZ concentration from 0.005 to 260 μM; the inset shows peak current plotted as a function of the MTZ concentration from 5 to 120 nM (n = 3).

In addition, a similar approach was employed to obtain the linear regression equation as I (mA) = 0.1780c (mM) + 0.02674 (R^2 = 0.9953) for the GCE/Bi electrode. Again, excellent linearity was found, but the calculated LOD was higher at 3.3 nM in this case, and the sensitivity was lower adopting a value of 0.18 μA μM^{-1}. Such comparison clearly illustrates that enhanced detection may be due to the use of both Gr and Bi. Again, this case may be connected to the adsorption of MTZ at the Gr nanoplatelets and the higher electroactive surface area of the GCE/Gr/Bi electrode.

Furthermore, the practicality of the developed sensor was analysed. In terms of the typical concentration of MTZ found in the environment, it has been reported that the levels of MTZ can range from 0.5 to 21.4 ng/L in drinking water, but are higher in river sediments, reaching levels of 1.21 μg/kg and ranging from 6.3 to 27.2 μg/kg in vegetables [28]. While the LOD of 0.90 nM may not be suitable for direct analysis of drinking water, the linear range is suitable for levels found in vegetables and sediments.

Table 5-1. Comparison of sensors in the electrochemical detection of MTZ.

Sensor materials	Technique	Linear range (μM)	LOD (nM)	Reference
CNF@AuNPs	DPV	0.1 – 100	24	[29]
C60-rGO-NF/SPE	SWV	0.25 – 34	210	[10]
CdS QDs	DPV	0.1 – 203	53	[30]
Ni/Fe-LDH	Amperometry	5 – 161	58	[31]
$Dy(VO_4)$/f-CNF/SPCE	LSV	1.5 – 1036	6	[8]
ZnV MS	DPV	0.05 – 59	9	[32]
ZnCo-based MOF	LSV	0.05 – 100	17	[33]
N, S, P-doped porous carbon	LSV	0.1 – 45	13	[34]
DyM/GCE	DPV	0.01 – 2363	3	[35]
αFe_2O_3/CPE	CV	0.8 – 100	285	[36]
O-gCN/GCE	DPV	0.01 – 2060	5	[37]
MWNT-CS-Ni/GCE	DPV	0.1 – 150	25	[38]
NiO/Ni	DPV	0.01 – 1.63	6	[39]
AgNP/CuMOF/PPy–rGO	SWV	0.08 – 160	24	[40]
μAl_2O_3/CPE	DPV	0.5 – 1000	253	[41]
GCE/Bi	CV	0.02 – 240	3	This work
GCE/Gr/Bi	CV	0.005 – 260	0.9	This work

Further, a comparison of the GCE/Gr/Bi and GCE/Bi electrodes with some previously reported sensors for the detection of MTZ is listed in Table 5-1, focusing on the more recent reports. From Table 5-1, it is clear that in many of these studies, two linear concentration ranges are evident and for this comparison the lower concentration ranges, which have been employed by the authors to estimate the LOD values, are only provided. In this study, it is evident that the GCE/Gr/Bi electrode compares well with them in terms of the LOD values and linear concentration ranges. On the other hand, it is the simplicity of the GCE/Gr/Bi sensor that makes it suitable for the electrochemical detection of MTZ, especially in terms of water analysis.

5.3.10 Evaluation of reproducibility, selectivity and stability

The reproducibility and selectivity are very important factors for the developed sensors. First, the reproducibility of the GCE/Bi and GCE/Gr/Bi electrodes for the detection of MTZ was evaluated using five different electrodes prepared on different days, and the obtained results are described in Table 5-2, where five separate experiments were done at a relatively high concentration of 2.0 mM for both the GCE/Bi and GCE/Gr/Bi electrodes and a lower concentration of 0.1 mM for the GCE/Gr/Bi electrode. It is obvious in Table 5-2 that the % RSD values are low and well below 5%, demonstrating that two modified electrodes display good reproducibility for the detection of MTZ.

Table 5-2. Reproducibility of GCE/Bi and GCE/Gr/Bi in the detection of MTZ (n = 5).

	Reduction Peak Current (μA)					Mean	RSD (%)
	1	2	3	4	5	(n = 5)	(n = 5)
GCE/Bi (2.0 mM MTZ)	147.3	143.9	143.5	144.6	147.0	145.26 ± 1.77	1.22
GCE/Gr/Bi (2.0 mM MTZ	278.3	274.5	273.6	277.5	276.8	276.14 ± 2.01	0.73
GCE/Gr/Bi (0.1 mM MTZ	69.53	69.75	69.93	69.14	69.48	67.57 ± 0.31	0.43

Furthermore, the selectivity was inspected using a variety of interfering compounds, such as inorganic salts, which are present in aquatic environments, and some organic compounds (e.g. glucose). The interferents included additional phosphates (KH_2PO_4), cations including Mg^{2+} ($MgCl_2$), Zn^{2+} ($ZnCl_2$), Ca^{2+} ($CaCl_2$), NH_4Cl (AC) to give NH_4^+ cations, sulfates (Na_2SO_4), nitrates ($NaNO_3$), carbonates (Na_2CO_3), chlorides ($CaCl_2$), and citric acid (CA). For organic compounds, apart from glucose, nitrophenols, (ortho- and para-nitrophenol, *o*-NP and *p*-NP) and hydrocortisone (HC) were also chosen as interferents as these can be electrochemically reduced at a similar potential as MTZ. For clarity, the CV technique was employed to record the interference study in a 0.1 mM MTZ solution in a neutral PBS. The interferents of the inorganic ions and glucose were added at a concentration of 1.0 mM, to give a 10-fold excess over the concentration of MTZ, while the concentrations of *o*-NP, *p*-NP and HC were used at 0.1 mM. When the CV curves of the mixed systems containing MTZ and interferents were obtained, the reduction peak currents of MTZ were taken. The normalised reduction peak currents (I/I_0, where I represents the peak current in the presence of the interferent and I_0 expresses the peak current in the absence of the interferent) are shown in Figure 5-14(a). The reduction peak currents of MTZ are nearly identical, except for the addition of nitrates and *o*-NP, where an increase in the current is observed. This is consistent with the reduction of nitrates and *o*-NP at the modified electrode, but the interference is low giving a 1.3% increase in the reduction peak current. Besides, adding salts including sulfate, chloride, carbonate, and phosphate that are frequently observed in aquatic environments have little influence on the reduction peak current due to that these salts are not electroactive, but they may be adsorbed on the electrode surface in competition with the adsorption of MTZ at the GCE/Gr/Bi electrode. Fortunately, the adsorption of MTZ at the GCE/Gr/Bi electrode is not affected by these interferents. In addition, for the nitrophenols, it is evident that the reduction of *o*-NP occurs at a potential similar to that of MTZ, causing an increase in the reduction peak current of MTZ (see Figure 5-14(b)), whereas the reduction of *p*-NP occurs at a lower potential than MTZ, as shown in the Figure 514(c). It can be observed that the reduction of *p*-NP occurs with a significant peak current at the GCE/Gr/Bi electrode, but the reduction

peaks associated with MTZ and *p*-NP are well separated, thus *p*-NP is not an interferent for the electrochemical detection of MTZ.

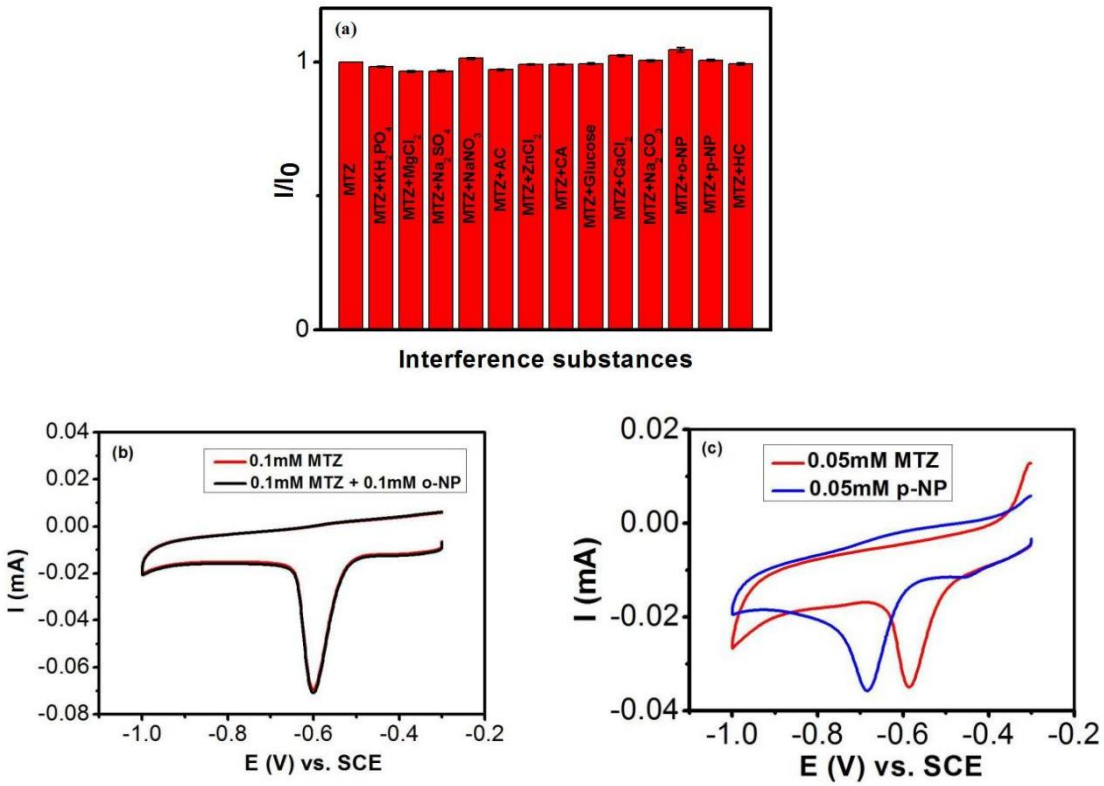

Figure 5-14. (a) Normalised peak currents, (I/I_0), of 0.1 mM MTZ at GCE/Gr/Bi in a PBS containing 10-fold concentrations of various inorganic ions and glucose, and with equimolar concentrations of organic compounds (phenols and HC), **(b)** 0.1 mM MTZ in the presence and absence of 0.1 mM *o*-NP at GCE/Gr/Bi and **(c)** shows CVs recorded in 0.05 mM MTZ and also in 0.05 mM *p*-NP.

Again, the stability is an important indicator for evaluating sensors. For this purpose, using CV technique, the stability of the modified electrodes was explored by cycling the modified electrodes continuously, then the reduction peak current of MTZ was recorded following repeated cycling. Figure 5-15 shows the peak currents as a function of the cycle number under stationary and mild stirring conditions for the GCE/Bi and GCE/Gr/Bi electrodes. It is worth noting that the peak currents remain essentially constant over the 40 cycles, suggesting there is no electrode fouling. However, for the unmodified GCE, the data are listed in Table 5-3, significant fouling was observed. The currents are higher with mild stirring. This may be due to that the mild stirring (at 100 rpm) enhances the diffusion of MTZ, and this is reflected in higher

peak currents that also remain constant over the cycling period. Based on the observation above, the prepared electrodes exhibit good stability.

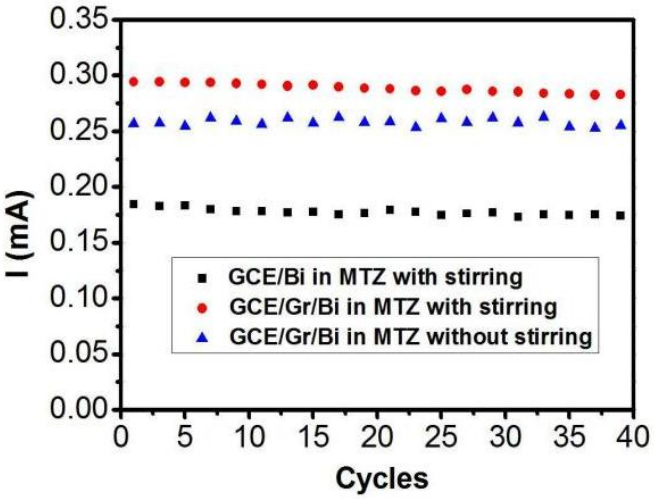

Figure 5-15. Peak currents of MTZ plotted as a function of CV cycle number with and without stirring.

Table 5-3. The peak currents of MTZ (2 mM) at bare GCE during scanning 10 cycles.

1st cycle	2nd cycle	3rd cycle	4th cycle	5th cycle
93 µA	54 µA	46 µA	43 µA	41 µA
6th cycle	7th cycle	8th cycle	9th cycle	10th cycle
40 µA	39 µA	38 µA	36 µA	34 µA

5.3.11 Evaluation of regeneration of the modified electrode

Additionally, one significant advantage of using the electrodeposited bismuth film modified electrode is the possibility of easy regeneration of the bismuth layer to obtain a new electrode surface. Two approaches were used to explore this possibility. Firstly, the electrodeposited bismuth film at the GCE/Gr/Bi electrode was oxidised and removed from the electrode surface by applying a potential of 0.60 V vs. SCE for 400 s, then a freshly electrodeposited bismuth film was generated by applying a potential of

−1.0 V vs. SCE for 100 s. This removal and regeneration step was repeated five times, and the resulting voltammograms are described in Figure 5-16. Good repeatability is achieved with a 0.5% error in the peak currents.

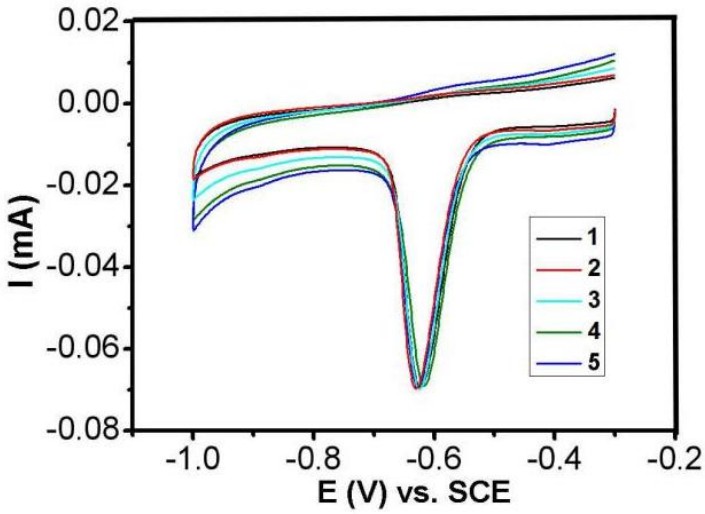

Figure 5-16. CV curves of MTZ using the regenerated Bi film at the GCE/Gr/Bi electrode.

Secondly, an in-situ method was attempted to regenerate the bismuth film, that is, the Bi(III) solution was mixed with the MTZ solution, then the electrode was cycled in the mixed solution to 0.0 V vs. SCE to remove the previously electrodeposited Bi film. For this experiment, the pH of the MTZ solution was adjusted to 1.23 to prevent the precipitation of insoluble bismuth hydroxides. As a result, the reduction peak of MTZ was moved to more positive potentials to coincide with the peak associated with the Bi(III) reduction. As shown in Figure 5-17(a) and 5-17(b), it is found that the peak, arising from the reduction of Bi(III) and MTZ, is sensitive to the MTZ concentration and an approximate linear relationship is obtained with the linear regression equation as I (mA) = −0.1023c (mM) -1.1321 (R^2 = 0.96).

Consequently, this study clearly demonstrates that the bismuth film on the electrode surface can be regenerated either through an ex-situ or in-situ strategy, with the ex-situ method providing very good reproducibility and is the more promising strategy for the application of the developed sensor.

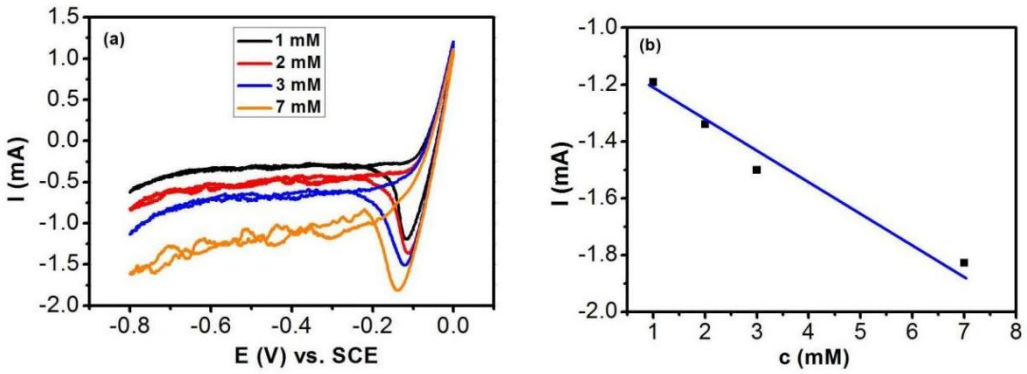

Figure 5-17. (a) CV curves recorded for GCE in a mixture of MTZ (1 to 7 mM) and $Bi(NO_3)_3$ (5 mM) and **(b)** peak current as a function of the MTZ concentration (n = 1).

5.3.12 Water analysis

Finally, the performance of the developed sensor in the analysis of MTZ in tap water was examined employing a typical spiking and recovery experiment. Firstly, the tap water was spiked with different concentrations of MTZ, and then the recovery was analysed using the GCE/Gr/Bi electrode. Meantime, the deionized water was also employed for comparison purpose. The data recorded are summarised in Table 5-3, where it is evident that good recovery is achieved in the tap water, with the recovery varying between 101.36 to 97.95%. Moreover, these recovery values are compared with that obtained when using deionized water. It can be seen from Table 5-3 that they are similar to each other. This analysis indicates good performance of the GCE/Gr/Bi sensor for the detection of MTZ.

Table 5-3. Determination of MTZ in deionised water and tap water using GCE/Gr/Bi. Sufficient phosphate was added to the deionised and tap water samples to give a 0.1 M phosphate solution (n = 3).

Sample	Added/ μM	Found/ μM	Recovery
Deionised water	10.0	10.17 (± 0.29)	101.7%
	50.0	49.22 (± 1.57)	98.44%
	100.0	102.15 (± 1.94)	102.15%
Tap water	10.0	9.86 (± 0.16)	98.6%
	50.0	50.68 (± 1.06)	101.36%
	100.0	97.95 (± 2.75)	97.95%

5.4 Conclusion

In this chapter, a facile and effective electrochemical sensor for the detection of MTZ was developed using a simple electrodeposition procedure. The Gr nanoplatelets were initially electrochemically deposited on the surface of GCE to form the GCE/Gr electrode, followed by the electrodeposition of Bi from an acidified Bi(III) solution for 100 s to form the GCE/Gr/Bi electrode. The SEM photographs indicated that the Bi species was well dispersed across the surface of the GCE/Gr electrode, making the GCE/Gr/Bi electrode perform well for the detection of MTZ, delivering an impressive linear concentration range, good selectivity, good recovery and a low LOD value. Especially, the simplicity of the sensor fabrication process combined with the ability to readily regenerate the Bi layer on the electrode surface makes this an interesting sensor. Moreover, this simple preparation approach could be applied in the analysis of other analytes, where the regeneration of a new clean sensor surface is very important.

5.5 References

[1] Malfertheiner, P.; Megraud, F.; O'Morain, C.; Bazzoli, F.; El-Omar, E.; Graham, D.; Hunt, R.; Rokkas, T.; Vakil, N.; Kuipers, E. J.; Andersen, L.; Atherton, J.; Asaka, M.; Bazzoli, F.; Bytzer, P.; Chan, F.; Coelho, L. G. V.; De Wit, N.; Delchier, J. C.; Di Mario, F.; El-Omar, E.; Fock, K. M.; Forman, D.; Fujioka, T.; Gasbarrini, G.; Genta, R.; Goh, K .L.; Graham, D. Y.; Hirschl, A.; Hungin, P.; Hunt, R.; Isakov, V. A.; Jones, R.; Kist, M.; Koletzko,;S.; Kuipers, E. J.; Kupcinskas, L.; Ladas, S.; Lanas, A.; Machado, J.; Malfertheiner, P.; McColl, K. E. L.; Mégraud, F.; Michetti, P.; Moayyedi, P.; Omorain, C.; Pilotto, A.; Quina, M.; Rokkas, T.; Sharma, P.; Simsek, Y.; Sipponen, P.; Sollano, J.; Stockbrügger, R.; Sugano, K.; Vaira, D.; Vakil, N.; Vieth, M.; Xiao, S. Current concepts in the management of helicobacter pylori infection: The maastricht III consensus report, *Gut*. **2007**, *56*, 772–781, doi: 10.1136/gut.2006.101634.

[2] Freeman, C. D.; Klutman, N. E.; Lamp, K. C.; Metronidazole. A therapeutic

review and update, *Drugs*. **1997**, *54*, 679–708, doi: 10.2165/00003495-199754050-00003.

[3] Ceruelos, A. H.; Romero-Quezada, L. C.; Ledezma, J. C. R.; López, L. Contreras, Therapeutic uses of metronidazole and its side effects: An update, *Eur. Rev. Med. Pharmacol. Sci*. **2019**, *23*, 397–401, doi: 10.26355/eurrev_201901_16788.

[4] Quincey, D. J.; Kay, P.; Wilkinson, J.; Carter, L. J.; Brown, L. E. High concentrations of pharmaceuticals emerging as a threat to Himalayan water sustainability. *Environ. Sci. Pollut. Res*. **2022**, *29*, 16749–16757, doi: 10.1007/s11356-021-18302-8.

[5] dos Anjos, M. V.; Bergoza, L.; Fonseca, G.; Possa, E.; dos Santos, P.; Silva, S. M. E.; Tasso, L. Fast determination of free metronidazole in rat plasma and peritoneal fluid using HPLC-UV method. *Biomed. Chromatogr*. **2023**, *37*, e5543, doi: 10.1002/bmc.5543.

[6] Li, J.; Wang, Y. B.; Wu, L.; Li, K. Y.; Feng, W. Fabrication of multi-walled carbon nanotubes/oxide reinforced hollow fibers by sol-gel technique for rapid determination of metronidazole in milk, *Anal. Methods*, **2014**, *6*, 1404-1411, doi: 10.1039/ c3ay41645c.

[7] Wang, H.; Qian, D.; Xiao, X.; Deng, C.; Liao, L.; Deng, J.; Lin, Y. W. Preparation and application of a carbon paste electrode modified with multi-walled carbon nanotubes and boron-embedded molecularly imprinted composite membranes, *Bioelectrochem*. **2018**, *121*, 115–124, doi: 10.1016/j.bioelechem.2018.01.006.

[8] Muthukutty, B.; Arumugam, B.; Chen, S. M.; Ramaraj, S. K. Low potential detection of antiprotozoal drug metronidazole with aid of novel dysprosium vanadate incorporated oxidized carbon nanofiber modified disposable screen-printed electrode, *J. Hazard. Mater*. **2021**, *407*, 124745, doi: 10.1016/j.jhazmat.2020.124745.

[9] Ammar, H. B.; Brahim, M. B.; Abdelhédi, R.; Samet, Y. Boron doped diamond sensor for sensitive determination of metronidazole: Mechanistic and analytical study by cyclic voltammetry and square wave voltammetry. *Mater. Sci. Eng. C*. **2016**, *59*, 604–610, doi: 10.1016/j.msec.2015.10.025.

[10] Materón, E. M.; Wong, A.; Freitas, T. A.; Faria, R. C.; Oliveira, O. N. A sensitive electrochemical detection of metronidazole in synthetic serum and urine samples using

low-cost screen-printed electrodes modified with reduced graphene oxide and C60, *J. Pharm. Anal*. **2021**, *11*, 646–652, doi: 10.1016/j.jpha.2021.03.004.

[11] Velusamy, V.; Palanisamy, S.; Kokulnathan, T.; Chen, S. W.; Yang, T. C. K.; Banks, C. E.; Pramanik, S. K. Novel electrochemical synthesis of copper oxide nanoparticles decorated graphene-β-cyclodextrin composite for trace-level detection of antibiotic drug metronidazole. *J. Colloid Interface Sci*. **2018**, *530*, 37–45, doi: 10.1016/j.jcis.2018.06.056.

[12] Chinnaraj, S.; Palani, V.; Yadav, S.; Arumugam, M.; Sivakumar, M.; Maluventhen, V.; Singh, M. Green synthesis of silver nanoparticle using goniothalamus wightii on graphene oxide nanocomposite for effective voltammetric determination of metronidazole. *Sens. Bio-Sensing Res*. **2021**, *32*, 100425, doi: 10.1016/j.sbsr.2021.100425.

[13] Vivekanandan, A. K.; Subash, V.; Chen, S. M.; Chen, S. H. Sonochemical synthesis of nickel-manganous oxide nanocrumbs decorated partially reduced graphene oxide for efficient electrochemical reduction of metronidazole, *Ultrason. Sonochem*. **2020**, *68*, 105176, doi: 10.1016/j.ultsonch.2020.105176.

[14] Yang, M.; Hu, Z. Electrodeposition of bismuth onto glassy carbon electrodes from nitrate solutions, *J. Electroanal. Chem*. **2005**, *583*, 46–55, doi: 10.1016/j.jelechem.2005.04.019.

[15] Hutton, E. A.; Ogorevc, B.; Hočevar, S. B.; Weldon, F.; Smyth, M. R.; Wang, J. An introduction to bismuth film electrode for use in cathodic electrochemical detection, *Electrochem. Commun*. **2001**, *3*, 707–711, doi: 10.1016/S1388-2481(01)00240-5.

[16] Hočevar, S. B.; Ogorevc, B.; Wang, J.; Pihlar, B. A study on operational parameters for advanced use of bismuth film electrode in anodic stripping voltammetry. *Electroanalysis*, **2002**, *14*, 1707–1712, doi: 10.1002/elan.200290014.

[17] Królicka, A.; Pauliukaite, R.; Svancara, I.; Metelka, R.; Bobrowski, A.; Norkus, E.; Kalcher, K.; Vytřas, K. Bismuth-film-plated carbon paste electrodes, *Electrochem. Commun*. **2002**, *4*, 193–196, doi: 10.1016/S1388-2481(01)00301-0.

[18] Švancara, I.; Baldrianová, L.; Tesařova, E.; Hočevar, S. B.; Elsuccary, S. A. A.; Economou, A.; Sotiropoulos, S.; Ogorevc, B.; Vytřas, K. Recent advances in anodic stripping voltammetry with bismuth-modified carbon paste electrodes, *Electroanalysis*.

2006, *18*, 177–185, doi: 10.1002/elan.200503391.

[19] Zhang, H.; Cui, J.; Zeng, Y.; Zhang, Y.; Pei, Y. Direct electrodeposition of carbon dots modifying bismuth film electrode for sensitive detection of Cd^{2+} and Pb^{2+}, *J. Electrochem. Soc*. **2022**, *169*, 017501, doi: 10.1149/1945-7111/ac47e7.

[20] Bahinting, S. E. D.; Rollon, A. P.; Garcia-Segura, S.; Garcia, V. C. C.; Ensano, B. M. B.; Abarca, R. R. M.; Yee, J. J.; de Luna, M. D. G. Bismuth film-coated gold ultramicroelectrode array for simultaneous quantification of Pb(II) and Cd(II) by square wave anodic stripping voltammetry, *Sensors*. **2021**, *21*, 1–19, doi: 10.3390/s21051811.

[21] Li, H.; Zhao, J.; Zhao, S.; Cui, G. Simultaneous determination of trace Pb(II), Cd(II), and Zn(II) using an integrated three-electrode modified with bismuth film, *Microchem. J*. **2021**, *168*, 106390, doi: 10.1016/j.microc.2021.106390.

[22] Lezi, N.; Economou, A.; Barek, J.; Prodromidis, M. Screen-printed disposable sensors modified with bismuth precursors for rapid voltammetric determination of 3 ecotoxic nitrophenols. *Electroanalysis*. **2014**, *26*, 766–775, doi: 10.1002/elan.201400001.

[23] Singh, B.; Singh, A.; Sharma, A.; Mahajan, P.; Verma, S.; Padha, B.; Ahmed, A.; Arya , S. Electrochemical sensing and photocatalytic degradation of 2,4-dinitrophenol via bismuth(III) oxide nanowires. *J. Mol. Struct*. **2022**, *1255*, 132379, doi: 10.1016/j.molstruc.2022.132379.

[24] Abollino, O.; Giacomino, A.; Malandrino, M. Voltammetry | stripping voltammetry, in: Encycl. *Anal. Sci*. **2019**, pp 238–257, doi: 10.1016/B978-0-12-409547-2.14491-9.

[25] Azizian-Kalandaragh, Y.; Sedaghatdoust-Bodagh, F.; Habibi-Yangjeh, A. Ultrasound-assisted preparation and characterization of β-Bi_2O_3 nanostructures: exploring the photocatalytic activity against rhodamine B, *Superlattice. Microst*. **2015**, *81*, 151–160, doi: 10.1016/j.spmi.2014.12.038.

[26] Hobosyan, M. A.; Yolchinyan, S. A.; Martirosyan, K. S. A novel nano-energetic system based on bismuth hydroxide. *RSC Adv*. **2016**, *6*, 66564–66570, doi: 10.1039/c6ra12854h.

[27] Balamurugan, K.; Karthik, R.; Chen, S. M.; Sukanya, R.; Subramanian, B. T.; Biju, V. M. N.; Shim, J. J.; Breslin, C. B. Heterostructures of mixed metal oxides

($ZnMnO_3$/ZnO) synthesized by a wet-chemical approach and their application for the electrochemical detection of the drug chlorpromazine, *Compos. B Eng*. **2022**, *236*, 109822, doi: 10.1016/j.compositesb.2022.109822.

[28] Hanna, N.; Sun, P.; Sun, Q.; Li, X.; Yang, X.; Ji, X.; Zou, H.; Ottoson, J.; Nilsson, L. E.; Berglund, B.; Dyar, O. J.; Tamhankar, A. J.; Lundborg, C. S. Presence of antibiotic residues in various environmental compartments of Shandong province in eastern China: its potential for resistance development and ecological and human risk, *Environ. Int*. **2018**, *114*, 131–142, doi: 10.1016/j. Envint.2018.02.003.

[29] Zhang, L.; Yin, M.; Qiu, J.; Qiu, T.; Chen, Y.; Qi, S.; Wei, X.; Tian, X.; Xu, D. An electrochemical sensor based on CNF@AuNPs for metronidazole hypersensitivity detection, *Biosens. Bioelectron*. *X*. **2022**, *10*, 100102, doi: 10.1016/j.biosx.2021.100102.

[30] Gopi, Kesavan, P. K. G.; Chen, S. M.; Ravikumar, C. H. Cadmium sulfide quantum dots anchored on reduced graphene oxide for the electrochemical detection of metronidazole, *New J. Chem*. **2021**, *45*, 3022–3033, doi: 10.1039/d0nj05501h.

[31] Nejati, K.; Asadpour-Zeynali, K. Electrochemical synthesis of nickel-iron layered double hydroxide: application as a novel modified electrode in electrocatalytic reduction of metronidazole. *Mater. Sci. Eng. C* **2014**, *35*, 179–184, doi: 10.1016/j.msec.2013.11.003.

[32] Kesavan, G.; Chen, S. M. Sonochemical-assisted synthesis of zinc vanadate microstructure for electrochemical determination of metronidazole, *J. Mater. Sci. Mater. Electron*. **2021**, *32*, 9377–9391, doi: 10.1007/s10854-021-05601-6.

[33] Baikeli, Y.; Mamat, X.; Wumaer, M.; Muhetaer, M.; Aisa, H.;A.; Hu, G. Electrochemical determination of metronidazole using a glassy carbon electrode modified with nanoporous bimetallic carbon derived from a ZnCo-based metal-organic framework. *J. Electrochem. Soc*. **2020**, *167*, 116513, doi: 10.1149/1945-7111/ab9d94.

[34] Yalikun, N.; Mamat, X.; Li, Y.; Hu, X.; Wang, P.; Hu, G. N, S, P-triple doped porous carbon as an improved electrochemical sensor for metronidazole determination. *J. Electrochem. Soc*. **2019**, *166*, B1131–B1137, doi: 10.1149/2.0321913jes.

[35] Karthik, R.; Mutharani, B.; Chen, S. M.; Kumar, J. V.; Abinaya, M.; Chen, T. W.; Lei, W.; Hao, Q. Synthesis, characterization and catalytic performance of nanostructured dysprosium molybdate catalyst for selective biomolecule detection in

biological and pharmaceutical samples, *J. Mater. Chem. B*. **2019**, *7*, 5065–5077, doi: 10.1039/c9tb01020c.

[36] Zoubir, J.; Bougdour, N.; Radaa, C.; Idlahcen, A.; Bakas, I.; Assabbane, A. Elaboration of a novel nanosensor using nanoparticles of α-Fe2O3 magnetic cores for the detection of metronidazole drug. urine human and tap water, *Sensors Int*. **2022**, *3* , 100160, doi: 10.1016/j.sintl.2022.100160.

[37] Kesavan, G.; Vinothkumar, V.; Chen, S. M.; Thangadurai, T. D. Construction of metal free oxygen-doped graphitic carbon nitride as an electrochemical sensing platform for determination of antimicrobial drug metronidazole, *Appl. Surf. Sci*. **2021**, *556*, 149814, doi: 10.1016/j.apsusc.2021.149814.

[38] Mao, A.; Li, H.; Yu, L.; Hu, X. Electrochemical sensor based on multi-walled carbon nanotubes and chitosan-nickel complex for sensitive determination of metronidazole. *J. Electroanal. Chem*. **2017**, *799*, 257–262, doi: 10.1016/j.jelechem.2017.05.049.

[39] Darbandi, M.; Mohajer, M. F.; Eynollahi, M.; Asadpour-Zeynali, K. Sensitive sensing platform based on NiO and NiO-Ni nanoparticles for electrochemical determination of Metronidazole, *Chem. Phys*. **2022**, *560*, 111590, doi: 10.1016/j.chemphys.2022.111590.

[40] Saedi, H.; Fat'hi, M. R.; Zargar, B. Synthesis of AgNPs functionalized CuMOF/PPy–rGO nanocomposite and its use as an electrochemical sensor for metronidazole determination, *J. Chin. Chem. Soc*. **2021**, *68*, 1954–1964, doi: 10.1002/jccs.202100081.

[41] Zoubir, J.; Radaa, C.; Idlahcen, A.; Bakas, I.; Assabbane, A. A new voltammetric sensor for metronidazole based on electrocatalytic effect of Al_2O_3 modified carbon graphite. application. urine, tap water and river water, *Mater. Sci*. *Energy Technol*. **2021**, *4*, 296–306, doi: 10.1016/j.mset.2021.08.003.

Chapter 6

Developing a Sensitive Electrochemical Sensor for the Detection of Levofloxacin (LEVO) through a Sequential Electrodeposition of Graphene and Copper on GCE

6.1 Introduction

Even in today's technically developed society, human beings are still affected by life threatening infections caused by microbes including, respiratory tract infections, cellulitis, urinary tract infections, prostatitis, anthrax, endocarditis, meningitis, pelvic inflammatory disease, diarrhea, and tuberculosis. In order to treat these infections, various pharmaceutical antibiotics are extensively employed worldwide. Among the most important classes of synthetic antibacterial agents, fluoroquinolones are widely utilised in human therapy, veterinary medicine and breeding industries due to their effectiveness since 1980 [1]. Levofloxacin (LEVO) is one of the third-generation fluoroquinolone antibiotics [2]. As a specific type of fluoroquinolone antibacterial agent, LEVO is active against most gram-negative, some gram-positive and anaerobic bacteria [3] as well as mycobacteria and rickettsias [4]. Nowadays, LEVO is commonly applied to the clinical treatment of the genitourinary, respiratory and gastrointestinal tracts as well as skin and soft-tissue infections [5]. Although LEVO can be used to treat these severe infections, the excessive intake of LEVO can lead to infection resistance and serious side effects including liver problems**,** abdominal discomfort, angioneurotic edema and immunity disfunction and so on [6,7]. Moreover, the concentration of LEVO in water environments is increasing owing to the release of the metabolites from human and animal bodies and the wastewater generated by pharmaceutical factories and human residential areas [8], leading to the LEVO accumulation, which may pose a major risk to the ecological environment and human health, due to the emergence of potential drug-resistant bacteria. Therefore, it is essential to implement highly sensitive and stable techniques to analyse LEVO in versatile applications, such as environmental, pharmaceutical, and dietary sectors.

Up to now, numerous analytical techniques have been applied to determine the levels of LEVO, including liquid chromatography [9], surface-enhanced Raman scattering [10], chemiluminescence [11], spectrophotometry [12], nuclear magnetic resonance spectroscopy [13] and capillary electrophoresis [14]. However, most of these methods are deficient in simplicity and cost-effectiveness, such as complex

pre-treatment steps, time-consuming, complicated and expensive instrument. Compared to the above traditional analytical technologies, the electrochemical method has gained wide attention due to non-expensive instrumentation, easy operation, short analysis time, high sensitivity and selectivity, long-term stability and outstanding repeatability. However, the untreated or unmodified electrodes employed for the electrochemical analysis normally exhibit poor performance because of their surface being easily contaminated by analytes and intermediate products generated by the electrochemical reactions on the electrode. To solve these problems, the surfaces of glassy carbon electrodes have been decorated by using various modifiers including noble metals nanoparticles [15] and metal oxides [16], carbon-based nanomaterials such as carbon nanotubes (CNT) [17], reduced graphene oxide (rGO) [18] and conductive polymers [19], to give improved performance in the detection of LEVO.

Copper is an abundant metal on the earth's crust with little toxicity. It is inexpensive and has excellent conductivity, ductility and stability. The Cu nanoparticles (CuNPs) retain their original property while endowing it with new physical and chemical features. The CuNPs-based modified electrodes have been extensively studied as sensors [20]. Da Silva et al. synthesised rGO supported CuNPs (rGO/CuNPs) by the reduction of sodium borohydride, then the suspension containing CuNPs/rGO was dropped onto the GCE surface to construct the GCE/rGO/CuNPs electrode, which was used for the electrochemical detection of LEVO, achieving a LOD of 17 nM using DPV [21]. While this study indicated that the CuNPs can be used as a sensor to detect LEVO, some improvements can be made: (i) the CuNPs/rGO nanocomposite needed to be pre-prepared, resulting in the time-consuming and complex steps, (ii) the SEM image of the CuNPs/rGO did not show the uniform distribution of CuNPs on the rGO, (iii) the GCE was modified by dropping the CuNPs/rGO nanocomposite on the surface and drying, which may lead to instability of the modified electrode during the electrochemical measurements in the solution. To improve on this study, in this chapter, the electrodeposition of Gr and Cu was performed on the GCE to construct the GCE/Gr/Cu electrode, which was employed for the electrochemical detection of LEVO. No drop casting was necessary, the CuNPs were electrodeposited uniformly on the Gr using a pulsed deposition method to give very good reproducibility. Furthermore, the

results indicate that the preparation process of the sensor is time-saving with simple steps to give good stability of the prepared GCE/Gr/Cu in the electrochemical detection of LEVO.

6.2 Experimental Section

The phosphate buffer solutions (PBS, 0.1 M) at pH 4.0 to pH 10.0 were prepared with the combination of K_2HPO_4 and H_3PO_4. LEVO solution (0.1 mM) was prepared according to the procedure in Section 2.2.3.5. The mixed solution of $K_4Fe(CN)_6$ + $K_3Fe(CN)_3$ (1.0 mM) was prepared according to the procedure in Section 2.2.3.8. Gr dispersion was prepared according to the details in Section 2.2.3.9, respectively. The $Cu(Ac)_2$ solution (10 mM, pH 4.5) and NaOH solution (0.1 M) were prepared using the procedures in Sections 2.2.3.10 and 2.2.3.11, respectively. All the aqueous solution was prepared in double-distilled water at room temperature.

The modified electrodes, GCE/Gr, GCE/Cu and GCE/Gr/Cu, were fabricated according to the procedures in Sections 2.2.4.3, 2.2.4.4 and 2.2.4.7, respectively. The electroactive surface areas of bare GCE, GCE/Cu, GCE/Gr and GCE/Gr/Cu were measured in 1.0 mM $[Fe(CN)_6]^{3-/4-}$ containing 0.1 M KCl. The morphology and composition of the modified electrodes were characterised using SEM, EDX and elemental mapping. SEM with a Hitachi S–3200–N microscope was employed for the surface morphology characterisation and an Oxford Instrument INCAz-act ESX was used for EDX studies to analyse the chemical composition of the modified electrodes. Electrochemical studies were performed via electrochemical workstation (CHI700C, CHI760C) and Potentiostat (Solartron 1287 coupled with a 1255 FRA). The bare GCE and the modified GCE were employed as working electrodes, Ultra-pure Pt wire and saturated calomel electrode (SCE) were used as counter and reference electrodes in a three-electrode electrochemical system. Unless otherwise stated, the CV experiments were performed at a scan rate of 50 mV s^{-1}. The DPV data were recorded with a pulse amplitude of 50 mV, a pulse width of 0.05 s, sampling width of 0.0167 s, a pulse period of 0.50 s, and an increment of 4 mV.

6.3 Results and Discussions

6.3.1 Electrochemical behaviour of LEVO

The electrochemical behaviour of LEVO was studied in 0.1 mM LEVO at bare GCE. The CV curve of LEVO at bare GCE is shown in Figure 6-1, it can be seen that there is an oxidation peak at 0.95 V vs. SCE, with no corresponding reduction wave, suggesting that the oxidation of LEVO undergoes an irreversible electrochemical reaction process, which can be described in Scheme 6-1. This mechanism, which involves the transfer of two electrons and two protons, is based on the proposed oxidation mechanism reported in the literature [22].

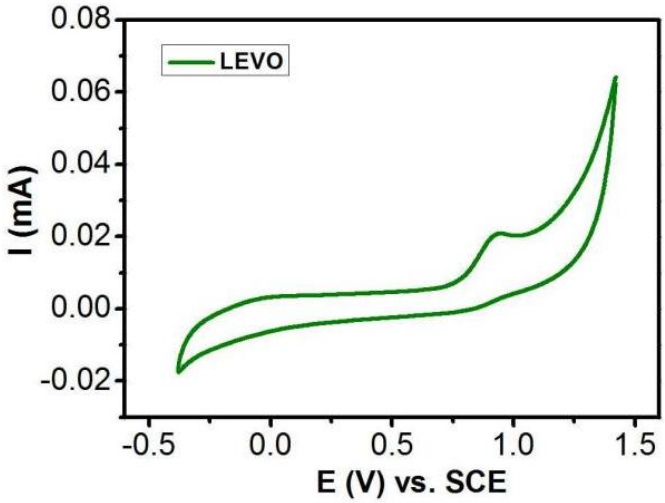

Figure 6-1. CV curve of bare GCE recorded in 0.1 mM LEVO in PBS at pH 7.

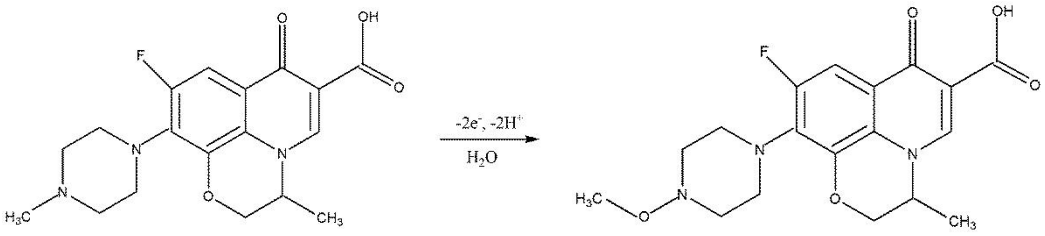

Scheme 6-1. Schematic illustrating the electrochemical oxidation of LEVO [22].

Figure 6-1 clearly illustrates the electrochemical activity of LEVO. Unfortunately, the oxidation current value of LEVO at the unmodified GCE is low, thereby the GCE needs to be modified or functionalised to improve its sensitivity for the determination of LEVO. Both Gr and Cu were chosen as the modifiers for the functionalisation of GCE.

6.3.2 Preparation of the Gr film modified electrode

The Gr film was fabricated on the GCE by cycling within potential range from 0.8 V to –1.5 V vs. SCE at 50 mV s^{-1} for 10 cycles to form the GCE/Gr electrode. Typical voltammograms from 1 to 10 cycles in PBS are illustrated in Figure 6-2.

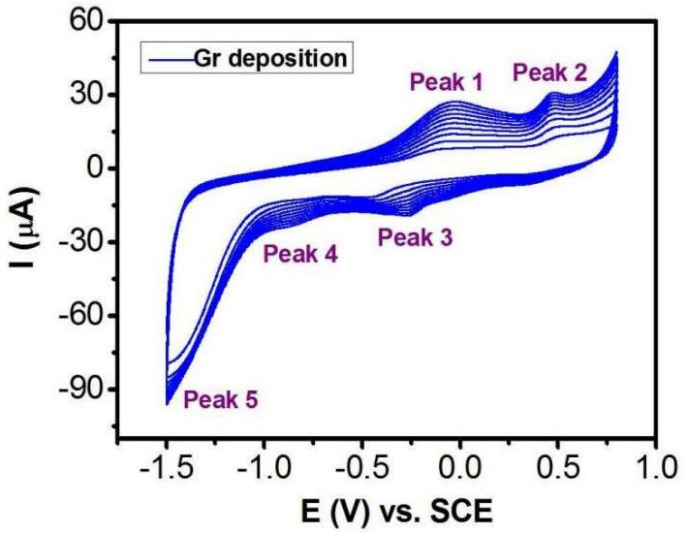

Figure 6-2. CV curves recorded in the potential range of –1.5 and 0.8 V vs. SCE at 50 mV s^{-1} in PBS (pH 7) during the deposition of Gr on GCE with 10 cycles.

It is evident that there are two oxidation waves at about 0 V (peak 1) and 0.48 V (peak 2) vs. SCE, while two reduction waves are observed at about –0.27 V (peak 3) and –1.5 V (peak 5) vs. SCE. Moreover, a smaller less defined reduction wave appears at about –0.87 V vs. SCE (peak 4). For all peaks (peaks 1-5), the peak currents increase with the increase of cycling, this is related to the oxidation and reduction of the Gr. The peaks 1 and 2 can be considered as the formation of oxygen-containing groups on the Gr while the peaks 3-5 correspond to the reduction of the oxygen-containing groups formed on the Gr. Furthermore, it can be seen that for peak 2, as the number of cycles

increases, the oxidation peak potentials remain basically unchanged, however for peaks 1 and 3, the considerable shifts in the potentials are observed, for peak 1, increasing from about –0.065 V for the first cycle to about –0.018 V vs SCE for 10th cycle, while for peak 3, increasing from about –0.45 V for the first cycle to about –0.26 V vs SCE for 10th cycle.

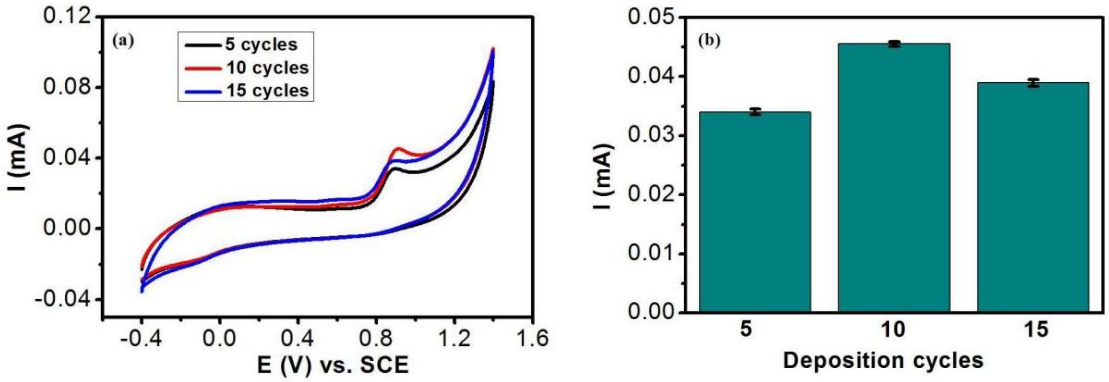

Figure 6-3. (a) CV curves of GCE/Gr recorded in 0.1 mM LEVO with the different scanning cycles of 5, 10, 15 for the deposition of Gr and **(b)** the oxidation peak current recorded in 0.1 mM LEVO as a function of the scanning cycles (n = 3).

In order to obtain the best performance for the detection of LEVO, different scanning cycles, including 5, 10, and 15 cycles, were designed to electrochemically deposit Gr on the GCE. After different scanning cycles, the prepared GCE/Gr was used for the detection of LEVO and the corresponding CV curves were recorded and shown in Figure 6-3 (a)**,** whilst the oxidation peak currents were computed and plotted as a function of scanning cycles, as shown in Figure 6-3 (b)**.** It is evident that 10 cycles give the highest peak current for the oxidation of LEVO. This may be the reason that the Gr film generated during 5 scanning cycles is thinner, while the Gr film generated during 15 scanning cycles is thicker, resulting in a decrease in conductivity. Accordingly, 10 cycles were considered as the optimal scanning cycles for the deposition of Gr onto the GCE.

6.3.3 Preparation of the Cu film modified electrode

The copper film modified electrode was prepared by the electrochemical reduction of Cu(II) to metallic Cu followed by the deposition of Cu on the surface of GCE. The copper complex, $Cu(Ac)_2$ solution, was employed. As shown in Figure 6-4, the CV curve of $Cu(Ac)_2$ at bare GCE gives a reduction peak at –0.17 V vs. SCE corresponding to the reduction of Cu(II) to Cu(0) and a oxidation peak at 0.14 V vs. SCE corresponding to the oxidation of Cu(0) to Cu(II). Based on this CV curve and according to the procedure described in the literature [23], a potentiostatic triple-pulse procedure was employed for the electrodeposition of Cu at the GCE or the GCE/Gr electrode.

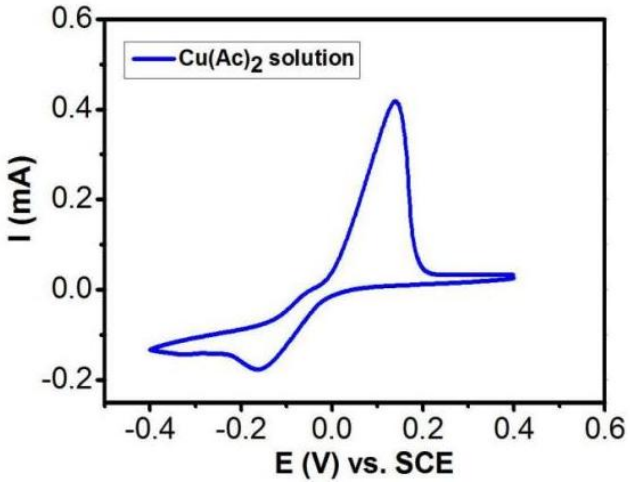

Figure 6-4. CV curve of bare GCE recorded in 10 mM $Cu(Ac)_2$ at a pH of 4.5.

First, a potential of 0.7 V vs. SCE was applied to the GCE or GCE/Gr for 5 s to remove any pre-adsorbed Cu^{2+} ions from the surface of the electrode, then the potential of –0.45 V was applied to the GCE or GCE/Gr for 2.5 s to seed sufficient copper nuclei at the surface of the GCE or GCE/Gr and finally, the potential of –0.25 V was applied to the GCE or GCE/Gr for 50 s to allow the growth of the copper nuclei to form CuNPs with certain size and shape. Further, the influence of the deposition time for the

electrodeposition of Cu on the performance of the GCE/Cu electrode for the detection of LEVO was investigated, Figure 6-5.

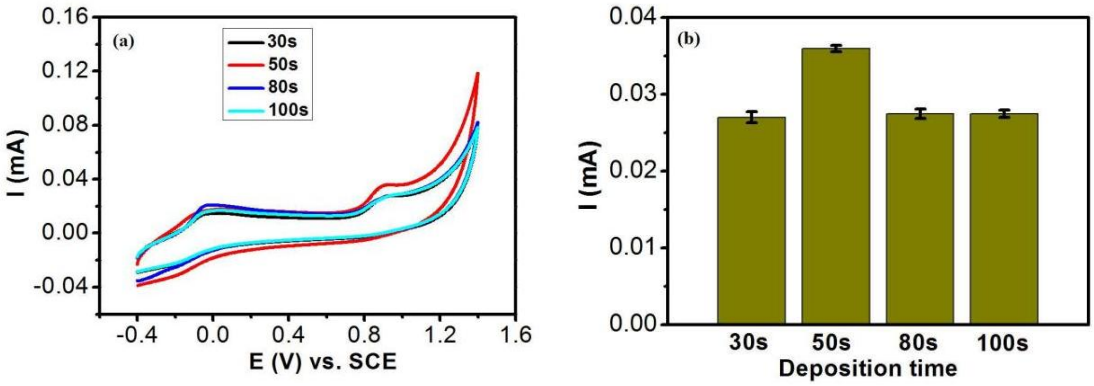

Figure 6-5. (a) CV curves of GCE/Cu recorded in 0.1 mM LEVO with the different deposition periods of 30 s, 50 s, 80 s and 100 s for the GCE/Cu electrode and **(b)** the oxidation peak current recorded in 0.1 mM LEVO as a function of the deposition period of Cu on the GCE, n = 3.

As revealed in Figure 6-5, when the deposition time of Cu increases from 30 s to 100 s, the oxidation peak current of GCE/Cu in 0.1 mM LEVO is increased from 30 s to 50 s, whereas when the deposition time of Cu is more than 50 s, the deposition of Cu is less effective. This may be the reason that a short deposition time (30 s) generates CuNPs with small size, while a long deposition time (more than 50 s) generates CuNPs with too large size. These CuNPs are not conducive to the oxidation of LEVO. A deposition time of 50 s produces CuNPs with a suitable size. These CuNPs are conducive to the oxidation of LEVO, thereby, the time of 50 s was selected as the best deposition period to decorate the CuNPs onto GCE and GCE/Gr. Interestingly, on comparing Figure 6-5 and Figure 6-3, it is evident that a new oxidation wave emerges in the vicinity of 0.0 V for the GCE/Cu, which is clearly connected with the deposited CuNPs. This seems to be related to the oxidation of the CuNPs, with the conversion of Cu to Cu_2O. A corresponding reduction wave is evident at about –0.2 V and this indicates the conversion of Cu_2O back to Cu.

6.3.4 Comparison of four electrodes for the electrochemical detection of LEVO

Based on the investigation above, the optimal experimental conditions, scanning cycles of 10 for the deposition of Gr and deposition time of 50 s for the fabrication of CuNPs, were utilised to construct three modified electrodes, GCE/Gr, GCE/Cu and GCE/Gr/Cu. Subsequently, the performance of the three modified electrodes for the oxidation of LEVO were compared with the unmodified GCE. Figure 6-6 illustrates the CV curves of the four electrodes recorded in 0.1 mM LEVO. By comparing the oxidation peak currents for each electrode, it is noticed that the unmodified GCE gives a low oxidation current of 0.02 mA, after the modification of Gr, the GCE/Gr electrode gives an oxidation current of 0.046 mA, whilst the GCE/Cu electrode gives an oxidation current of 0.034 mA. However an impressive peak current of 0.082 mA was found when the GCE/Gr/Cu electrode was used. Therefore, the highest peak current is achieved with the modification of GCE with the combination of CuNPs and the deposited Gr. The peak current value of the GCE/Gr/Cu was 4.1 times higher than that of the unmodified GCE. In addition, good reproducibility was achieved as illustrated in Table 6-1, where the data from four independent experiments are summarised together with the RSD %. Indeed, the greatest reproducibility is achieved with the GCE/Gr/Cu.

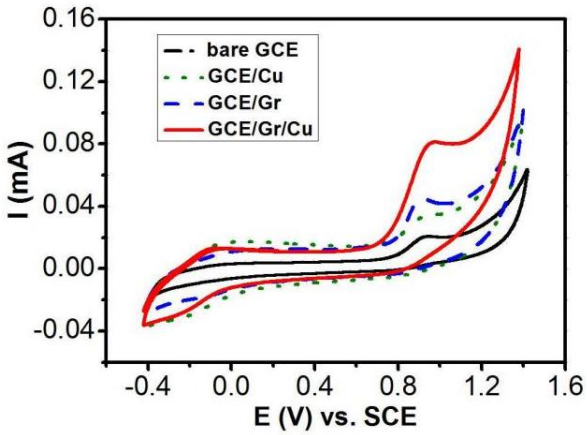

Figure 6-6. CV curves of bare GCE, GCE/Cu, GCE/Gr and GCE/Gr/Cu recorded in 0.1 mM LEVO in PBS (pH 7.0) at 50 mV s^{-1}.

Table 6-1. Reproducibility of GCE/Cu, GCE/Gr and GCE/Gr/Cu in the detection of LEVO.

0.1 mM LEVO	Oxidation Peak Current (μA)					Mean (n = 5)	RSD (%) (n = 5)
	1	2	3	4	5		
GCE/Cu	31.65	31.37	31.89	32.18	31.47	31.71 ± 0.35	1.08
GCE/Gr	46.20	45.55	44.25	45.20	45.85	45.41 ± 0.75	1.65
GCE/Gr/Cu	81.44	79.81	80.27	80.97	80.52	80.60 ± 0.63	0.78

6.3.5 Effective surface areas

The effective surface areas of the four electrodes including bare GCE, GCE/Cu, GCE/Gr and GCE/Gr/Cu were measured. The mixed solution containing 1.0 mM $[Fe(CN)_6]^{3-}/[Fe(CN)_6]^{4-}$ and 0.1 M KCl was employed as a probe, and then the CV curves of these four electrodes in this solution were recorded at different scan rates, Figure 6-7. The quasi-reversible behaviour of the probe is clearly evident in Figure 6-7, with the peak currents increasing with an increase in the scan rate. Using the oxidation peak current corresponding to the conversion of Fe (II) to Fe (III), the peak current was recorded as a function of the square root of the scan rate and is plotted in Figure 6-7. It can be seen that linear plots were obtained with the four electrodes, giving the linear regression equations as $I = 5.05 \times 10^{-5}\, v^{1/2} - 9.70 \times 10^{-7}$ ($R^2 = 0.999$) for the bare GCE, $I = 5.65 \times 10^{-5}\, v^{1/2} - 6.68 \times 10^{-7}$ ($R^2 = 0.998$) for the GCE/Cu, $I = 8.19 \times 10^{-5}\, v^{1/2} - 4.22 \times 10^{-6}$ ($R^2 = 0.999$) for the GCE/Gr and $I = 1.03 \times 10^{-4}\, v^{1/2} - 1.05 \times 10^{-6}$ ($R^2 = 0.994$) for the GCE/Gr/Cu. The Randles-Sevcik equation described in Equation 6–1 was applied to compute the effective surface area of the electrodes.

$$\boldsymbol{i_p = (2.69 \times 10^5)\, n^{3/2} D^{1/2} v^{1/2} AC} \qquad (6\text{–}1)$$

Here $\boldsymbol{i_p}$ is the peak current (A), $\boldsymbol{n}$ is the number of electrons, $\boldsymbol{D}$ is the diffusion coefficient ($cm^2\ s^{-1}$), $\boldsymbol{v}$ is the scan rate ($V\ s^{-1}$) and C is the concentration (mol/mL), and $\boldsymbol{A}$ is the effective surface area of the electrode (cm^2).

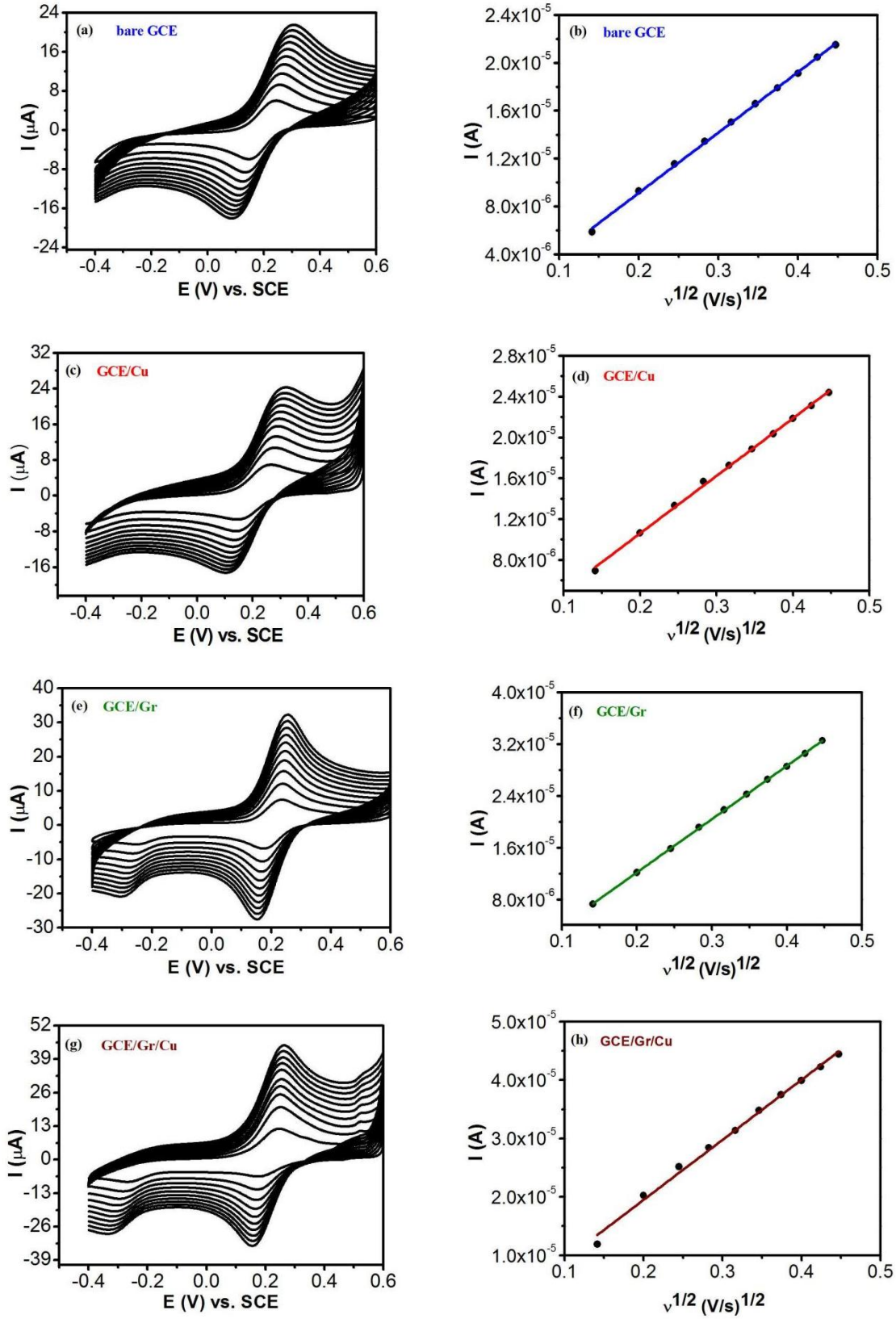

Figure 6-7. CV curves of bare GCE **(a)**, GCE/Cu **(c)**, GCE/Gr **(e)** and GCE/Gr/Cu **(g)** in 1.0 mM $[Fe(CN)_6]^{3-}/[Fe(CN)_6]^{4-}$ solution containing 0.1 M KCl at scan rates, 20, 40, 60, 80 100, 120, 140, 160, 180 and 200 mV s^{-1}; the oxidation peak current as a function of the square root of the scan rate for bare GCE **(b)**, GCE/Cu **(d)**, GCE/Gr **(f)** and GCE/Gr/Cu **(h)**, n = 3.

Using Equation 6-1, the surface areas were calculated as, 0.068 cm^2 ± 0.0015 for bare GCE, 0.076 cm^2 ± 0.0023 for the GCE/Cu, 0.11 cm^2 ± 0.0019 for the GCE/Gr and 0.14 cm^2 ± 0.0035 for the GCE/Gr/Cu. It is obvious that the effective surface area of the electrodes increases with the modifications, and this increasing surface area is consistent with the enhanced electrochemical oxidation of LEVO with the GC/Gr/Cu seen in Figure 6-6.

It is also evident from a comparison of the CVs in Figure 6-7 that the GCE/Gr and GCE/Gr/Cu exhibit more facile electron transfer. This is evident from the peak to peak separations, which were computed as 0.14 V ± 0.0035, 0.12 V ± 0.0025, 0.079 V ± 0.0019 and 0.075 V ± 0.0028 for the GCE, GCE/Cu, GCE/Gr and GCE/Gr/Cu at a scan rate of 60 mV s^{-1}. Therefore, it appears that the enhanced detection of LEVO at the GCE/Gr/Cu is connected to both an increase in the electroactive surface area and to a more conducting interface that facilitates the electron transfer step.

6.3.6 Morphology characterisation of GCE/Gr and GCE/Gr/Cu surface

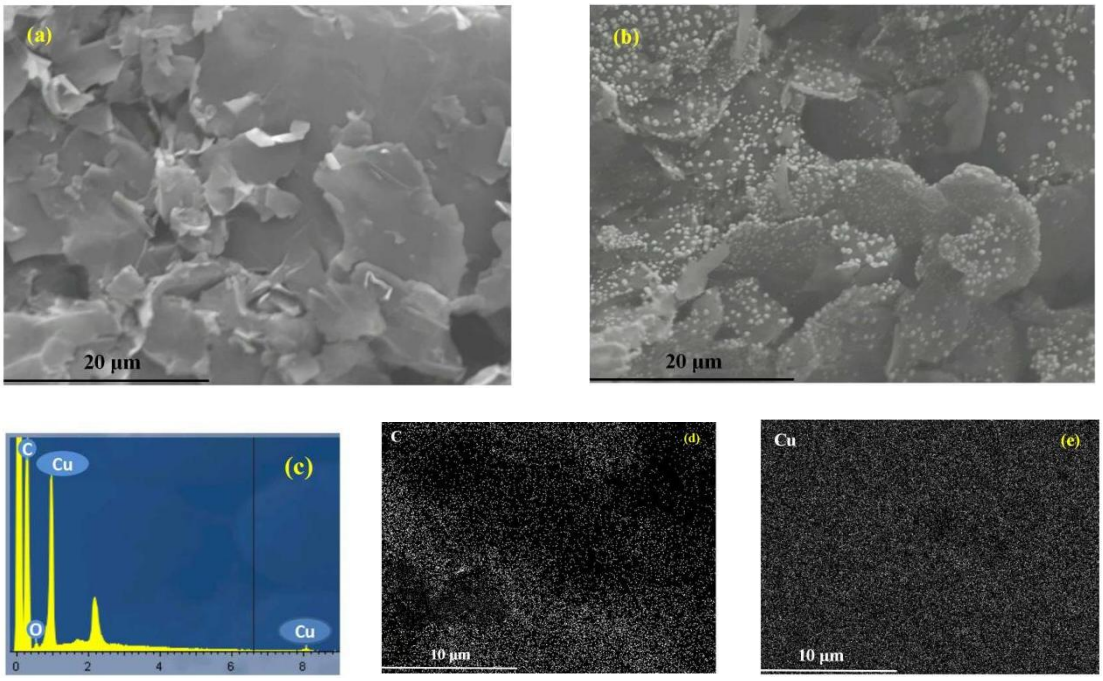

Figure 6-8. SEM micrographs of **(a)** GCE modified with electrodeposited Gr, **(b)** GCE modified with electrodeposited Gr and Cu, **(c)** EDX spectrum recorded at GCE/Gr/Cu and **(d,e)** mapping of C and Cu at the GCE/Gr/Cu.

SEM, EDX and elemental mapping techniques have been widely used to characterise the morphology and composition of the species on the solid surface. Here, the morphologies and composition of the prepared GCE/Gr and GCE/Gr/Cu electrodes were characterised by SEM, EDX and elemental mapping, as shown in Figure 6-8.

The SEM micrographs of the GCE/Gr and GCE/Gr/Cu electrodes are revealed in Figure 6-8 (a-b). It can be seen in Figure 6-8 (a) that the Gr sheets are well dispersed over the entire surface of the electrode, but with some aggregation observed at some sites. After the deposition of Cu for 50 s, as shown in Figure 6-8 (b) for the GCE/Gr/Cu electrode, it is evident that the CuNPs have been mostly deposited onto the Gr sheets, with the Cu deposition adopting ball like deposits and some larger nanoparticles. The typical size of the CuNPs were approximately 150 nm. Moreover, the EDX spectrum of the GCE/Gr/Cu electrode shows the presence of C and Cu, Figure 6-8 (c), clearly indicating that the Cu has been deposited on the electrode. Also, the mapping data for C and Cu, illustrated in Figure 6-8 (d, e), suggest that both the C and Cu are approximately evenly dispersed across the electrode surface. The EDX shows only a low signal for O, which suggests that the copper deposits are largely metallic nanoparticles, CuNPs.

6.3.7 Electrochemical characterisation of GCE/Cu, GCE/Gr and GCE/Gr/Cu in NaOH

To further confirm the deposition of Cu and Gr on the GCE, the voltammograms of the three modified electrodes were recorded in 0.1 M NaOH, Figure 6-9.

The following information can be obtained: (i) the CV curve of GCE/Cu in 0.1 M NaOH is similar to that reported in the literature [24], suggesting the CuNPs are crystalline, (ii) both the redox peaks of Cu in Figure 6-9 (a) and Gr in Figure 6-9 (b) are observed in Figure 6-9 (c)**,** demonstrating the deposition of Cu and Gr on the GCE, (iii) the redox peak current values of Cu for the GCE/Gr/Cu electrode are lower than that for the GCE/Cu electrode, meaning that the nucleation process on the Gr is more controlled compared to that on the GCE, owing to limited availability of active sites.

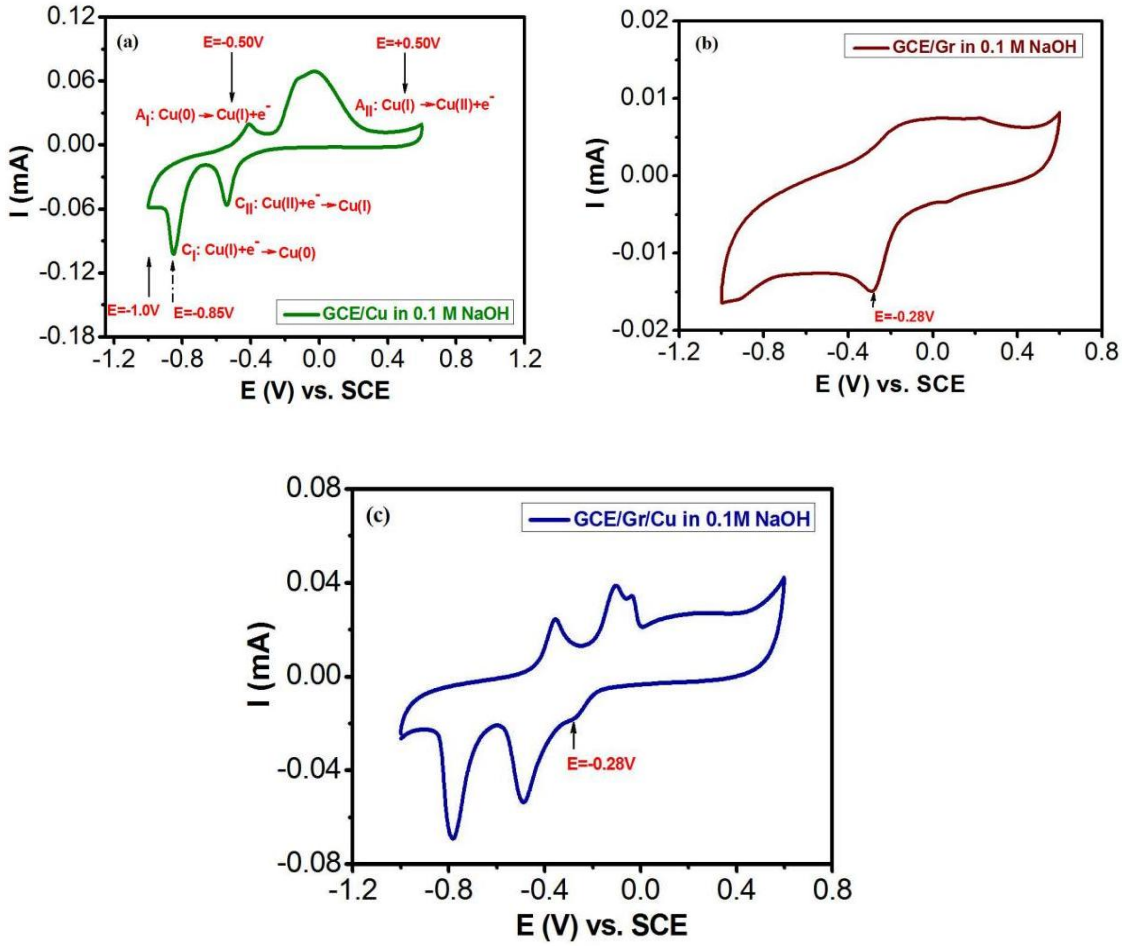

Figure 6-9. Voltammograms of the GCE/Cu **(a)**, GCE/Gr **(b)** and GCE/Gr/Cu **(c)** in 0.1 M NaOH with the scan rate of 20 mV s^{-1}.

6.3.8 Influence of scan rates

To understand the dynamic process of the developed electrochemical sensors in the oxidation reaction of LEVO, the effect of the scan rate on the electrochemical oxidation of LEVO was studied at different electrodes including the bare GCE, GCE/Cu, GCE/Gr, and GCE/Gr/Cu. The voltammograms of these electrodes recorded in 0.1 mM LEVO with different scan rates from 20 to 200 mV s^{-1} are displayed in Figure 6-10 (a), (b) and (c) for the bare GCE, Figure 6-11 (a), (b) and (c) for the GCE/Cu, Figure 6-12 (a), (b) and (c) for GCE/Gr and Figure 6-13 (a), (b) and (c) for GCE/Gr/Cu. The oxidation peak currents increase with respect to the increase in the scan rates for all the electrodes, Figure 6-10 (a) – Figure 6-13 (a). These observations were further analysed by plotting the oxidation peak current as a function of the square root of scan rates. As shown in Figure 6-10 (b) – Figure 6-13 (b), good linear relationships were obtained, giving

R^2 values and the linear regression equations as follows: $R^2 = 0.997$, $I = 0.0022\ v^{1/2} + 0.0013$ for the bare GCE, $R^2 = 0.999$, $I = 0.0039\ v^{1/2} + 0.00083$ for the GCE/Cu, $R^2 = 0.997$, $I = 0.0077\ v^{1/2} - 0.0046$ for the GCE/Gr and $R^2 = 0.997$, $I = 0.012\ v^{1/2} - 0.0051$ for the GCE/Gr/Cu, respectively. Furthermore, the logarithm of the oxidation peak current as a function of the logarithm of the scan rate was also plotted in Figure 6-10 (c) – Figure 6-13 (c), showing good linear relationships, providing the slopes of the logarithmic plots as 0.46 ± 0.012 for the bare GCE, 0.49 ± 0.011 for the GCE/Cu, 0.52 ± 0.015 for the GCE/Gr and 0.51 ± 0.017 for the GCE/Gr/Cu, respectively. These values are close to 0.5, further supporting a diffusion-controlled reaction process of LEVO on the surface of the four electrodes.

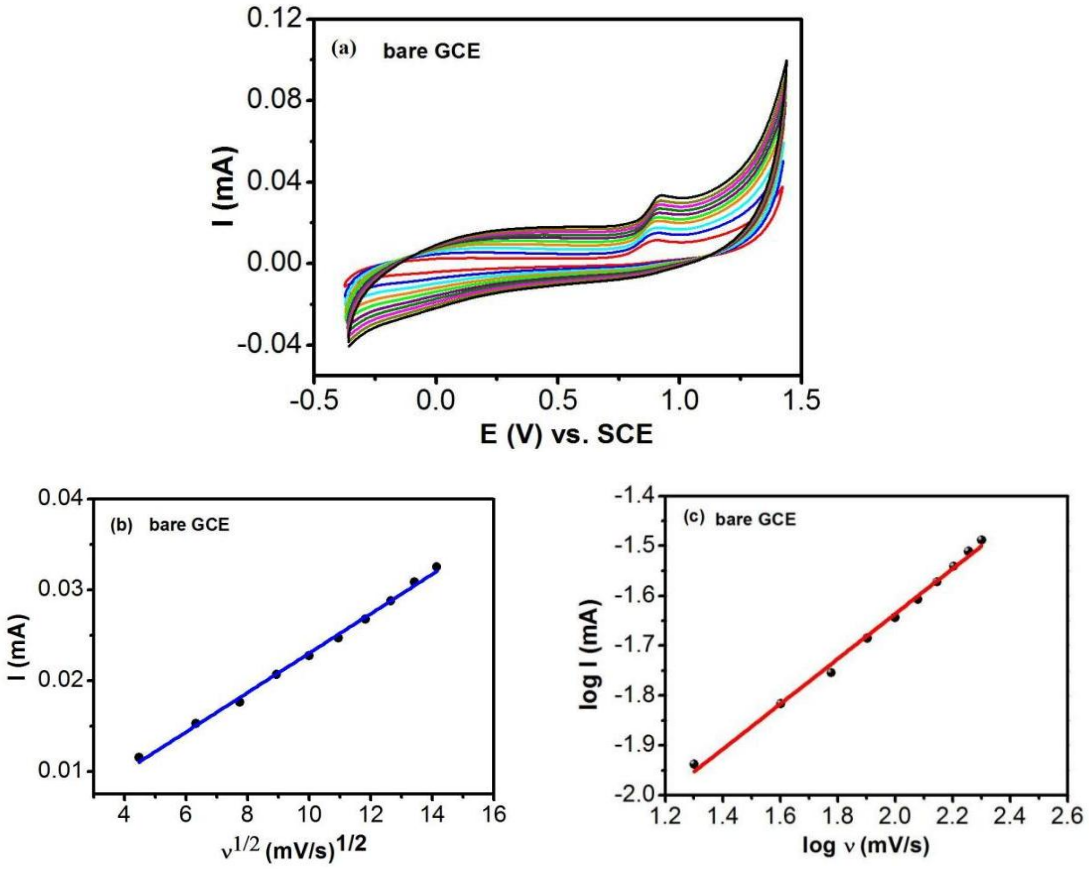

Figure 6-10. (a) CV curves of the bare GCE in 0.1 mM LEVO in PBS at scan rates between 20 and 200 mV s^{-1}, **(b)** peak currents plotted as a function of the square root of the scan rates and **(c)** logarithm of peak currents plotted as a function of the logarithm of scan rates, n = 3.

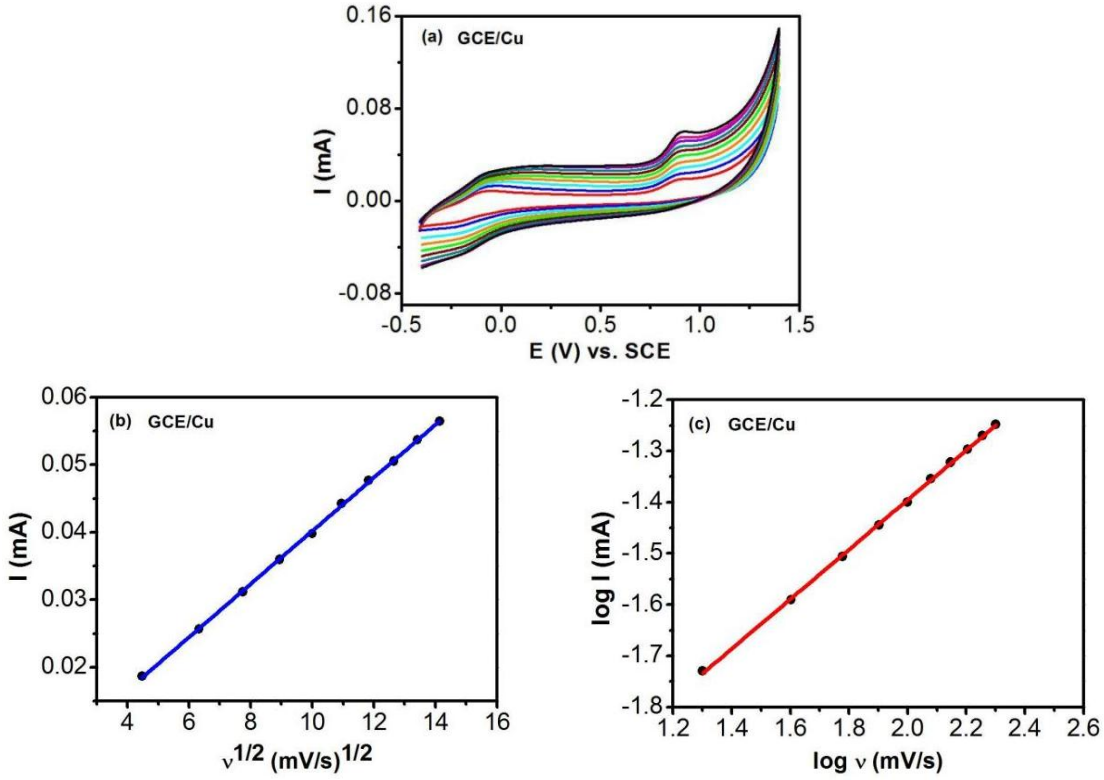

Figure 6-11. (a) CV curves of GCE/Cu in 0.1 mM LEVO in PBS at scan rates between 20 and 200 mV s^{-1}, **(b)** peak currents plotted as a function of the square root of the scan rates and **(c)** logarithm of peak currents plotted as a function of the logarithm of scan rates, n = 3.

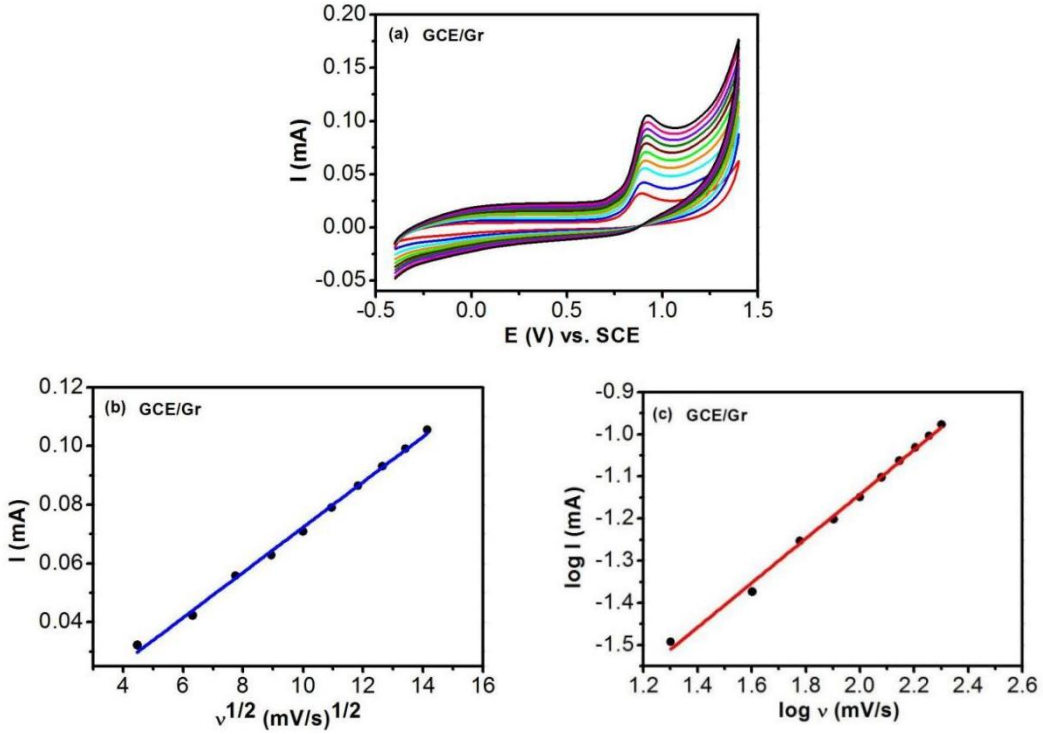

Figure 6-12. (a) CV curves of GCE/Gr in 0.1 mM LEVO in PBS at scan rates between 20 and 200 mV s^{-1}, **(b)** peak currents plotted as a function of the square root of the scan rates and **(c)** logarithm of peak currents plotted as a function of the logarithm of scan rates, n =3.

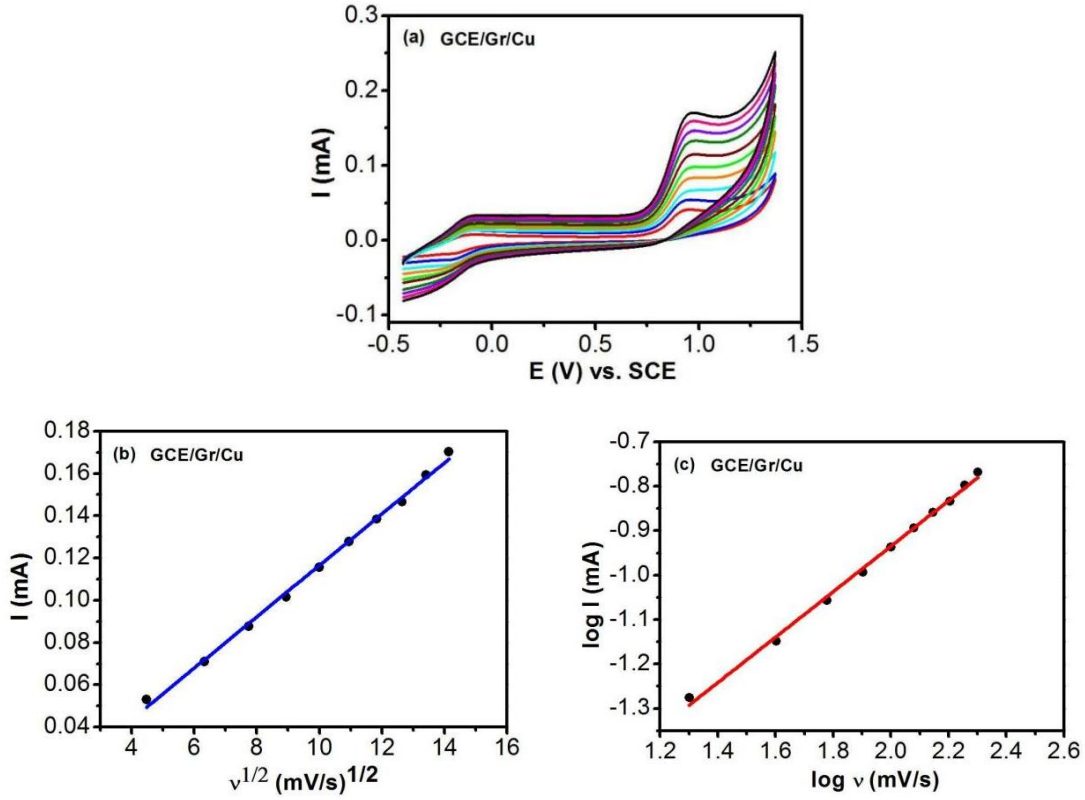

Figure 6-13. (a) CV curves of GCE/Gr/Cu in 0.1 mM LEVO in PBS at scan rates between 20 and 200 mV s^{-1}, **(b)** peak currents plotted as a function of the square root of the scan rates and **(c)** logarithm of peak currents plotted as a function of the logarithm of scan rates, n = 3.

Further, the rates of the electron transfer on four electrodes, bare GCE, GCE/Cu, GCE/Gr and GCE/Gr/Cu, were estimated using the Laviron method, which is expressed in Equation 6–2 and represents an irreversible redox reaction.

$$E_p = E^0 + \left(\frac{RT}{\alpha n F}\right)\ln\left(\frac{RTK_s}{\alpha n F}\right) + \frac{RT}{\alpha n F}\ln v \qquad (6–2)$$

In which, R, T and F stand for the gas constant, thermodynamic temperature, and Faraday constant, respectively, while E^0 represents the standard oxidation potential. The E^0 values were assessed as 806 mV vs. SCE for bare GCE, 820 mV vs. SCE for GCE/Cu, 813 mV vs. SCE for GCE/Gr and 864 mV vs. SCE for GCE/Gr/Cu by extrapolating the scan rate to 0 mV s^{-1}.

On plotting the peak potential (E_p) as a function of the natural logarithm of the scan rate (υ), linear plots were given for four electrodes, bare GCE, GCE/Cu, GCE/Gr

and GCE/Gr/Cu, as displayed in Figure 6-14, providing the linear regression equations as follows, E_p (V) = 0.034 lnυ (mV s^{-1}) + 0.806 (R^2 = 0.997) for the bare GCE, E_p (V) = 0.030 lnυ (mV s^{-1}) + 0.820 (R^2 = 0.997) for the GCE/Cu, E_p (V) = 0.026 lnυ (mV s^{-1}) + 0.813 (R^2 = 0.998) for the GCE/Gr and E_p (V) = 0.022 lnυ (mV s^{-1}) + 0.864 (R^2 = 0.998) for the GCE/Gr/Cu, respectively. On fitting these relationships to Equation 6–2, the K_s was computed as 26.31 s^{-1} ± 0.83 for the bare GCE, 33.33 s^{-1} ± 0.91 for the GCE/Cu, 38.46 s^{-1} ± 1.06 for the GCE/Gr and 46.17 s^{-1} ± 1.15 for the GCE/Gr/Cu, respectively. It is evident that the rate of the electron transfer on four electrodes increases with decorating with the Cu and Gr.

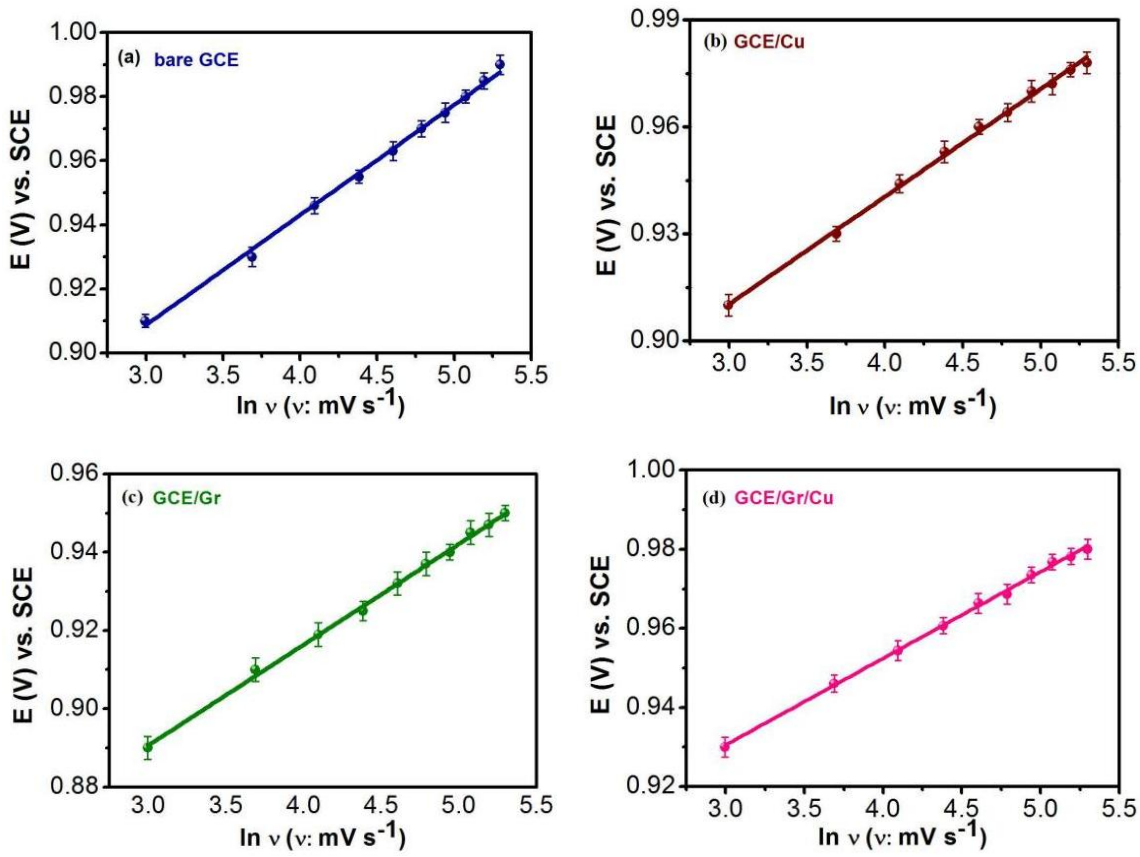

Figure 6-14. Peak potential plotted as a function of logarithm of scan rate in 0.1 mM LEVO for bare GCE **(a)**, GCE/Cu **(b)**, GCE/Gr **(c)** and GCE/Gr/Cu **(d)**, n = 3.

6.3.9 Influence of pH

As illustrated in Scheme 6.1, the oxidation of LEVO shows that the nitrogen moiety (–N-CH_3) in LEVO is oxidised to the –NO-CH_3 group, through a two-electron transfer reaction accompanied by the participation of two protons. Thus, the effect of the pH of the solution on the shift in the position of the oxidation peak of LEVO was investigated with the GCE/Gr/Cu electrode. The obtained results are exhibited in Figures 6-15, where Figure 6-15(a) represents the voltammograms of the GCE/Gr/Cu in 0.1 mM LEVO at different solution pH values of 4.0 to 11.

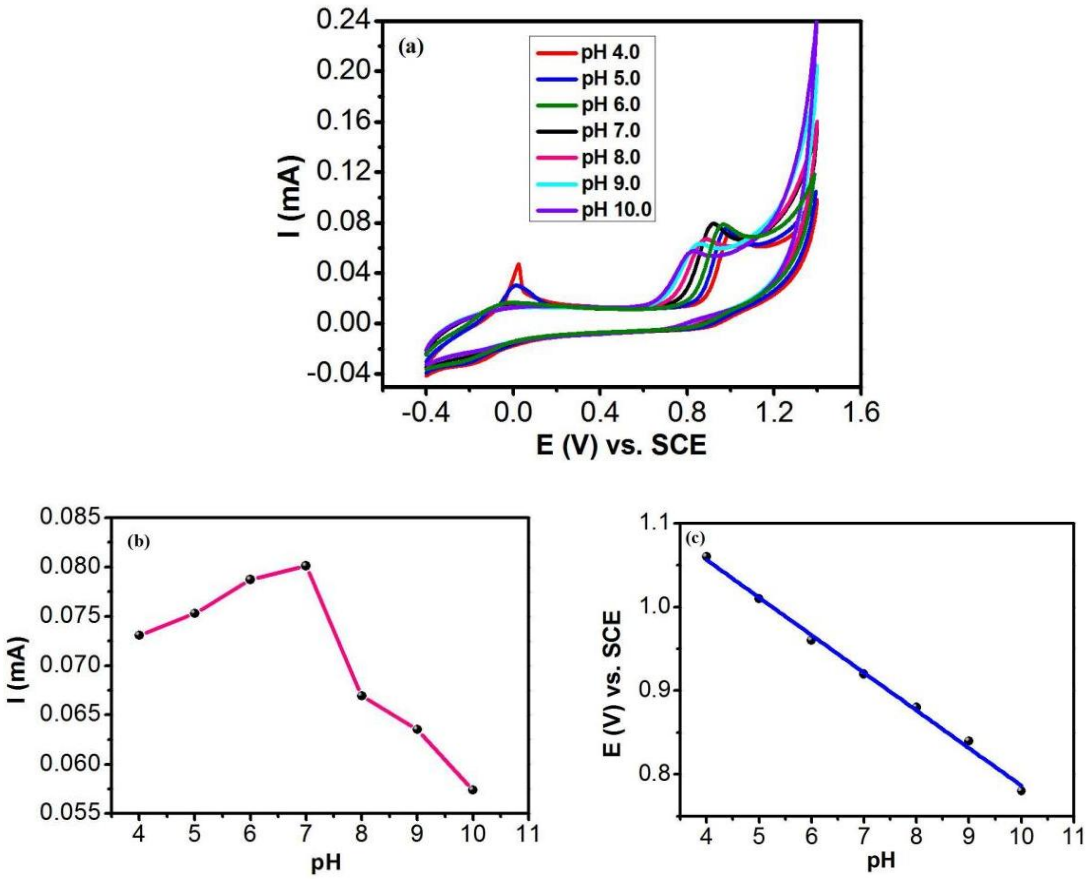

Figure 6-15. (a) CV curves of the GCE/Gr/Cu electrode in 0.1 mM LEVO in PBS with different pH values from 4 to 10, **(b)** oxidation peak currents versus pH values and **(c)** the relationship of oxidation peak potentials versus pH, n = 3.

It can be seen that the oxidation peak potential of LEVO shifts to lower values with an increase in the solution pH. This situation is related to the participation of the protons in the oxidation reaction process of LEVO, as illustrated in Scheme 6.1. Moreover, the effect of the solution pH on the oxidation peak current is displayed in Figure 6-15(b) with the GCE/Gr/Cu electrode. It is evident that the highest oxidation peak current appears at a pH of 7.0, thus the PBS with pH 7.0 was chosen to carry out the electrochemical detection of LEVO. Furthermore, the relationship between the solution pH and the oxidation peak potential of LEVO is summarised in Figure 6-15(c), where a linear region is obtained, providing the regression equation as $E = -0.046\ \text{pH} + 1.24$ ($R^2 = 0.996$). The obtained slope of 0.046 V/pH ±0.0013 displays some deviation from the theoretical slope of 0.0591(m/n) V/pH obtained from the Nernst equation at 298 K, where m expresses the number of protons transferred and n represents the number of electrons involved in the electron-transfer step.

6.3.10 Detection performance of the electrochemical sensor GCE/Gr/Cu

The sensing performance of the prepared GCE/Gr/Cu electrode in detecting LEVO was evaluated by varying the concentration of LEVO and the corresponding CV curves for a series of LEVO concentrations between 0.1 and 300 μM were recorded, Figure 6-16. The representative data are illustrated in Figure 6-16 (a). As can be seen clearly, the oxidation peak currents increase with an increase of the concentration of LEVO. When the oxidation peak current was plotted as a function of the concentration of LEVO from 0.1 and 300 μM, two linear regions were observed with different sensitivities, as represented in Figure 6-16 (b, c). As the concentration of the pollutants in the water environment is at lower levels, the low concentration range of 0.1 to 40 μM was taken as an example for the further study, giving a linear plot with a regression equation as $I\ (\mu A) = 1.39\ c\ (\mu M) + 15.27$ ($R^2 = 0.997$). According to the obtained sensitivity of 1.39 μA/μM ± 0.031 and the well-known equation for the LOD = $3S_b$/sensitivity, the LOD was computed as 11.86 nM ± 0.26.

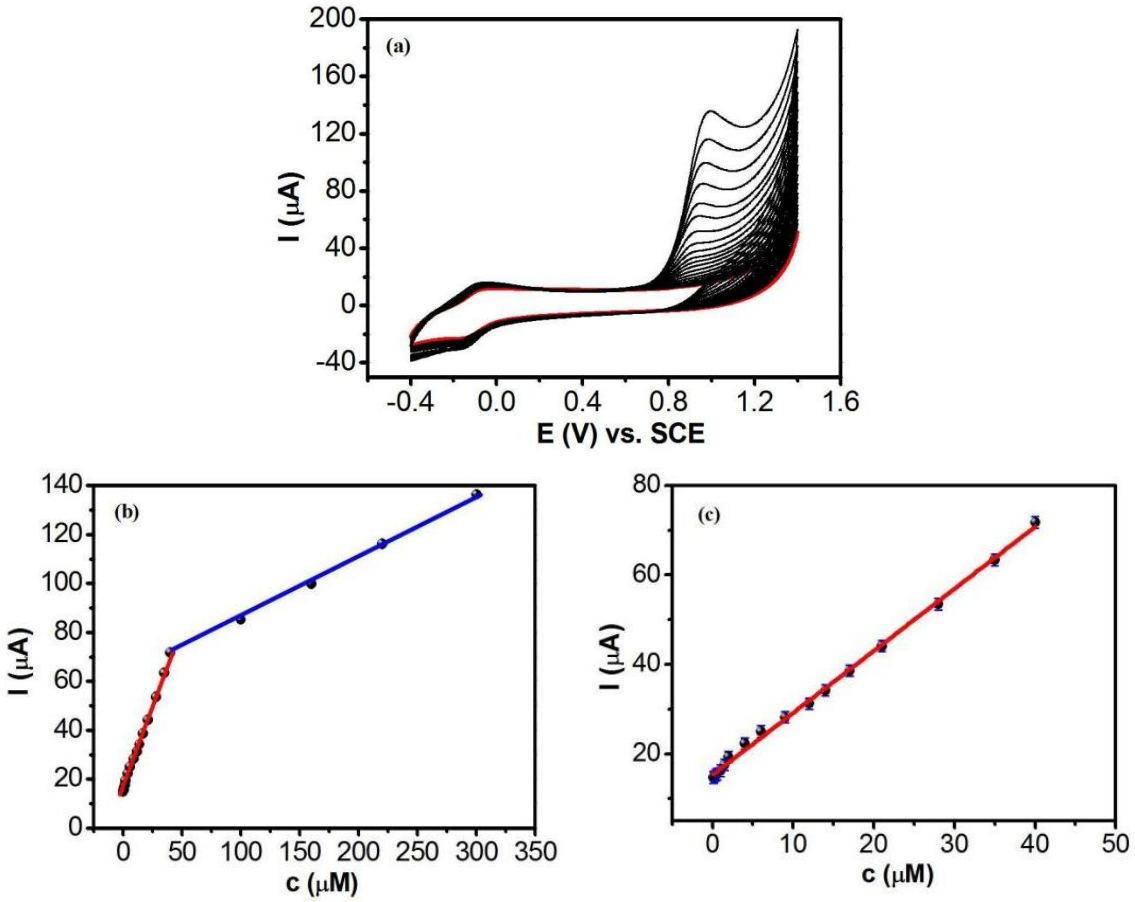

Figure 6-16. (a) Voltammograms of the GCE/Gr/Cu electrode recorded at 50 mV s^{-1} in LEVO at different concentrations from 0.1 to 300 μM in PBS (pH 7), the red curve is the GCE/Gr/Cu electrode in blank PBS, **(b)** the oxidation peak current plotted as a function of the LEVO concentration from 0.1 to 300 μM and **(c)** the oxidation peak current plotted as a function of the LEVO concentration from 0.1 to 40 μM, n = 3.

Similarly, the DPV technique was used to record the voltammograms, as depicted in Figure 6-17 (a), then the relationship of the peak currents versus the concentration of LEVO was plotted in Figure 6-17 (b), and again two linear regions are seen. The excellent linearity was obtained at the low concentration range between 0.2 to 22 μM, the linear regression equation was deduced as I (μA) = 0.93 c (μM) + 2.01 (R^2 = 0.998) with the LOD of 18.56 nM ± 0.35.

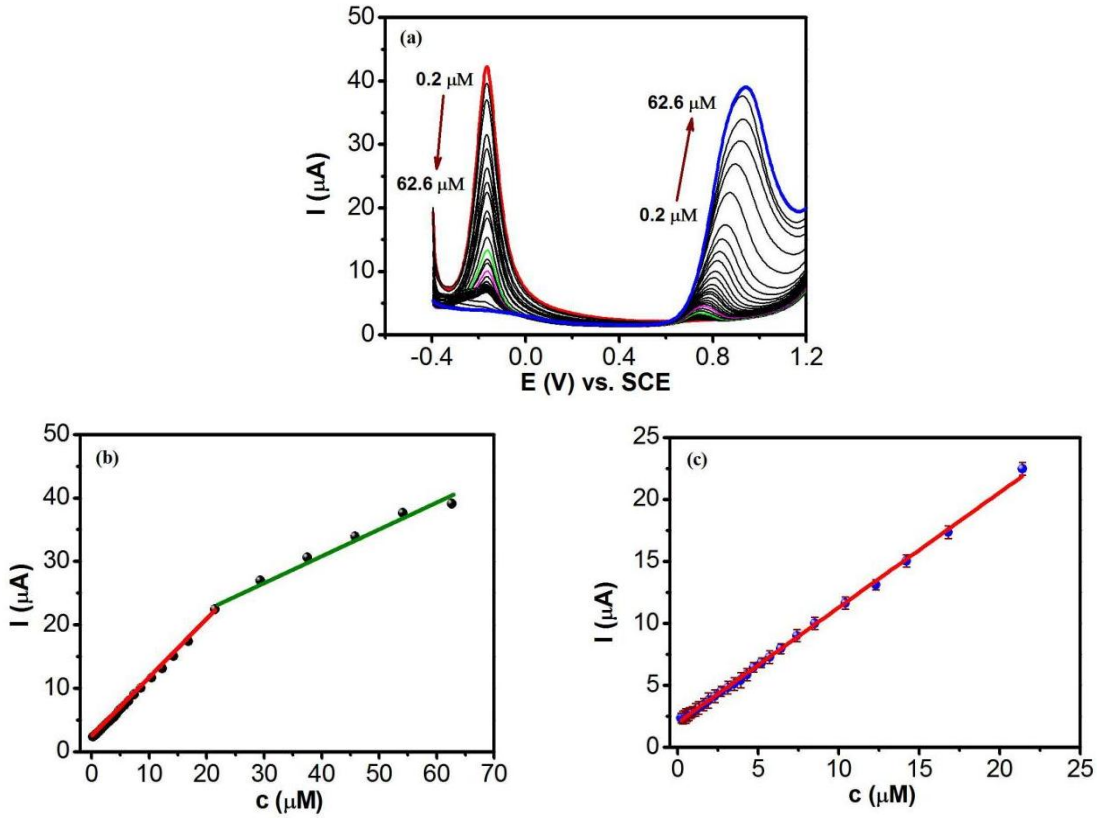

Figure 6-17. (a) DPV curves of the GCE/Gr/Cu electrode recorded in LEVO at different concentrations from 0.2 to 63 μM in PBS (pH 7), the red curve is the GCE/Gr/Cu electrode in blank PBS, green, pink and blue curves are the GCE/Gr/Cu electrode in different concentration of LEVO (1.9, 3.1 and 62.6 μM), **(b)** the oxidation peak current plotted as a function of the LEVO concentration from 0.2 to 63 μM and **(c)** the oxidation peak current plotted as a function of the LEVO concentration from 0.2 to 22 μM.

Comparing the voltammograms using CV and DPV techniques, it is seen that the redox peaks of Cu are maintained during the sensing performance test with the CV technique whereas the oxidation peak currents of Cu decay with the repeated DPV experiments. This may be connected to the manner in which the experiments were recorded. In the CV experiment, the potential was cycled in the forward and reverse direction and as a result the copper was converted from Cu to Cu_2O during the forward cycle and from Cu_2O to Cu during the reverse cycle. However, during the DPV experiment, there is little conversion of Cu_2O back to Cu and after the repeated DPV

traces which are only cycled in the forward direction, most of the copper resides as Cu_2O. This is consistent with the Pourbaix diagram shown in Figure 6-18**.** The Cu/Cu_2O transition occurs at approximately 60 mV vs. SHE, at a pH of 7, which corresponds to –180 mV vs. SCE. This is in good agreement with the copper related peaks in Figure 6-17(a), which occur at approximately -190 mV vs. SCE. As Cu_2O is the semiconductor, so its conductivity is worse than that of Cu, resulting in the lower LOD with DPV than CV.

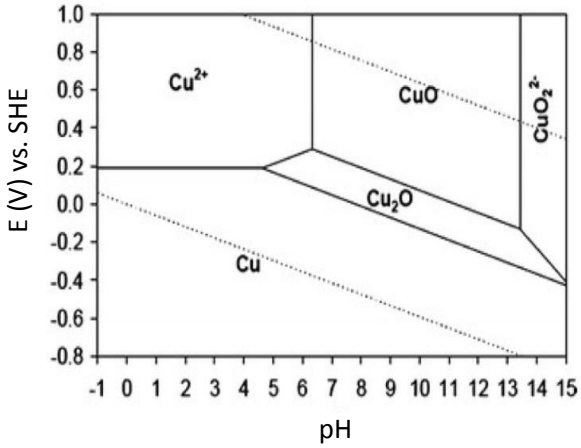

Figure 6-18. Pourbaix diagram of Cu.

The LODs for the two techniques were further compared with some recently reported sensors for the detection of LEVO. As listed in Table 6-2, the LOD is comparable to others and considerably lower than some of the quoted values, such as LOD values of 530 nM [25], 2880 nM [1], and 3900 nM [15]. In addition, the developed sensor shows simple fabrication and cost-effectiveness. Accordingly, the developed GCE/Gr/Cu sensor is suitable for the electrochemical detection of LEVO in terms of water analysis.

Table 6-2. Comparison of sensors in the electrochemical detection of LEVO.

Sensor materials	Technique	Linear range (μM)	LOD (nM)	Reference
BDD electrode	CV	48 – 100	10100	[1]
BDD electrode	SWV	10 – 80.9	2880	[1]
g-C_3N_4@GO/GCE	DPV	0.5 – 15	79	[2]
Au/PDDA/rGO/GCE	LSV	10 – 200	3900	[15]
Poly(PGR)/GCE	LSV	0.2 – 15	97	[22]
G-AuNPs/MIP	DPV	1.0 – 100	530	[25]
Cu-MOF/SPE	CV	0.1 –100	16	[26]
Cu-MOF/SPE	DPV	0.1 – 100	170	[26]
rGO/3D-CB/PLA	DPV	10 – 50	2170	[27]
poly(p-ABSA)-rGO/GCE	LSV	2 – 30	120	[28]
Co/Ni-MOF/GCE	LSV	0.1 – 500	22	[29]
MWCNTs/SnO_2	DPV	1.0 – 9.9	200	[30]
NFS/CPE	DPV	2.0 – 1000	90	[31]
AgNPs-CB-PEDOT:PSS/GCE	SWV	0.67 – 12	14	[32]
GCE/Gr/Cu	CV	0.1 – 40	11.86	This work
GCE/Gr/Cu	DPV	0.2 – 22	18.56	This work

For clarity, the CV curves of the GCE/Gr/Cu in 0.1 mM LEVO before and after the sensing performance tests were recorded and are compared in Figure 6-19. The CV curve of the GCE/Gr/Cu before the sensing performance test clearly shows the redox peak between 0.0 and –0.4 V vs. SCE, Figure 6-19 (curve 1), after the sensing performance test with CV technique, the GCE/Gr/Cu electrode was immersed in 0.1 mM LEVO and its CV curve was measured again, Figure 6-19 (curve 2), the same redox peak associated with the CuNPs is seen, whereas after the DPV measurement, Figure 6-19 (curve 3), the redox peaks are absent. Moreover, it is observed from Figure 6-19 (curves 2 and 3) that the peak current of the GCE/Gr/Cu electrode in 0.1 mM LEVO is somewhat higher after the CV experiment compared with that after the DPV

experiment. These finding are consistent with the LODs for the CV and DPV experiments, namely the LOD of 11.86 nM for CV experiment is somewhat lower than the LOD of 18.56 nM for the DPV experiment, indicating that most of the CuNPs were converted to Cu_2O NPs following the DPV experiment, further demonstrating that the CuNPs play a more significant role in the detection of LEVO compared to the Cu_2O NPs. In addition, this observation also suggests the stability of the GCE/Gr/Cu electrode during the CV experiment. On comparing the currents for the sensor after the CV and DPV experiments and the freshly prepared sensor, the peak current of the GCE/Gr/Cu electrode in 0.1 mM LEVO is somewhat higher, which may be related to the hydrophobic nature of graphene. After the CV and DPV experiments, the sensor surface is adequately wetted with the aqueous solution, enabling more efficient oxidation of the LEVO.

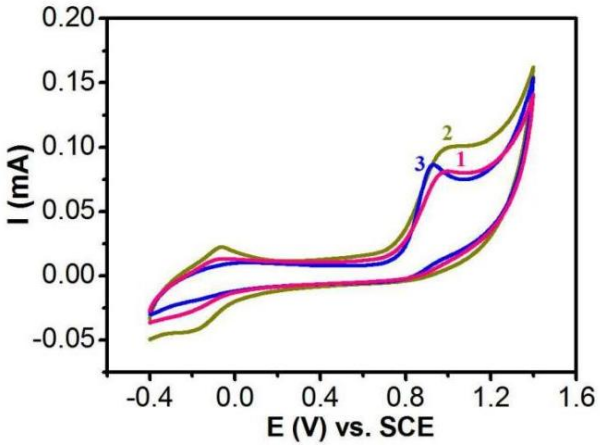

Figure 6-19. Voltammograms of the GCE/Gr/Cu electrode recorded at 50 mV s^{-1} in 0.1 mM LEVO in PBS (pH 7), the curve 1 is the CV curve of the freshly prepared GCE/Gr/Cu electrode, curve 2 is the CV curve of the GCE/Gr/Cu electrode after adding different concentration of LEVO with CV technique and curve 3 is the CV curve of the GCE/Gr/Cu electrode after adding different concentration of LEVO with DPV technique.

6.3.11 Evaluation of reproducibility, selectivity, and stability

The reproducibility, selectivity and stability are very important considerations for the performance of an electrochemical sensor. The reproducibility of the GCE/Cu, GCE/Gr, and GCE/Gr/Cu electrodes for the detection of LEVO was inspected by independently

preparing three corresponding electrodes through the same procedure on different days. Further these electrodes were studied in 0.1 mM LEVO. Figure 6-20 shows the voltammograms of the GCE/Cu electrodes at the Cu deposition times of 50 and 100 s in 0.1 mM LEVO and the histogram of the oxidation peak currents as a function of the deposition frequency of 5 times (mean: 0.032 mA ± 0.0035 for 50 s and 0.023 ± 0.0073 for 100 s). It is apparent that the GCE/Cu electrodes possess good reproducibility with the relative standard deviation (RSD) of 1.08% with 50 s deposition for the detection of LEVO.

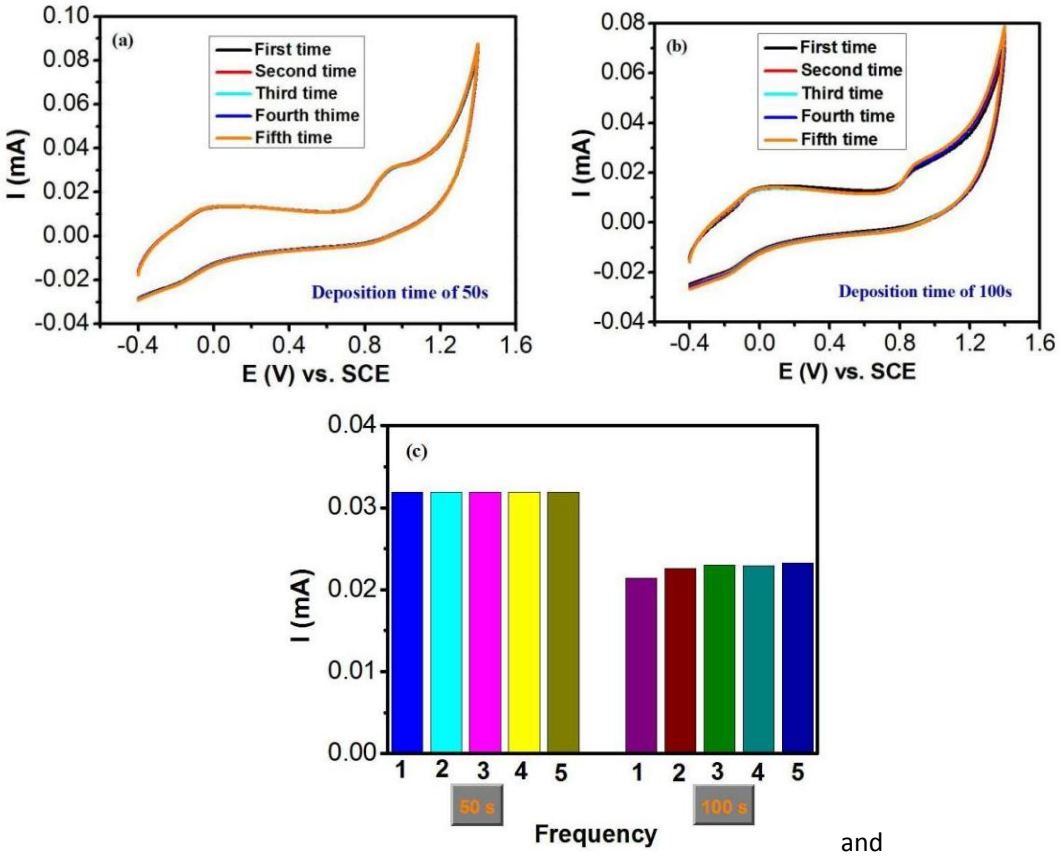

and

Figure 6-20. (a) Voltammograms of the GCE/Cu with Cu deposition of 50 s recorded in 0.1 mM LEVO at 50 mV s^{-1} for five times, **(b)** Voltammograms of the GCE/Cu with Cu deposition of 100 s recorded in 0.1 mM LEVO at 50 mV s^{-1} for five times and **(c)** the oxidation peak current versus the deposition frequency for different deposition time of 50 and 100 s (n = 5).

Figure 6-21 displays the voltammograms of the GCE/Gr electrode at the Gr deposition of 10 cycles in 0.1 mM LEVO and the histogram of the oxidation peak

currents as a function of the deposition frequency of 5 times (mean: 0.045 mA ± 0.0075). The same good reproducibility with the RSD of 1.65% is observed for the detection of LEVO.

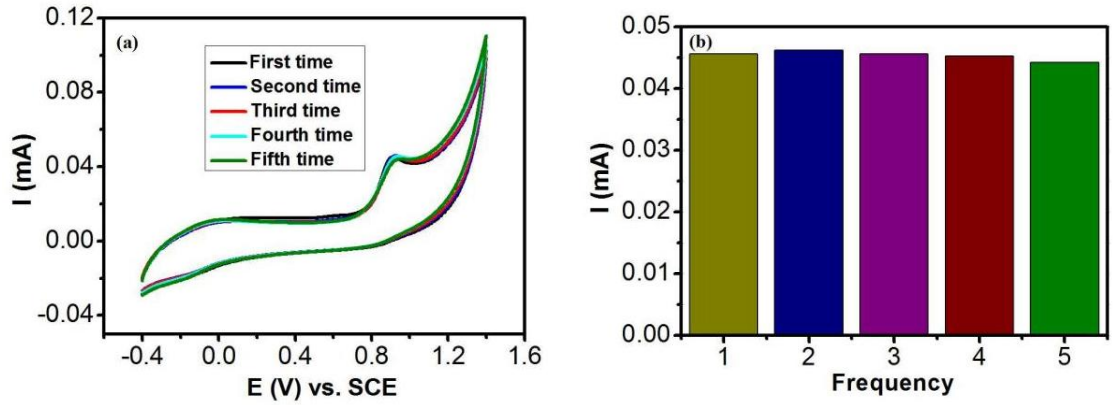

Figure 6-21. (a) Voltammograms of the GCE/Gr with Gr deposition of 10 cycles recorded in 0.1 mM LEVO at 50 mV s^{-1} for five times and **(b)** the oxidation peak current versus the deposition frequency (n = 5).

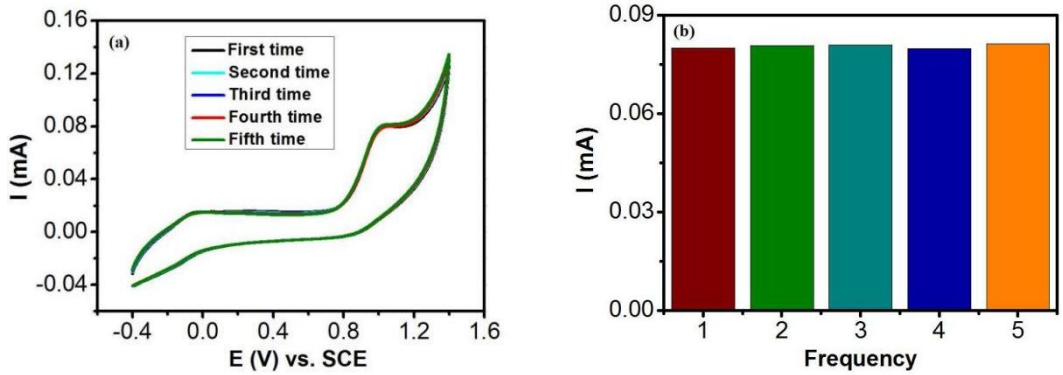

Figure 6-22. (a) Voltammograms of the GCE/Gr/Cu with Cu deposition of 50 s and Gr deposition of 10 cycles recorded in 0.1 mM LEVO at 50 mV s^{-1} for five times and **(b)** the oxidation peak current versus the deposition frequency (n = 5).

Further, the voltammograms of the GCE/Gr/Cu electrodes at the Cu deposition time of 50 s and Gr deposition of 10 cycles in 0.1 mM LEVO and the histogram of the oxidation peak currents as a function of the deposition frequency of 5 times are exhibited in Figure 6-22, giving the mean of 0.081 mA ± 0.0063 with the RSD of 0.78% for the detection of LEVO. Compared to the GCE/Gr, after the deposition of CuNPs, the

GCE/Gr/Cu electrode not only increases the sensitivity for the detection of LEVO, but also improves the reproducibility of the electrode.

The selectivity of the GCE/Gr/Cu electrode for the detection of LEVO was investigated through using a variety of interfering compounds, such as inorganic salts, which are present in aquatic environments, and some organic compounds, which have similar structures with LEVO. The CV technique was utilised to record the interference study in 0.1 mM LEVO. When the CV curves of the mixed solutions containing LEVO and interferents were obtained, the oxidation peak currents of LEVO were taken. The normalised oxidation peak currents (I/I_0, where I represents the peak current in the presence of the interferent and I_0 expresses the peak current in the absence of the interferent) are displayed in Figure 6-23. It is evident that the oxidation peak currents of LEVO are nearly identical, in the presence of a 10-fold concentration of common inorganic salts like CH_3COONa (NaAc), Na_2SO_4, Na_2CO_3, $NaNO_2$, $NaNO_3$ and equimolar concentrations of glucose (Glu), ascorbic acid (AA), 4-(2,4-dichlorophenoxy) butyric acid (2,4-DB), Hydrocortisone (HC), *p*-Nitrophenol (*p*-NP), *o*-Nitrophenol (*o*-NP), 4-Chloro-2-methylphenoxyacetic acid (MCPA) and Metronidazole (MTZ) had no obvious influence in the analysis of LEVO. Therefore, the GCE/Gr/Cu electrode exhibited a good selectivity for the electrochemical detection of LEVO.

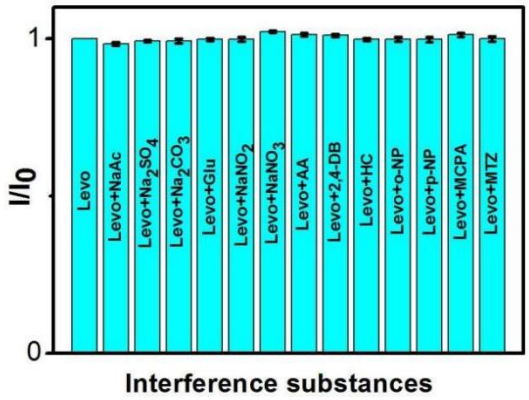

Figure 6-23. Normalised oxidation peak currents, (I/I_0), of 0.1 mM LEVO at the GCE/Gr/Cu in a PBS containing 10-fold concentrations of various inorganic ions and equimolar concentrations of organic compounds, n = 3.

The long-term stability is one of the most important properties of sensors. The long-term stability of the GCE/Gr/Cu was monitored in the PBS over 21 days. The GCE/Gr/Cu was stored in the PBS at room temperature and measured in 0.1 mM LEVO at intervals of two days. The GCE/Gr/Cu preserved 96.82% of its primary amperometric response after 21 days, Figure 6-24, which indicated that the GCE/Gr/Cu has relatively high long-term storage stability for the electrochemical determination of LEVO.

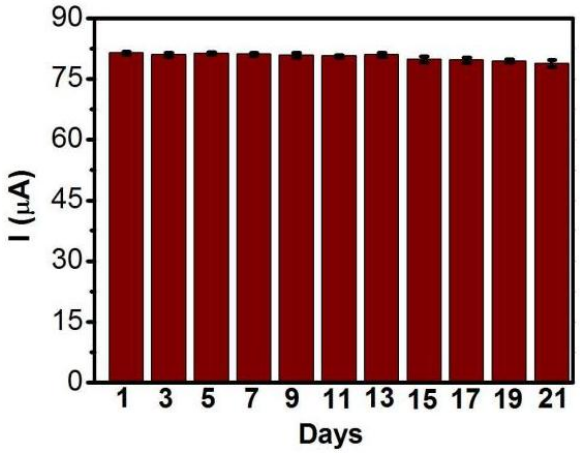

Figure 6-24. The amperometric responses of the GCE/Gr/Cu to 0.1 mM LEVO in 21 days in 0.1 M PBS (pH = 7) (n = 3).

6.3.12 Water analysis

The LEVO analysis in tap water was accomplished to study the analytical practicability of the developed GCE/Gr/Cu sensor using a typical spiking and recovery experiment. Firstly, the tap water was used to prepare 0.1 M PBS at pH 7.0, then the stock solution of 0.1 mM LEVO was added with different volumes to make the LEVO solution at different concentrations, 5.0 μM, 10.0 μM and 20.0 μM, finally, the recovery was analysed with the GCE/Gr/Cu sensor. For comparison purposes, the deionised water was also utilised with the same procedure. The results obtained are revealed in Table 6-3, where it is obvious that good recovery is achieved in the tap water, with the recovery varying between 105.6 to 96.6%. Furthermore, these recovery values are compared with that recorded when deionised water was used. It is clear in Table 6-3 that they are

similar to each other. This observation demonstrates good performance of the GCE/Gr/Cu sensor in the analysis of LEVO.

Table 6-3. Determination of LEVO in deionized water and tap water using GCE/Gr/Cu. Sufficient phosphate was added to the deionised and tap water samples to give a 0.1 M phosphate solution (n = 3).

Sample	Added/ μM	Found/ μM	Recovery
Deionized water	5.0	5.27 (± 0.09)	105.6%
	10.0	9.88 (± 0.15)	98.8%
	20.0	19.32 (± 0.29)	96.6%
Tap water	5.0	5.19 (± 0.11)	103.8%
	10.0	10.35 (± 0.19)	103.5%
	20.0	19.54 (± 0.32)	97.7%

6.4 Conclusion

In this chapter, a facile and cost-effective electrochemical sensor for the detection of LEVO was developed using the simple electrodeposition procedure with one of the most abundant metals in the earth's crust. The optimal experimental conditions for the electrodeposition were investigated and obtained as scanning cycles of 10 for Gr deposition and the deposition period of 50 s for the Cu deposition. Under the optimal experiment conditions, the Gr nanoplatelets were initially electrochemically deposited on the surface of GCE to generate the GCE/Gr electrode, subsequently, the Cu nanoparticles were electrochemically deposited on the surface of GCE/Gr to form the GCE/Gr/Cu. The SEM photographs indicated that the Gr and Cu have been successfully deposited on the GCE and the CuNPs were well dispersed across the surface of the GCE/Gr electrode. Further, EDX and mapping measurements confirmed the deposition of Gr and Cu. The prepared GCE/Gr/Cu electrode was utilised to determine LEVO, showing good sensing performance with low electron transfer resistance, providing a promising platform in the detection of antibiotics. Moreover, the low LOD of 11.86 nM in the concentration range from 0.1 to 40 μM using CV technique and 18.56 nM in the concentration range from 0.2 to 22 μM using DPV technique were attained for the

detection of LEVO with the GCE/Gr/Cu electrode. Besides, the GCE/Gr/Cu exhibited excellent reproducibility, stability, and selectivity. Therefore, the GCE/Gr/Cu has the potential to serve as a cost-effective, highly sensitive and stable sensor for the electrochemical detection of LEVO and possibly other antibiotics.

6.5 References

[1] Rkik, M.; Ben Brahirn, M.; Samet,Y. Electrochemical determination of levofloxacin antibiotic in biological samples using boron doped diamond electrode, *J. Electroanal. Chem*. **2017**, *794*, 175–181, doi: 10.1016/j.jelechem.2017.04.015.

[2] Yi, W. W.; Han, C. X.; Li, Z. P.; Guo, Y. J.; Liu, M. Dong, C. A strategy of electrochemical simultaneous detection of acetaminophen and levofloxacin in water based on g-C_3N_4 nanosheet-doped graphene oxide, *Environmental Science-Nano*, **2021**, *8*, 258–268, doi: 10.1039/d0en00858c.

[3] Tunitskaya, V. L.; Khomutov, A. R.; Kochetkov, S. N.; Kotovskaya, S. K.; Charushin, V. N. Inhibition of DNA gyrase by levofloxacin and related fluorine-containing heterocyclic compounds, *Acta Nat.* **2011**, *3*, 94–99, doi: 10.32607/20758251-2011-3-4-94-99.

[4] Angulo, F. J.; Johnson, K. R.; Tauxe, R. V.; Cohen, M. L. Origins and consequences of antimicrobial-resistant nontyphoidal *Salmonella*: Implications for the use of fluoroquinolones in food animals, *Microb. Drug Resist.* **2000**, *6*, 77–83, doi: 10.1089/mdr.2000.6.77.

[5] Mohammed, I.; Al-Ogaili, N.; Jasem, A. Y. Application of levofloxacin and doxycycline in treatment of vaginal chlamydial infection, *Mater. Today-Proceedings*, **2021**, *57*, 488–491, doi: 10.1016/j.matpr.2022.01.386.

[6] Petitjeans, F.; Nadaud, J.; Perez, J. P.; Debien, B.; Olive, F.; Villevieille, T.; Pats, B. A case of rhabdomyolysis with fatal outcome after a treatment with levofloxacin, *Eur. J. Clin. Pharmacol*. **2003**, *10*, 779–780, doi: 10.1007/s00228-003-0688-x.

[7] Panahi, L.; Surani, S. S.; Udeani, G.; Patel, N. P.; Sellers, J. Hepatotoxicity Secondary to Levofloxacin Use, *Cur. J. Med. Sci.* **2021**, *13*, e15973, doi:

10.7759/cureus.15973.

[8] Lin, Y. C.; Yu, T. H.; Lin, C. F. Pharmaceutical contamination in residential, industrial, and agricultural waste streams: risk to aqueous environments in Taiwan, *Chemosphere*, **2008**, *74*, 131–141, doi: 10.1016/j.chemosphere.2008.08.027.

[9] Santoro, M. I. R. M.; Kassab, N. M.; Singh, A. K.; Kedor-Hackmam, E. R. M. Quantitative determination of gatifloxacin, levofloxacin, lomefloxacin and pefloxacin fluoroquinolonic antibiotics in pharmaceutical preparations by high-performance liquid chromatography, *J. Pharmaceut. Biomed. Anal*. **2006**, *40*, 179–184, doi: 10.1016/j.jpba.2005.06.018.

[10] Yang, Z. C.; Chen, G. Q.; Ma, C. Q.; Gu, J.; Zhu, C.; Li, L.; Gao, H. Magnetic Fe_3O_4@COF@Ag SERS substrate combined with machine learning algorithms for detection of three quinolone antibiotics: ciprofloxacin, norfloxacin and levofloxacin. *Talanta,* **2023**, *263*, 124725, doi: 10.1016/j.talanta.2023.124725.

[11] Shao, X. D.; Li, Y.; Liu, Y. Q.; Song, Z. H. Flow injection chemiluminescence determination of levofloxacin in medicine and biological fluids based on its enhancing effect on luminol-H_2O_2 reaction, *Spectroscopy* **2009**, *23*, 209–216, doi: 10.1155/2009/816252.

[12] Maleque, M.; Hasan, M. R.; Hossen, F.; Safifi, S. Development and validation of a simple UV spectrophotometric method for the determination of levofloxacin both in bulk and marketed dosage formulations. *J. Pharm. Anal.* **2012**, *2*, 454–457, doi: 10.1016/j.jpha.2012.06.004.

[13] Salem, A.; Mossa, H. A. Method validation and determinations of levofloxacin, metronidazole and sulfamethoxazole in an aqueous pharmaceutical, urine and blood plasma samples using quantitative nuclear magnetic resonance spectrometry, *Talanta* **2012**, *88*, 104–114, doi: 10.1016/j.talanta.2011.10.016.

[14] Sun, H. W.; Zuo, Y. L. Effective separation and simultaneous detection of ceftriaxone sodium and levofloxacin in human urine by capillary zone electrophoresis, *Curr. Anal. Chem*. **2013**, *9*, 157–162, doi: 10.2174/157341113804486482.

[15] Borowiec, J.; Yan, K.; Tin, C. C.; Zhang, J. D. Synthesis of PDDA functionalized reduced graphene oxide decorated with gold nanoparticles and its electrochemical

response toward levofloxacin. *J. Electrochem. Soc.* **2015**, *162*, H164–H169, doi: 10.1149/2.0811503jes.

[16] Sharma,T. S. K.; Hwa, K. Y. Facile synthesis of Ag/$AgVO_3$/N-rGO hybrid nanocomposites for electrochemical detection of levofloxacin for complex biological samples using screen-printed carbon paste electrodes, *Inorg. Chem.* **2021**, *60*, 6585–6599, doi: 10.1021/acs.inorgchem.1c00389.

[17] Koçak, Ç. C. Poly(taurine-glutathione)/carbon nanotube modified glassy carbon electrode as a new levofloxacin sensor, *Electroanalysis*, **2019**, *31*, 1552–1561, doi: 10.1002/elan.201900096.

[18] de Farias, D. M.; de Faria, L. V.; Lisboa, T. P.; Matos, M. A. C.; Muñoz, R. A. A.; Matos, R. C. Determination of levofloxacin in pharmaceutical formulations and urine at reduced graphene oxide and carbon nanotube-modified electrodes, *J. Solid State Electrochem.* **2020**, *24*, 1165–1173, doi: 10.1007/s10008-020-04589-z.

[19] Huang, J. Y.; Bao, T.; Hu, T. X.; Wen, W.; Zhang, X. H.; Wang, S. F. Voltammetric determination of levofloxacin using a glassy carbon electrode modified with poly(o-aminophenol) and graphene quantum dots, *Microchim. Acta* **2017**, *184*, 127–135, doi: 10.1007/s00604-016-1982-5.

[20] Hu, X.; Liu,T. T.; Zhuang, Y. X.; Wang, W.; Li,Y.Y.; Fan,W. H.; Huang,Y. M. Recent advances in the analytical applications of copper nanoclusters, *Trends Anal. Chem*. **2016**, *77*, 66–75, doi: 10.1016/j.trac.2015.12.013.

[21] da Silva, M. K. L.; Simões, R. P.; Cesarino, I. Evaluation of reduced graphene oxide modified with antimony and copper nanoparticles for levofloxacin oxidation, *Electroanalysis* **2018**, *30*, 2066 – 2076, doi: 10.1002/elan.201800265.

[22] Koçak, C. C.; Aslişen, B.; Karabiberoğlu, S.; Özdokur, K. V.; Aslan, A.; Koçak, S. Electrochemical determination of levofloxacin using poly(pyrogallol red) modified glassy carbon electrode, *ChemistrySelect*, **2022**, *7*, e202201864, doi: 10.1002/slct.202201864.

[23] Mokwebo, K.V.; Murphy, E.; Guin, S. K.; Camisasca, A.; Giordani, S.; Breslin, C.; Iwuoha, E. I.; Dempsey, E. Copper-modified carbon nano-onions as electrode modifiers for the electroanalysis of the antiretroviral drug Efavirenz, *Electrochim. Acta*, **2023**, *461*, 142639, doi: 10.1016/j.electacta.2023.142639.

[24] Kunze, J.; Maurice,V.; Klein, L. H.; Strehblow, H. H.; Marcus, P. In situ scanning tunneling microscopy study of the anodic oxidation of Cu(111) in 0.1 M NaOH, *J. Phys. Chem. B* **2001**, *105,* 4263–4269, doi: 10.1021/jp004012i.

[25] Wang, F.; Zhu, L. H.; Zhang, J. D. Electrochemical sensor for levofloxacin based on molecularly imprinted polypyrrole graphene-gold nanoparticles modifified electrode. *Sens. Actuator B-Chem.* **2014**, *192*, 642–647, doi:10.1016/j.snb.2013.11.037

[26] Zhou, J.; Liu, J.; Pan, P.; Li,T.; Yang, Z. C.; Wei, J.; Li, P.; Liu, G. Y.; Shen, H. D.; Zhang, X. D. Electrochemical determination of levofloxacin with a Cu–metal–organic framework derivative electrode, *J. Mater. Sci: Mater Electron* **2022**, *33*, 9941–9950, doi: 10.1007/s10854-022-07985-5.

[27] Lisboa, T. P.; Oliveira, R. S.; de Oliveira, W. B. V.; de Souza, C. C.; Alves, G. F.; Matos, M. A. C.; Matos, R. C. A 3D carbon black disposable electrochemical sensor modified with reduced graphene oxide used for the sensitive determination of levofloxacin. *New J. Chem*. **2023**, *47*, 2240–2247, doi: 10.1039/d2nj05338a.

[28] Han, L.; Zhao, Y. F.; Chang, C.; Li, F. A novel electrochemical sensor based on poly(p-aminobenzene sulfonic acid)-reduced graphene oxide composite film for the sensitive and selective detection of levofloxacin in human urine. *J. Electroanal. Chem*. **2018**, *817*, 141–148, doi: 10.1016/j.jelechem.2018.04.008.

[29] Jin, Y. F.; Xu, G. R.; Li, X. B.; Ma, J. J.; Yang, L.; Li, Y. C.; Zhang, H.; Zhang, Z.; Yao, D. H.; Li, D. H. Fast cathodic reduction electrodeposition of a binder-free cobalt-doped Ni-MOF film for directly sensing of levofloxacin. *J. Alloy. Compd*. **2021**, 851, 8, doi: 10.1016/j.jallcom.2020.156823.

[30] Cesarino, V.; Cesarino, I.; Moraes, F. C.; Machado, S. A. S.; Mascaro, L. H. Carbon nanotubes modified with SnO_2 rods for levofloxacin detection. *J. Braz. Chem. Soc.* **2014**, *25*, 502–508, doi: 10.5935/0103-5053.20140017.

[31] Fekry, A. M. An innovative simple electrochemical levofloxacin sensor assembled from carbon paste enhanced with nano-sized fumed silica, *Biosensors-Basel*, **2022**, *12*, 906, doi: 10.3390/bios12100906.

[32] Wong, A. Santos, A. M.; Fatibello-Filho, O. Simultaneous determination of paracetamol and levofloxacin using a glassy carbon electrode modified with carbon

black, silver nanoparticles and PEDOT: PSS film, *Sens. Actuators B* **2018**, *255*, 2264–2273, doi: 10.1016/j.snb.2017.09.020.

Chapter 7

Study On the Removal of 4-Chloro-2-methylphenoxyacetic Acid (MCPA), *p*-Nitrophenol (*p*-NP), Metronidazole (MTZ) and Levofloxacin (LEVO) from Aquatic Environments by Magnetic Graphene Adsorbent

7.1 Introduction

With the rapid development of modern industry and social economy and the continuous improvement of human living standards, more and more organic pollutants, mainly coming from the chemical industry, petroleum industry, agriculture, animal husbandry and daily life, are discharged into water. These include pesticides/herbicides and pharmaceutical drugs such as 4-chloro-2-methylphenoxyacetic acid (MCPA), *para*-nitrophenol (*p*-NP), metronidazole (MTZ) and Levofloxacin (LEVO). MCPA is one of the more commonly employed herbicides, which is harmful to aquatic species, animals and can impact on human health even at relatively low concentrations [1]; *p*-NP is an important intermediate of chemical raw materials, which not only can generate carcinogen nitrosamine, increasing the risk of cancer in humans, but also can cause protein denaturation in the human body, leading to a series of symptoms including dizziness, anemia, liver, and nervous system damage [2]; MTZ and LEVO are commonly employed in the treatment of infections caused by bacteria in both humans and animals, which have genotoxic and mutagenic side effects and their accumulation in aquatic environment can lead to antibiotic resistance, causing interference or even interruption in the circle of ecosystems [3,4]. Moreover, because of good solubility, chemical stability and nondegradable, these pollutants can persist in aquatic environments for long times, leading to bioaccumulation in plants, animals, and aquatic life, further entering the human body through the food chain. This is a serious threat to ecosystems and human health. Therefore, concerns in removing organic pollutants from water environment are growing greatly [5,6].

To ensure the safe use of water resources, various strategies have been utilised to clean up organic pollutants from wastewater, including biological treatments [7], catalytic degradation [8], membrane separation [9], and adsorption [10]. However, due to pollutants with different characteristics, some technologies cannot meet the practical requirements for the treatment of pollutants, which limits their application in the field of water treatment. Among these techniques, adsorption has the best potential, and it is a

preferred method for advanced wastewater treatment because of its comparatively low cost, easy operation, high removal efficiency with less secondary pollution. [11]. Nowadays, adsorption is widely investigated and employed for the removal of pollutants [12]. Effective adsorbents are needed and are critical in efficiently removing pollutants from water environments [13]. Materials with good chemical stability, large specific surface area and feasibility of manufacturing in large quantities are essential in formulating adsorbents [14]. According to these features, a series of carbon-based materials, such as graphite powder [15], activated carbon [16], carbon fiber [17], porous carbon [18], and carbon nanotubes [19], have been used as the adsorbents to remove pollutants from aqueous solutions. Compared to these carbon materials, graphene with honeycomb and one-atom-thick structure exhibits large specific surface area, good electronic characteristics, and mechanical strength, which have resulted in its study and applications in different fields [20]. In recent years, graphene has been identified as a promising adsorbent, which can remove not only heavy metals [21], but also organic pollutants from aqueous solutions [22]. Especially, compared to other adsorbents, the superiority of graphene is to selectively adsorb those compounds containing benzene rings or similar structure (e.g., imidazole ring) via strong π−π interactions [23]. Consequently, graphene is anticipated to become a promising adsorbent in the removal of compounds containing benzene or imidazole rings from aqueous solutions.

Magnetic adsorbents have exhibited important roles in treating environmental pollution, attributed to the good combination of outstanding adsorption performance and strong magnetism [24]. In this Chapter, four pollutants, MCPA, *p*-NP, MTZ and LEVO were chosen as adsorbates. Their structures are illustrated in Figure 7-1. It can be seen that there are a benzene ring in the molecular structures of MCPA, *p*-NP and LEVO, and an imidazole ring in the molecular structure of MTZ. The magnetic graphene nanoplatelets supporting nano zero-valent iron (Gr/Fe) were prepared and used as adsorbents to remove four pollutants from aqueous solutions. The effects of adsorbent dosage, initial concentration of adsorbate, solution pH, contact time of adsorbate and adsorbent on the adsorption capacity have been investigated in detail.

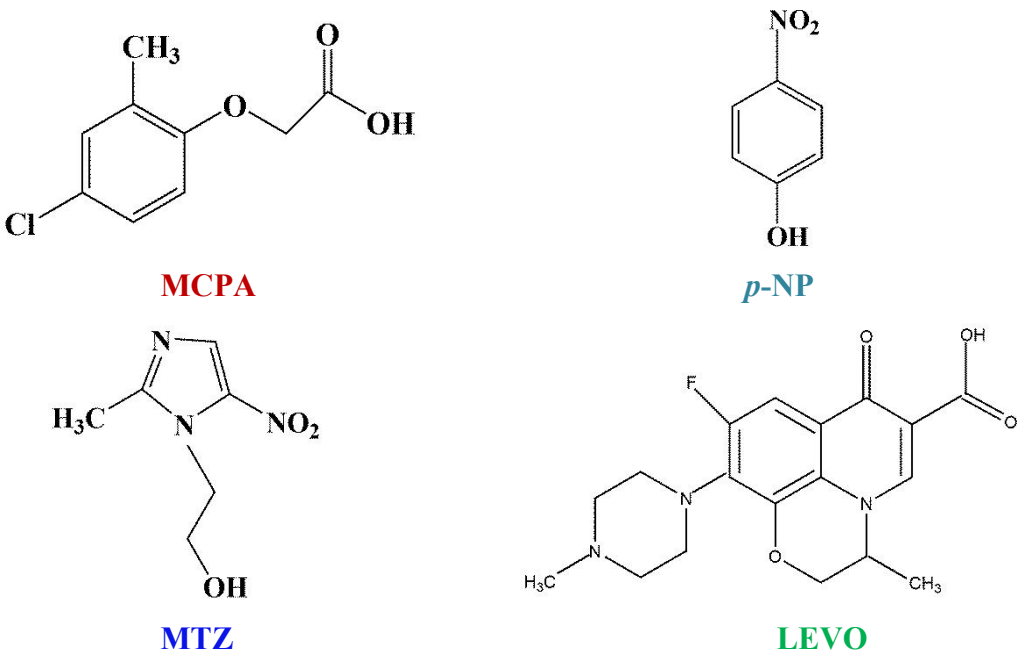

Figure 7-1. The molecular structures of MCPA, *p*-NP, MTZ and LEVO drawn by ChemDraw.

7.2 Experimental Section

7.2.1 Preparation of magnetic graphene Gr/Fe

The Gr/Fe was prepared according to the procedure described in Section 2.2.5.1 in Chapter 2.

7.2.2 Characterisation of the adsorbent and adsorbate

The magnetic graphene, Gr/Fe, was characterised by SEM, EDX and elemental mapping (Hitachi S-3200-N). The UV-vis spectra of MCPA, *p*-NP, MTZ and LEVO were measured, and all the adsorption experiments were monitored using a UV-vis Spectrometer (CARY 50 Conc) with quartz cells of 1 cm. The IR characterisation of the adsorbent and adsorbate was conducted with a Thermo Fisher IR spectrometer (Nicolet iS50 FT-IR microscope) between 4000 and 500 cm^{-1}.

7.2.3 Adsorption experiments

All adsorption experiments were carried out according to the description in Section 2.2.5.2 in Chapter 2.

7.2.4 The preparation of four solutions

1.0 mM adsorbate solutions were prepared according to the procedure shown in Section 2.2.5.2.1 in Chapter 2.

7.2.5 Adsorbent dosage experiments

The effect of adsorbent dosage on the adsorption of the four compounds was conducted according to the procedure presented in Section 2.2.5.2.2 in Chapter 2.

7.2.6 Adsorption kinetics experiments

All adsorption kinetic experiments were completed according to the procedure revealed in Section 2.2.5.2.3 in Chapter 2.

7.2.7 Adsorption experiments at different pH

The effect of the initial solution pH on the adsorption of the adsorbate by the adsorbent was evaluated according to the method described in Section 2.2.5.2.4 in Chapter 2.

7.2.8 Recovery experiments

The recovery experiments were performed according to the process displayed in Section 2.2.5.2.5 in Chapter 2.

7.3 Results and discussion

7.3.1 UV-vis spectra characterisation of the adsorbates

The UV-vis spectra of the four compounds are revealed in Figure 7-2, which give the characteristic absorption wavelengths at 229 nm for MCPA, 319 nm for *p*-NP, 320 nm for MTZ and 288 nm for LEVO. These wavelengths were employed to monitor the changes in absorbance before and after adding the adsorbent.

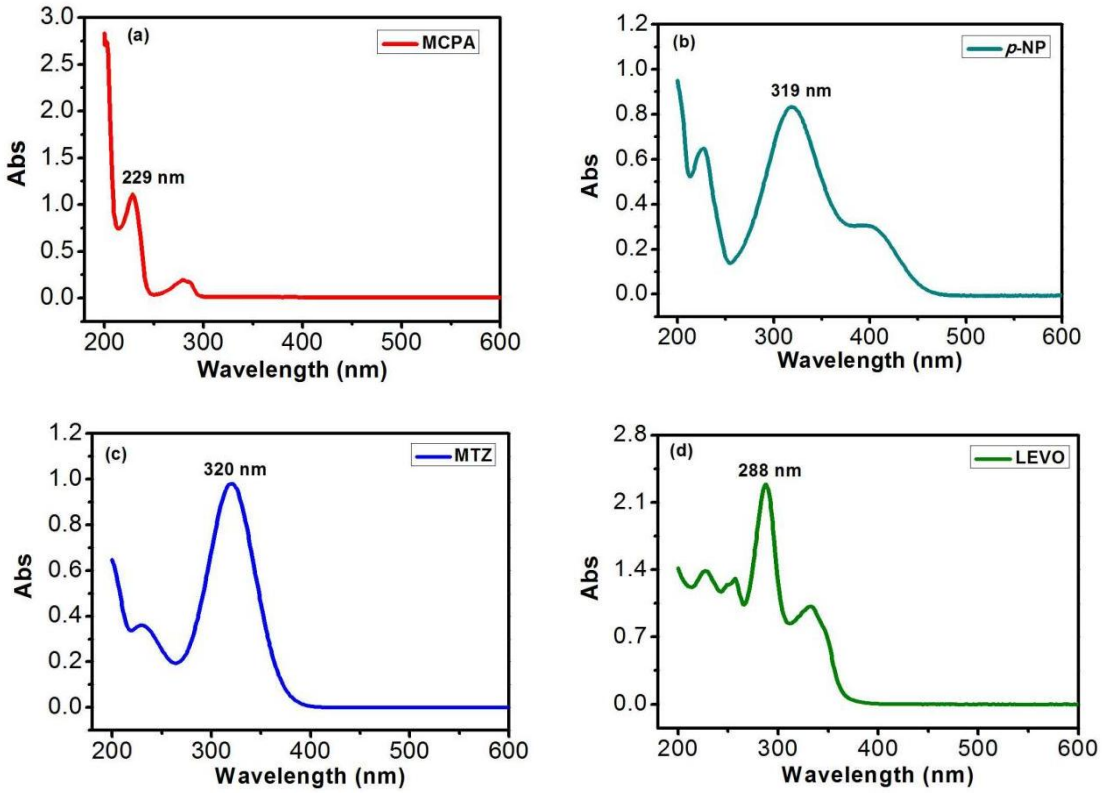

Figure 7-2. UV-vis spectra of MCPA **(a)**, *p*-NP **(b)**, MTZ **(c)** and LEVO **(d)** in 0.1 mM in aqueous solution.

The concentrations of the four compounds in solution were computed according to the Beer-Lambert law described in Equation 7-1:

$$A = \varepsilon\, b\, c \qquad (7\text{-}1)$$

Where, ***A*** is the absorbance of the sample at a fixed wavelength, ***c*** is the concentration of the solution (mol/L), ***b*** is the path length (depends on the dimensions of the glass cuvette and is 1 cm in this experiment) and ***ε*** is the molar extinction coefficient, which is related to the properties of the absorbing substances and the wavelength of the incident light, and ***ε*** indicates the extent to which the molecules absorb radiation at that wavelength.

7.3.2 Morphology characterisation of the magnetic graphene Gr/Fe

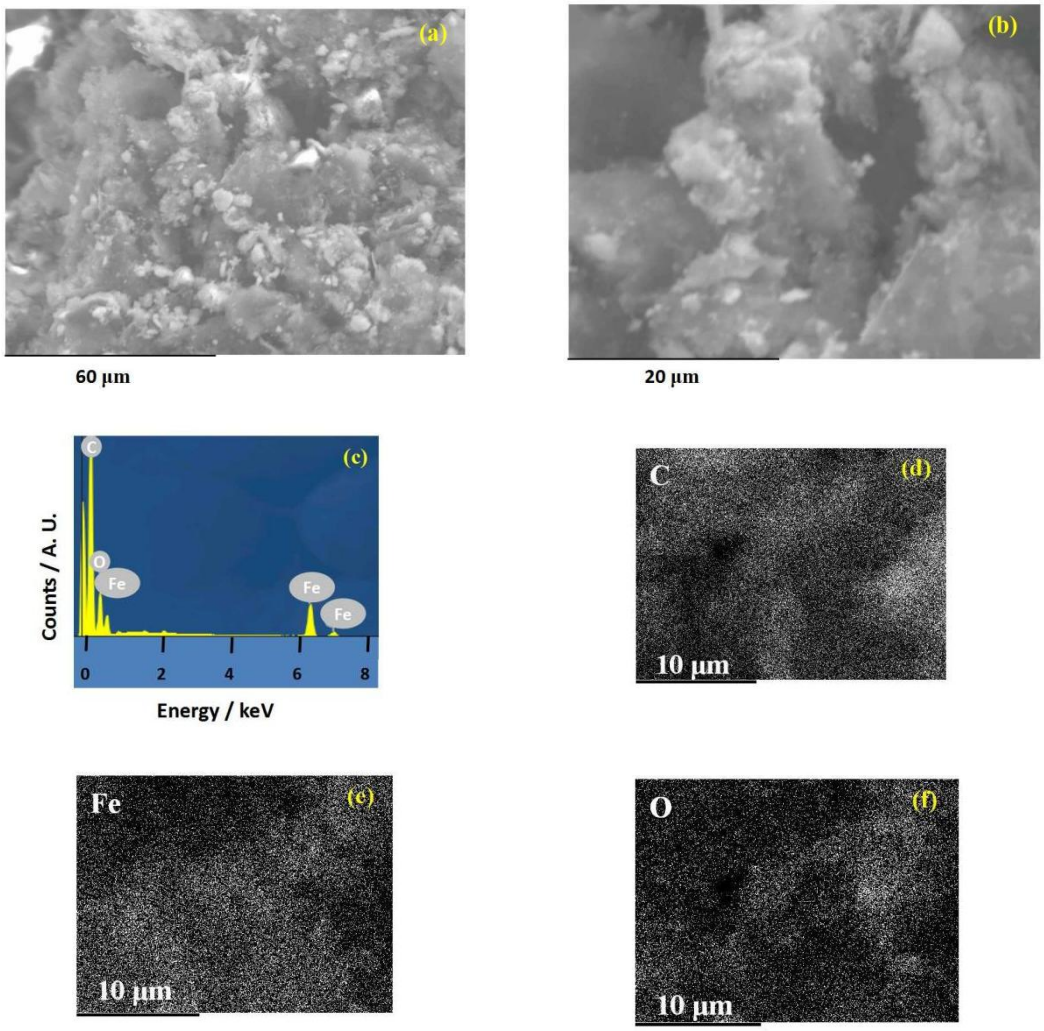

Figure 7-3. **(a, b)** SEM micrographs of Gr modified with deposited Fe, **(c)** EDX spectrum recorded at Gr/Fe and **(d, e, f)** mapping of C, O and Fe at Gr/Fe.

In order to prepare the easily separated adsorbent, Fe nanoparticles were deposited on the Gr surface to form magnetic graphene, Gr/Fe, which was characterised by SEM, EDX and element mapping. The SEM micrographs in Figure 7-3 (a,b) show that the Gr nanoplatelets are clearly evident in the SEM images. Some Gr nanoplatelets are stacked, and the Fe nanoparticles are distributed homogeneously over the graphene nanoplatelets, also with some evidence of aggregation at some sites. Moreover, the EDX spectrum displays the presence of C, O and Fe, clearly indicating that the Fe has been deposited onto the Gr nanoplatelets, Figure 7-3 (c). The presence of oxygen is consistent with the presence of oxygen-containing functional groups on the Gr, adsorbed H_2O molecules, and possibly some Fe_3O_4 nanoparticles. The mapping data for C, O and Fe are illustrated in Figure 7-3 (d, e, f), further demonstrating that the three components of C, O and Fe are nearly evenly distributed.

7.3.3 Comparison of the adsorbents Gr and Gr/Fe

Under the same experimental conditions, Gr and Gr/Fe were employed as the adsorbents for the comparison of their adsorption capacities. The results are shown in Figure 7-4, it can be seen that the adsorption capacity of the Gr/Fe for the four compounds is slightly higher than that of the Gr (for MCPA: Removal% is 30.85 ± 0.46 with Gr adsorbent and 33.63 ± 0.96 with Gr/Fe adsorbent; for *p*-NP: Removal% is 50.28 ± 0.90 with Gr adsorbent and 52.88 ± 1.6 with Gr/Fe adsorbent; for MTZ: Removal% is 36.98 ± 0.62 with Gr adsorbent and 38.33 ± 1.22 with Gr/Fe adsorbent; for LEVO: Removal% is 40.75 ± 0.58 with Gr adsorbent and 42.89 ± 1.58 with Gr/Fe adsorbent). This may be due to the reason that the deposition of Fe nanoparticles on the Gr surface prevents the aggregation of graphene nanoplatelets, thus increasing the number of active adsorption sites to enhance the removal percentage of the four pollutants. Moreover, the deposition of Fe nanoparticles endows the Gr with magnetism, which facilitates the removal of the magnetic graphene adsorbent through an external magnetic field. Therefore, the Gr/Fe adsorbent was used to remove the four pollutants. To our knowledge, a graphene magnetic nanocomposite comprising, rGO/Fe_3O_4, has been

utilised to adsorb *p*-NP [25] and LEVO [26]. However, a detailed study on the application of the Gr/Fe on the removal of these four pollutants has not been reported.

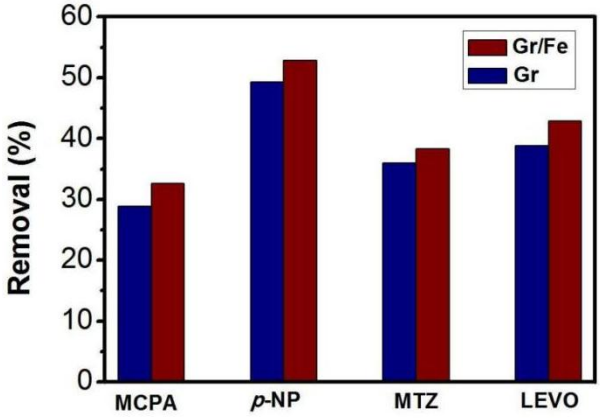

Figure 7-4. Effect of the adsorbents Gr and Gr/Fe on the removal percentage of MCPA, *p*-NP, MTZ and LEVO, n = 3.

7.3.4 Effect of adsorbent dosage

The effect of different dosages of adsorbent on the removal of the four pollutants was investigated using UV-vis spectroscopy, as shown in Figure 7-5. It can be seen that the absorbance of adsorbates decreases as the adsorbent dose increases (Figures 7-5a,c,e and g). The removal percentages (%) of the pollutants were calculated according to the Equation 7–2, and the relationship between the removal percentages and adsorbent dosages are plotted, Figures 7-5b,d,f and h, indicating that the removal percentages of the four pollutants increase with increasing adsorbent dose. This observation is consistent with the higher adsorbent doses leading to an increase in the specific surface area of the adsorbent and the number of active sites for adsorption of the adsorbate. Moreover, according to the fitting curve equations, Removal% = 79.04 (Gr/Fe dosage) + 26.14 ($R^2 = 0.998$) for MCPA, Removal% = 53.46 (Gr/Fe dosage) + 49.38 ($R^2 = 0.998$) for *p*-NP, Removal% = 28.92 (Gr/Fe dosage) + 35.81 ($R^2 = 0.978$) for MTZ, Removal% = 38.82 (Gr/Fe dosage) + 44.94 ($R^2 = 0.989$) for LEVO. Using these equations, the optimal dosages for a removal rate of 100% were calculated to be 0.93 g/L ± 0.032 for MCPA, 0.95 g/L ± 0.039 for *p*-NP, 2.22 g/L ± 0.078 for MTZ and 1.42 g/L ± 0.041 for LEVO, respectively.

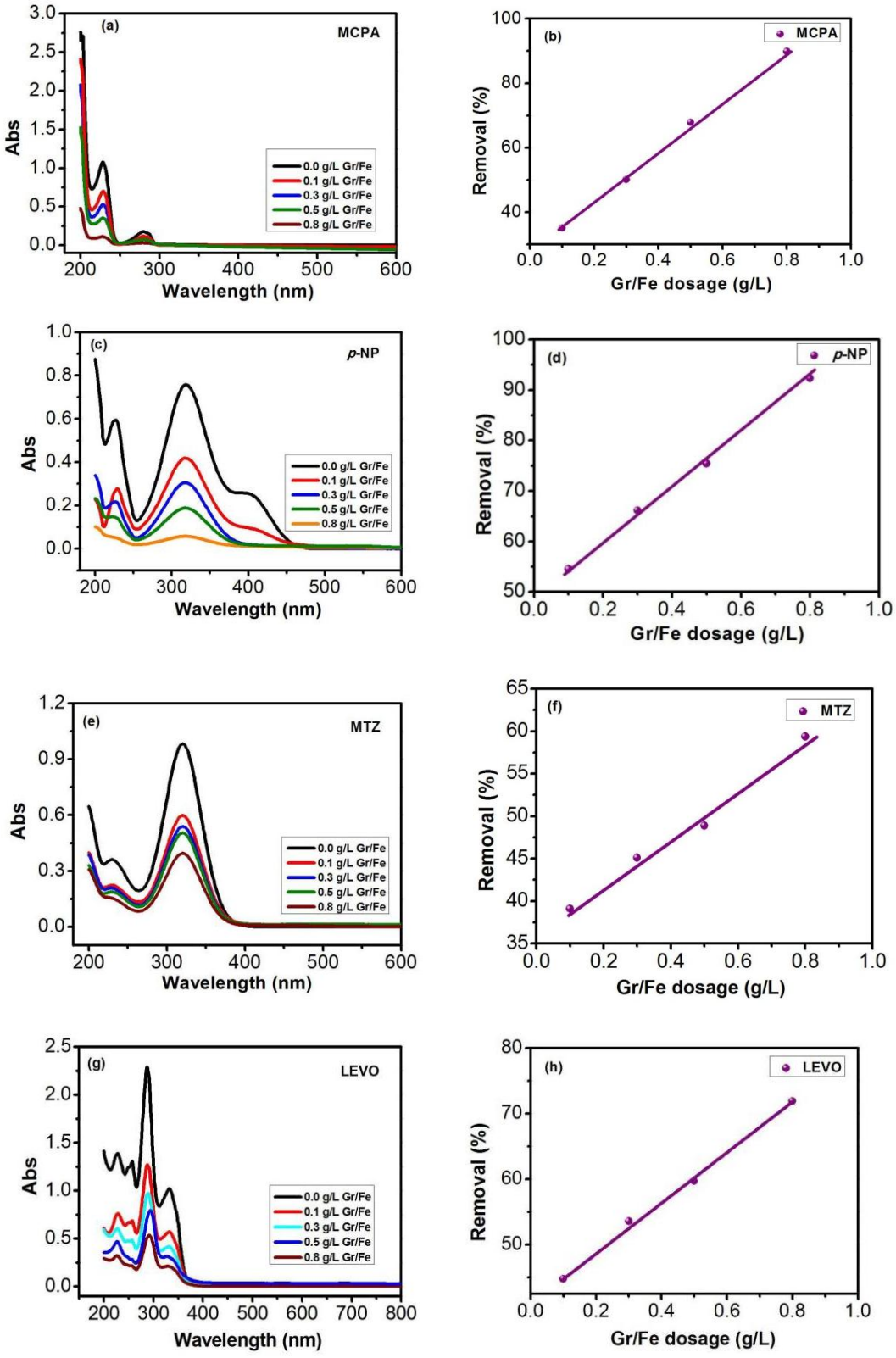

Figure 7-5. UV-vis spectra of MCPA (**a**, 0.1 mM), *p*-NP (c, 0.1 mM), MTZ (**e**, 0.1 mM) and LEVO (**g**, 0.1 mM) after adding different adsorbent dosage, 0.1, 0.3, 0.5 and 0.8 g/L; the removal percentage of pollutants versus the Gr/Fe dosage for MCPA **(b)**, *p*-NP **(d)**, MTZ **(f)** and LEVO **(h)**, n = 3.

The optimal dosages are consistent with the structures of the four pollutants, namely, there are benzene rings in three pollutants, MCPA, *p*-NP and LEVO, whereas there is an imidazole ring in MTZ, thus the removal of MCPA, *p*-NP and LEVO needs a lower dose of Gr/Fe due to the strong π–π interaction between the three pollutants and graphene while the removal of MTZ needs a higher dose of Gr/Fe due to the comparatively weak π–π interaction between MTZ and graphene.

$$\text{Removal\%} = (C_0\text{-}C_e)/C_0 \times 100\% \quad (7\text{–}2)$$

Where, C_0 and C_e are the initial and equilibrium concentrations of the four compounds in solution (mg/L).

7.3.5 Study on the adsorption kinetics

In order to better understand the mechanism of the adsorption process, the adsorption kinetics was studied by recording the adsorption capacity change of the adsorbent with the contact time of the adsorbent and the adsorbate. For this purpose, the concentration of the four compounds and adsorbent were fixed, and the effect of contact time on adsorption was monitored from 20 min to 720 min. The adsorption capacity (q_t) was computed based on Equation 7–3, and plotted at different periods of time (t). As described in Figure 7-6, Figures 7-6a, c, e and g reveal the absorbance variation of the four compounds with the increase of the contact time and Figures 7-6b, d, f and h describe the adsorption kinetic curves. It is evident that the absorbance initially decreases on increasing the contact time over a period of 210 min for MCPA, 270 min for *p*-NP and MTZ, and 390 min for LEVO. Then, it maintains almost unchanged, Figures 7-6a, c, e and g. A similar trend is observed in the plots of the adsorption capacity (q_t) versus the contact time (t), Figures 7-6b, d, f and h. This indicates that the contact time requiring to reach equilibrium is 210 min for MCPA, 270 min for *p*-NP and MTZ, and 390 min for LEVO, respectively.

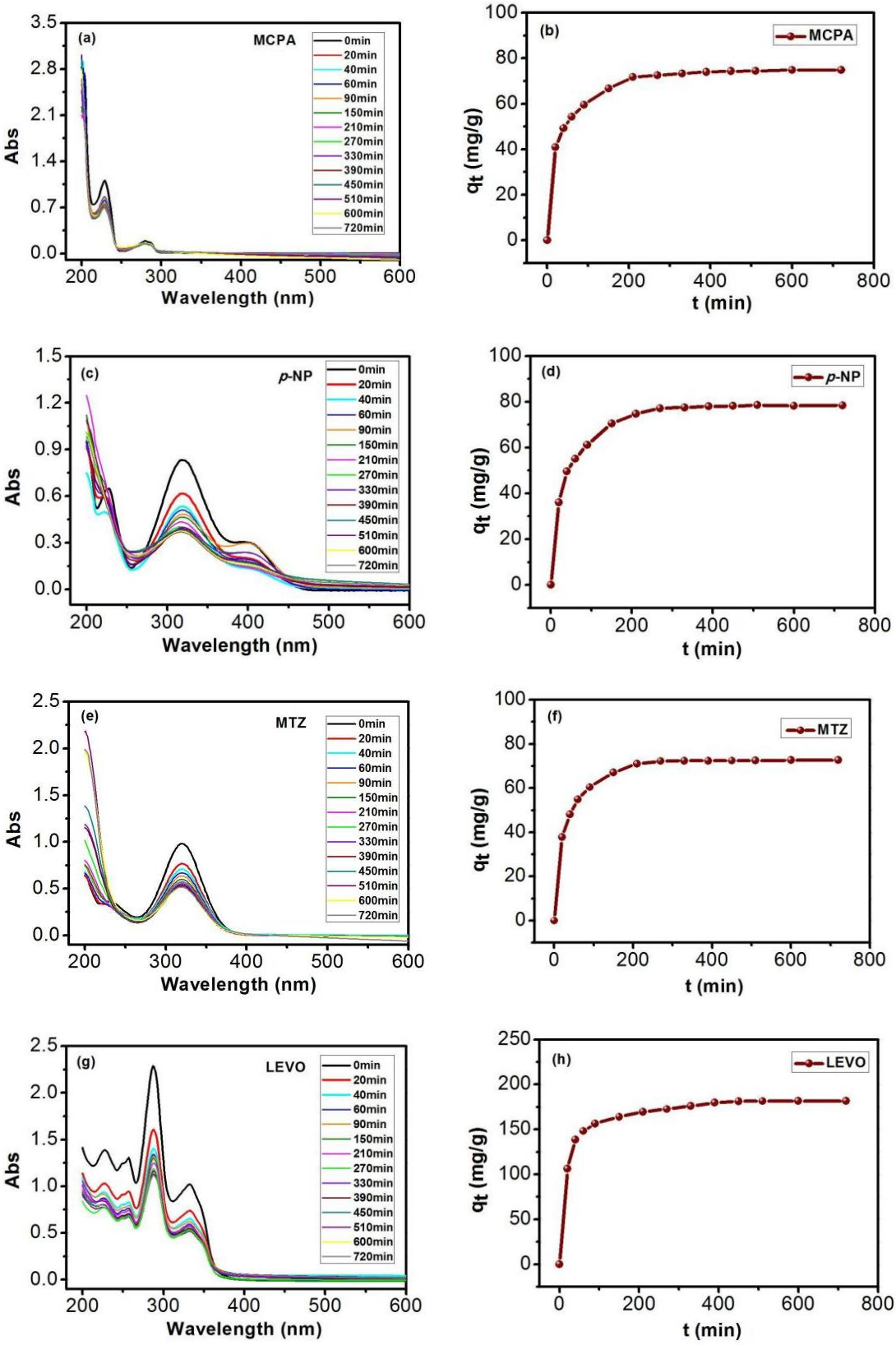

Figure 7-6. UV-vis spectra of MCPA (**a**, 0.1 mM), *p*-NP (**c**, 0.1 mM), MTZ (**e**, 0.1 mM) and LEVO (**g**, 0.1 mM) after adding the Gr/Fe (0.1 g/L) at different contact time; the adsorption capacity (q_t) of the adsorbent versus the contact time (t) for MCPA **(b)**, *p*-NP **(d)**, MTZ **(f)** and LEVO **(h)**, n = 1.

Moreover, it can be found from Figure 7-6 that in the first 20 min, the adsorption capacity of the adsorbent for the four compounds rapidly increased and then rose slowly until reaching the adsorption equilibrium within 210 min for MCPA, 270 min for *p*-NP and MTZ, 390 min for LEVO. The equilibrium adsorption capacities were estimated at about 75.53 mg/g for MCPA, 78.68 mg/g for *p*-NP, 73.11 mg/g for MTZ, 183.39 mg/g for LEVO, respectively.

Further, two conventional kinetic models based on pseudo-first order (see Equation 7–4) [27] and pseudo-second order equations (see Equation 7–5) [28] were employed to analyse the experimental data. The corresponding fitting curves are shown in Figure 7-7 and the values of the kinetic parameters are given in Table 7-1.

$$q_e = (C_0\text{-}C_e) \times V / m \qquad (7\text{–}3)$$

Where, C_0 and C_e are the initial and equilibrium concentrations, respectively, of the four compounds in solution (mg/L), V represents the volume of the solution (L), m expresses the mass of the adsorbent (g), q_e (mg/g) is the equilibrium adsorption capacity of the adsorbent.

Pseudo-first-order model: $\ln (q_e\text{-}q_t) = \ln q_e - k_1 t$ (7–4)

Pseudo-second-order model: $t/q_t = 1/(k_2 q_e^2) + t/q_e$ (7–5)

Where, q_e is the adsorption capacity of the adsorbent at equilibrium (mg/g), q_t is the adsorption capacity of the adsorbent at various times t (mg/g), k_1 is the rate constant of the pseudo-first order adsorption (1/min), k_2 is the rate constant of the pseudo-second order adsorption (g/(mg min)). The values of q_e, k_1 and k_2 can be obtained from the corresponding slope and intercept of the linear plots of ln (q_e-q_t) versus t for the pseudo-first order model and t/q_t versus t for the pseudo-second order model, respectively.

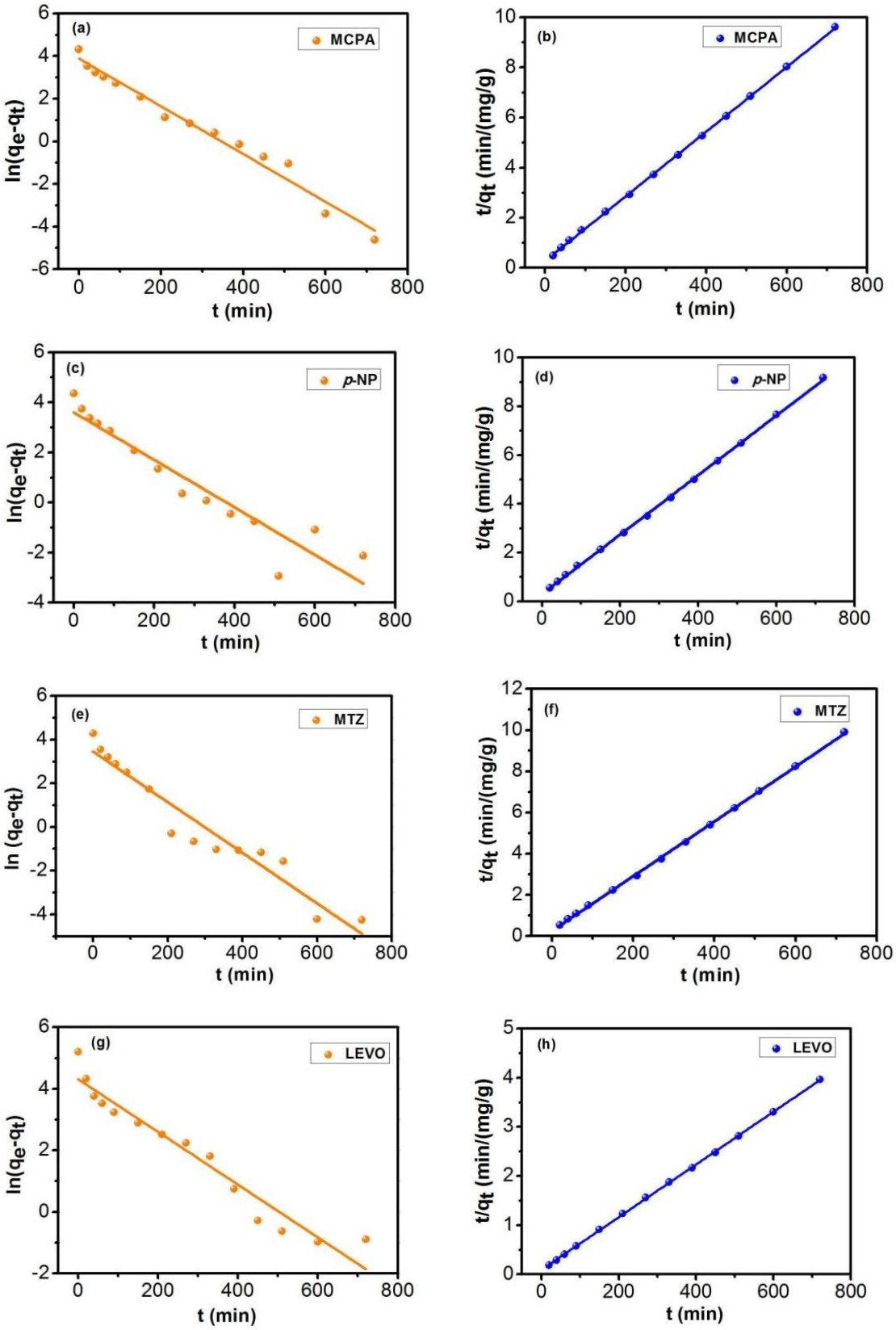

Figure 7-7. Adsorption kinetics of four compounds adsorbed by the Gr/Fe: pseudo-first-order model for MCPA **(a)**, *p*-NP **(c)**, MTZ **(e)** and LEVO **(g)** and pseudo-second-order model for MCPA **(b)**, *p*-NP **(d)**, MTZ **(f)** and LEVO **(h)**.

Comparing the correlation coefficient R^2 values indicates that the R^2 values for the pseudo-second order model are much higher than that for the pseudo-first order model, suggesting that the adsorption of the four compounds onto Gr/Fe follows the pseudo-second order kinetic model. Furthermore, the adsorption capacities obtained from fitting the results are 77.52 mg/g for MCPA, 81.90 mg/g for *p*-NP, 75.13 mg/g for MTZ, and 186.56 mg/g for LEVO, which are close to the experimental adsorption capacities. This observation further supports the above deduction, namely, the adsorption of the four compounds by the Gr/Fe does follow the pseudo-second order kinetic model, indicating that external film diffusion, adsorption, and internal particle diffusion are important in the adsorption event [29].

Table 7-1. Parameters of pseudo-first order and pseudo-second order kinetic models for the adsorption of the four compounds by the Gr/Fe (n = 1).

Compounds	Pseudo-first-order			Pseudo-second-order			$q_{e,exp}$ (mg/g)
	k_1 (1/min)	$q_{e,cal}$ (mg/g)	R^2	k_2 (1/min)	$q_{e,cal}$ (mg/g)	R^2	
MCPA	0.0112	48.47	0.97	0.00060	77.52	0.99	75.53
p-NP	0.00949	36.78	0.89	0.00051	81.90	0.99	78.68
MTZ	0.01157	31.65	0.93	0.00075	75.13	0.99	73.11
LEVO	0.00857	74.74	0.94	0.00032	186.56	0.99	183.39

7.3.6 Study on the adsorption isotherms

When the amount of the Gr/Fe adsorbent was fixed and the concentrations of the adsorbates, including MCPA, *p*-NP, MTZ and LEVO, were changed, the adsorption capacities of the Gr/Fe adsorbent were assessed. The results indicated that the adsorption capacities of the Gr/Fe adsorbent increased with increasing the initial concentrations of the adsorbates, Figure 7-8. This may be due to the increase in the driving force of the concentration gradient, as increasing the concentrations of the adsorbates can accelerate the diffusion of adsorbates to the solid surfaces. However, no

linear relationship between the adsorption capacities of adsorbent and concentrations of the adsorbate was observed. For the four compounds, the same changes in the trend were seen, that is, after increasing the concentration of the four compounds from 4.0 to 20.0 mg/L for MCPA, from 2.8 to 13.9 mg/L for *p*-NP, from 3.4 to 17.1 mg/L for MTZ and from 7.2 to 36.1 mg/L for LEVO, there is only a little increase on the adsorption capacities. It is expected that a saturated adsorption capacity will be reached at high concentration of the four compounds. It is evident that the adsorption capacities of the Gr/Fe adsorbent depend on the concentration of the four compounds. Similar findings have been reported in the removal of other pollutants using graphene-based materials as adsorbents [13].

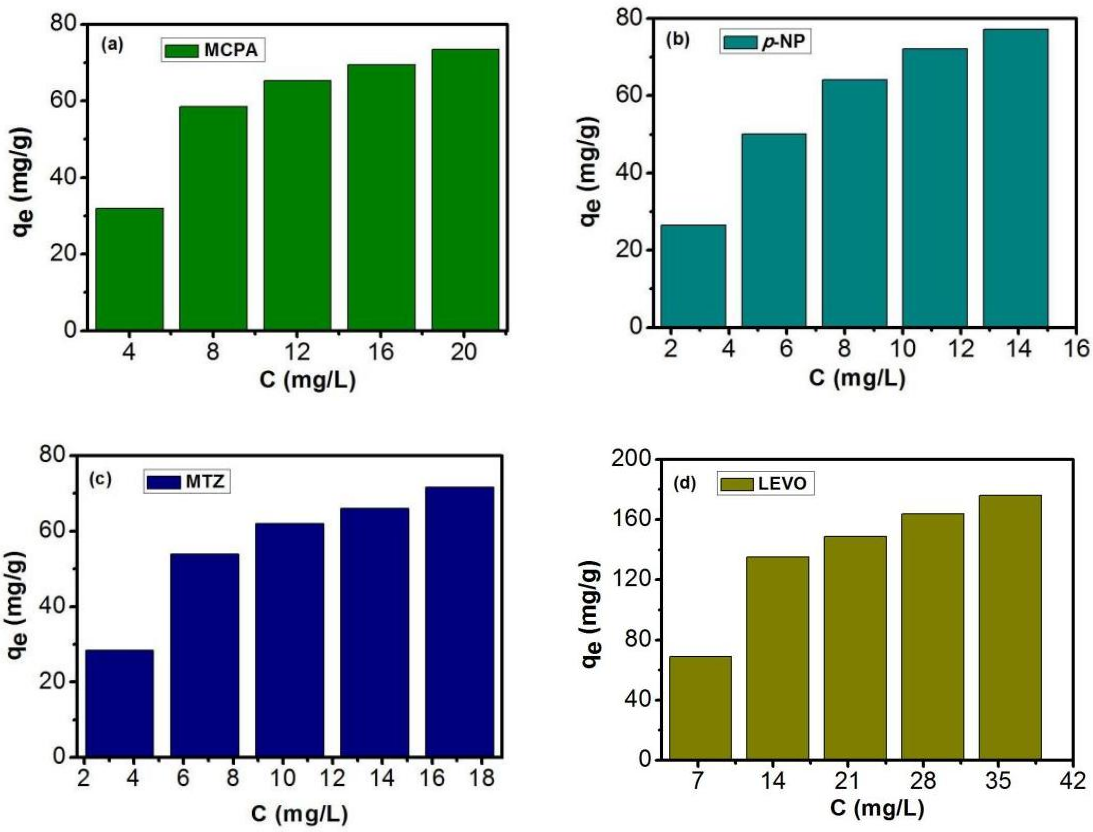

Figure 7-8. The effect of the initial concentrations of MCPA (**a**: 4.0, 8.0, 12.0, 16.0 and 20.0 mg/L), *p*-NP (**b**: 2.8, 5.6, 8.4, 11.1 and 13.9 mg/L), MTZ (**c**: 3.4, 6.8, 10.3, 13.7 and 17.1 mg/L) and LEVO (**d**: 7.2, 14.5, 21.7, 28.9 and 36.1 mg/L) on the adsorption capacity of the Gr/Fe adsorbent (0.1 g/L), n = 1.

Further, the adsorption isotherm models were employed to describe the equilibrium of the adsorption process between the absorbent and the adsorbate. The commonly used adsorption isotherm models are the Langmuir and Freundlich models, where the Langmuir isotherm model assumes that the adsorption of the adsorbate takes place on a uniform solid surface with a monolayer coverage and there is no subsequent interaction between the adsorbed components [30]. In contrast, the Freundlich isotherm model is considered as an empirical model related to multilayer adsorption on the heterogeneous solid surface [31]. The equations corresponding to the two isotherm models are given in the Equations 7–6 and 7–7, respectively. The plots based on fitting the experimental data are revealed in Figure 7-9 and the relative parameters computed from the data fitting are described in Table 7-2. Comparing the correlation coefficient R^2 values for the two models, it is obvious that the Langmuir model gives better fitting of the adsorption data than the Freundlich model, demonstrating that the adsorption of MCPA, *p*-NP, MTZ and LEVO onto the Gr/Fe was carried out in a monolayer adsorption manner. Moreover, it can be seen that according to the Langmuir model for the adsorption of the four compounds by the Gr/Fe adsorbent, that good linear relationships were gained when C_e/q_e was plotted against C_e, and then the values of q_{max} and k_L were obtained based on the slope and intercept. The maximum adsorption capacities of Gr/Fe in 0.1 mM adsorbate are 78.62 mg/g for MCPA, 80.51 mg/g for *p*-NP, 76.51 mg/g for MTZ and 177.94 mg/g for LEVO.

Langmuir model: $$C_e/q_e = 1/(q_m \cdot K_L) + C_e/q_m \quad (7–6)$$

Freundlich model: $$\log q_e = 1/n \log C_e + \log K_F \quad (7–7)$$

Where, q_e is the adsorption capacity of the adsorbent at equilibrium (mg/g), q_m is the maximum adsorption capacity of the adsorbent (mg/g), C_e expresses the equilibrium concentration of the adsorbate in solution (mg/L), n is the Freundlich constant that represents the adsorption strength, K_L is the Langmuir constant (L/mg), related to the affinity of the binding sites, and K_F is the Freundlich constant representing the adsorption capacity. The values of q_m and K_L can be obtained from the slope and

intercept of the linear plots of C_e/q_e versus C_e for the Langmuir model. The parameters, n and K_F can be determined from the slope and intercept of the linear plot of log q_e against log C_e.

Table 7-2. Isotherm parameters for the adsorption of four compounds onto the Gr/Fe based on the Langmuir and Freundlich models (n = 1).

Compounds	Langmuir model				Freundlich model		
	q_{max} (mg/g)	k_L (L/g)	R^2	R_L	k_F (L/g)	1/n	R^2
MCPA	78.62	0.96	0.99	0.050	38.71	0.28	0.81
p-NP	80.52	2.77	0.99	0.025	51.07	0.27	0.93
MTZ	76.51	1.15	0.99	0.048	39.02	0.29	0.81
LEVO	177.94	1.45	0.99	0.019	103.99	0.19	0.73

In addition, a dimensionless equilibrium parameter, R_L, was used to further describe the adsorption process related to the Langmuir model. R_L is defined as follows in Equation 7–8 [14]:

$$\mathbf{R_L = \frac{1}{1 + k_L C_0}} \qquad (7–8)$$

where k_L expresses the Langmuir constant (L/g) and C_0 represents the highest initial concentration of the adsorbate (mg/L). According to Equation 7–8, R_L can be calculated. The value of R_L indicates whether the isotherm is unfavorable ($R_L > 1$), favorable ($R_L < 1$), linear ($R_L = 1$), or irreversible ($R_L = 0$). It is clear that in Table 7-2, R_L values are between 0 and 1, suggesting the adsorption of the four compounds by the Gr/Fe is favorable.

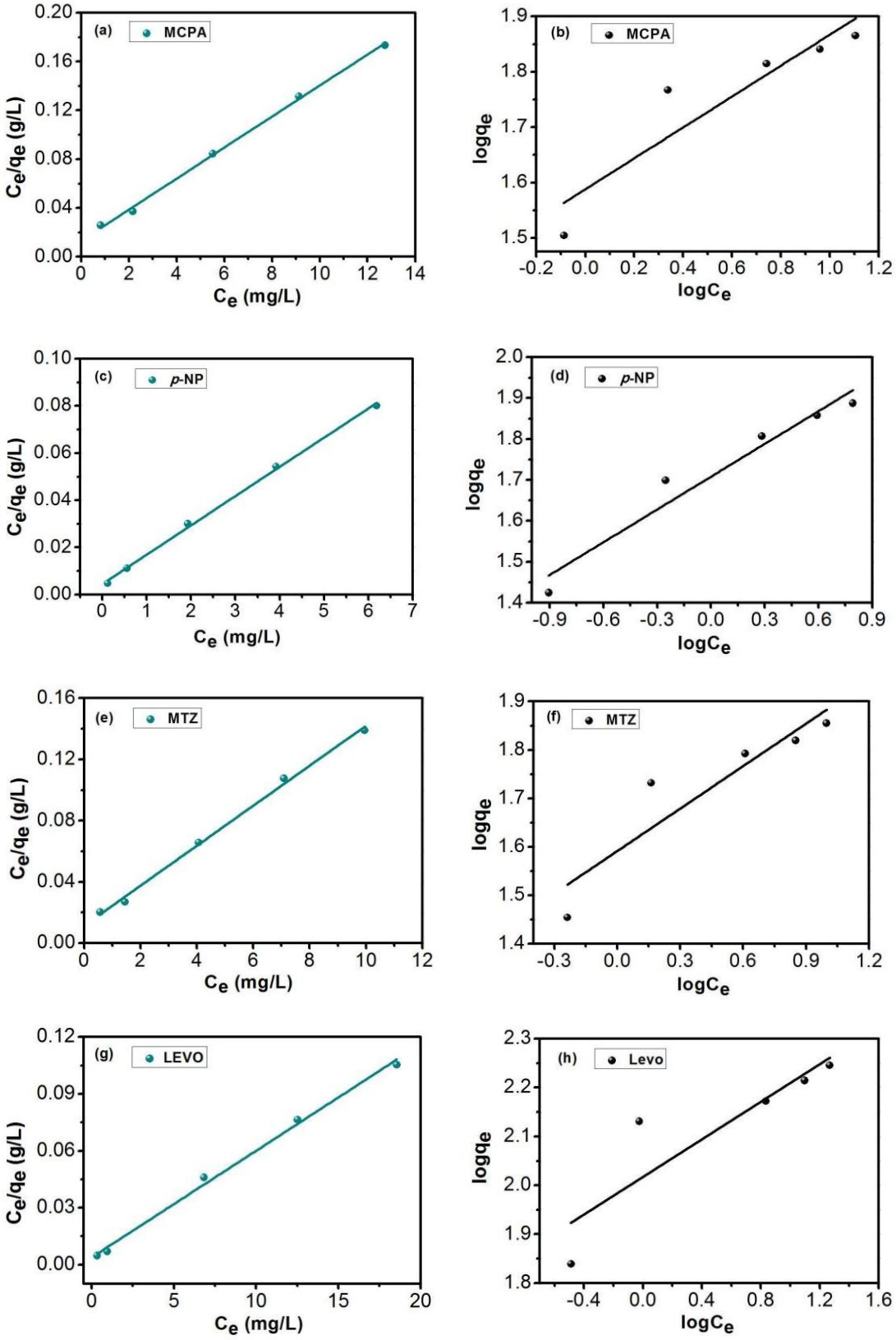

Figure 7-9. The equilibrium isotherm for four compounds adsorbed by the Gr/Fe: the Langmuir isotherm for MCPA **(a)**, *p*-NP **(c)**, MTZ **(e)** and LEVO **(g)** and the Freundlich isotherm for MCPA **(b)**, *p*-NP **(d)**, MTZ **(f)** and LEVO **(h)**.

7.3.7 Effect of the solution pH on the adsorption

The solution pH is one of the most important factors to determine the adsorption behavior of the adsorbent as the net charge of the adsorbent and adsorbate could be changed with the variation of the solution pH. Figure 7-10 exhibits the effect of the solution pH on the adsorption of the four compounds onto Gr/Fe with the initial solution pH ranging from 3.0 to 9.0. From Figure 7-10, it can be observed that the change of the solution pH displays different effects on the removal percentage of the four compounds. This was attributed to the fact that the four pollutants have different molecular structures and functional groups (see Figure 7-1) as well as pK_a values (see Table 7-3) [15,26,32,33].

Both MCPA and *p*-NP have pK_a values. When the solution pH is lower than the pK_a, the molecules are present in the neutral form, whereas when the solution pH is higher than the pK_a, the molecules exist in both the neutral and negative ion forms and exhibit the anionic forms at higher pH. For MTZ and LEVO, there are two pK_a values. When the solution pH is lower than the pK_{a1}, the molecules exist in the neutral form, when the solution pH is between the pK_{a1} and pK_{a2} values, the molecules exist as zwitterion forms. When the solution pH is higher than the pK_{a2}, the molecules are converted to the anionic forms.

The surface charge of Gr/Fe is negative from pH 3 to pH 9 originating from the surface nature of graphene nanoplatelets [34]. Therefore, at lower pH, the four pollutants are adsorbed on the Gr/Fe via π–π interaction, exhibiting high removal percentage of the four pollutants. In contrast, at higher pH, the four pollutants gave low removal percentage by the Gr/Fe adsorbent, attributed to repulsion between the pollutants and Gr/Fe, resulting in retarded adsorption efficiency. Meanwhile, the negative charge on the Gr/Fe surface is enhanced on increasing the solution pH, enhancing the electrostatic repulsion between the pollutants and Gr/Fe. These findings indicate that the electrostatic interaction impacts the final removal efficiency for the pollutants. The obtained results are in good agreement with other adsorption results [15,33,35,36].

Table 7-3. The pK_a of four compounds.

Compounds	pK_a	References
MCPA	pK_a = 3.07	[32]
p-NP	pK_a = 7.15	[25]
MTZ	pK_{a1} = 2.58, pK_{a2} = 14.44	[15]
LEVO	pK_{a1} = 5.8, pK_{a2} = 8.0	[33]

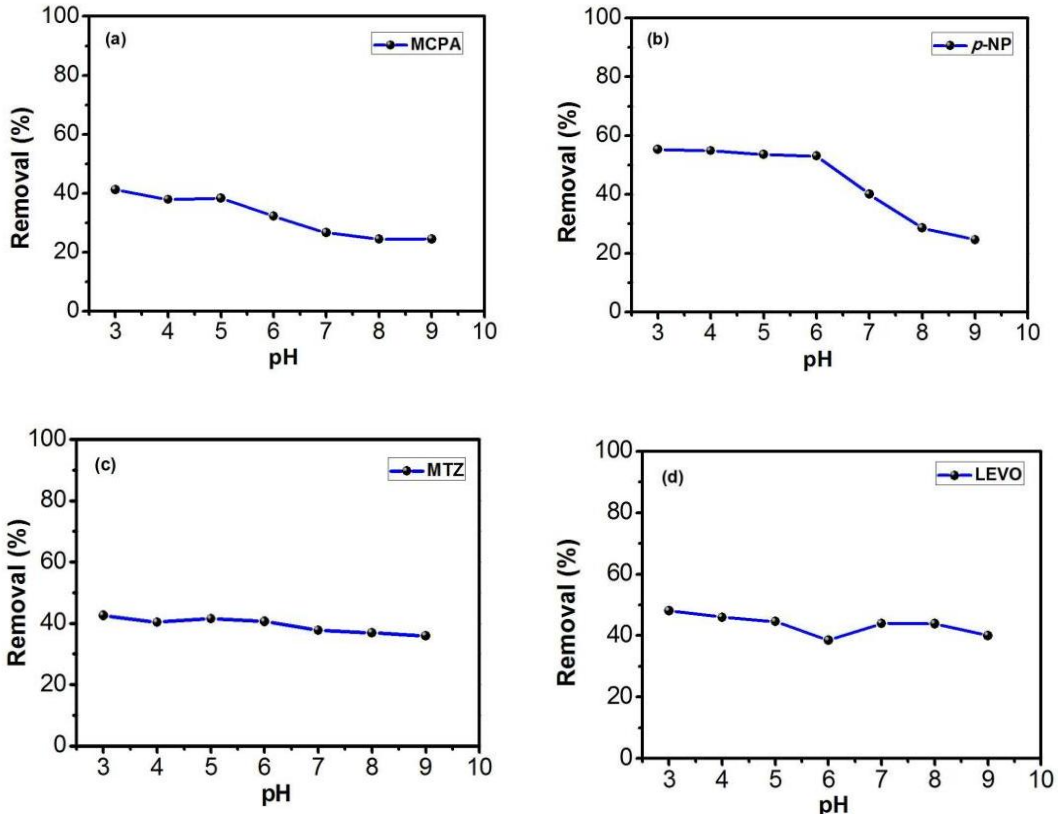

Figure 7-10. Effect of the solution pH on the adsorption of MCPA (**a**, 0.1 mM), *p*-NP (**b**, 0.1 mM), MTZ (**c**, 0.1 mM) and LEVO (**d**, 0.1 mM) onto Gr/Fe (0.1 g/L).

7.3.8 Study on the effect of the interference

It is well known that industrial wastewater involves not only pollutants but also high concentrations of various salts, which are often determined in industrial sewage, thus these salts might affect the removal of pollutants. In this work, the salts, such as $CaCl_2$,

KH_2PO_4, Na_2SO_4, $NaNO_3$, were selected for studying their effect on the removal of the four compounds when they coexist with the interferents. For this purpose, the experiments were conducted in the mixed solutions containing the salts and the four compounds at concentration ratios of 100:1 corresponding to a 100-fold excess of the $CaCl_2$, KH_2PO_4 and Na_2SO_4 interferents. However, as $NaNO_3$ itself exhibits a strong absorption in the UV region and its absorption band overlaps partially with that of the four compounds, the concentration ratio was set up as 1:1 for MCPA and 10:1 for the other three compounds, to decrease the interference caused by UV absorption of $NaNO_3$. As shown in Figure 7-11 and Table 7-4, it can be seen that the changes for the effect of interference on the removal of the four compounds are from 95.6 to 101.1% for $CaCl_2$, from 96.5 to 104.8% for KH_2PO_4, from 95.1 to 100.9% for Na_2SO_4 and from 89.1 to 100.5% for $NaNO_3$, indicating that the coexistence of $CaCl_2$, KH_2PO_4, Na_2SO_4 and $NaNO_3$ does not show significant effect on the removal of the four compounds.

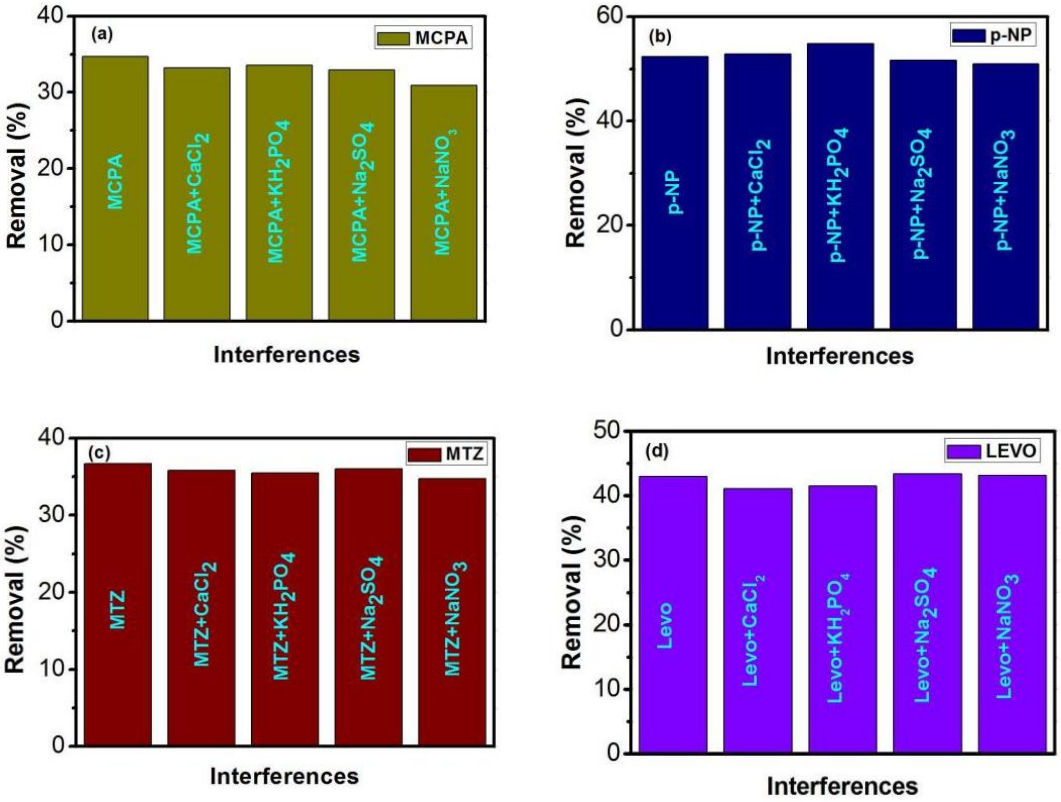

Figure 7-11. Effect of the interferences on the removal of MCPA (**a**, 0.1 mM), *p*-NP (**b**, 0.1 mM), MTZ (**c**, 0.1 mM) and LEMO (**d**, 0.1 mM) with the Gr/Fe adsorbent (0.1 g/L), n = 3.

Table 7-4. The effect of interference on the removal of four compounds (n = 3).

	Removal% with inteference : Removal% without interference (%)			
	$CaCl_2$	KH_2PO_4	Na_2SO_4	$NaNO_3$
MCPA	95.8 ± 3.48	96.7 ± 2.87	95.1 ± 2.36	89.1 ± 3.72
p-NP	101.1 ± 2.82	104.8 ± 3.33	98.8 ± 2.43	97.4 ± 1.85
MTZ	97.7 ± 1.66	96.6 ± 2.70	98.1 ± 3.35	94.8 ± 3.79
LEVO	95.6 ± 1.92	96.5 ± 2.33	100.9 ± 2.55	100.5 ± 1.81

7.3.9 IR characterisation after adsorption of four compounds onto Gr/Fe

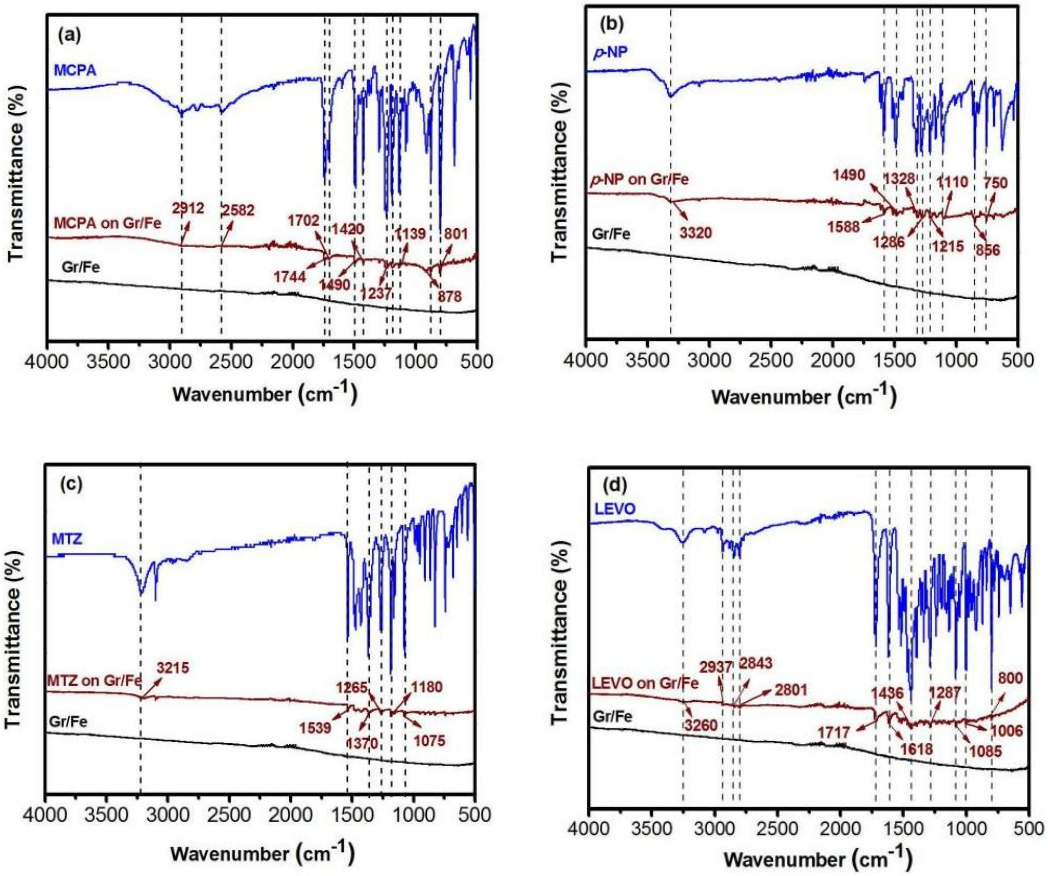

Figure 7-12. IR spectra of Gr/Fe (black curves), MCPA (**a**, blue curve), *p*-NP (**b**, blue curve), MTZ (**c**, blue curve), LEVO (**d**, blue curve), Gr/Fe adsorbing four compounds (red curves).

Infrared (IR) spectroscopy is a useful technique for identifying the presence of characteristic functional groups on solid surfaces. In order to confirm the adsorption of the four compounds onto the Gr/Fe, the FTIR spectra of the four compounds, Gr/Fe and Gr/Fe following adsorption of the four compounds were recorded and compared. As illustrated in Figure 7-12, it can be seen that the Gr/Fe doesn't show any strong bands (black curves), however, after the adsorption of the four compounds onto the Gr/Fe, some new vibration peaks appear in red curves, and these new peaks are in accordance with that from the IR spectra of the four compounds. This observation demonstrates that the four compounds have indeed been adsorbed on the surface of the Gr/Fe.

7.3.10 Reproducibility of the Gr/Fe adsorbent

The reproducibility of the adsorption process is one of the most important factors for its practical application in removing pollutants. For this purpose, the Gr/Fe adsorbent was synthesised five times by using the same preparation procedure on different days and employed to remove the four pollutants. After each adsorption experiment, the removal percentages (%) of each pollutant was calculated and the obtained results are listed in Table 7-4, where five separate experiments were done at a concentration of 0.1 mM for each pollutant using the Gr/Fe of 0.1 g/L. It is evident that the % RSD values are lower than 5%, demonstrating that the Gr/Fe adsorbent displays good reproducibility for the removal of the four pollutants.

Table 7-4. Reproducibility of the Gr/Fe adsorbent in the removal of four pollutants.

Pollutants	Removal percentages (%)					Mean (n = 5)	RSD (%) (n = 5)
	1	2	3	4	5		
MCPA	34.79	33.72	31.98	35.23	32.45	33.63 ± 1.41	4.21
p-NP	54.52	51.76	55.32	52.56	50.98	53.03 ± 1.83	3.46
MTZ	39.09	37.45	36.92	40.73	37.48	38.33 ± 1.56	4.08
LEVO	44.78	41.61	43.95	45.38	42.37	43.62 ± 1.59	3.65

7.3.11 Regeneration of the Gr/Fe adsorbent

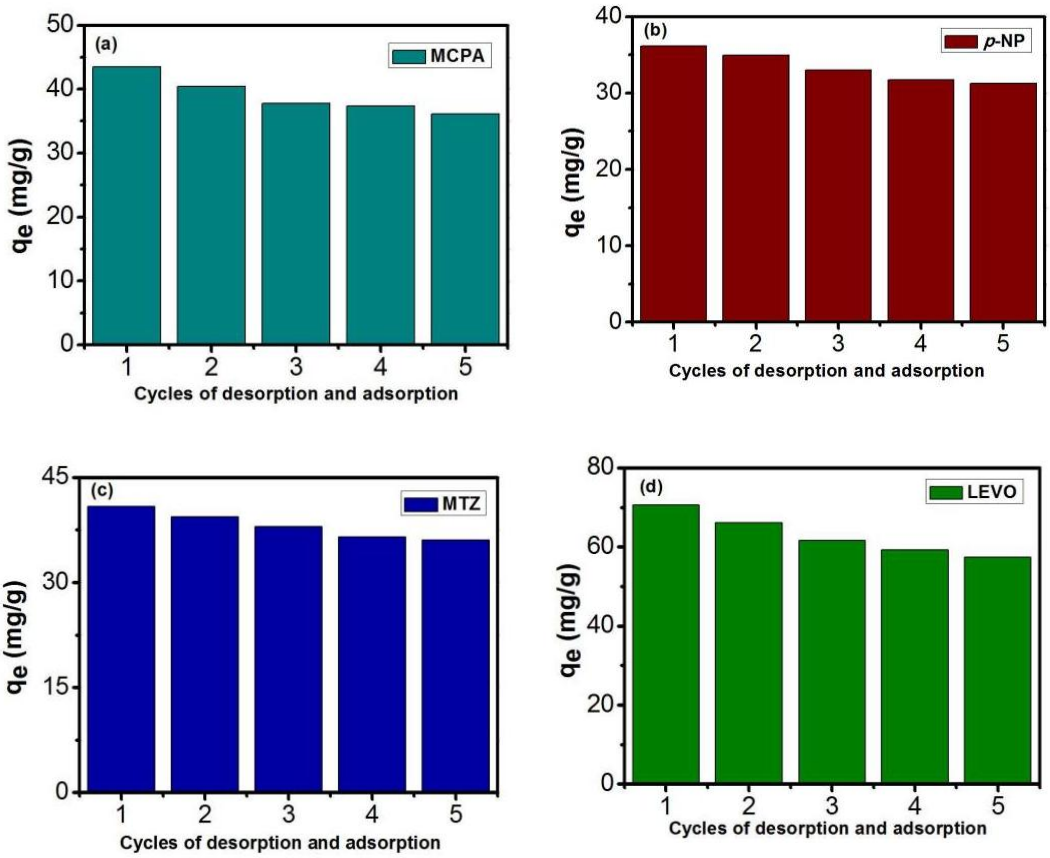

Figure 7-13. The regeneration experiments on the removal of MCPA (**a**, 0.1 mM), *p*-NP (b, 0.1 mM), MTZ (**c**, 0.1 mM) and LEVO (**d**, 0.1 mM) with the Gr/Fe adsorbent (0.05 g/L) for 5 times, n = 3.

In order to evaluate the cost-effectiveness and applicability of the Gr/Fe adsorbent, the investigation was conducted on its regeneration by immersing the recovered Gr/Fe in 0.1 M NaOH for 10 min and washing in sequence first with distilled water for five times while stirring, followed, with absolute ethanol for five times, then drying in a vacuum oven over night. After the treatment, the regenerated adsorbent Gr/Fe was used to remove the four pollutants again. The adsorption capacities of the regenerated adsorbent Gr/Fe are shown in Figure 7-13, it is noticed that after five regeneration cycles, compared to the adsorption capacities of the freshly prepared adsorbent Gr/Fe, the adsorption capacities of the adsorbent Gr/Fe decrease by 16.98% ± 0.71 for MCPA,

13.63% ± 0.52 for *p*-NP, 11.68% ± 0.38 for MTZ and 18.63% ± 0.67 for LEVO, respectively. This observation may be due to the following reasons: (i) for the adsorbent Gr/Fe, the component Gr plays a major role in adsorbing pollutants; (ii) the adsorbent Gr/Fe was separated by a magnet, resulting in the loss of the Gr component. Nevertheless, the results demonstrated that the Gr/Fe adsorbent can be efficiently regenerated by an appropriate treatment procedure, hereby providing beneficial cost-savings.

7.4 Conclusions

In this chapter, the magnetic adsorbent based on Gr and Fe was synthesised as Gr/Fe, which was characterised by SEM, EDX and element mapping, displaying the Fe nanoparticles were uniformly dispersed on the Gr nanoplatelets. The magnetic Gr/Fe adsorbent was utilised for the removal of MCPA, *p*-NP, MTZ and LEVO from aqueous solutions. The kinetic studies indicated that the experiment data fitted best to the kinetic model of pseudo-second order. The adsorption data followed the Langmuir isotherm model, which revealed that monolayer adsorption of the four compounds occurred on the Gr/Fe. The study on the effect of the solution pH on the adsorption capacity of the Gr/Fe adsorbent demonstrated that the low solution pH is favorable for the removal of the four pollutants as compared to higher solution pH. The study on the regeneration of the Gr/Fe adsorbent suggested that the use of magnetic adsorbent Gr/Fe could be recycled for the removal of the pollutants from aqueous solutions. Therefore, the magnetic adsorbent exhibits the advantages of simple preparation, easy separation, and reuse.

7.5 References

[1] Liu, Y. X.; Lonappan, L.; Brar, S. K.; Yang, S. M. Impact of biochar amendment in agricultural soils on the sorption, desorption, and degradation of pesticides: A review, *Sci. Total Environ*. **2018**, *645*, 60–70, doi: 10.1016/j.scitotenv.2018.07.099.

[2] Mei, M.; Huang, X.; Yu, J.; Yuan, D.: Sensitive monitoring of trace nitrophenols in water samples using multiple monolithic fiber solid phase microextraction and liquid chromatographic analysis, *Talanta* **2015**, *134*, 89–97, doi: 10.1016/j.talanta.2014.10.059.

[3] Lala, V. G.; Rabat, B.; Haagensen, M.; Kathan, P.; Mahomed, A. Metronidazole-induced encephalopathy, *SA J. Radio*. **2021**, *25*, a2016, doi: 10.4102/sajr.v25i1.2016.

[4] Panahi, L.; Surani, S. S.; Udeani, G.; Patel, N. P.; Sellers, J. Hepatotoxicity secondary to levofloxacin use, *Cureus J. Med. Sci*. **2021**, *13*, e15973, doi: 10.7759/cureus.15973.

[5] Blachnio, M.; Kusmierek, K.; Swiatkowski, A.; Derylo-Marczewska, A. Adsorption of phenoxyacetic herbicides from water on carbonaceous and non-carbonaceous adsorbents, *Molecules* **2023**, *28*, 5404, doi: 10.3390/molecules28145404.

[6] Tchinsa, A.; Hossain, M. F.; Wang, T.; Zhou, Y. B. Removal of organic pollutants from aqueous solution using metal organic frameworks (MOFs)-based adsorbents: A review, *Chemosphere*, **2021**, *284*, 131393, doi: 0.1016/j.chemosphere.2021.131393.

[7] Liu, K.; Chen, J. F.; Sun, F. F.; Liu, Y. Y.; Tang, M. Z.; Yang, Y. W. Historical development and prospect of intimately coupling photocatalysis and biological technology for pollutant treatment in sewage: A review, *Sci. Total Environ*. **2022**, *835*, 155482, doi: 10.1016/j.scitotenv.2022.155482.

[8] Alqassem, B.; Othman, I.; Abu Haija, M.; Banat, F. Comparative catalytic activity of pure, mixed and P-modified $CoFe_2O_4$ nanoparticles for water treatment at neutral pH, *Catal. Commun*. **2021**, *150*, 106267, doi: 10.1016/j.catcom.2020.106267.

[9] Gao, H. P.; Wang, Y. G.; Afolabi, M. A.; Xiao, D. Q.; Chen, Y. S. Incorporation of cellulose nanocrystals into graphene oxide membranes for efficient antibiotic removal at high nutrient recovery, *ACS Appl. Mater. Interfaces*, **2021**, *13*, 14102–14111, doi: 10.1021/acsami.0c20652.

[10] Madima, N.; Mishra, S. B.; Inamuddin, I.; Mishra, A. K. Carbon-based nanomaterials for remediation of organic and inorganic pollutants from wastewater. A review, *Environ. Chem. Lett*. **2020**, *18*, 1169–1191, doi: 10.1007/s10311-020-01001-0.

[11] Sobrinho, M. A. D.; da Silva, J. I. New trends in environmental applications

of adsorption, *Environ. Sci. Pollut. Res*. **2022**, *29*, 79786–79787, doi: 10.1007/s11356-022-23259-3.

[12] Ren, J. R.; Zhu, Z. L.; Qiu, Y. L.; Yu, F.; Ma, J.; Zhao, J. F. Magnetic field assisted adsorption of pollutants from an aqueous solution: A review, *J. Hazar. Mater*. **2021**, *408*, 124846, doi: 10.1016/j.jhazmat.2020.124846.

[13] Xu, J.; Wang, L.; Zhu, Y. F. Decontamination of bisphenol A from aqueous solution by graphene adsorption, *Langmuir* **2012**, *28*, 8418−8425, doi: 10.1021/la301476p.

[14] Liu, T. H.; Li, Y. H.; Du, Q. J.; Sun, J. K.; Jiao, Y. Q.; Yang, G. M.; Wang, Z. H. Xia, Y. Z.; Zhang, W.; Wang, K. L.; Zhu, H. W.; Wu, D. H, Adsorption of methylene blue from aqueous solution by graphene, *Colloid Surface B*. **2012**, *90*, 197–203, doi:10.1016/j.colsurfb.2011.10.019.

[15] Carrales-Alvarado, D. H.; Rodriguez-Ramos, I.; Leyva-Ramos, R.; Mendoza-Mendoza, E.; Villela-Martinez, D. E. Effect of surface area and physical-chemical properties of graphite and graphene-based materials on their adsorption capacity towards metronidazole and trimethoprim antibiotics in aqueous solution, *Chem. Eng. J*. **2020**, *402*, 126155, doi: 10.1016/j.cej.2020.126155.

[16] Kulaishin, S. A.; Vedenyapina, M. D.; Kurmysheva, A. Y. Influence of the Surface Characteristics of Activated Carbon on the Adsorption of Herbicides, *Solid Fuel Chem*. **2022**, *56*, 181–198, doi: 10.3103/S0361521922030041.

[17] Talari, M. H.; Tabrizi, N. S.; Babaeipour, V.; Halek, F. Adsorptive removal of organic pollutants from water by carbon fiber aerogel derived from bacterial cellulose, *J. Sol-Gel Sci. Technol*. **2022**, *101*, 345–355, doi: 10.1007/s10971-021-05708-6.

[18] El Ouahedy, N.; Zbair, M.; Ojala, S.; Brahmi, R.; Pirault-Roy, L. Porous carbon materials derived from olive kernels: application in adsorption of organic pollutants, *Environ. Sci. Pollut. Res*. **2020**, *27*, 29967–29982, doi: 10.1007/s11356-020-09268-0.

[19] Sajid, M.; Asif, M.; Baig, N.; Kabeer, M.; Ihsanullah, I. Mohammad, A. W. Carbon nanotubes-based adsorbents: Properties, functionalization, interaction mechanisms, and applications in water purification, *J. Water Process Eng*. **2022**, *47*, 102815, doi: 10.1016/j.jwpe.2022.102815.

[20] Ren, S.; Rong, P.; Yu, Q. Preparations, properties and applications of graphene in

functional devices: A concise review, *Ceram. Int*. **2018**, *44*, 11940–11955, doi: 10.1016/j.ceramint.2018.04.089.

[21] Krishna, R. H.; Chandraprabha, M. N.; Samrat, K.; Murthy, T. P. K.; Manjunatha, C.; Kumar, S. G. Carbon nanotubes and graphene-based materials for adsorptive removal of metal ions-A review on surface functionalization and related adsorption mechanism, *Appl. Surf. Sci. Adv*. **2023**, *16*, 100431, doi: 10.1016/j.apsadv.2023.100431.

[22] Kong, Q. P.; Zhang, H. Z.; Lan, Y. L.; Shi, X. Q.; Fang, Z. L.; Chang, Q.; Liu, J.; Wei, C. H. Functional graphene oxide for organic pollutants removal from wastewater: a mini review, *Environ. Technol*. **2023**, *44*, 3183–3195, doi: 10.1080/09593330.2022.2053754.

[23] Cai, X.; Tan, S.; Lin, M.; Xie, A.; Mai, W.; Zhang, X.; Lin, Z.; Wu, T.; Liu, Y. Synergistic antibacterial brilliant blue/reduced graphene oxide/quaternary phosphonium salt composite with excellent water solubility and specific targeting capability, *Langmuir* **2011**, *27*, 7828−7835, doi: 10.1021/la201499s.

[24] Shen, Z. T.; Kuang, Y. X.; Zhou, S. X.; Zheng, J.; Ouyang, G. F. Preparation of magnetic adsorbent and its adsorption removal of pollutants: An overview, *Trac-Trend Anal. Chem*. **2023**, *167*, 117241, doi: 10.1016/j.trac.2023.117241.

[25] Shah, J.; Jan, M. R.; Zeeshan, M.; Iqbal, M. Removal and extraction of para-nitrophenol from aqueous samples using graphene magnetic nanocomposite *Arab J Sci Eng*. **2017**, *42*, 4465–4472, doi: 10.1007/s13369-017-2713-x.

[26] Lin, J. Y.; Liu, Y.; Hu, S.; Zhang, Y. F.; Qian, C.; Li, A.; Zhang, S. P.Ultra-fast adsorption of four typical pollutants using magnetically separable ethanolamine-functionalized graphene, *Sep. Purif. Technol*. **2021**, *271*, 118862, doi: 10.1016/j.seppur.2021.118862.

[27] Gotovac, S.; Honda, H.; Hattori, Y.; Takahashi, K.; Kanoh, H.; Kaneko, K. Effect of nanoscale curvature of single-walled carbon nanotubes on adsorption of polycyclic aromatic hydrocarbons, *Nano Lett*. **2007**, *7*, 583–587, doi: 10.1021/nl0622597.

[28] Teoh, Y. P.; Ali Khan, M.; Choong, T. S. Y. Kinetic and isotherm studies for lead adsorption from aqueous phase on carbon coated monolith, *Chem. Eng. J*. **2013**, *217*, 248–255, doi: 10.1016/j.cej.2012.12.013.

[29] Zhao, G. X.; Li, J. X.; Wang, X. K. Kinetic and thermodynamic study of 1-naphthol adsorption from aqueous solution to sulfonated graphene nanosheets, *Chem. Eng. J*. **2011**, *173*, 185−190, doi: 10.1016/j.cej.2011.07.072.

[30] Langmuir, I. The constitution and fundamental properties of solids and liquids. Part I. Solids, *J. Am. Chem. Soc*. **1916**, *38*, 2221−2295, doi: 10.1021/ja02268a002.

[31] Rodríguez, A.; Gracía, J.; Ovejero, G.; Mestanza, M. Adsorption of anionic and cationic dyes on activated carbon from aqueous solutions: Equilibrium and kinetics, *J. Hazard. Mater*. **2009**, *172*, 1311− 1320, doi:10.1016/j.jhazmat.2009.07.138.

[32] Isiyaka, H. A.; Jumbri, K.; Sambudi, N. S.; Zango, Z. U.; Abdullah, N. A. F.; Saad, B.; Mustapha, Adsorption of dicamba and MCPA onto MIL-53(Al) metal-organic framework: response surface methodology and artificial neural network model studies, *RSC Adv*. **2020**, *10*, 43213–43224, doi: 10.1039/d0ra07969c.

[33] Wang, Q. H.; Yang, M.; Qi, X. D.; Wang, J. X.; Sun, K.; Li, Z. H.; Deng, G. W. A novel graphene oxide decorated with halloysite nanotubes (HNTs/GO) composite used for the removal of levofloxacin and ciprofloxacin in a wide pH range, *New J. Chem*. **2021**, *45*, 18315-18326, doi: 10.1039/d1nj03807a.

[34] Kamaraj, R.; Pandiarajan, A.; Gandhi, M. R.; Shibayama, A.; Vasudevan, S. Eco-friendly and easily prepared graphene nanosheets for safe drinking water: Removal of chlorophenoxyacetic acid herbicides, *ChemistrySelect.* **2017**, *2*, 342–355, doi: 10.1002/slct.201601645.

[35] Daiem, M. M. A.; Rivera-Utrilla, J.; Sánchez-Polo, M.; Ocampo-Pérez, R. Single, competitive, and dynamic adsorption on activated carbon of compounds used as plasticizers and herbicides, *Sci. Total Environ*. **2015**, *537*, 335–342, doi: 10.1016/j.scitotenv.2015.07.131.

[36] Zhao, R. G.; Li, Y. J.; Ji, J. H.; Wang, Q. Y.; Li, G. R.; Wu, T.; Zhang, B. Efficient removal of phenol and *p*-nitrophenol using nitrogen-doped reduced graphene oxide, *Colloid Surface A-Physicochem. Eng. Aspect* **2021**, *611*, 125866, doi: 10.1016/j.colsurfa.2020.125866.

Chapter 8

Conclusions and Future Work

8.1 General Conclusions

In **Chapter 3** a new and simple electrochemical sensor for the electrochemical detection of MCPA was developed through activating a glassy carbon electrode (A-GCE). The activated electrode A-GCE was characterised by cyclic voltammetry, electrochemical impedance spectroscopy and scanning electron microscopy (SEM). Optimum conditions for the preparation of the sensor were obtained and a highly efficient sensor for the detection of MCPA was constructed by selecting phosphate anions as the supporting electrolyte, an ideal potential window from −2.0 to 2.4 V vs. SCE and the suitable number of 30 cycles in PBS (0.05 M) adjusted to a pH of 5.3. The constructed sensor achieved good sensitivity towards MCPA with a peak current density of 11.23 mA cm^{-2}. The influence of the solution pH on the oxidation of MCPA was studied, revealing that the oxidation peak current became lower in more alkaline solutions. The influence of the scan rates on the oxidation reaction of MCPA at the sensor A-GCE was examined, confirming that the oxidation reaction of MCPA at A-GCE was an absorption-controlled process. The sensing performance of the A-GCE sensor was evaluated with the detection of MCPA at different concentrations and impressive electrochemical detection achieved, with a wide dynamic linear region, extending from 1 to 850 μM and a LOD value of 0.02 μM obtained using cyclic voltammetry, while the LOD was further reduced to 0.008 μM with DPV. This was accompanied by good reproducibility and stability. It was further observed that 4-chloro-2-methylphenol produced from the oxidation of MCPA was reduced at the activated GCE. This shows that the A-GCE can not only be employed in the electrochemical detection of MCPA but may also be used to follow the degradation efficiency of MCPA by monitoring the 4-chloro-2-methylphenol concentration.

Chapter 4 fabricated a novel electrochemical sensor for the electrochemical detection of *para*-nitrophenol (*p*-NP), an aromatic aquatic pollutant, through the modification of a simple activated GCE with bismuth dendrites (A-GCE/Bi). The results showed that a simple A-GCE combined with a 400 s period for the electrodeposition of bismuth can be used to give the effective detection of *p*-NP in aqueous systems. The prepared sensor

A-GCE/Bi was characterised by cyclic voltammetry, electrochemical impedance spectroscopy and scanning electron microscopy (SEM) coupled with electron dispersive X-Ray analysis (EDX) and elemental mapping. To achieve the best sensing performance, the deposition potentials and time used to deposit the Bi dendrites on the GCE were investigated and the optimum conditions for the deposition of Bi on GCE were found. Subsequently, a highly efficient sensor, A-GCE/Bi, for the detection of *p*-NP was fabricated by the modification of A-GCE with the Bi film at the deposition potential of −1.0 V and the time of 400 s in 1.0 mM $Bi(NO_3)_3$ at a pH of 1.2~1.5. The fabricated sensor displayed good detection of *p*-NP with a peak current of 55.62 μA compared with bare GCE, A-GCE and GCE/Bi, at the same concentration of *p*-NP. The influence of the solution pH on the reduction of *p*-NP was examined, showing that the reduction peak current gave a highest value at pH 7.0. The influence of the scan rates on the reduction of *p*-NP at the A-GCE/Bi sensor was studied, demonstrating that the reduction reaction of *p*-NP at A-GCE/Bi was a mixed diffusion adsorption process. The sensing performance of the A-GCE/Bi was evaluated using DPV technique. An impressive limit of detection of 0.18 nM coupled with very good reproducibility, repeatability, recovery in water and acceptable selectivity were achieved. The good detection in the presence of the bismuth dendrites was attributed to enhanced adsorption of the *p*-NP. While various electrocatalytic materials have been synthesised and then drop-cast onto GCE to form a myriad of electrochemical sensors, this simple electrodeposition approach avoids the need for drop-casting. Moreover, the bismuth dendrites can be easily regenerated making this combination suitable in complex media that may otherwise contaminate or poison the electrode surface.

Chapter 5 constructed a simple and effective sensor for the electrochemical detection of metronidazole (MTZ). This sensor was fabricated through a facile electrodeposition process, where Gr nanoplatelets were initially deposited onto the glassy carbon electrode followed by an electrodeposition of Bi from an acidified Bi(III) solution. The prepared sensor GCE/Gr/Bi was characterised by cyclic voltammetry and scanning electron microscopy (SEM) coupled with electron dispersive X-Ray analysis (EDX) and elemental mapping. The SEM image showed the Bi was well dispersed across the

surface of the GCE/Gr. To attain the best sensing performance, the deposition potentials and time employed in the deposition of Bi on the GCE were tested and the optimum conditions for the deposition of Bi film on GCE were found. Further, a highly efficient sensor for the detection of MTZ was prepared by the modification of GCE/Gr with Bi nanostructures at the deposition potential of −1.0 V for 100 s in 1.0 mM $Bi(NO_3)_3$ at a pH of 1.2~1.5. The influence of the scan rates on the reduction of MTZ at the GCE/Gr/Bi was surveyed. The results indicated that the reduction reaction of MTZ at the GCE/Gr/Bi was an adsorption-controlled process. The developed sensor performed well to give a linear concentration range, good selectivity, good recovery and a low LOD value of 0.9 nM. Nevertheless, it is the simplicity of the sensor fabrication process coupled with the ability to readily regenerate the Bi deposits that makes this an interesting sensor. Indeed, this simple approach could be employed in the analysis of other analytes, where the generation of a new clean surface is important.

Chapter 6 manufactured a simple, easily prepared, and cost-effective GCE/Gr/Cu sensor, which was successfully employed in the electrochemical detection of the antibiotic levofloxacin (LEVO). The sensor was fabricated using a binder-free sequential electrodeposition approach of Gr and Cu, providing a promising platform in the electrochemical detection of antibiotics. The developed sensor GCE/Gr/Cu was characterised by cyclic voltammetry and scanning electron microscopy (SEM) coupled with electron dispersive X-Ray analysis (EDX) and elemental mapping. The CuNPs were mostly deposited onto the Gr sheets, with the Cu deposition adopting ball like deposits and some larger nanoparticles. To perform the best sensing property for the detection of LEVO, the deposition conditions of Gr and CuNPs on the GCE were investigated, including scanning cycles for Gr deposition and deposition time for CuNPs formation, and the best conditions in detecting LEVO were found. The Gr was assembled on the GCE, GCE/Gr, by electrodeposition from a suspension of Gr dispersed in PBS in the potential range from −1.5 to 0.8 V vs. SCE with 10 cycles. The CuNPs was formed on the GCE/Gr, GCE/Gr/Cu, by electrodeposition from an aqueous solution of $Cu(Ac)_2$ in NaAc and HAc at a pH of 4.5 at the potential of −0.25 V vs. SCE for 50 s. The prepared GCE/Gr/Cu revealed better detection of LEVO than bare GCE,

GCE/Gr and GCE/Cu, at the same concentration of LEVO. Further, the investigation of the influence of the scan rates on the oxidation of LEVO indicated that the oxidation reaction of LEVO at the GCE/Gr/Cu was a diffusion-controlled process. The sensing performance of the GCE/Gr/Cu was evaluated with the detection of LEVO in different concentrations by using CV and DPV techniques, delivering a limit of detection of 11.86 nM for CV and 18.56 nM for DPV. Moreover, very good reproducibility, selectivity, and stability over an extended period of 21 days were seen. Therefore, the simply prepared GCE/Gr/Cu has the potential to serve as an efficient, sensitive, and stable sensor for the effective electrochemical detection of LEVO and indeed other antibiotics.

Chapter 7 used magnetic graphene nanoplatelets as the adsorbent to adsorb and remove the four pollutants, MCPA, *p*-NP, MTZ and LEVO. The magnetic graphene nanoplatelets, Gr/Fe, were synthesised by the deposition of zero-valent iron (Fe) onto graphene nanoplatelets (Gr) and characterised for surface morphology and composition by scanning electron microscopy (SEM) coupled with electron dispersive X-Ray analysis (EDX) and elemental mapping. Using the liquid-phase reduction method, the zero-valent iron (Fe) was formed by the chemical reduction of Fe^{II} in the presence of $NaBH_4$. The UV-vis spectra of MCPA, *p*-NP, MTZ and LEVO were measured, and their characteristic absorption wavelengths were found. The adsorption performance of the Gr/Fe as the adsorbent for MCPA, *p*-NP, MTZ and LEVO from aqueous samples, was investigated using UV-vis spectroscopy and the characteristic absorption wavelengths were used to monitor the changes in the absorbance before and after adding the adsorbent. Accordingly, the decreases in the concentrations of the four compounds were computed based on the Beer-Lambert law. Different experimental factors, such as adsorbent dose, contact time between adsorbent and adsorbate, initial pH, and concentration of the adsorbate solution, were studied. The study on the influence of the solution pH on the adsorption capacity of the adsorbent indicated at low pH the removal percentages of the four compounds were high and then decreased with an increase of the solution pH. Further, experimental data indicated that the kinetic models were explained best by the pseudo-second-order kinetic model and the isotherm data followed the

Langmuir isotherm. The reproducibility, selectivity, and reusability of the Gr/Fe as the adsorbent were evaluated. The findings implied that the Gr/Fe adsorbent displayed good reproducibility, acceptable selectivity, and reusability. The π-π interaction was considered as the main mechanism involved in the adsorption process.

8.2 Future Work

As detailed above in Section 8.1, electrochemical sensors were developed for four water contaminants and these sensors exhibited impressive stability, selectivity, and sensitivity. It would be interesting to use these sensors with other analytes/contaminants and in more complex environments (such as wastewater, sea water) to establish the true potential of the bismuth nanostructures, copper nanoparticles and graphene nanosheets. In addition, the morphologies of the electrodeposited Bi and Cu nanostructures could be altered to determine if the morphology has any influence on the performance of the sensors. The nature of graphene (graphene sheets, graphene oxide, reduced graphene oxide, graphene quantum dots) appears to be important and a thorough study on the influence of the nature of graphene would be interesting. In terms of real time monitoring of the pollutants, screen printed electrodes are useful. Carbon-based screen-printed electrodes could be employed with the developed bismuth, graphene, and copper electrocatalysts for the real time analysis of water samples. Since glassy carbon can be easily activated and appears to facilitate the electron transfer reaction, it would be important to establish if screen printed carbon could be activated using a similar approach. While electrodeposition approaches avoid the need to use binders, such as Nafion, it would be interesting to design a study to compare both approaches, (1) electrodeposition of the electrocatalysts and (2) drop casting of the electrocatalysts using binders.

The magnetic graphene adsorbents have exhibited the ability to remove four structurally different pollutants from aquatic environments. To improve its adsorption capacity, the magnetic graphene could be further modified with metal-organic frameworks and/or

cyclodextrins or calixarenes to provide the adsorbents with molecular recognition characteristics for specific pollutants. Furthermore, the magnetic graphene could be synthesised by the fabrication of graphene and Fe_3O_4 composites to compare the effectiveness of Fe and Fe_3O_4 as the magnetic component. Finally, real water systems are complex and contain different inorganic and organic pollutants. Consequently, it is necessary to investigate the competition and synergetic mechanisms between graphene-based composites and inorganic and/or organic pollutants in real water environment systems.

Publications

1. **Yu, T**.; Glennon, L.; Fenelon, O.; Breslin, C. B.* . Electrodeposition of bismuth at a graphene modified carbon electrode and its application as an easily regenerated sensor for the electrochemical determination of the antimicrobial drug metronidazole. *Talanta*. **2023**, *251*, 123758.

2. **Yu, T**.; Herdman, K.; Kasturi, P. R.; Breslin, C. B.* The ultrasensitive detection of p-nitrophenol using a simple activated carbon electrode modified with electrodeposited bismuth dendrites. *Microchemical Journal*, **2023**, *195*, 109453.

3. **Yu, T.**; Fenelon, O.; Herdman, K. M.; Breslin, C. B.* The electrochemical detection of 4-chloro-2-methylphenoxyacetic acid (MCPA) using a simple activated glassy carbon electrode. *Journal of the Electrochemical Society*, **2022**, *169*, 037514.

4. **Yu, T.**; Breslin, C. B.* Two dimentional graphene and graphene-like materials and their promising applications in the generation of hydrogen peroxide. *Journal of the Electrochemical Society*, **2020**, *167*, 126502.

5. **Yu, T.**; Breslin, C. B.* Graphene modified composites and electrodes and their potential applications in the Electro-Fenton process. *Materials*, **2020**, *13*, 2254.

6. **Yu, T.**; Bresli, C. B.* Two-dimensional titanium carbide MXenes and their emerging applications as electrochemical sensors. *Journal of the Electrochemical Society*, **2019**, *167*, 037514.

7. Healy, B.; **Yu, T**.; da Silva Alves, D. C.; Okeke, C.; Breslin, C. B.* Cyclodextrins as molecular recognition systems: applications in the fabrication of electrochemical sensors. *Materials*, **2021**, *14*, 1668.

8. Fox, C. M.; **Yu, T.**; Breslin, C. B.* Electrochemical formation of silver nanoparticles and their catalytic activity immobilised in a hydrogel matrix. *Colloid and Polymer Science,* **2020**, *298*, 549-558.

9. Annibaldi, V.; **Yu, T.**; Breslin, C. B.* Electrostatic interactions between viologens and a sulfated β–cyclodextrin; formation of insoluble aggregates with benzyl viologens. *Journal of Inclusion Phenomena and Macrocyclic Chemistry*, **2020**, *96*, 155-167.

10. da Silva Alves, D. C.; Healy, B.; **Yu, T**.; Breslin, C. B.* Graphene-based materials immobilized within chitosan: applications as adsorbents for the removal of aquatic pollutants. *Materials*, **2021**, *14*, 3655.

11. Healy, B.; Rizzuto, F.; de Rose, M.; **Yu, T**.; Breslin, C. B.* Electrochemical determination of acetaminophen at a carbon electrode modified in the presence of β-cyclodextrin: Role of the activated glassy carbon and the electropolymerised β-cyclodextrin. *Journal of Solid State Electrochemistry*, **2021**, *25*, 2599-2609.

12. Harley, C. C.; Annibaldi, V.; **Yu, T.**; Breslin, C. B.* The selective electrochemical sensing of dopamine at a polypyrrole film doped with an anionic cyclodextrin. *Journal of Electroanalytical Chemistry*, **2019**, *855*, 113614.

13. Healy, B.; **Yu, T.**; Alves, D. C. S.; Breslin, C. B. Review of recent developments in the formulation of graphene-based coatings for the corrosion protection of metals and alloys. *Corrosion and Materials Degradation*, **2020**, *1*, 296-327.